Cerebrospinal Fluid Flow in Normal and Hydrocephalic Brains

BY

BRIAN J. SWEETMAN
B.S., University of Illinois at Chicago, 2001
M.S., University of Illinois at Chicago, 2007

THESIS

Submitted as partial fulfillment of the requirements for the degree
of Doctor of Philosophy in Bioengineering
in the Graduate College of the
University of Illinois at Chicago, 2011

Chicago, Illinois

This dissertation is dedicated to my wife, Jessica, without whom it would never have been accomplished.

ACKNOWLEDGEMENTS

I would like to express the highest gratitude to my advisor, Prof. Andreas Linninger for providing invaluable guidance, support, and encouragement throughout my graduate studies. I am also grateful to my committee members Prof. Thomas Royston, Prof. Craig Foster, Michalis Xenos, PhD, and Madhawa Hettiarachchi, PhD for their insights and suggestions which added great value to this work.

I would also like to acknowledge my graduate student colleagues at LPPD who have helped in various aspects of this work: Ian Gould (help with dissertation editing and code verification), Sukhraaj Basati (helpful discussions and insights about hydrocephalus), and Nikhil Sindhwani (helpful discussions regarding solid mechanics). I would also like to acknowledge the valuable collaboration with LPPD graduate students Ying Hsu, Seon Kim, and Eric Lueshen as well as undergraduate researchers Nicholas Vaičaitis, Cierra Hall, Brian Henry, and Laura Zitella.

TABLE OF CONTENTS

TABLE OF CONTENTS (continued)

CHAPTER PAGE

TABLE OF CONTENTS (continued)

CHAPTER PAGE

TABLE OF CONTENTS (continued)

CHAPTER PAGE

TABLE OF CONTENTS (continued)

CHAPTER PAGE

LIST OF TABLES

TABLE PAGE

LIST OF FIGURES

FIGURE PAGE

LIST OF FIGURES (continued)

FIGURE PAGE

LIST OF FIGURES (continued)

FIGURE PAGE

LIST OF FIGURES (continued)

FIGURE PAGE

FIGURE PAGE

FIGURE PAGE

FIGURE PAGE

FIGURE PAGE

FIGURE PAGE

LIST OF FIGURES (continued)

FIGURE PAGE

FIGURE PAGE

SUMMARY

A series of computational models were developed to better understand clinical measurements of cerebrospinal fluid flow in normal and hydrocephalic human brains. Because the available clinical measurements include information about CSF flow in only a few points of interest, the models are useful for quantifying CSF pressures and velocities throughout the entire craniospinal system.

A 2d model of the craniospinal system was used to predict the onset of acute communicating hydrocephalus by increasing the CSF outflow resistance. Predicted pressures and pressure gradients in the disease state were in good agreement with pressure measurements in hydrocephalic dogs (Linninger, Tsakiris et al. 2005).

A 3d model of the craniospinal system was used to quantify complex flow patterns in the ventricular system. We found that large Womersley numbers in the ventricular system lead to a phase lag between the flow direction and the instantaneous pressure gradient. More work is needed to assess whether significance changes in ventricular flow patterns are a cause or consequence of hydrocephalus or other cerebrospinal fluid disorders.

Finally, this dissertation presents a novel method for integrating blood flow, CSF flow, and brain tissue motion into one comprehensive intracranial dynamics model. We seek to use the model to quantify CSF motion as a function of cerebral vasculature expansion in the brain. Overall, the models presented in this dissertation provide insight into the complex mechanical interactions occurring in the brain, and in the future may be a useful tool for assessing abnormal brain function.

1. AN OVERVIEW OF "CEREBROSPINAL FLUID FLOW IN NORMAL AND HYDROCEPHALIC BRAINS"

Cerebrospinal fluid (CSF) is a colorless liquid that bathes the brain and spinal cord; the density and viscosity of CSF is approximately that of water. CSF is produced via active transport through the capillary network of the choroid plexi, which are found throughout the brain's ventricular system (Johanson, Duncan et al. 2008). Due to constant CSF production there is bulk flow of CSF throughout the cranio-spinal system. However, clinical studies focused on describing the flow of CSF have shown that CSF flow is pulsatile. A small amount of CSF flows into the spinal canal during cardiac systole with an equal amount flowing back to the brain during cardiac diastole.

The prevalence of diseases such as hydrocephalus and syringomyelia has motivated scientists to investigate the natural flow patterns of CSF. Cine-phase-contrast-MRI (CINE-MRI) is a noninvasive imaging technique which allows scientists to quantify the flow of CSF in various regions of the cranio-spinal system. The collaboration between Andreas Linninger (Professor in Bioengineering and Director of the Laboratory for Product and Process Design at the University of Illinois at Chicago) and Neurosurgeon Dr. Richard Penn has led to a library of CSF flow data from normal and hydrocephalic patients. This library of historical data serves as the basis of this dissertation.

This dissertation will describe the methods for measuring CSF flow in the cranio-spinal system as well as describe the methods for developing mathematical models of the human brain. Through the chapters to follow, the importance of mathematical modeling of the cranio-spinal system will become evident. However, the fundamental message is this: measurements capture phenomena; mathematical models help explain phenomena.

The chapter to follow describes a clinical study of CSF flow in normal patients and patients with hydrocephalus. In the study, the net CSF flow through the lateral ventricles was compared between normal subjects and patients with hydrocephalus. A significant finding was that in normal subjects the net CSF flow is out of the ventricles (in the direction from brain to spinal canal), whereas in hydrocephalic patients the net CSF flow is into the ventricles (in the direction from spinal canal to brain). When the hydrocephalic patients are treated with a ventricular shunt, in the majority of patients, net CSF flow reverses, resembling the pattern observed in normal patients. Moreover, an already existing mathematical model was used to quantify and support the clinical findings.

Remaining chapters describe various mathematical models aimed at describing certain aspects of intracranial dynamics. Advancements in scientific computing and in our own understanding allow mathematical models to improve as well. Thus, predictions of CSF flow and pressures become more precise. This in fact is a major goal of mathematical modeling. With a better model, we can have greater assurance of predictive outcomes. The first model I describe in this dissertation is a compartmental model of the cranio-spinal system that includes the brain, cerebral vasculature, and CSF. All three domains are represented as cylinders. The power of this approach is that all mass and momentum transfers between different compartments can be represented analytically. It is a straightforward matter to change physiological conditions or parameters in the model to study a clinical experiment. In fact, the model becomes a virtual laboratory where clinical tests can first be tested on the model before unknown risks are undertaken in the clinical setting.

Compartmental models represent one type of modeling choice. Another, which is described in three separate chapters is a distributed model. In such a model, the domains are not simplified

into cylindrical compartments, but rather the geometry of the physical domain is retained. Those chapters will describe the methods for developing such models and describe aspects of the CSF flow that could not be understood using clinical measurements alone. For example, these models have the ability to predict pressure gradients in the cranio-spinal system. Moreover, pressure wave speed in the spinal canal and flow dynamics such as the Womersley number can be assessed only with mathematical models such as those described here. Furthermore, having shown the excellent match of the CSF flow field between measurements and the model, one can change the normal CSF reabsorption in the model to better understand the dynamics of hydrocephalus.

This dissertation closes with a final chapter devoted to an emerging field in mathematical modeling, that of multi-scale modeling. It is inconceivable to use a distributed model to capture the dynamics of the three largest contributors to intracranial dynamics, namely the cerebral vasculature, brain tissue, and CSF. The number of vessels in the cerebral vasculature network is well over one billion (Pardridge 2011). Currently, it is not possible to discretize the entire cerebral vasculature network simultaneously with the CSF and brain tissue for the purpose of developing a fluid-structure interaction model of all three domains. The length scale of the cerebral vasculature compared to the length scale of the brain and CSF is about 10,000 times smaller and makes simultaneous discretization of all domains infeasible. To circumvent this constraint, we have developed a multi-scale approach in which the vasculature is represented as discrete cylinders in which simplified flow laws can be applied. However, the brain tissue and CSF is discretized using a continuum (finite volume) approach. The work described in the final chapter should be seen as a first step; it is a conceptual framework. Comparisons or attempts to match the model with clinical data would at this stage be unfounded for several reasons. First,

the model is two-dimensional, whereas the brain of course is three-dimensional. Removing the third dimension puts obvious limits on the model, but however, is a necessary step to establish proof of concept. Secondly, the material properties of the brain are assumed linear elastic. In reality, the brain is a porous medium through which interstitial fluid freely flows. Thirdly, more clinical data is needed before attempting to predict quantitatively the blood flow through specific vessels or regions of the brain. Once the model is advanced to three-dimensions and more clinical data is at our disposal, one can discuss quantitative predictions of the model. At this stage, we should be content with the conceptual mathematical framework and qualitative results and conclusions. The numerous steps required to build the model and the mathematical framework used at each stage of the analysis are fully documented in the final chapter.

2. VENTRICULAR WALL MOVEMENTS AND CSF FLOW IN HYDROCEPHALUS

2.1. Summary

The dynamics of fluid flow in normal pressure hydrocephalus (NPH) are poorly understood. In the normal case, cerebrospinal fluid (CSF) flows out of the brain through the ventricles. However, ventricular enlargement during NPH may be caused by CSF back flow into the brain through the ventricles. A previous study showed this reversal of flow; additional clinical data is provided on NPH patients and supplemented with computer simulations to better understand the CSF flow and wall displacement and emphasize its clinical implications. In three NPH patients, CINE-MRI was used to measure the CSF flow and ventricular wall movement during the cardiac cycle. The CSF flow measurements were obtained at the outlet of the aqueduct of Sylvius. Calculation of the ventricular wall movement was determined from the complete set of CINE-MRI images obtained axially at the middle of the lateral ventricle. The data was obtained before and after CSF removal with a ventriculoperitoneal (VP) shunt with an adjustable valve. In order to supplement the clinical data, a computational model was used to predict the transmural pressure and flow. In normal subjects, net CSF flow was out of the brain tissue at 1.2 ml/min. For NPH patients, the net CSF flow was in the opposite direction—into the brain tissue—before shunting. After shunting, the magnitude of the fluid flow into the brain decreased, resembling the flow patterns observed in normal subjects. The MRI based measurements of the CSF flow direction and the lateral ventricle volume size change, and computer modeling of fluid dynamics lead us to conclude that the directional pattern and magnitude of CSF flow in NPH patients may be an indication of the disease state. This has practical implications for shunt design and understanding the mechanisms which produce hydrocephalus.

2.2. Introduction

In a large CINE-MRI study of normal (N=28) and hydrocephalus patients (NPH=11), Kim et. al (Kim, Choi et al. 1999) noted that patients with normal pressure hydrocephalus (NPH) had a net flow of CSF through the aqueduct from the 4th ventricle into the 3rd which they noted is opposite to that found in normal subjects. The "retrograde" net flow reversed to the normal "anterograde", with ventricular cranio-caudal flow pattern after ventricular-peritoneal shunting. This observation has important implications for an understanding of fluid dynamics of hydrocephalus and the effect of shunting. It means that in hydrocephalus, the brain parenchyma absorbs CSF via a transependymal route rather than produces it. Shunting is able to reverse this abnormality and allow flow again in the normal brain to ventricle route. We have confirmed their findings in normal subjects and in a small group of NPH patients and provide a computational model based on fluid dynamics to explain theirs and our findings. To see if the hyperdynamic flow patterns that they found in hydrocephalus cause abnormal ventricle wall movements, we have also measured lateral ventricular wall displacement in our normal subjects and in NPH patients. We found that wall movements are slightly larger in the hydrocephalus patients but do not change significantly with shunting, a result predicted by our fluid dynamic modeling. This has clinical implications for shunt design. If the pulsating CSF flow is the root cause of ventricular dilatation, then reducing such flow could be easily achieved by constructing a mechanical system that dampens CSF oscillations. Our findings suggest such a solution would not work and that the fundamental problem to be treated is the accumulation of CSF in the ventricles and the abnormal flow into brain tissue.

2.3. Methods

The details of the CINE-MRI techniques used in the study had been described in full in a previous article (Zhu, Xenos et al. 2006). The scans were done on the 3T GE Sigma system, GE

medical systems (Milwaukee Wisconsin USA), equipped with a standard quadrature birdcage head coil. Eight normal subjects, (ages 23 to 52, mean 35, equal males and females) were used as controls. Three patients diagnosed with normal pressure hydrocephalus and one with congenital aqueductal stenosis were studied before and after treatment with ventricular peritoneal shunting. (Medtronic Inc. Strata Shunt®, adjustable valve). The diagnosis of normal pressure hydrocephalus was made by clinical criteria, primarily gait disturbance and early mentation changes, and confirmed by a positive response to three or four days of continuous lumbar drainage. In retrospect the third patient with the diagnosis of NPH did not have the syndrome. He did not improve clinically with shunting, but his ventricular size did not decrease and his dementia progressed without further gait problems. The patient with aqueductal stenosis was shunted because of headaches and memory problems 12 years after his previous shunt revision. He is included to look for shunting changes in ventricular wall dynamics in obstructive hydrocephalus, not for aqueductal flow. Scans on the patients were taken a week before shunting and then 2-6 months later. The patients signed consent forms for the additional MRI scanning, and the study was approved by the institutional review Board at the University of Chicago. Note that some of the data on normal subjects was previously published but has been reanalyzed here (Linninger, Sweetman et al. 2009; Linninger, Xenos et al. 2009).

The CINE-MRI images were collected at an axial slice across the middle of the lateral ventricle (LV) to investigate the LV volumetric change, and an axial slice across the junction between the aqueduct of Sylvius and the 4th ventricle to measure the CSF flow rate. For the slice across LV, velocities in three directions were measured; images at 16 equidistant time frames were reconstructed per cardiac cycle. For the slice at the other location, only the velocity perpendicular to the slice plane was measured; 32 images were acquired at equidistant time

frames per cardiac cycle. Flow compensation and peripheral gating were applied for the two CINE-MRI measurements. A low maximum measurable velocity of 5 cm/sec was chosen at the limit to achieve a reasonable velocity resolution. Other MR imaging parameters were: TR/TE = 18/8.3 ms, flip angle = 200, FOV = 240 mm, slice thickness = 5 mm, matrix size = 256x192, 75% phase field of view to achieve an effective matrix resolution of 256x256. The pixel velocity in regions of CSF was corrected by subtraction of the time-average "velocity" of a nearby solid brain tissue within a 29x29mm^2 region having this pixel at its center. The CSF flow at the junction of the aqueduct of Sylvius and the 4th ventricle is estimated by the product of the average velocity at the cross section of the CSF pathway and the corresponding area. To estimate the LV wall movement, the edge between solid brain tissue and lateral ventricle was first manually drawn based on an image that showed the best cross section from a T1-weighted image that has been acquired at exactly the same scan plane. This drawing marks the initial pixel positions during a full cardiac cycle. The position shift of each pixel at the edge of the lateral ventricle was then estimated for each time frame of the cardiac cycle by integrating the velocity over time, including all three components of the velocity.

2.4. Results

The flow data on eight normal subjects was reanalyzed to calculate the net flow per cycle, then the net flow per minute. Every normal subject had net flow out through the cranial-caudal aqueduct, see Table 1. Using our standardized technique the average flow was 1.1 ml per minute with a range of 0.5 to 1.9 ml/min and a standard deviation of 0.6 ml/min. The average ventricular wall movement for these same subjects was 0.168 mm with a range of 0.12 to 0.18 mm.

In contrast, two of the three patients who had the initial clinical diagnosis of normal pressure hydrocephalus had a net flow into the third ventricle and lateral ventricles. The third patient that by later clinical course proved not to have NPH had flow in the normal direction. After

ventricular peritoneal shunting using an adjustable valve on a low pressure setting, the direction reversed in the first case and in the second was markedly reduced. In the non NPH patient the cranio-caudal flow increased. Table 1 also shows calculations of the displacement of the ventricular wall and lateral ventricle volume before and after shunting. The ventricular wall displacement was higher in hydrocephalics than in normals, 0.21 to 0.30mm compared to 0.17mm. Shunting had no significant effect on this movement. In the two patients who had excellent clinical responses to shunting with major improvements in gait and mentation, the ventricular size decreased and the inward flow pattern reversed to the normal direction. The patient with minimal clinical improvement, patient three, had no change in ventricular size and flow was initially outward; with shunting the outward flow increased. The patient with congenital aqueductal stenosis responded to shunting with a complete remission of his symptoms of mental confusion and headaches. His ventricular size decreased and the ventricular wall movement slightly increased after shunting.

Table 1: Observations of net flow and wall displacement during cardiac cycle and calculation of ventricular volume in patients with NPH before and after treatment and in healthy volunteers.

		Net Flow (ml/min)			Wall displacement (mm)			LV Vol (ml)		
Case or Group	Dx	Preop	Postop	Control	Preop	Postop	Control	Preop	Postop	Control
Case 1	AS	NP	NP		0.22	0.27		188	131	
Case 2	NPH	-8.8	-1.5		0.27	0.30		130	98	
Case 3	NPH	-5.6	0.76		0.24	0.21		172	120	
Case 4	"NPH"	1.17	3.07		0.25	0.26		123	123	
8 healthy volunteers				1.14±0.599			0.168±0.038			33±9.4

The patient in Case 4 did not have improvement with shunting and did not in retrospect have true NPH. Abbreviations: AS=congenital aqueductal stenosis; LV=lateral ventricle; NP=measurement not performed. † Group mean values (± SD) are given for 8 healthy volunteers.

Models of CSF flow and ventricular wall movement

In a recently published paper we modeled the combined blood, CSF flow and brain tissue dynamics of normals and in patients with hydrocephalus (Linninger, Xenos et al. 2009). Figure 1 shows the model and areas of interest for this chapter. The direction of flow is schematically

shown as well as wall displacement. The model predicted a reversal in the aqueduct net flow as the ventricular size enlarges due to impaired CSF absorption in the subarachnoid space. That model also predicted that as the ventricles enlarge the movement of the ventricular wall increases. This was shown as a graph of wall movement versus percentage change of ventricular size (Figure 6 in Linninger et al. (Linninger, Xenos et al. 2009)).

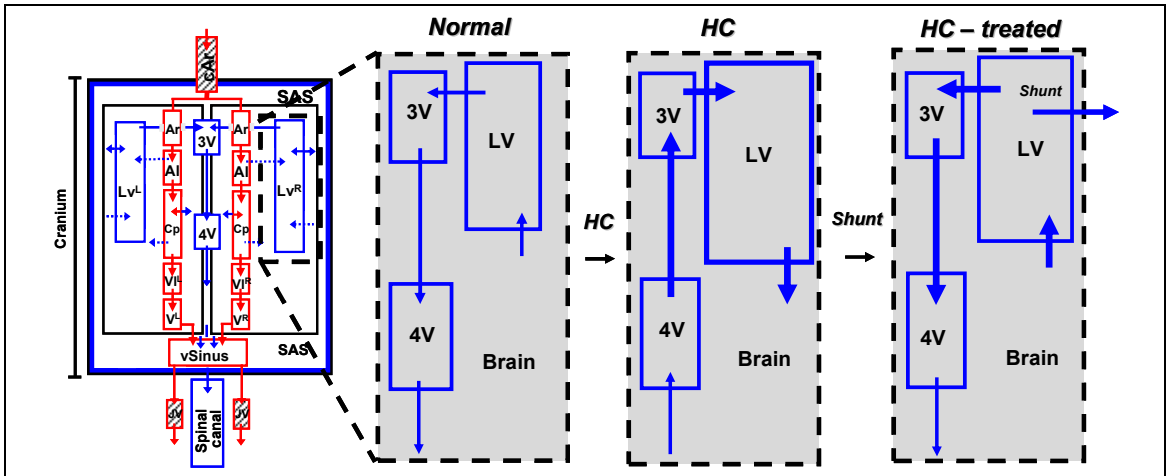

Figure 1. Schematic of the model highlighting areas of interest. Note that the normal pattern of CSF flow is from the third ventricle (3V) to the fourth ventricle (4V) and that this reverses in hydrocephalus. The obstruction to flow out of the subarachnoid space (SAS) to the venous sinus (vSinus) causes a reversal of the pressure gradient from the brain parenchyma to the lateral ventricles (LV), which in turn results in the flow direction change. The model predicts this reversal. The shunt reduces the gradient and brings the flow pattern back to normal. cAr = carotid artery; Ar = artery; AI = arteriole; Cp = capillary; V = vein; VI = venule. Superscript L and R refer to left and right, respectively. The thickness of the arrows indicates volume of flow and the relative size of the boxes indicate degree of wall displacement relative to the normal size.

To predict the effect of ventricular peritoneal shunting on the flow, we added in the right lateral ventricle of the model a drainage function with a valve set at a low resistance. After producing hydrocephalus by an absorption block, opening the drain resulted in the normalization of the flow pattern. Figure 2 shows the predicted transmural pressures which are calculated from the flow in normal subjects and in hydrocephalic patients before and after shunting. The magnitude of the average ventricular pressure (dashed line) varies when compared to the average

parenchyma pressure (solid line). In normals and in the shunted cases, ventricular pressure is lower than brain parenchymal pressure; this relationship is reversed in untreated hydrocephalus.

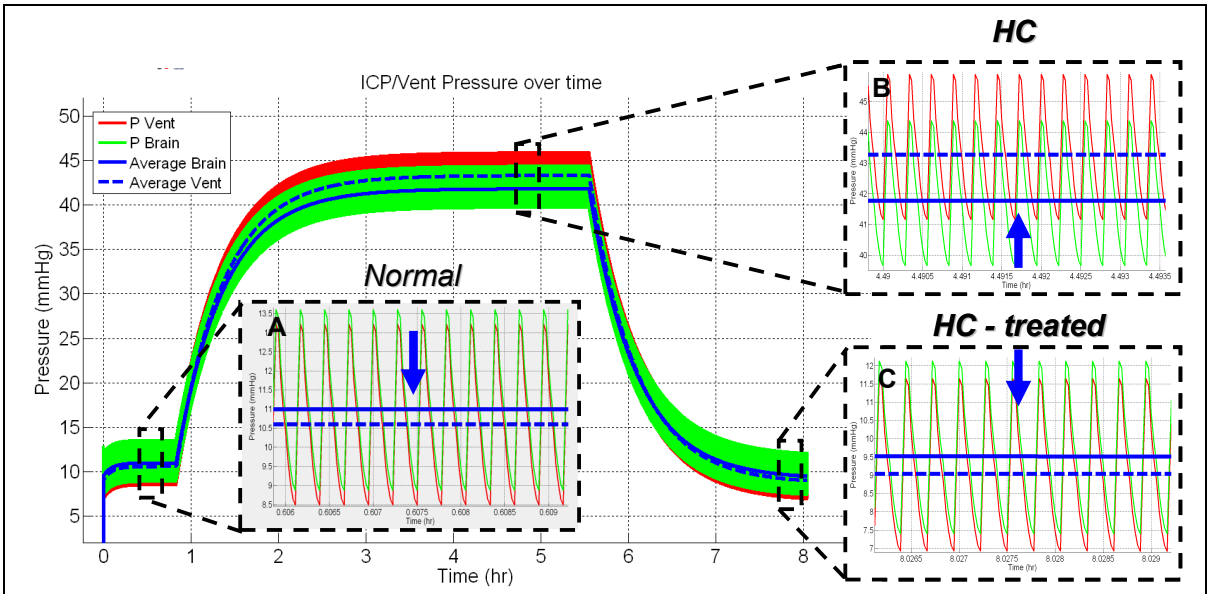

Figure 2. Computer simulation showing the pressure across the ventricle and brain parenchyma. The normal case (Frame A) shows a higher average brain pressure (solid line), which indicates flow from the brain to the ventricles. Frame B shows higher ventricular pressure (dashed line) due to hydrocephalus, which indicates flow reversal. Frame C shows the effect of fluid removal from the right ventricle and the reversal of pressure to normal.

2.5. Discussion

Our CINE-MRI studies show changes in the direction or magnitude of the net CSF flow in patients after shunting but no significant change in the ventricular wall movement. In our normal subjects the net flow is outward through the aqueduct. This flow pattern was shown by Grietz and confirmed by Huang (Greitz, Hannerz et al. 1994; Huang, Chung et al. 2004). Kim et al. also have found outward net flow in 28 healthy volunteers and what they call “retrograde” or reverse net flow caudal to cranial into the ventricles in 11-normal pressure hydrocephalus patients (Kim, Choi et al. 1999). The flow normalized after shunting. Our NPH patients confirm this reversal of flow with shunting. The flow of CSF into the ventricular system in hydrocephalus should not be a surprise. Cisternography with In 111 EDTA was one of the early methods used to

try to differentiate cerebral atrophy from clinically significant hydrocephalus. Distribution of the marker into the ventricular system from the basal cisterns and only later over the convexities was taken as an indication of communicating hydrocephalus. While the test is poorly predictive of the outcome of shunting, it still indicates a profoundly abnormal flow pattern in many hydrocephalus patients. Prior physiological measurements on normal production and convection of interstitial fluid by the brain parenchyma clearly established flow into the ventricles from the brain (Davson and Segal 1996; Abbott 2004). This fluid contributes up to one third of the total CSF exiting through the aqueduct. Increasing ventricular pressure slows this convective flow (Davson and Segal 1996). The net cranial to caudal flow in normal subjects is seen by CINE-MRI (Kim, Choi et al. 1999; Huang, Chung et al. 2004) and it is within the range measured by earlier physiological tracer studies. All of our eight normal subjects had this net outward flow pattern.

Shunting has a major effect on CSF dynamics and in particular the pressure volume relationship (Czosnyka, Czosnyka et al. 2004; Czosnyka, Cieslicki et al. 2005). The CSF compartment after shunting becomes more compliant. Even though the shunt is placed into the ventricle and removes CSF, the change in flow pattern in our patients after shunting reversed to normal. Most likely fluid drainage reduces the small pressure gradient from the ventricle to the brain tissue. The restitution of net CSF production of the brain parenchyma can then occur. Current MRI measurements are not sensitive enough to show such slow net fluid movements within the brain parenchyma, so other types of methods will be necessary to demonstrate this in humans. The CINE-MRI measurements show only a small increase in ventricular wall displacement during hydrocephalus. Shunting did not decrease this movement and in our only obstructive case the movement appeared to increase after shunting. In view of the small sub-

millimeter wall movement and its lack of change when ventricular volume decreases, theories which postulate wall movement as a cause of hydrocephalus may have to be reconsidered.

Computational models provide quantitative and qualitative information critical to the understanding of the disease. Our computational model suggests a net flow of CSF into the brain parenchyma during hydrocephalus, as shown in Figure 3. The fluid flow throughout the brain is plotted; showing that in the hydrocephalic case the net flow is into the brain, but reverses or decreases in the treated patient.

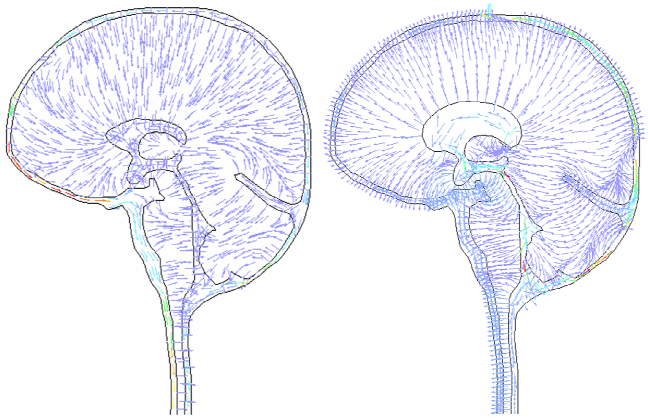

Figure 3. Computer simulation of CSF net flow in the normal and hydrocephalic brain. Net flow is from the parenchyma to the ventricles in the normal case (left); net flow is from the ventricles to the brain parenchyma in the hydrocephalic case (right).

The slight increase in wall movement is also predicted by our model. The measurements that we have made on ventricular wall movement pre-and post-shunting are difficult to interpret without an understanding of the forces at play at the ventricular wall during the cardiac cycle. For this the stresses on the wall need to be modeled using the known flow patterns of CSF and the laws of fluid dynamics. Using a number of modeling techniques we have simulated CSF and ventricular wall movements in normals and in communicating hydrocephalus (Linninger, Sweetman et al. 2009; Linninger, Xenos et al. 2009). The simulation results are consistent with

our CINE-MRI measurements. As would be expected, as hydrocephalus develops fluid increases in the ventricles and the entire compliance of the intracranial space is reduced and pressure increases. This increase is reflected also in an elevated pulse pressure. The maximum driving force on the ventricular wall due to the expansion of the less compliant brain is greater and results in a larger excursion of the wall. Since the ventricles are enlarged, the to and fro movement of CSF through the aqueduct is significantly increased (Egnor, Zheng et al. 2002; Chiang, Takoudis et al. 2009). This increased flow velocity has been taken as a measure of hydrocephalus and reflects larger ventricles and a reduced intracranial compliance. Our CINE-MRI measurements show an approximate 50% increase in wall movement between normal subjects and our hydrocephalic patients. It should be noted that these movements are very small, only 10ths of a millimeter. Using a viscoelastic model of the brain parenchyma, Wilkie et al. estimated that for a pulse pressure of 10 mmHg, simulating early hydrocephalus, the wall movement would be approximately 100 nanometers (Wilkie, Drapaca et al. 2010). For normals, the movement would be even less, perhaps 50 nanometers.

Our computational model has been extended to show the effect of shunting on aqueductal flow and ventricular wall movement. The results of this modeling are consistent with our MRI measurements of ventricular size and wall movement. Of note is how small the calculated forces acting on the ventricular wall are during the cardiac cycle. The model predicts a transmural pressure in normals ranging from 0.6 mm of mercury in systole to minus 0.2 mm of mercury in diastole. This cycle of transmural pressure drives CSF back and forth through the aqueduct. In hydrocephalus stroke volume is known to increase but according to our model the transmural pressure is no higher. This is in spite of a higher pulse amplitude and absolute CSF pressure. The larger stroke volume is most likely due to the lower compliance in the intracranial space. As

others have shown, the flow through the aqueduct is directly related to its increasing size in hydrocephalic patients and also to ventricular size (Chiang, Takoudis et al. 2009). Intuitively if the ventricle surface enlarges and the ventricle wall movement is the same more CSF will be driven to and fro in the aqueduct for the same pressures.

What are the stresses due to the cyclic pressure gradients on the ventricular wall? The distribution of stress has been estimated by finite element models for hydrocephalus and they predict that the regions of high curvature will be subjected to higher stresses than the flat areas (Pena, Bolton et al. 1999; Taylor and Miller 2004; Linninger, Sweetman et al. 2009). This modeling has been used to explain the early enlargement and edema in the frontal, temporal, and occipital horns. The wall movement we measured is an average of all the movements along the ventricular surface of the MRI slice through the largest area of the lateral ventricles. The technique is not sensitive enough to accurately measure different regions of the ventricle such as the flat surface along the thalamus or the curved regions like frontal horns. However, the gradual displacement of the ventricles in hydrocephalus is in the order of centimeters with volume changes often over 100 ml. This is two orders of magnitude higher than the cyclic wall movements of 0.1 to 0.3 mm. This means that the pulsating stresses on the wall are at least one hundred times less. If shunting were to work primarily by reducing pulse pressure one would expect the wall movements to decrease post shunting but this is not the case for the two patients who had deceases in ventricular volume. A surgical device which damps pulse amplitude alone would not deal with the primary pathology. The blockage to CSF absorption in the subarachnoid space must be compensated for by providing a new low resistance pathway, one that is large enough to decrease the abnormal pressure gradient and which allows fluid flow from the brain to the ventricle.

2.6. Conclusion

The CINE-MRI findings of Kim and our confirmatory observations provide an important clue to how shunts work. Shunting by removing fluid enables the brain once again to return to the normal pattern of transependymal flow outward into the ventricles. A small steady pressure gradient in the wrong direction into the brain tissue is enough to enlarge the ventricles (Linninger, Tsakiris et al. 2005; Levine 2008). Our measurements and those of others (Kim, Choi et al. 1999) of the net flow inward suggest such a gradient. Recent very precise measurements of pulse pressure amplitudes over thousands of cycles in hydrocephalus patients are also consistent with this analysis (Eide 2008). These patients had median pressure amplitudes of 0.4 mm of mercury higher in the ventricles compared to the brain parenchyma. In one patient who had the monitors still in place after shunting the pulse amplitude difference was reversed, the pressure becoming higher in the parenchyma than in the ventricles. These small differences in pressure found in patients are consistent with our CINE-MRI measurements. Modeling based on basic fluid dynamics also supports the view that small pressure gradients create ventricular enlargement (Linninger, Tsakiris et al. 2005; Levine 2008).

There are clinical consequences to this view of hydrocephalus. The first is that a mechanical system that dampens the increased oscillatory fluid movements found in hydrocephalus is unlikely to decrease ventricular size or reduce symptoms. Such a system would be easy to construct by providing a compliant chamber for CSF to flow into and out of. However, unless CSF is removed and the pressure gradients reversed, hydrocephalus will not change. Another clinical consequence of this understanding is that the shunt brings the flow pattern of CSF in the brain back to normal. A shunt that continues to function when normal flow patterns are achieved may cause harm by overdrainage. Unfortunately, at present there is no easy way to adjust shunt flow precisely to the value which would produce a normal state. “Smart shunts” that adjust to

physiological measurements have been suggested but have not yet been developed for use in patients.

Measurements of flow patterns of CSF as obtained by CINE-MRI may be useful for predicting the outcome of shunting. At present such measurements are time consuming and expensive. For the measurements to be worthwhile, they would have to be more accurate than current lumbar CSF drainage testing. Larger CINE-MRI studies will have to be done to establish how well they correlate with clinical response to shunting. If proven to be accurate in predicting patient outcome, the measurements have the great advantage of being non-invasive.

3. A MODEL OF BLOOD, CEREBROSPINAL FLUID AND BRAIN DYNAMICS

3.1. Summary

Using first principles of fluid and solid mechanics a comprehensive model of human intracranial dynamics is proposed. Blood, cerebrospinal fluid and brain parenchyma as well as the spinal canal are included. The compartmental model predicts intracranial pressure gradients, blood and cerebrospinal fluid flows and displacements in normal and pathological conditions like communicating hydrocephalus. The system of differential equations of first principles conservation balances is discretized and solved numerically. Fluid-solid interactions of the brain parenchyma with cerebral blood and CSF are calculated. The model provides the transitions from normal dynamics to the diseased state during the onset of communicating hydrocephalus. Predicted results were compared with physiological data from Cine phase–contrast magnetic resonance imaging to verify the dynamic model. Bolus injections into the cerebrospinal fluid are simulated in the model and found to agree with clinical measurements.

3.2. Introduction

Motivation

A variety of central nervous system diseases alter intracranial dynamics and changes in dynamics may in turn result in changes to the brain. An important example is hydrocephalus in which the cerebral ventricles enlarge, thus in effect displacing and compressing brain tissue. This condition is well described clinically, but its fundamental dynamic principles are poorly understood. The goal of our research is to provide such an understanding and by doing so point the way to new treatment based on this knowledge.

Current mathematical models do not incorporate the interaction between the cerebral vasculature, parenchyma and cerebrospinal fluid (CSF) during the cardiac cycle, and many models do not account properly for conservation of the fluid volume (Sorek, Bear et al. 1988; Lakin, Stevens et al. 2003). According to the Monro-Kellie doctrine, the cranium is a closed

system, enclosing the brain, CSF and cerebral blood; but for intracranial dynamics to be described correctly the spinal canal and its pulsating CSF displacements need to be included. The flow of CSF with each cardiac pulse into and out of the spinal subarachnoid space is well known by clinicians and has been measured by Cine phase–contrast MRI (Pelc, Bernstein et al. 1991; Loth, Yardimci et al. 2001; Raksin, Alperin et al. 2003; Zhu, Xenos et al. 2006). As we will show, it is critically important in accounting for CSF flow patterns inside the ventricular and subarachnoidal systems.

Background

Some early models of the brain vasculature have simplified the dynamics by lumping numerous compartments (Sorek, Feinsod et al. 1988; Sorek, Bear et al. 1989; Ursino and Lodi 1997; Stevens 2000). Other approaches use bundles of tubes to represent different types of cerebral blood vessels (Zagzoule and Marc-Vergnes 1986). Monro's first model of the intracranial cavity consisted of two compartments, brain and blood. This model was expanded by Karni to contain several fluid structures, including arterial, capillary, venous, venous sinus, jugular bulb, and cerebrospinal fluid pathways (Sorek, Bear et al. 1988). To refine the model, Karni et al, added an additional component, brain tissue, to the previous six compartments model. Piechnik and collaborators developed a mathematical model to study autoregulation and cerebral species transport in the human brain (Piechnik, Czosnyka et al. 2001). Marmarou derived a widely used mathematical model that describes intracranial pressure dynamics (Marmarou, Shulman et al. 1978). However, his model does not explicitly incorporate brain vasculature or the porous parenchyma in the calculations. Many researchers have based their experimental work on this model which correlates well with experimental data, but does not predict blood alterations or brain water content change (Czosnyka, Czosnyka et al. 2004).

For the current study, a more complete dynamic model consisting of the bi-phasic brain, arteries, arterioles, capillaries, veinules, veins, venous sinus, ventricles, subarachnoid space and the spinal canal will be described and compared to experimental results obtained from Cine phase–contrast MRI measurements. This multi-compartment mathematical model accounts for cerebral hemodynamics, the expansion or compression of the parenchyma and the CSF flow dynamics. The expansion of the vasculature is linked with the volumetric change of the brain parenchyma. In turn, changes in cerebral volume affect the space available to the ventricles and the cerebrospinal fluid. Due to the full coupling of the distensible blood vessels, CSF spaces, and the brain parenchyma, it is possible to solve dynamic force and mass balances of the entire system. The model is used to simulate normal and pathological conditions to determine the temporal change in intracranial pressures and volumes for the various brain structures. The brain parenchyma pressure is a function of the force interaction with the embedded cerebral vasculature and CSF. Hence, elevation of intracranial pressure (ICP) is not an input to the model, but is calculated by solving the model equations for the brain interacting with CSF and blood. Similarly, ventricular expansion is only possible as a function of force balances and flow equations. The objective is to describe and quantify the dynamic interactions between blood flow, ICP, extensions of the cerebral vasculature and brain parenchyma during the cardiac cycle, and how it is changed in pathological conditions. The modeling results should consistently describe the transient force interactions between blood, CSF and brain. Predictions of accurate states are a secondary objective.

Outline

The methods section describes the MRI techniques and acquisition of experimental data. Section two introduces the mathematical equations describing blood and CSF flow as well as the

equations for fluid and solid motion in the bi-phasic parenchyma. Results are presented in section three for normal intracranial dynamics and their validation with experimental MRI measurements. The pathological conditions of communicating hydrocephalus are predicted qualitatively and quantitatively. We show the use of standard clinical tests like a bolus injection to determine brain parameters, and compare results with previously published experiments in section four (Czosnyka, Czosnyka et al. 2002; Czosnyka, Czosnyka et al. 2004; Czosnyka, Cieslicki et al. 2005). Section five discusses our new mechanistic explanation of hydrocephalus, its implications, and the limitations of current models.

3.3. Methods

Measuring ICP in dog brains

Prior experiments with dogs were conducted to establish whether pressure gradients exist between the ventricles, brain tissue and subarachnoid space in acute or chronic hydrocephalus (Penn, Lee et al. 2005). The outcome of these experiments showed that no transmantle pressure differences between the ventricles and subarachnoid space could be detected in any of the dogs before kaolin administration or afterwards when hydrocephalus developed.

Cine phase-contrast MRI in the human brain

CSF flow velocity vectors were determined in eleven subjects, six normal and five with hydrocephalus, in several regions of interest using a Cine phase-contrast MRI technique. These velocity vectors were measured over the cardiac cycle using simultaneous gating (Dumoulin, Souza et al. 1988; Pelc, Bernstein et al. 1991) on a 3T GE Signa scanner, GE Medical Systems, Milwaukee, WI. The data acquisition and velocity calculation we used have been discussed elsewhere (Zhu, Xenos et al. 2006). Experimental results are summarized in Table 2.

Table 2. Comparison of maximum CSF flow velocity at prepontine area and junction between the aqueduct of Sylvius, *AS*, and 4th ventricle, *4V*. CH: Communicating hydrocephalus

	Average peak to peak flow velocity at prepontine (mm/s)	Average peak to peak flow velocity at AS and V4 (mm/s)	Average peak to peak flow velocity ratio (Prepontine/AS and V4)
Normal CSF (N_N=6)	37.06 ± 12.21	6.91 ± 3.95	5.36
CH (N_{HC}=5)	19.35 ± 7.11	23.56 ± 19.69	0.82

Size changes of the lateral ventricle were also determined by MRI. The axial slice with the largest size of the lateral ventricles was used. The edge between brain tissue and lateral ventricle was drawn based on T2- or T1-weighted images. This drawing marks the initial pixel positions during a full cardiac cycle. The position-shift of each pixel at the edge of the lateral ventricle is then estimated for each time frame of the cardiac cycle by integrating the velocity over time. The edge points of the lateral ventricle at each cardiac time frame were connected by spline interpolation (De Boor 2000). The area change of the enclosed region was then calculated by comparison with the time-averaged area of this enclosed region throughout the cardiac cycle assuming that the lateral ventricle changes its size uniformly. The total lateral ventricle volume change was estimated based on the T1-weighted volume images, after conversion of voxel dimensions to milliliters (Zhu, Xenos et al. 2006).

Cine phase–contrast MRI was also used to measure the timing of the arterial pulse wave; with mean blood pressure of 100 mmHg absolute. Figure 1 displays the MRI measurements of blood flow in the basilar artery (ml/min) (Zhu, Xenos et al. 2006). Table 2 provides a comparison of the aqueduct of Sylvius and fourth ventricle flow velocity and the prepontine flow velocity in normal and hydrocephalic subjects scanned with the Cine phase-contrast MRI technique. These measurements were used as a reference for the predictions of the mathematical model of intracranial dynamics.

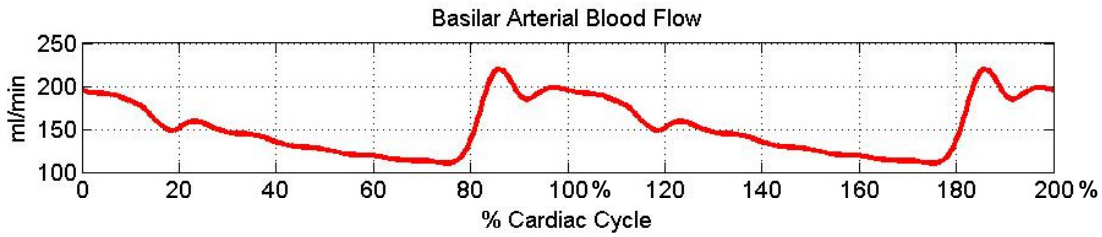

Figure 4. MRI was used to measure the blood flow in the basilar artery (ml/min) as a function of the cardiac cycle (100% = 1 beat). The basilar artery signal was represented with discrete Fourier series of seventeen coefficients: $c_0 = 102.3530$; $a_1 ... a_8 = (-0.0345, -0.0511, -0.0267, -0.0111, -0.0013, 0.0050, 0.0027, 0.0061)$; $b_1 ... b_8 = (0.1009, 0.0284, -0.0160, -0.0070, -0.0174, -0.0041, -0.0041, 0.0005)$.

Mathematical Model of Intracranial dynamics

In order to better understand the dynamic forces linking CSF with blood motion, a multi-compartment dynamical model of intracranial dynamics was designed. The model accounts for the force interaction of three principal elements – the cerebral vasculature, the CSF pathways and the bi-phasic brain parenchyma. Blood is modeled as viscous and incompressible fluid flowing through the cerebral vasculature, which is divided into arteries, arterioles, capillaries, veinules, veins and venous sinus. The CSF system includes the lateral, third and fourth ventricles, cerebral and spinal subarachnoid spaces which are all connected. The brain parenchyma, divided in two hemispheres, is treated as a bi-phasic medium composed of extracellular fluid and a solid cell matrix. The network of intracranial compartments and their connectivity is depicted in Figure 5. All compartments, except the spinal subarachnoid space, are enclosed inside the cranium. The Monro-Kellie doctrine of constant cranial volume is enforced rigorously. However, CSF can be displaced into the expandable spinal subarachnoid space which is not confined by the skull bone.

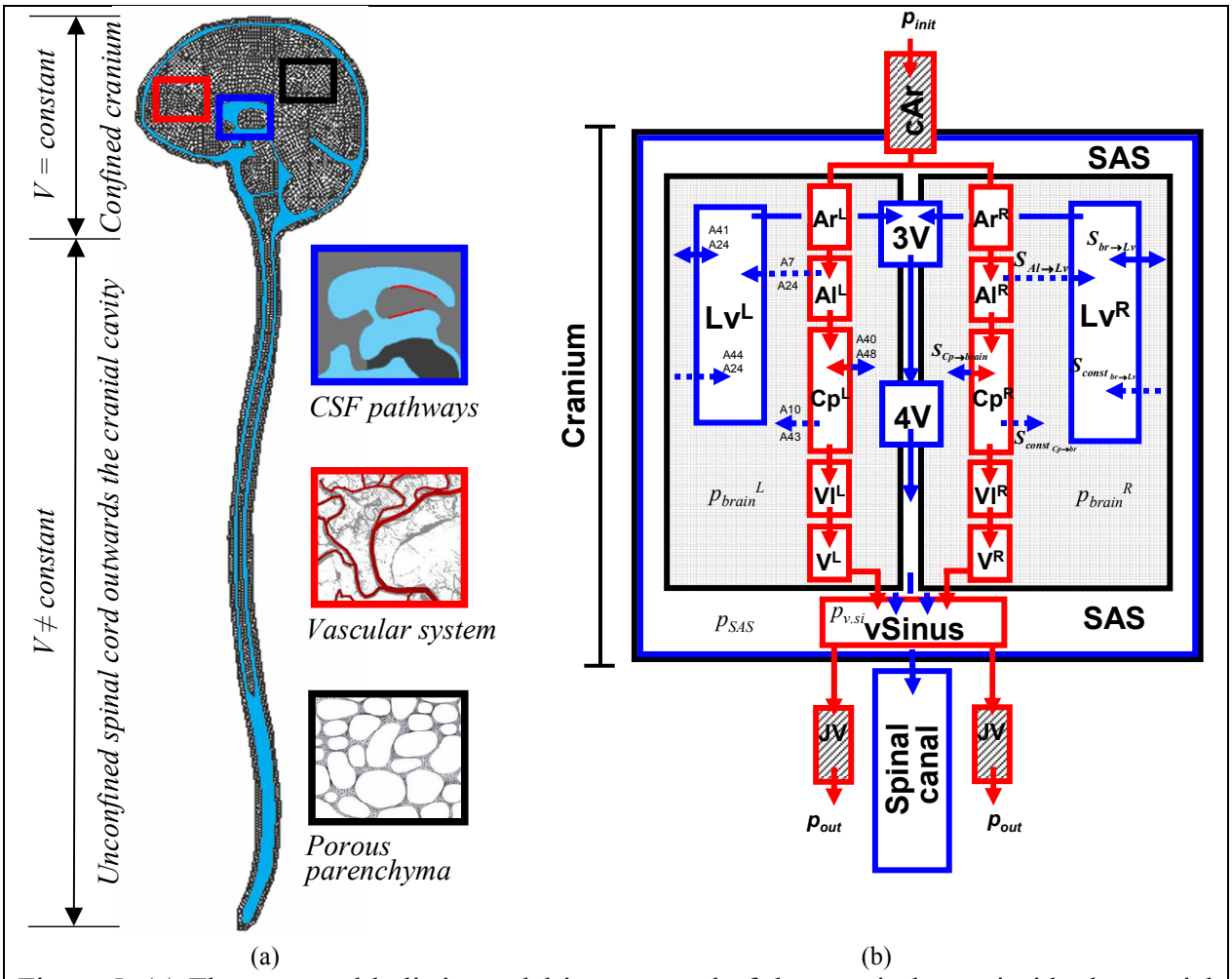

Figure 5. (a) The proposed holistic model is composed of three main layers inside the cranial vault–the *ventricular system*, the cerebral and spinal subarachnoid space, blue, where CSF flows, the *vascular system*, red, where blood flows; and the *parenchyma*, a bi-phasic medium with extracellular fluid motion and constant solid cell matrix, black. (b) The main blood compartments are the carotid artery, *cAr*, main arteries, *Ar*, arterioles, *Al*, capillaries, *Cp*, veinules, *Vl*, veins, *V*, venous sinus, *vSinus*, and jugular veins, *JV*. The CSF system is composed of the lateral ventricles, *Lv*, third and fourth ventricles, *3V*, *4V*, subarachnoid space, *SAS*, and the *spinal canal* outside of the cranium. The parenchyma is divided into the right and left hemisphere, indicated by superscript, L/R for individual compartments. The arterial pressure in the carotid is p_{init}; the venous pressure in the jugular vein is p_{out}. The ICP in the parenchyma is $p_{brain}^{L/R}$, and $p_{v.si}$ is the venous sinus pressure. Mass transfer fluxes between compartments are indicated by labels carrying the equation number with prefix A. Other mass transfer terms $S_{I\to II}$ describing fluid source and sink terms are explained in section 2. Dashed arrows indicate CSF production, while solid arrows signify pressure driven fluid exchange.

Fluid flow in our model is governed by the pressure difference between the carotid arteries and the jugular veins, Figure 5. The model contains one main artery as input, labeled cAr. The

carotid pressure signal, p_{init} is displayed in Figure 6c–Pin. This signal was based on Cine phase–contrast MRI measurements of a normal subject and was used as a dynamic boundary condition in the model; it was fitted using discrete Fourier series consisting of 17 coefficients enumerated in Figure 4.

$$p_{init}(t) = c_0 \left[1 + \sum_{k=1}^{8} a_k \cos(\omega t) + \sum_{k=1}^{8} b_k \sin(\omega t) \right], \ \omega = 2k\pi, \ k = 1, 2, ..., 8 \qquad (1\text{-}1)$$

The venous pressure signal, labeled p_{out} was assumed to be flat compared to the arterial signal with 3 mmHg absolute value and zero amplitude. The effects of gravity or body activity on the venous and intracranial pressures were neglected. Additional interior input conditions include the constant CSF production from the arterioles to the ventricles through the choroid plexus and the diffuse capillary production through the brain parenchyma to the ventricles.

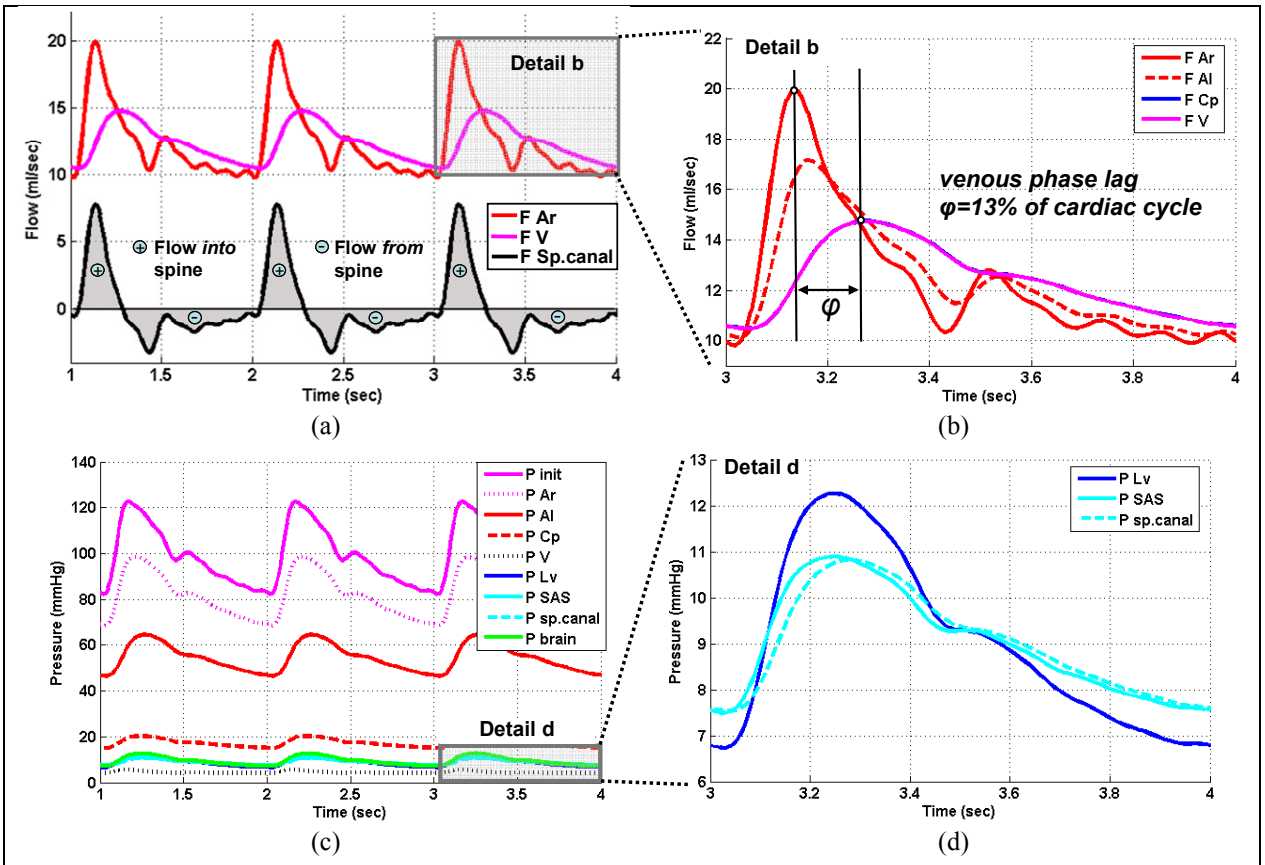

Figure 6. Simulated normal intracranial dynamics for an individual with a carotid blood pressure of 120/80 mmHg. (a) The flow in the vascular system (arteries, arterioles, capillaries, veinules, veins and venous sinus) has a mean value of 12.3 ml/s. The forward volume at each cardiac cycle in the spinal canal is approximately 0.9 ml (black line). (b) Detail b shows the volumetric blood flow rate for the arterial (upper red curve), arteriole (red dashed curve), capillary (blue curve), and the venous system (magenta curve). Frame (c) plots the intracranial pressure waveforms predicted by the model. Red lines represent blood pressures. The green line is the parenchymal pressure which is close to the ventricular, cerebral and spinal subarachnoid ICP. (d) Detail d displays the time dependent pressures for the ventricular system (dark blue), subarachnoid space (light blue), and the spinal canal (dashed).

We formulated mass and momentum balances to mathematically describe the flow of blood and CSF and its interaction with the bi-phasic brain compartments. The spatial dimensions were discretized to obtain 84 differential equations with 84 unknown deformations, coupled pressures and flows between the interacting blood, CSF and brain parenchyma. The model has three types of variables for each fluid compartment: the pressure at the center, p, inflow and efflux, f_{in} and f_{out}, as well as the hydraulic cross-sectional area, A. The equations for the right and left brain

hemisphere can be adjusted for symmetry or alternatively account for unilateral differences such as in Bering's one-sided hydrocephalic experiments on dogs (Bering 1962). Time integration was implemented by a fully implicit Euler scheme. The fully discretized algebraic system was solved numerically using a globally convergent step-size controlled Newton-Raphson method. Details of the numerical techniques can be found elsewhere, (Linninger, Xenos et al. 2007; Zhang, Kulkarni et al. 2007). Flow through each arterial, venous, or cerebrospinal fluid compartment is governed by three basic balances: continuity, momentum and distensibility which are described next.

The continuity equation

Continuity ensures that fluid is neither gained nor lost, consistent with the assumption of incompressible blood and CSF flow. The continuity equations can be written as in (1-2),

$$l\frac{\partial A}{\partial t} = f_{in} - f_{out} + S_{I\to II} \qquad (1\text{-}2)$$

where l is the hydraulic length of the compartment, $\partial A/\partial t$ is the change in cross-sectional area with respect to time, f_{in} and f_{out} are the volumetric flow rates in and out of the compartment, respectively. The source or sink terms, $S_{I\to II}$ account for mass transfer between different compartments as described next.

Fluid exchange between compartments

In addition, some fluid compartments also have permeable boundaries allowing fluid exchange with another phase. For example, CSF production involves mass exchange, $S_{I\to II}$, transferring blood plasma from the choroid plexuses into the ventricles, $S_{Al\to Lv}$. A second source of CSF production occurs throughout the brain parenchyma, which is accounted for by a constant CSF production from the brain capillaries into the extracellular space of the parenchyma, $S_{const_{Cp\to brain}}$. This diffusely produced CSF may also further seep from the extracellular space of the

parenchyma into the ventricles, $S_{brain \to Lv}$. Seepage from the capillary bed, $S_{Cp \to brain}$ may occur in both directions depending on the net Starling pressure difference between the capillary pressure and the surrounding brain, (Starling 1896). The specific equations for mass transfer between phases, $S_{I \to II}$, are given in the sections for vasculature, CSF and parenchyma.

Pressure Drops

Our model uses a simplified axial momentum balance similar to the Hagen-Poiseuille law.

$$p_{in} - p = \Delta p = a f_{in} \text{ with } a = 8\pi\mu l / A^2 \qquad (1\text{-}3)$$

p_{in} is the pressure of the upstream compartment and p is the pressure of the current compartment. The term a is a flow resistance term that accounts for the pressure drop in the fluid along the length of the compartment due to viscous forces; it is a function of the dynamic fluid viscosity, μ, the hydraulic length of the compartment, l, and square of the compartment's cross-sectional area, A. The momentum equation relates the pressure drop, Δp, to volumetric flow rate, f_{in}. Positive Δp along the vessel's axis causes flow into a compartment, otherwise the flow occurs in the opposite direction. For a thinner vessel, the flow resistance a increases and a larger pressure drop would be necessary to maintain the same flow rate.

Table 3. Physical parameters and their source for cerebral compartments of the intracranial dynamic model.

Location	*Elastance (Pa)*	*Volume at rest (cc)*
Arteries, *Ar*	27.3×10^4 (Zagzoule and Marc-Vergnes 1986)	30.0 (Zagzoule and Marc-Vergnes 1986)
Arterioles, *Al*	40.0×10^4 (Zagzoule and Marc-Vergnes 1986)	16.0 (Zagzoule and Marc-Vergnes 1986)
Capillaries, *Cp*	44.0×10^4 (Zagzoule and Marc-Vergnes 1986)	20.0 (Zagzoule and Marc-Vergnes 1986)
Veinules, *Vl*	117.0×10^4 (Zagzoule and Marc-Vergnes 1986)	70 - 80 (Zagzoule and Marc-Vergnes 1986)
Veins, *V*	$(5.0 - 27.3)\times10^4$ (Zagzoule and Marc-Vergnes 1986)	
Venous sinus, *vSinus*	2.6×10^4 (Zagzoule and Marc-Vergnes 1986)	13 (Zagzoule and Marc-Vergnes 1986)
Ventricles, *Lv*	$(0.1 – 1.0)\times10^4$ (Kaczmarek, Subramaniam et al. 1997; Smillie, Sobey et al. 2005)	15–20 (Gjerris and Borgesen 1992; Lakin, Stevens et al. 2003)
Cerebral SAS, *SAS*	8.0×10^4 (estimated)	30 (Fishman 1980)
Spinal SAS, *sp. canal*	1.0×10^6 (Wilcox, Bilston et al. 2003; Bertram, Brodbelt et al. 2005)	90-100 (Fishman 1980)
Brain parenchyma	$(1.0\text{-}10.0)\times10^3$ (Kaczmarek, Subramaniam et al. 1997; Smillie, Sobey et al. 2005)	1400 (Fishman 1980)

Compartment expansion or compression

The cerebral vasculature, made up of arteries, arterioles, capillaries, veinules, and veins has varying degrees of distensibility. Arteries that surround the brain are typically more compliant than vessels deeply embedded within the brain tissue. We therefore have assigned different values of elastance to each of the cerebral vasculature compartments; these values are given in Table 3 taken from literature. Fluid traction of blood or CSF flow may deform the distensible vascular vessels or CSF compartments. Distensibility of the cerebral vasculature and CSF spaces is incorporated using the steady state force balances implemented in eq. (1-4).

$$p_{lumen} - p_{brain} = E\left(\frac{A - A_0}{A_0}\right) \qquad (1\text{-}4)$$

The change in a vessel's cross-sectional area, $A - A_0$, is governed by the vessel's elastance, E, and the pressure difference between the vessel lumen and the bi-phasic brain compartment, $p_{lumen} - p_{brain}$. A_0 is the cross-sectional area at zero transmural pressure (Luo and Pedley 1998). The greater the transmural pressure across the vessel wall, the more expansion or constriction of

the vessel will occur. When the blood pressure exceeds the intracranial pressure of the surrounding brain tissue, the vessel dilates. Conversely, the vessel may be compressed when the ICP outside is higher. This simple linear distensibility model does not properly describe complex non-linear phenomena like collapsible vessels described by Luo and Pedley (Luo and Pedley 1998) and also neglects autoregulation. Nevertheless, it fully couples the blood and CSF flow equations with the intracranial brain parenchyma pressure by accounting for: (i) vessel distensibility and brain compliance as a function of the elastance, (ii) effect of vessel expansion on the bi-phasic brain parenchyma (change in brain parenchyma volume and porosity) and (iii) pressure increase of the brain parenchyma due to the effect of vessels' interaction with the parenchyma. It also incorporates the possibility of changes in blood distribution patterns in response to vessel dilation or compression, which in turn follows from the force interactions between the blood and the soft deformable brain tissue as well as coupling with the continuity and axial momentum balances. The specific network connectivity for vasculature, CSF filled spaces and brain parenchyma is discussed next.

Cerebral vasculature

Blood flow exiting the carotid artery, cAr, bifurcates into the cerebral arteries for the right and left brain hemisphere, Ar. The blood then flows into the arterioles, Al. Choroid CSF production diverts plasma from the choroidal blood to generate newly produced CSF in the lateral ventricles, Lv. The choroidal CSF production accounts for about two-thirds of the total CSF production and was found clinically to be almost invariant to pressure changes suggesting an active transport process (Kaczmarek, Subramaniam et al. 1997). Accordingly, the mass transfer is a pressure independent constant equal to, $S_{Al\rightarrow Lv} = 0.35$ ml/min. Blood further flows into the capillary bed, where there is also CSF mass transfer from the capillary bed into the

parenchyma. This diffuse CSF production rate is $S_{const_{Cp\rightarrow brain}}$ = 0.12 ml/min. Moreover, the model accounts for CSF seepage allowing capillaries to reabsorb excess fluid or discharge plasma when the interstitial pressure is lowered. The seepage model is governed by the Starling pressure difference which accounts for hydrostatic as well as osmotic pressure differences. Because our model does not balance ions, the effective Starling pressure for fluid seepage is reduced to the hydrostatic pressure difference between capillaries and surrounding brain tissue (Starling 1896). Hence, extracellular fluid reabsorption into the capillaries may occur when intracranial pressure rises relative to the capillary pressure. All equations for the mass transfer coupling between blood and CSF have been reported in (Del Bigio and Bruni 1988).

Cerebrospinal fluid (CSF) system

Similar to blood flow, CSF flow in the ventricles and the subarachnoid spaces satisfies continuity, axial momentum and distensibility equations. CSF production is integrated with the cerebral vasculature as described above. Two-thirds are produced in the choroid plexuses, while one-third of CSF has its origin in the distributed capillary bed generating CSF at a constant rate. This diffuse CSF may travel through the parenchyma into ventricles, or traverse the pia to reach the cerebral subarachnoid space. The distribution of the diffusely produced CSF depends on the pressure gradients between the compartments according to the laws of fluid flow in porous media known as Darcy's law. The pressure dependent fluxes are depicted as mass transfer flows, $S_{Cp\rightarrow brain}$ and $S_{brain\rightarrow Lv}$, in Figure 5. The CSF exiting the lateral ventricles, Lv, enters the third ventricle, 3V. CSF from the third ventricle flows through the fourth ventricle, 4V, into the cerebral subarachnoid space, SAS. From the cerebral subarachnoid space, CSF is believed to be reabsorbed into the venous sinus through the arachnoid granulations (Del Bigio and Bruni 1988; Segal 2001). We account for CSF reabsorption by a mass transfer flux $f_{reabsorption}$, which is a

function of the pressure difference between the subarachnoid space and the venous sinus, $p_{SAS} - p_{v.si}$ and a reabsorption constant, k, according to eq. (1-5). The significance of reabsorption for hydrocephalus will be discussed later.

$$f_{reabsorption} = k\ (p_{SAS} - p_{v.\mathrm{si}}) \qquad (1\text{-}5)$$

In addition, CSF may be displaced into the spinal canal. Previous MRI measurements (Loth, Yardimci et al. 2001) have shown that in normal subjects about 0.5-2cc of CSF are displaced from the cranial cavity into the spinal canal and back in every cardiac cycle. These measurements also confirm that the net CSF exchange is zero, thus indicating that the CSF reabsorption in the spinal canal is negligible. Thus, we set the CSF outflow, f_{out}, in the continuity equation for the spinal canal to zero. For the displacement to occur, the spinal subarachnoid space must be distensible. This expandability does not violate the Monro-Kellie doctrine because the CSF in the spinal canal is not confined by the cranial vault. The spinal canal compliance is largest in the lumbar area. Moreover, a detailed finite element analysis of the spinal canal expansion in response to CSF influx showed a hyperlinear increase of stiffness with large deformation (Linninger, Sweetman et al. 2009). Accordingly, we accounted for the nonlinear deformation of the spinal canal. The complete set of momentum equations describing the flow into the spinal canal and venous sinus from the SAS are found in (Biot 1941).

Brain parenchyma

The brain is a bi-phasic, anisotropic, three-dimensional structure. The Biot-theory of consolidation describes stresses, strains and fluid motion in a consolidating porous media. However, current three-dimensional brain consolidation models with full fluid-structure interaction in addition to the cerebral vasculature and CSF spaces are still computationally intractable. Therefore, we captured the main dynamic properties without performing a three-

dimensional spatial discretization of the brain parenchyma. The brain is merely divided in left and right hemispheres, each one modeled by a single lumped compartment. In the proposed simplified bi-phasic brain model, each hemisphere is treated as an incompressible, deformable medium composed of two phases, the solid cell matrix, representing neurons, glial cells, and axon fibers, and the extracellular fluid. The solid phase normally occupies 70% of its total size. The model assumes that the volume of the solid cell matrix does not change. Thus, size changes of the parenchyma can occur only when extracellular fluid content is altered.

The extracellular fluid content of each brain hemisphere consists of fluid similar to CSF. It occupies 30% of the parenchyma volume and was considered as a viscous and incompressible fluid. The continuity and pressure driven fluid exchange of the bi-phasic brain are given in eqs. (1-6)-(1-8).

Continuity for the extracellular fluid for each brain hemisphere

$$l_{exf}\frac{\partial A_{exf}}{\partial t} = f_{exf_{in}} - f_{exf_{out}}\,, \tag{1-6}$$

Fluid exchange in each hemisphere according to pressure difference

$$\begin{aligned} p_{Cp} - p_{exf\_br\_hem} &= a_{exf} S_{Cp\to br}\,, \\ p_{exf\_br\_hem} - p_{Lv} &= a_{exf} S_{br\to Lv}\,, \end{aligned} \qquad \text{with } a_{exf} = \mu_{exf} l_{exf} / k_{exf}\,, \tag{1-7}$$

Volume consistency – Monro-Kellie doctrine

$$V_{total\_br\_hem} = \sum_{b} V_b + \sum_{CSF} V_{CSF} + V_{br\_hem} = \text{constant}, \quad V_{br\_hem} = V_{exf\_br} + V_{solid\_br}\,. \tag{1-8}$$

The subscript, exf, refers to the extracellular fluid flow inside the left and right brain hemispheres. Each brain hemisphere is modeled as a cylinder with cross-sectional area, A_{exf}, and equivalent hydraulic length, l_{exf}. The SAS interacts with the two brain hemispheres. The third and fourth ventricles are shared by both hemispheres as shown in Figure 5. Each brain hemisphere contains arteries, arterioles, capillaries, veinules, veins, and also encases the lateral

ventricles. The pressure difference, $p_{Cp} - p_{exf\_br\_hem}$, in eq. (1-7) drives seepage of extracellular fluid flow from capillaries into the brain, $S_{Cp \rightarrow brain}$. The term $p_{exf\_br\_hem} - p_{Lv}$ in eq. (1-7) accounts for the extracellular fluid flow from the brain into the ventricles, $S_{br \rightarrow Lv}$. The parameter a_{exf} is a function of the extracellular fluid viscosity, μ_{exf}, the hydraulic length of the brain hemisphere, l_{exf}, and the brain parenchyma permeability, k_{exf}, (Biot 1941; Biot 1955; Nield and Bejan 2006). This pressure driven flow can be considered a simplified version of Darcy's law with the hydraulic permeability of the brain parenchyma, k_{exf}, given in Table 4, brain parenchyma. The pressure difference between the brain, $p_{exf\_br\_hem}$, and the surrounding compartments, p_b, p_{CSF}, fully couples the brain parenchyma with the cerebral blood and CSF compartments.

Table 4. Material properties for the bi-phasic model of intracranial dynamics. Predicted amplitudes and phase lag for the arterial and venous systems agree with MRI measurements (Kim, Thacker et al. 2007).

Location	*Material property*	*Value/reference*	
Brain parenchyma	porosity, ϕ permeability, k_{exf} (m^2) density, ρ_{exf} (kgm^{-3}) viscosity, μ_{exf} $(kgm^{-1}s^{-1})$	0.3 (Lakin, Stevens et al. 2003) 0.7×10^{-15} (Lakin, Stevens et al. 2003) 1050 (Pellicer, Gaya et al. 2002) 0.001	
Blood	density, ρ_b (kgm^{-3}) viscosity, μ_b $(kgm^{-1}s^{-1})$	1050 (Pedley 1980) 0.004 (Pedley 1980)	
CSF	density, ρ_{CSF} (kgm^{-3}) viscosity, μ_{CSF} $(kgm^{-1}s^{-1})$	998.2 (Lakin, Stevens et al. 2003) 0.001 (Lakin, Stevens et al. 2003)	
CSF production	choroid plexus, $S_{Al\rightarrow Lv}$, (ml/min)	0.35 (Linninger, Tsakiris et al. 2005)	
	capillaries diffuse prod., $S_{Cp\rightarrow br} + S_{const_{Cp\rightarrow br}}$, (ml/min)	0.12 (estimated)	
Reabsorption @ sagittal sinus	Permeability, k, (m^2)	*N:*	0.5×10^{-14}
		HC:	0.1×10^{-14}
	Reabsorption, R, $(mmHg/ml/min)$	*N:*	16.0 (Kosteljanetz 1985; Gjerris and Borgesen 1992; Czosnyka, Czosnyka et al. 2004)
		HC:	88.9
	Porosity, ϕ	0.3 (Lakin, Stevens et al. 2003)	
Arterial flow	max/min (ml/min)	1194/588* (Baledent, Henry-Feugeas et al. 2001; Kim, Thacker et al. 2007)	
Venous flow	max/min (ml/min)	882/630* (Kim, Thacker et al. 2007)	
Cerebral blood flow	mean (ml/min)	738	
Phase lag	% cardiac cycle	Predicted 13% / 12% in (Kim, Thacker et al. 2007)	

*N=normal, HC=hydrocephalic, *model predictions*

The model also satisfies the Monro-Kellie doctrine stating that total of volumes of all parenchyma, blood and CSF compartments remain constant for each brain hemisphere. The volume consistency of the brain parenchyma and all fluid spaces was enforced through eq. (1-8), for each brain hemisphere. In eq. (1-8) the volume of the brain parenchyma, V_{br_hem}, is the sum of the volume of extracellular fluid, V_{exf_br}, and the volume of the solid part of the brain, V_{solid_br}. As a result, expansion of the ventricles is only possible when other compartments compress. In

principle, volume conservation gives rise to the following options for spatial redistribution: (i) Reduced CSF spaces by displacing CSF into the spinal canal, which is not limited by the cranial Monro-Kellie doctrine; (ii) Compression of the brain parenchyma by diminished extracellular fluid content; (iii) Compression of the cerebral vascular bed, which is however expected to influence the cerebral blood flow. The mathematical analysis will provide quantitative results about the forces and conditions likely to occur in normal and diseased states. The fluid content change relates the volume of the extracellular fluid to the invariant cell matrix of constant volume. This relation is expressed through the brain porosity, ϕ, shown in eq. (1-9).

Porosity, ϕ of bi-phasic brain hemisphere

$$\phi_{br\_hem} = \frac{V_{exf\_br}}{V_{exf\_br} + V_{solid\_br}} = \frac{V_{exf\_br}}{V_{br\_hem}}, \quad \text{initial } \phi_{br\_hem_0} = 0.3 \tag{1-9}$$

Eq. (1-9) is applied for each brain hemisphere. A complete description of the equations for each bi-phasic brain compartment and the coupled blood and CSF equations is provided in (Baledent, Henry-Feugeas et al. 2001). This brain model does not resolve spatial distribution of stresses and strains of the brain. Nevertheless, due to its full coupling with the embedded CSF and blood force and mass balances, it conserves the main features of the porous brain matrix and the induced fluid changes that occur in intracranial dynamics.

3.4. Results

This section introduces the results of the computer predictions for the interactions of all cerebral compartments. The emphasis lies on comparing the differences between normal and hydrocephalic cases to highlight pathological changes and offer to mechanistic explanations.

Blood and CSF flow dynamics

The predicted blood and CSF flows in normal subjects are depicted in Figure 6a and Figure 6b. The total cerebral flow through arteries, arterioles, capillaries and veins, has a mean flow rate

of 12.3 ml/s, or 738 ml/min, which is consistent with physiological values (Zagzoule and Marc-Vergnes 1986). The maximum arterial pulsatile flow rate is 19.9 ml/s and the minimum is 9.8 ml/s, matching similar findings to those in (Baledent, Henry-Feugeas et al. 2001). The maximum venous pulsatile flow rate is 14.7 ml/s and the minimum is 10.5 ml/s. The pulsatility index (PI) as defined in (Gosling and King 1974) and given in eq. (1-10) was calculated and found to be 0.82 in the arteries and 0.34 in the venous system. These pulsatility indices agree with clinically reported measurements (Kim, Thacker et al. 2007).

$$\text{Pulsatility index} = \frac{\text{maximum systolic flow rate - minimum diastolic flow rate}}{\text{mean flow rate}} \qquad (1\text{-}10)$$

Figure 6a also shows the forward/backward CSF flow of approximately 0.9 cc from the cranium into the spinal canal, Fsp. canal. The predicted CSF displacement agrees with previous published experimental results based on Cine phase–contrast MRI (Loth, Yardimci et al. 2001). The CSF stroke-volume into the spinal canal was also predicted for hydrocephalic cases. In hydrocephalus, our model predicts a diminished CSF fluid exchange with the spinal canal. The net forward flux in the hydrocephalic case is only 0.25 ml with each cardiac cycle, indicating a reduction of 72% of the CSF pulsatility in the cervical area. Our Cine MRI measurements of CSF flow velocities also showed a reduction of CSF flow in the cervical area in hydrocephalus, Figure 7.

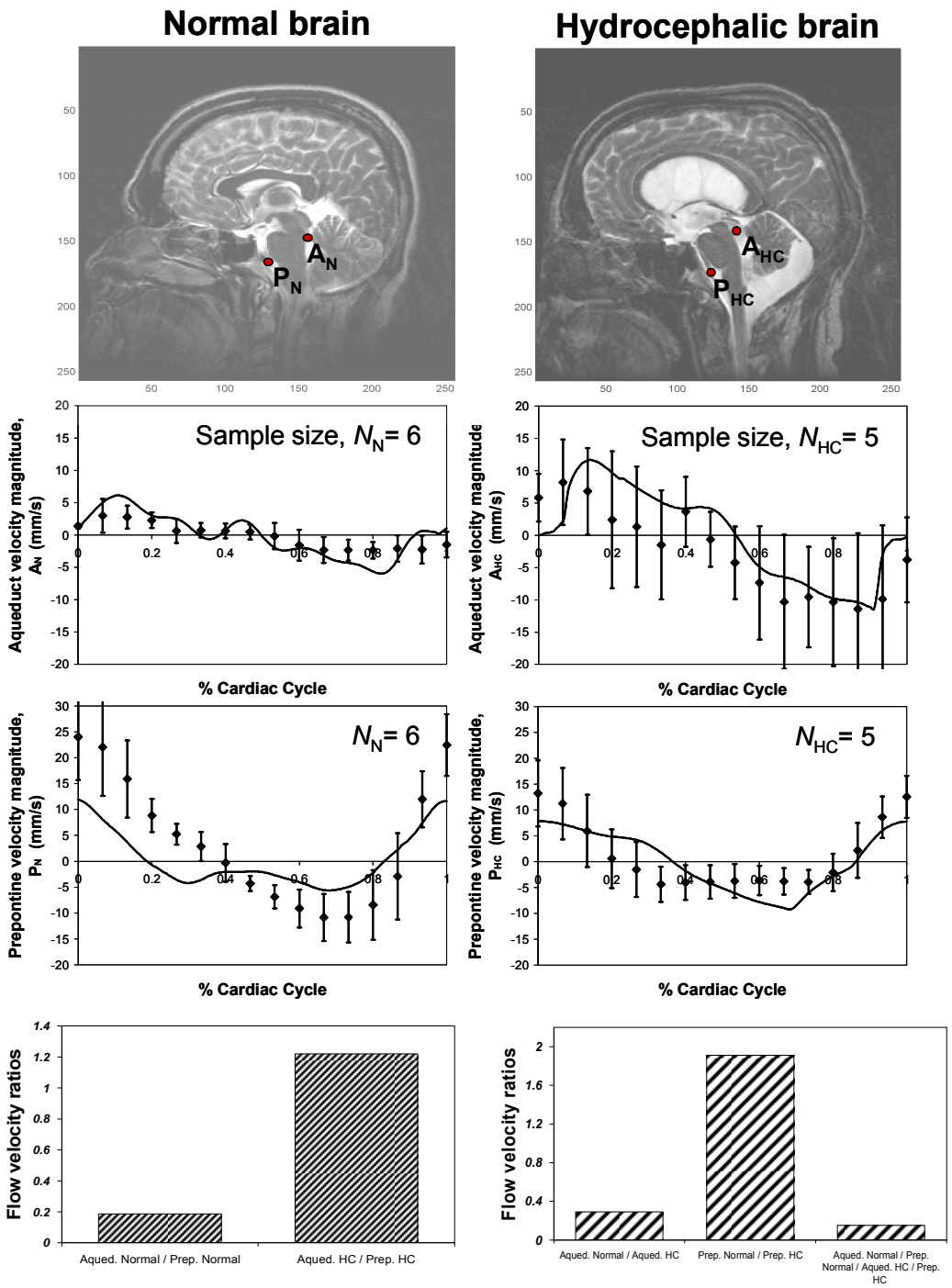

Figure 7. In normal brains the average peak to peak velocity at the aqueduct of Sylvius is 6.9 mm/s. In the hydrocephalic case, the amplitude is 3.4 times higher with peak to peak velocity 23.56 mm/s. At the same time the velocity amplitude in the prepontine area is decreased in hydrocephalus. The peak to peak velocity in the prepontine area is about 37 mm/s in normal cases and 19 mm/s in hydrocephalic cases. Velocity measurements based on 6 normal and 5 hydrocephalic subjects are shown in dots, computer predictions are shown in solid lines.

Hemodynamics

Figure 6c plots predicted blood pressures and pulse waveforms in the normal human brain. The mean pressure in arteries is 82 mmHg, in the arterioles is 55 mmHg, in capillaries is 18 mmHg and drops to 5 mmHg in the veins. Normally, the mean pressure in the brain parenchyma is slightly above the ventricular ICP. Figure 6d shows the simulated intracranial pressure signals of the lateral ventricles, cerebral and spinal subarachnoid spaces, for one cardiac cycle. In the ventricles, cerebral and spinal subarachnoid spaces, the pressure has a mean value of 9.1 mmHg. The model predicts approximately 5 mmHg pulse pressure in the ventricular system. This value compares well to a range of 3-5 mmHg reported in (Czosnyka, Cieslicki et al. 2005). The pulse pressure in the subarachnoid space and spinal canal was computed to be about 3.5 mmHg. The computer predictions also show that the pressure and flow amplitudes of the cerebral veins are attenuated. Our model links this dampening to the dilation of the compliant cerebral vascular bed made possible by CSF displacement into the spinal canal. We note that without the CSF displacement into the spinal canal, the vasculature could not deform the nearly incompressible parenchyma. In addition, the model predicts a phase lag between the arterial and the venous wave forms in the order of 13% of the cardiac cycle as depicted in Figure 6b. The dampening of the cerebral hemodynamics is clinically well established; our model prediction is in excellent agreement with previous gated MRI blood flow measurements yielding a phase lag of 12% (Kim, Thacker et al. 2007).

Ratio of aqueduct flow to prepontine flow

The detailed analysis of MRI measurements of CSF flow in normal and hydrocephalic brains shows substantial changes in the flow patterns. Figure 7 shows the computational fluid dynamics simulations and clinical MRI measurements, based on six normal and five communicating hydrocephalic subjects (Linninger, Tsakiris et al. 2005; Linninger, Xenos et al. 2007). Compared

in detail are the CSF flows in two regions of interest - in the aqueduct of Sylvius and in the prepontine area. In normal subjects, the flow velocity amplitude is much higher in the prepontine area than in the aqueduct. In hydrocephalus, the aqueduct flow is increased, while the velocity in the prepontine area is reduced. The ratio of the aqueduct to the prepontine velocity amplitude is about seven times larger in hydrocephalic cases than in normals. This change suggests that the ratio of the prepontine to the aqueduct flow amplitude could be an indicator for the status of communicating hydrocephalus. While this ratio has not been used for diagnosis yet, its significance might be confirmed in future research. Figure 8 shows snapshots of simulated velocity fields at the peak of the systole using patient-specific lateral brain sections of a normal and a hydrocephalic subject, where a two dimensional simulation of the flow field is created as previously published (Linninger, Xenos et al. 2007). The discussion will present a mechanistic explanation for these changes in the flow patterns occurring in hydrocephalus.

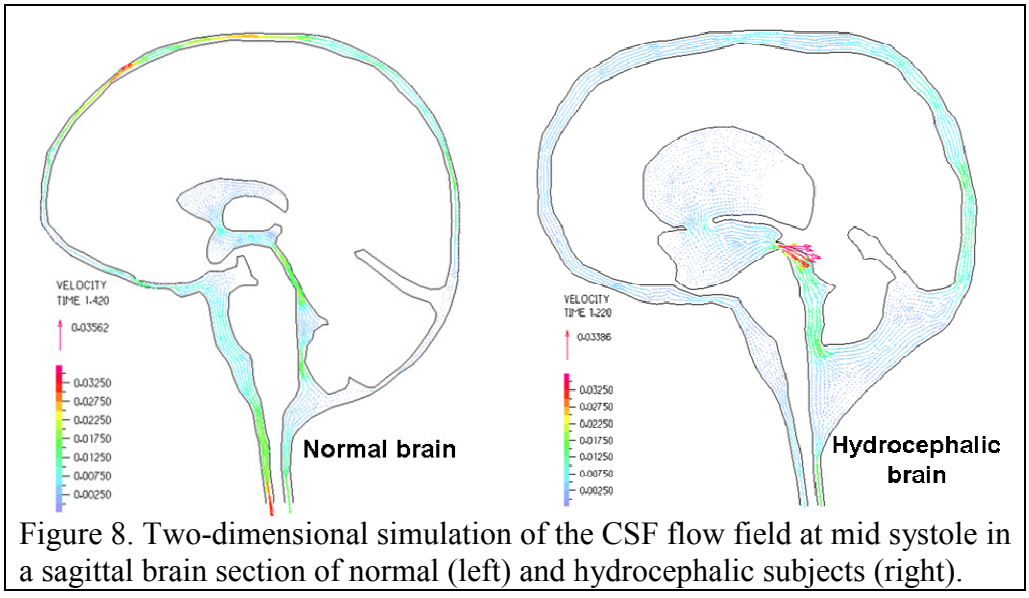

Figure 8. Two-dimensional simulation of the CSF flow field at mid systole in a sagittal brain section of normal (left) and hydrocephalic subjects (right).

Pulsatile dilation of the lateral ventricles for normal subjects and hydrocephalic patients

The MRI technique described in the methods section was also used to demonstrate the timing for the expansion and contraction of the ventricles in normal and hydrocephalic subjects. When

the flow in the lateral ventricles is from superior to inferior, meaning flow from the ventricular system to the cerebral and spinal subarachnoid spaces, the ventricles contract as shown in Figure 9. When CSF streams upwards from the spinal subarachnoid spaces, then the ventricles expand. We have recently discussed the role of the choroid plexus in driving the CSF flow in the ventricular system (Linninger, Tsakiris et al. 2005). In systole, when the fluid space inside the lateral ventricle is compressed, there is outwards CSF flow because the space available for the CSF inside the lateral ventricle is simultaneously confined by the parenchyma as well as by the expanding choroid plexus. Figure 9 compares the percent area change from the MRI measurements with the computational predictions. Since the MRI ventricular size calculation is based on only a single slice, the timing of the wall movement and its relative magnitude (not the absolute amount of fluid moved) can be derived. Note that the model predicts that with hydrocephalus and larger ventricles, the percent movement of the wall is less. Calculation of the total fluid force out of the ventricle cannot yet be done because the detailed geometry of the whole ventricular system is not included.

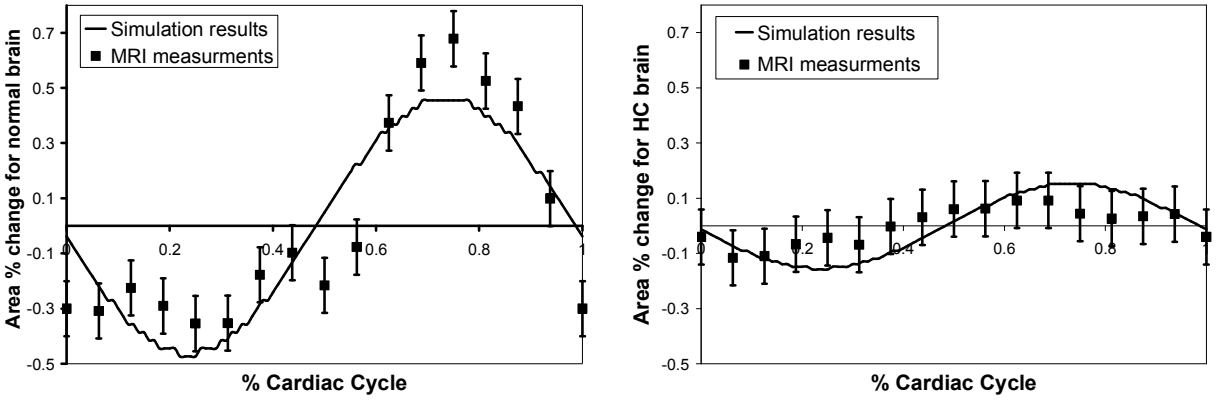

Figure 9. Area change for normal and hydrocephalic subjects. Comparison of the MRI area measurements with the simulated results from the computational model.

Transmantle pressure differences

Flow reversal in the aqueduct of Sylvius requires a sign change of the pressure gradients along a streamline. The ventricular space has a higher pressure when CSF is flowing through the

aqueduct to the subarachnoid space. The subarachnoid space must have the higher pressure when CSF flows from the subarachnoid space back into the ventricles. Accordingly, the transmantle pressure difference - defined as the pressure difference between the ventricles and cerebral subarachnoid space - changes sign. Figure 10 shows the pressures in the ventricular system, cerebral and spinal subarachnoid spaces in three different phases of hydrocephalus. Initially, the absolute intracranial pressure is low not exceeding 11 mmHg as in Figure 10a. As hydrocephalus gradually develops in our simulation, the intracranial pressure increases to 15 mmHg in the ventricular and subarachnoid spaces shown in Figure 10b. Finally, the intracranial pressure reaches 35 mmHg in the diseased steady state as in Figure 10c. Despite elevated pressure in acute hydrocephalus, the transmantle pressure signal remains almost unchanged as depicted in Figure 10. The maximum transmantle pressure difference in normals is 0.56 mmHg (75 Pa), while in acute communicating hydrocephalus it does not exceed 0.62 mmHg (83 Pa). Despite the marked ICP rise, transmantle pressure differences hardly change. On average, the pressure is higher at the ventricular side, $p_{LV} > p_{SAS}$, but even this type of compression of the parenchyma from the inside is reversed in each cardiac cycle. Accordingly, the parenchyma experiences dynamic load changes, not static pressure differences with a high pressure at the ventricular side, p_{LV}, opposed to lower pressures at the interface to the subarachnoid space, p_{SAS}. Overall, the transmantle pressure does not exceed modest values in both normal and hydrocephalic cases.

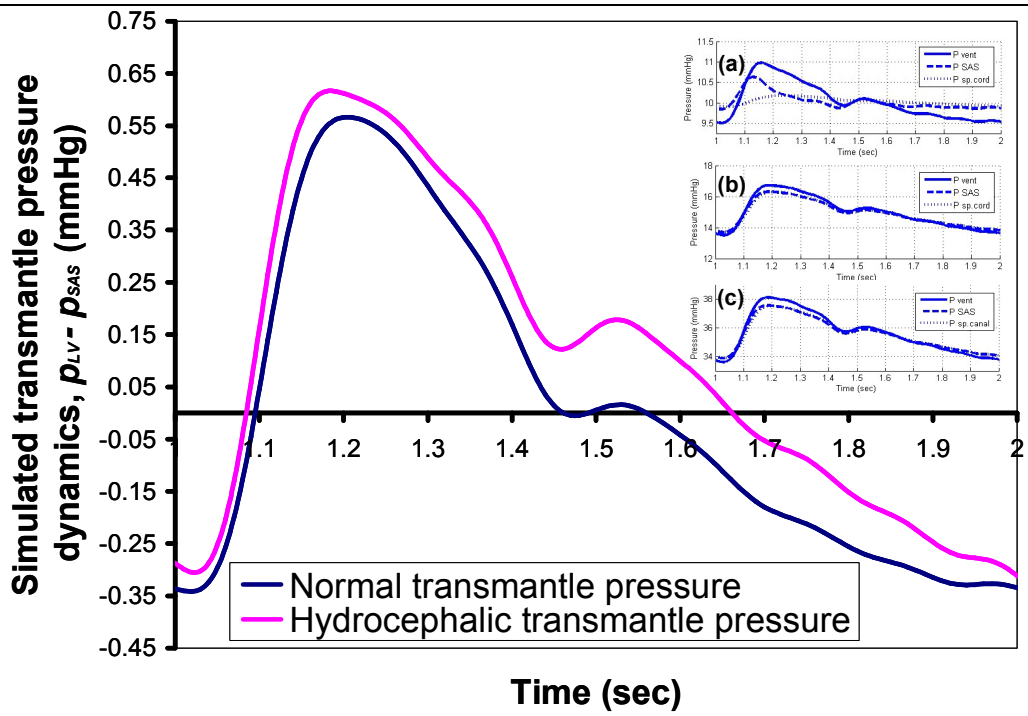

Figure 10. Intracranial pressure signals in (a) normal conditions for an individual with carotid blood pressure of 120/90 mmHg, (b) transient phase and (c) fully developed communicating hydrocephalus. The simulations support prior experimental measurements in animal models that showed only small transmantle pressure differences occur in communicating hydrocephalus. Moreover, in each cardiac cycle, there is a pressure sign change, indicating a pulsating loading pattern of the parenchyma.

Communicating hydrocephalus

The model is able to predict the transition from the normal to the acute diseased state. In all disease simulations only the reabsorption constant was reduced according to eq. (1-11); all outcomes follow naturally from the dynamic interactions between the three compartments, blood, CSF and brain parenchyma. The dynamic transitions predicted by the model for the induction of acute communicating hydrocephalus can be compared to our dog models. Kaolin injected into dogs' cisterna magna raises the resistance of reabsorption pathways in the subarachnoid villi (Penn, Lee et al. 2005). In humans, the increase of the reabsorption resistance may be due to inflammation of meninges. The acute communicating hydrocephalus is simulated by reducing the reabsorption constant between the subarachnoid space and the sagittal sinus as in eq. (1-11).

$$f_{\text{reabsorption}} = k(p_1 - p_2)\,,\ \begin{cases} \text{normal case:} \quad k = 6.4\times10^{-12}\,\dfrac{m^3/s}{Pa} \ \text{ or } \ R = 16.0\dfrac{mmHg}{ml/\min} \\ \text{hydrocephalic: } k = 1.4\times10^{-12}\,\dfrac{m^3/s}{Pa} \ \text{ or } \ R = 88.9\dfrac{mmHg}{ml/\min} \end{cases} \qquad (1\text{-}11)$$

p_1, is the pressure in the cerebral subarachnoid space and, p_2, is the pressure in the venous sinus. Increased reabsorption resistance causes an ICP rise of 25 mmHg, which is about 3325 Pa above normal as depicted in Figure 11b. For the same outflow resistance of $R = 88.9\ mmHg/ml/\min$, previous researchers found an ICP elevation from normal dynamics of 15-25 mmHg (1995-3325 Pa) (Gjerris and Borgesen 1992). Figure 11a also depicts the pressure trajectories of the ventricular system and the brain parenchyma. The ICP of the brain parenchyma follows the ventricular pressure rise in a period of 22 hours. The detail of Figure 11b indicates sign changes in the transmantle pressure differences confirming our dog experiments and earlier calculations (Linninger, Tsakiris et al. 2005; Penn, Lee et al. 2005). The model also correctly predicts the increase in intracranial pulse pressure as has been observed experimentally (Czosnyka, Cieslicki et al. 2005; Penn, Lee et al. 2005).

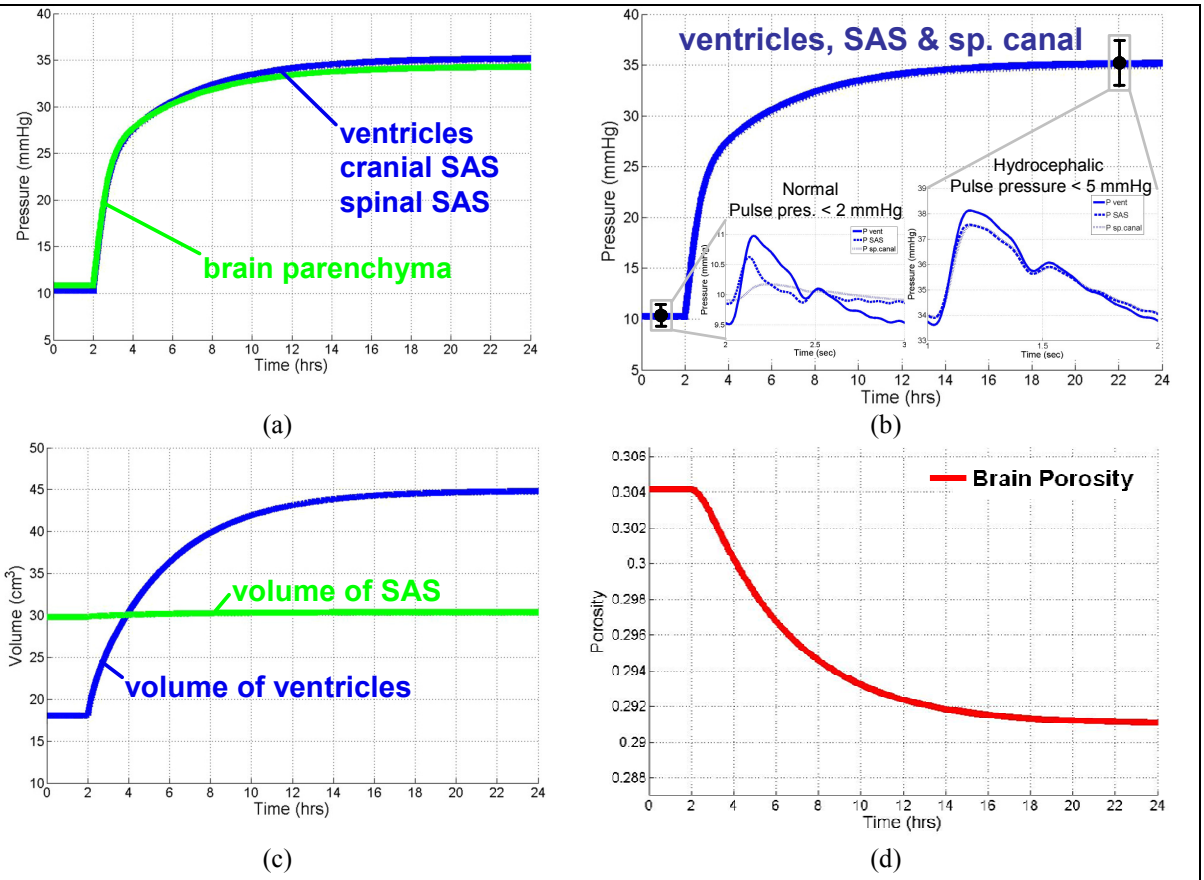

Figure 11. Simulated acute communicating hydrocephalus for an individual with carotid blood pressure of 120/90 mmHg. (a) Predicted intracranial pressures for the induction of communicating hydrocephalus. (b) Simulated intracranial pressures and pressure amplitudes for the ventricular system for the induction of communicating hydrocephalus. (c) Volume increase in the ventricular system and cerebral subarachnoid space for the induction of communicating hydrocephalus case. (d) Porosity changes of the brain parenchyma prompted by the onset of simulated acute communicating hydrocephalus.

Figure 11c shows the volume increase for the lateral ventricles and the cerebral subarachnoid space. In this simulation, the ventricular volume grew to 27 ml, an increase of about 150%. The extracellular fluid content in the brain parenchyma is reduced by 25.4 ml. The brain porosity falls from 0.3 to 0.291 or a reduction of about 5% as depicted in Figure 11d. Figure 12 summarizes the relative expansion and compression of the main cerebral structures and spinal canal occurring in hydrocephalus. The CSF volume increases significantly, and its expansion reduces the extracellular fluid volume in the brain parenchyma. The model also predicts

phenomena which are difficult to measure like a small reduction of blood volume which is smallest in the capillaries and larger in the arterial and venous systems.

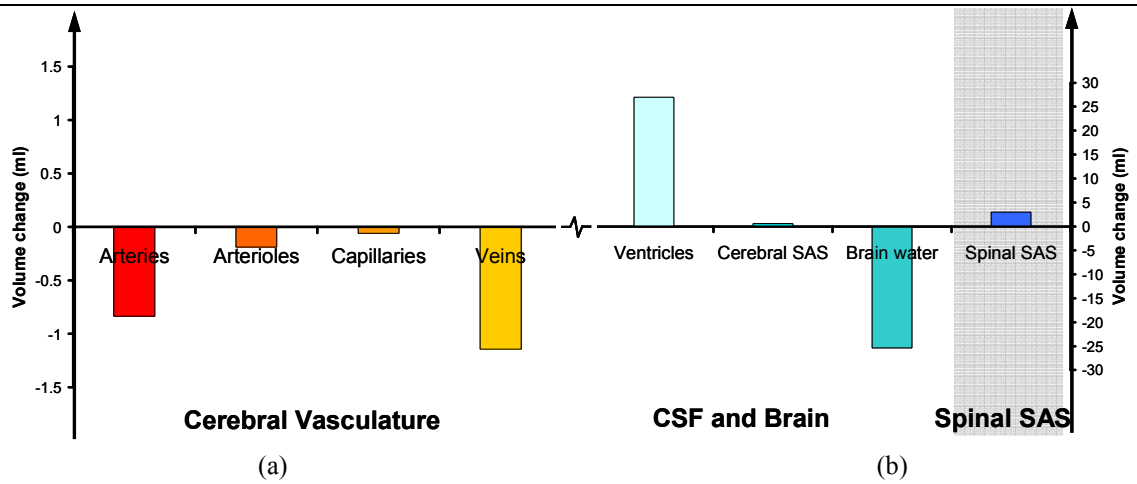

Figure 12. The volume change predicted for hydrocephalus relative to normal (baseline) in the vascular and ventricular systems as well as in the brain parenchyma. (a) Volume changes predicted by the model in each vascular substructure of the hydrocephalic human brain in contrast to normal, (b) volume changes of the ventricular system, the brain parenchyma and the spinal canal.

Clinical infusion tests and the model

Standard clinical methods such as bolus injections to determine cerebrospinal compliance in humans permit another test of the model's predictions. The bolus test is done by injecting fluid into the spinal subarachnoid space, while recording the induced pressure rise. The well-known pressure-volume curves provide clinically important information about the brain compliance and are often used for determining treatment options (Kosteljanetz 1985; Czosnyka, Czosnyka et al. 2004). If our model is accurate, it should predict compliance curves consistent with clinical observations.

Bolus injections were simulated by inserting a corresponding CSF source in the fluid equations of the subarachnoid space. Dynamic responses of the overall system showed characteristic ICP trajectories with a peak pressure and subsequent relaxation phase as in the detail of Figure 13a. Figure 13a also shows the typical polynomial relationship between infusion

volume and peak pressure. The reported computational trends correlate well with experimental data (Czosnyka, Czosnyka et al. 2004). Figure 13b uses the data of the same simulation to correlate pulse amplitude and mean intracranial pressure. The pulse amplitude increases with rising ICP with the slope of $\alpha = 0.128$ in these simulations. Moreover, we calculated the system's overall mean resistance and found it to be, R=16.0 mmHg/ml/min. The predicted resistance for the normal brain falls within the range of clinically observed normal reabsorption resistances of 13 - 18 mmHg/ml/min (Marmarou, Shulman et al. 1978; Czosnyka, Czosnyka et al. 2004).

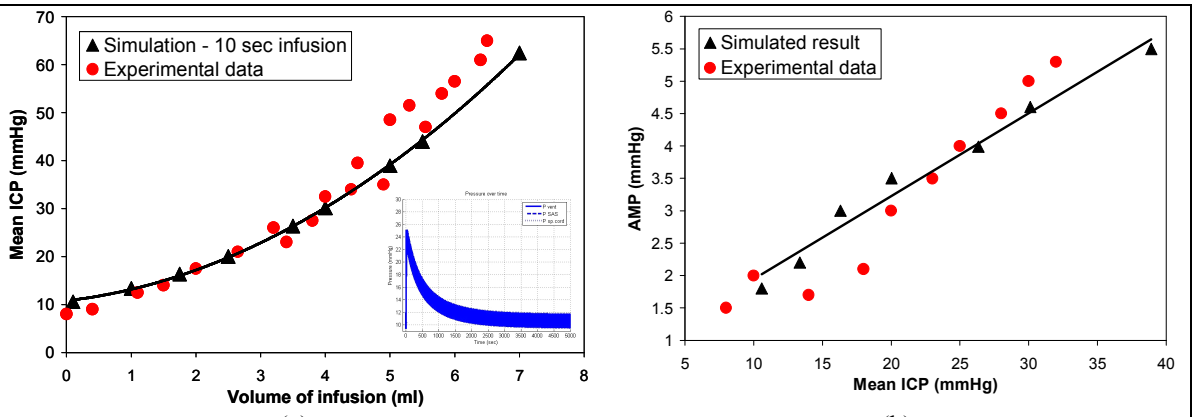

(a) (b)

Figure 13. Experimental results of bolus injections in humans versus simulated results from the holistic mathematical model, (a) Mean pressure – volume of infusion (P-V) for short time infusion. In the zoomed window on the right lower side the ventricular ICP trajectories after bolus injection in the subarachnoid space are presented. (b) Experimental results versus simulated relationship between pulse amplitude, AMP, and mean ICP for different infusion times.

Using eq. (1-12), we also calculated the pressure-volume index (Czosnyka, Czosnyka et al. 2004). We found the pressure-volume index (PVI) for the normal brain to be in the range of 13.5 - 19 ml. The hydrocephalic brain simulations gave a PVI of 8.0 - 10.0 ml. These values are below the clinically reported threshold of 13, indicating that our model correctly reproduces the loss of the pressure-volume compensatory reserve (Czosnyka, Czosnyka et al. 2004).

$$PVI = \frac{dV}{\log_{10}\left(\dfrac{p_p - p_0}{p_b - p_0}\right)}, \begin{cases} \text{where } p_p: \text{ peak pressure} \\ p_b: \text{ baseline pressure} \\ p_0: \text{ reference pressure} \end{cases} \tag{1-12}$$

These comparisons demonstrate how clinical measurements can be fit into the model, and how individual patient data can be analyzed to derive specific values for that patient.

3.5. Discussion

We have developed a model for intracranial dynamics in which the interactions of all compartments are quantified by fundamental mass and force conservation balances. Under normal conditions, CSF motion is produced by the vascular expansion and pulsatile brain deformation. Since the parenchyma is incompressible, its deformation is passed on to the ventricles, forcing CSF displacement from the confined cranium into the spinal canal. The Monro-Kellie doctrine is fully satisfied in our model and we have predicted a CSF displacement into the spinal canal of about 0.9 ml in each cardiac cycle. For normal dynamics, the pulsations of the lateral ventricles as well as the amplitudes and pressure gradients of arteries, arterioles, capillaries, veinules and veins can be calculated. It is important to recognize that in simulating communicating hydrocephalus we have simplified the situation for analysis. Firstly, the model does not divide the cerebral subarachnoid space into compartments. Quite likely some forms of hydrocephalus are caused by adsorption blocks at the arachnoid granulations and others by more proximal blocks at the base of the brain. These two situations cannot be distinguished in the current state of the model so the volume changes and pressure in the single cerebral subarachnoid space may be different from what actually occurs. The model, as it stands, predicts that the cerebral subarachnoid space is slightly increased with hydrocephalus. Clinical MRI observations, on the other hand, show a decrease in subarachnoid space in communicating hydrocephalus. MRI measurements need to be quantified in cases of acute hydrocephalus, and

our model needs further spatial development to account for changes of the parenchymal cell matrix.

In the current model we have chosen to neglect inertia terms for convenience and to avoid problems that come from wave reflection when using wave equations that include spatial and time derivatives. In the future, the inertia terms should be included, specifically for large arteries in which there are large Womersley numbers. Furthermore, it may be fruitful to divide the vasculature into a more refined network of vessels. The larger arteries and veins are in the cerebral subarachnoid space and the large draining sinuses of the brain may be coupled to the CSF pressure because they share a dural wall. These possible refinements of the model and their effect on dynamics need to be explored further.

Finally, it needs to be stated clearly that the model only deals with normal brain dynamics and acute onset of hydrocephalus. It does not at this point predict what happens if the developing hydrocephalus changes the brain tissue due to compression or stretching. A number of clinical studies show that plastic changes occur and that hydrocephalus is not perfectly reversible. This is particularly true for the aging brain that no longer has the same physical structure as the adult brain. Some of the non-reversibility of the brain tissue might be due to its porous nature and some due to biochemical/structural changes which take place with deformation. This point was explained in Hakim's original model for normal pressure hydrocephalus over thirty years ago (Hakim, Venegas et al. 1976).

The lack of reliable measurements of the properties of the brain tissue and CSF absorption also are a problem for all mathematical models. As explained in a recent article on the assessment of CSF outflow resistance, different measurement tests can provide quite different absolute values of Rout (Eklund, Smielewski et al. 2007). Such measurements all assume that the

CSF outflow is linearly dependent on the pressure difference between ICP and the dural sinus, a constant dural sinus pressure and a constant CSF formation rate. They also assume that the only volume change is that of CSF, not blood or spinal subarachnoid space.

While our model has a number of simplifications and is not discretized in three dimensions, it does for the first time couple the three key elements important in intracranial dynamics (the brain, CSF, and blood), and it does so with first principle equations. It provides quantitative explanations for a series of important observations.

Why does the prepontine fluid flow decrease? The systolic pulse pressure expands the vasculature producing CSF displacement from the cranium into the spinal subarachnoid space. At normal ICP, the soft tissues in the spinal canal outside the dura can be deformed. However, when the ICP is gradually elevated as in hydrocephalus, the ability of the spinal canal to receive CSF displacements is diminished, thus reducing the system compliance. Impaired compliance explains (i) the reduced CSF flow into spinal canal observable as lower cisternal velocity magnitudes, and (ii) an increase in mean ICP and amplitude reflecting a stiffer cerebrospinal system.

Why does the aqueduct flow increase simultaneously? The model suggests that small changes in hemodynamics are responsible. Increased stiffness leads to larger pulse pressures of the cerebral vasculature, which in turn interacts with the bi-phasic parenchyma. At the same time, elevated ICP slightly compresses the cerebral vasculature and drains the parenchyma. Similar compressive trends were reported by previous experimental studies (Greitz, Hannerz et al. 1994; Czosnyka, Czosnyka et al. 2004). Compression also impacts the overall blood flow; however, changes in blood flow need to be treated with caution as we did not account for auto-regulation. The compressed state with larger pulse pressures heightens the pressure and size

changes that the ventricles experience. In effect, the forward and backward CSF flows in the lateral and third ventricles are larger in the hydrocephalic case. Therefore, the observable CSF flow in the aqueduct increases. At the same time, cisterna magna flow decreases because of the reduction of the spinal compliance as described above. The proposed mathematical model correctly predicts both aqueduct flow increase and cistena magna flow decrease using no assumptions other than mass and force conservation balances. While predictions do not prove these points, they offer plausible explanations for the complex changes in flow patterns between cerebral vasculature and CSF compartments occurring in hydrocephalus.

Transmantle pressure gradients

MRI techniques do not provide absolute intracranial pressures. However, it is possible to accurately reconstruct flows and the necessary pressure differences using the equations of motion together with measured CSF velocities (Linninger, Xenos et al. 2007; Zhang, Kulkarni et al. 2007). These pressure predictions are independent of any assumptions made for the parenchyma. These predictions and actual measurement in dogs confirm that transmantle pressure differences do not cause communicating hydrocephalus as proposed by most previous theories. Previous theories of hydrocephalus (Hakim, Venegas et al. 1976; Kaczmarek, Subramaniam et al. 1997; Smillie, Sobey et al. 2005) postulating large transmantle pressure gradients are not supported by our model or the evidence of Cine phase–contrast MRI measurements, or by clinical measurements.

A mechanistic explanation of communicating hydrocephalus

Our model also explains ventricular expansion in the acute onset of communicating hydrocephalus. The model predicts that fluid exchange between the main cerebral compartments occurs in communicating hydrocephalus. Normally, the ventricular system drains CSF from the arteries of the choroid plexus and from the brain parenchyma. CSF is reabsorbed into the venous

system at the superior sagittal sinus. Impaired reabsorption causes CSF to accumulate and hydrocephalus to develop. Despite a gradual ICP increase, CSF is continuously produced because CSF production is only a weak function of ICP, perhaps due to active transport mechanisms underlying CSF production (Segal 2001; Brown, Davies et al. 2004). Continued CSF production leads to CSF accumulation in the ventricles, at the same time CSF transport from the vascular to the ventricular system through the extracellular space is diminished. Finally, as the ICP further rises, the CSF reabsorption flow is restored, but requires much higher ICP to off-set increased reabsorption resistance. In this final state, only a small amount of CSF is predicted to seep back into the vasculature from the ventricles through the extracellular space, which constitutes a complete reversal of CSF flow direction when compared to the normal state. The ventricles stay enlarged unless treatment restores the original conditions. This explanation of ventricular expansion is consistent with the laws of fluid mechanics and poroelasticity despite the occurrence of only small transmantle pressure differences.

3.6. Conclusions

The model of intracranial dynamics incorporates interactions of all significant intracranial contents including the vascular system, CSF and the parenchyma. It does so for each pulsation of the cardiac cycle or multiple cycles over time. By changing one factor, the resistance to CSF absorption, communicating hydrocephalus and its onset can be simulated. This first principle model has been compared to actual Cine phase–contrast MRI of normal subjects and patients with hydrocephalus and found to properly reflect the observed dynamic flow patterns. To account for the all relevant system interactions, we have included the spinal canal with its more compliant epidural surface compared to the brain. The spinal subarachnoid space is normally very compliant because of the soft tissue and vessels that surrounds the dural face and acts as a cushion. Its deformability permits CSF displacement from the cranium into the spinal canal.

Normal pulsations amount to approximately 0.9 ml of flow back and forth through the foramina of magnum with each cycle. At high ICP, compliance decreases as the spinal canal is stretched. Thus, less CSF can be exchanged from the cranium to the spinal canal against a more compressed tissue. Our model incorporates these characteristics and plausibly explains the decrease in the cisternal CSF flow in hydrocephalus.

Some aspects of the mystery of acute communicating hydrocephalus have been explained. The model, however, does not aim to explain chronic forms of hydrocephalus, hemodynamic effects caused by pseudo-tumors or dural sinus thrombosis. Future work will resolve in more detail the cerebral vascular tree to increase the fidelity of the predictions as well as to quantify the effect of brain deformations on the local blood flow, straining or elongation of blood vessels in the periventricular area. More questions about the physiological consequences of the physical changes in its chronic phase arise. How does the brain and vasculature adapt to stretching or compressing, and what specifically causes damage to the brain? Knowing the fundamental physics of the central nervous system provides a scientific understanding of the forces that affect the brain tissue and may help predict when irreversible damage will occur. The same type of physical analysis can be applied to tumors, hemorrhagic strokes and sub-dural hemorrhages, and can potentially lead to a better understanding of these pathological states. Much work remains to be done in expanding the model, but the integration of the major components (blood, CSF, and parenchyma) appears to provide a good start into understanding intracranial dynamics.

4. NORMAL AND HYDROCEPHALIC BRAIN DYNAMICS—THE ROLE OF REDUCED CEREBROSPINAL FLUID REABSORPTION IN VENTRICULAR ENLARGEMENT

4.1. Summary

CINE phase-contrast MRI (CINE-MRI) was used to measure cerebrospinal fluid (CSF) velocities and flow rates in the brain of six normal subjects and five patients with communicating hydrocephalus. Mathematical brain models were created using the MRI images of normal subjects and hydrocephalic patients. In our model, the effect of pulsatile vascular expansion is responsible for pulsatile CSF flow between the cranial and the spinal subarachnoidal spaces. Simulation results include intracranial pressure gradients, solid stresses and strains, and fluid velocities throughout the cranio-spinal system. Computed velocities agree closely with our *in vivo* CINE-MRI CSF flow measurements. In addition to normal intracranial dynamics our model captures the transition to acute communicating hydrocephalus. By increasing the value for reabsorption resistance in the subarachnoid villi, our model predicts that the poroelastic parenchyma matrix will be drained and the ventricles enlarge despite small transmantle pressure gradients during the transitional phase. The poroelastic simulation thus provides a plausible explanation on how reabsorption changes could be responsible for enlargement of the ventricles without large transmantle pressure gradients.

4.2. Introduction

A more complete understanding of cerebrospinal fluid (CSF) flow through the ventricular system, brain parenchyma, and subarachnoidal spaces may be necessary in explaining diseases of the central nervous system such as hydrocephalus, Chiari malformations (Greitz 2004), and syringomyelia (Greitz 2006). Precise knowledge about fluid flow and complex fluid-tissue interactions in the human brain has in the past been hampered by experimental inaccessibility.

However, state of the art medical techniques such as CINE-MRI and CT angiography allow us to non-invasively measure CSF flow rates and blood flow, and have great potential for improving the quantitative understanding of intracranial dynamics. Despite progress in medical imaging, measuring fluid pressures and tissue stresses in the brain still requires invasive procedures. Therefore, using CINE-MRI data we have developed and validated computational models based on first principle conservation balances for predicting fluid pressures and solid stresses. First principles models satisfy the laws of motion, while at the same time predicted results align with the experimental measurements. By using this computational approach we propose to better explain experimental measurements by quantifying the driving forces, flows, and interactions that are responsible for the patterns that we see in normal as well as diseased dynamics. This model based approach should not be confused with data fitting in which experimental values are reproduced by suitable mathematical functions that do not conserve basic physical quantities like momentum or mass. The first principles approach, if correctly applied, will not only render agreement between experiment and proposed models, but by induction also show that the physical principles that supported the model might be at work in reality.

Due to the geometric complexity of the cranio-spinal system, many attempts to quantify CSF flow have relied on analyzing the system as a series of compartments, each compartment idealized as a simple geometric entity like a cylindrical tube. In the approach, governing equations are solved analytically (Kaczmarek, Subramaniam et al. 1997; Smillie, Sobey et al. 2005), and the results are useful in helping us understand the basic fundamentals of fluid flow through such structures. However, because compartmental models simplify the true geometry, results are merely qualitative. Others have attempted to quantify CSF flow and brain movement using the distributed finite volume and finite element methods (Jacobson, Fletcher et al. 1999;

Pena, Bolton et al. 1999; Taylor and Miller 2004; Linninger, Xenos et al. 2007). A mathematical model is created by converting human MRI brain images into a grid of finite elements, preserving the patient-specific brain geometry. With the introduction of suitable boundary conditions and material properties, the discretized equations of fluid flow and solid deformation are solved numerically over each element. This approach is hampered by the geometric complexity of the human brain; realistic brain models require large computational meshes and computer power. Consequently, some researchers have limited their analysis of the cranio-spinal system to small substructures, such as a sagittal section of the parenchyma (Pena, Bolton et al. 1999; Taylor and Miller 2004), axisymmetric model of the spinal cord (Bertram, Brodbelt et al. 2005), or a reconstructed aqueduct of Sylvius (Jacobson, Fletcher et al. 1996; Jacobson, Fletcher et al. 1999; Fin and Grebe 2003). Results obtained from isolated substructures may explain details about fluid flow and geometry dependent stresses in a small region (Pena, Bolton et al. 1999), but do not provide insights into the main pathology leading to a complex disease like hydrocephalus. To better understand normal and hydrocephalic intracranial dynamics, a *holistic* model of the physics of the central nervous system is needed—one that incorporates the interaction between blood flow, cerebral vasculature expansion, soft tissue stresses, and CSF dynamics including production, flow, and reabsorption.

A poroelastic model for the deformable parenchyma is a necessary step to quantify changes that occur in the hydrocephalic brain. Recently, we have studied the CSF flow patterns and pressure fields in a normal subject and a patient with communicating hydrocephalus (Linninger, Xenos et al. 2007). In this present work, we include a poroelastic fluid-tissue interaction model which accounts for brain motion due to systolic expansion of the cerebral vasculature and CSF flow within the spinal canal.

In the next section we describe our methodology, including a discussion of the governing equations and boundary conditions used in our simulations. Section three presents results validating the predicted CSF flow and pressure field patterns. The experiments and computations show significant changes in flow patterns in hydrocephalus. This report closes with a critical discussion of our findings and future challenges for understanding hydrocephalus.

4.3. Methods

4.3.1. CSF Flow Measurements

Using CINE-MRI, we have previously measured cranial CSF velocities and flow rates, as well as the deformation of the lateral ventricular space in six normal subjects and five patients with hydrocephalus. All participants signed the consent forms approved by the Institutional Review Board at the University of Chicago and the University of Illinois at Chicago. More information on the CINE-MRI protocol for obtaining CSF flow measurements using sixteen equidistant time frames throughout the cardiac cycle is provided in our previous publications (Zhu, Xenos et al. 2006; Linninger, Xenos et al. 2007).

4.3.2. Image Reconstruction

T_1 and T_2 images from six normal subjects and five communicating hydrocephalus patients were used to reconstruct accurately the geometry of the ventricular system, the cranial and spinal subarachnoidal spaces, and the brain parenchyma. The image reconstruction was performed using Mimics 11.0 (Materialise, Belgium) software. Reconstructed surfaces and volumes were then meshed with computational grid generation methods, Gambit 2.4.6 software. The three-dimensional normal and hydrocephalic brain meshes were composed of 486,542 and 498,857 tetrahedral elements, respectively. The two-dimensional normal and hydrocephalic brain meshes were composed of 8,328 and 8,515 triangles, respectively. All simulations were confirmed to have reached convergent solutions after successive grid refinements with a time step size of 0.01

sec using an implicit Euler scheme. The computational meshes served as the computational domain for the fluid-structure-interaction (FSI) finite element analysis presented in subsequent sections. A sample three-dimensional reconstruction of the ventricular system for a hydrocephalic subject is given in Figure 14. Computed velocity fields are displayed at equally spaced cross sections.

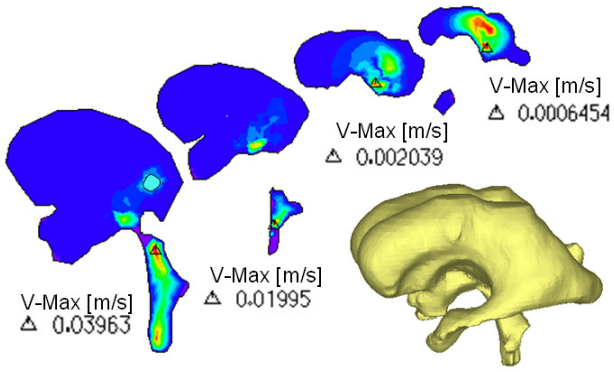

Figure 14. Maximum three-dimensional CSF flow velocity in the ventricular system of a communicating hydrocephalus patient. The velocity field is displayed in sagittal cross-sections of 5 mm increments from the mid-sagittal plane. This simulation predicts a maximum aqueductal velocity of 39.6 mm/s. Image reconstruction of the ventricular system was performed using MIMICS, 11.0.

4.3.3. Mathematical Model

We have created anatomically accurate poroelastic, finite element models for normal subjects and communicating hydrocephalus patients. Both types of models include CSF spaces as well as the brain parenchyma and spinal canal. For the normal subject, the anterior-posterior length of the cranium was 16.3 cm, the superior-inferior length of the entire model was 67.2 cm, and the spinal canal, measured from the cerebellomedullary cistern to the lowest point of the model, was 51.5 cm. These same dimensions in the hydrocephalic patient model were 19.4 cm, 70.0 cm, and 52.5 cm, respectively. Our finite element model is depicted in Figure 15.

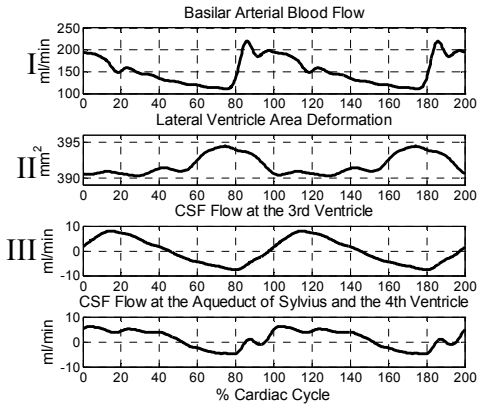

(a) Normal subject.

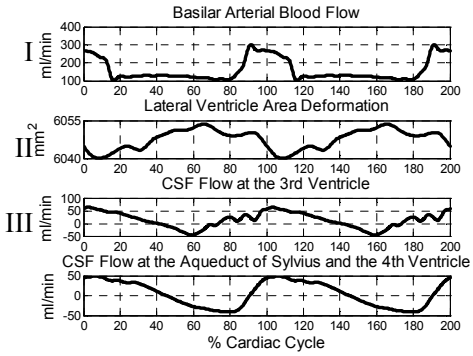

(b) CH patient.

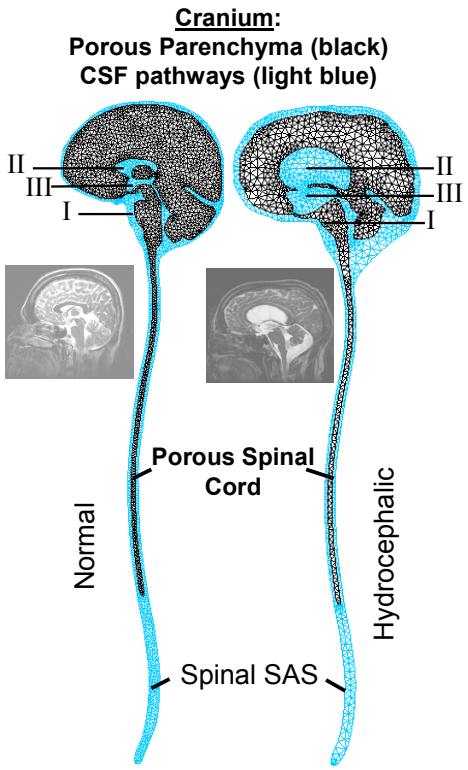

(c)

Figure 15. Blood and CSF flow, CINE-MRI measurements, in both a normal subject (a) and a patient with communicating hydrocephalus (b). Blood flow patterns were used in volumetric source term boundary conditions. Grid reconstruction was used to convert mid-sagittal MRI scans into discretized computational domains necessary for CFD-FSI analysis (c). CH: Communicating hydrocephalus

CSF velocity and pressure fields throughout the cranio-spinal system were calculated by solving the Navier-Stokes and Darcy equations for fluid flow coupled with the equations of solid motion. The governing equations for CSF motion in the ventricular and subarachnoidal spaces are given in eqs. (1-13)-(1-14).

Continuity for clear CSF flow

$$\begin{aligned} \nabla \cdot \vec{u} &= S_f \quad \text{Constant CSF production in ventricles} \\ \nabla \cdot \vec{u} &= 0 \quad \text{Subarachnoidal space and spinal canal} \end{aligned} \tag{1-13}$$

Momentum for clear CSF flow in ventricles and subarachnoidal space

$$\rho_f\left(\frac{\partial\vec{u}}{\partial t}+\vec{u}\cdot\nabla\vec{u}\right)=-\nabla p+\mu\nabla^2\vec{u} \tag{1-14}$$

ρ_f is the fluid density, $\vec{u}$ the velocity vector, p the fluid pressure, and μ the CSF viscosity. S_f is a fluid source term that accounts for the constant production of CSF. The total CSF production was set to 0.35ml/min (Johanson, Duncan et al. 2008). Outside of the ventricular system no CSF is produced in our model; thus the continuity equation for an incompressible fluid reduces to $\nabla\cdot\vec{u}=0$. Even though position does influence intracranial pressure (ICP), currently we have no scanner allowing us to include position-dependent flow measurements. Hence, gravitational influences were neglected in the current model. CSF was treated as an incompressible, viscous, Newtonian fluid.

The parenchyma and spinal cord were modeled as poroelastic media. Their two phases are the deformable cell matrix and the interstitial fluid. The interstitial fluid, occupying about 30% of the bulk volume, is essentially incompressible CSF. Additionally, the cell matrix occupies 70% of the bulk, is composed of mainly water and proteins, and can be deformed. The change of fluid content, $\partial\xi/\partial t$ is equal to the volume change of the parenchyma as described by Darcy's law (Biot 1941), eq. (1-15). The Darcy velocity, $\vec{q}$, is the relative motion of the extracellular fluid with respect to the solid cell matrix, eqs. (1-15)-(1-16). The average pore fluid velocity is $\vec{u}_f$, and $\vec{u}_s$ is the velocity of the solid structure (Biot 1941; Biot 1955; Peters and Smith 2002). The permeability of the solid matrix is k, fluid viscosity is μ, and fluid pressure is p.

Continuity for the extracellular fluid

$$\frac{\partial\xi}{\partial t}=-\nabla\cdot\vec{q}\ \text{ with }\ \vec{q}=\vec{u}_f-\vec{u}_s \tag{1-15}$$

Darcy's law for the extracellular fluid flow inside the parenchyma

$$-\nabla p = \frac{\mu}{k}\vec{q} \Rightarrow \frac{\partial \xi}{\partial t} = \frac{k}{\mu}\nabla^2 p \qquad (1\text{-}16)$$

The cell matrix must obey the dynamic force balance according to the theory of dynamic consolidation as in eq. (1-17), in which ρ_s is the density of the solid phase, $\vec{d}$ is the displacement vector of the solid cell matrix, G is the shear modulus, ν is the Poisson ratio, and ε_v is the volumetric strain (Biot 1941). The medium was assumed to be saturated. The force balance for the solid phase of the poroelastic medium is given in (1-17).

$$\rho_s \frac{\partial^2 \vec{d}}{\partial t^2} = G\nabla^2 \vec{d} + \frac{G}{1-2\nu}\nabla \varepsilon_v - \nabla p \text{ with } \varepsilon_v = \nabla \cdot \vec{d} \text{ and } \dot{\vec{d}} = \vec{u}_s \qquad (1\text{-}17)$$

Equations (1-13)-(1-17) were solved over finite element meshes reconstructed from real subjects' brain images with the commercial FSI code ADINA 8.3 (Adina R&D Inc., Watertown MA, USA). Material properties used in the simulations for both solid and fluid constituents are given in Table 5. In the next sections we explain the boundary conditions of solid displacement, CSF formation, and fluid pressure imposed on each of the finite element models.

Table 5: Material Parameters

Location	*Young's Modulus [Pa]*	*Poisson ratio*	*Density (solid) [kgm^{-3}]*	*Density (fluid) [kgm^{-3}]*	*Viscosity [kgm^{-1}s^{-1}]*	*Permeability [m^2]*	*Porosity*
Parenchyma	1x10^4	0.45	1,000			1x10^{-14}	0.3
Upper Spinal Dura	1x10^7	0.30	1,000				
Mid Spinal Dura	1x10^6	0.30	1,000				
Lower Spinal Dura	1x10^5	0.30	1,000				
CSF (SAS and ventricular pathway)				1,000	0.001		
Porous Reabsorption region			1,000	1,000	0.001	1x10^{-8}	0.3

4.3.4. Displacement Boundary Conditions

Special displacement boundary conditions emulated the expansion and dilation of cerebral vasculature occurring during the cardiac cycle. The experimental basilar arterial blood flow waveforms shown in Figure 15a, b were reconstructed using Fourier series and used as a

dynamic forcing function for the expansion terms. Vascular expansion terms representing the Circle of Willis and the choroid plexus were assumed to concur with the timing of the blood flow signal. The expansion terms representing arterioles inside the parenchyma were also applied dynamically, with a phase lag of about 30%. This phase lag led to CSF velocity, magnitudes, and directions consistent with the MRI signals. As displayed in Figure 15a, b the phase lag between maximum basilar arterial blood flow and maximum ventricular contraction for both the normal and hydrocephalic patient is about 20-35% of the cardiac cycle—the maximum basilar arterial blood flow precedes the maximum ventricular contraction. Therefore, our assumptions are consistent with the MRI data.

The increase in cerebral vasculature volume during systole is about 1.5 ml; typically 0.8 ml is displaced from the cranium into the spinal canal (Greitz 2004). Accordingly, the volumetric dilation terms were set to 0.5 to 1 ml at specific locations inside the brain in the choroid plexus. The effect of the total volumetric expansion was verified by integrating the calculated flow rate through the cranio-cervical junction over one cardiac cycle. The calculation confirmed a CSF pulsatile volumetric exchange between the cranial and spinal subarachnoidal space of 0.5 ml in normals. As observed in the real brain, expanding vasculature in our model causes forces in the parenchyma, leading to compression and dilation of the poroelastic brain, which in turn induces interstitial fluid flow inside the porous medium and within the CSF spaces. In our model the deforming brain tissue also causes stresses on the lateral ventricles. The ventricles compress slightly, and CSF is forced out of the ventricular system. Therefore, as a consequence of the vascular expansion, a portion of the CSF is displaced out of the cranium into the compliant spinal canal. This CSF exchange is well known clinically and is possible due to distensibility of the lower lumbar region and the rigidity of the skull. Deformable boundaries such as the lateral

ventricles, the lumbar region of the spinal canal, and portions of the cortex are governed by fluid-structure constrains as given in eqs. (1-18)-(1-20).

$$\vec{d}_f = \vec{d}_s \tag{1-18}$$

$$n \cdot \boldsymbol{\sigma}_f = n \cdot \boldsymbol{\sigma}_s \tag{1-19}$$

$$\vec{u} = \dot{\vec{d}}_s \tag{1-20}$$

Equation (1-18) ensures displacement compatibility between the fluid, $\vec{d}_f$, and solid, $\vec{d}_s$, domains along the deformable interface. Also along the fluid-solid interface the stresses normal to the interface, $n \cdot \boldsymbol{\sigma}$, must balance as in (1-19). Finally, the velocity of the fluid, $\vec{u}$, at the interface is equal to the velocity of the solid wall, $\dot{\vec{d}}_s$, as shown in (1-20). At non-deformable interfaces, no-slip boundary conditions apply for the fluid.

4.3.5. Fluid, Pressure Boundary Conditions

In this section we briefly discuss the fluid boundary conditions. CSF is generated in the choroid plexus and is also produced in the brain parenchyma. The production is known to be constant at a rate of 0.35 ml/min and largely pressure independent, suggesting active transport mechanisms (Johanson, Duncan et al. 2008). In the real brain, the choroid plexus is situated at the bottom of the lateral and third ventricles. For simplicity, the bulk CSF production in the model is introduced only in the lateral ventricle.

An ICP of 500 Pa is normal. In hydrocephalus, the ICP can rise to 3000 Pa or higher (Troupp 1975). Accordingly, we assumed a baseline ICP of 500 Pa for the normal case and 2700 Pa for the hydrocephalic case. These baseline pressure values were applied at the sagittal sinus. The sagittal sinus is represented as a porous structure surrounding the cranial subarachnoidal space.

4.4. Results

4.4.1. Predicted CSF Flow Patterns in the Cranio-Spinal System

Figure 15 displays experimentally obtained blood flow in the basilar artery, lateral ventricle deformation, CSF flow at the third ventricle, and CSF flow at the junction of the aqueduct of Sylvius and the fourth ventricle for a typical normal subject and a patient with communicating hydrocephalus. Figure 16 summarizes two-dimensional analyses of CSF flow measurements for normal subjects and hydrocephalic patients at six locations of interest obtained with CINE-MRI.

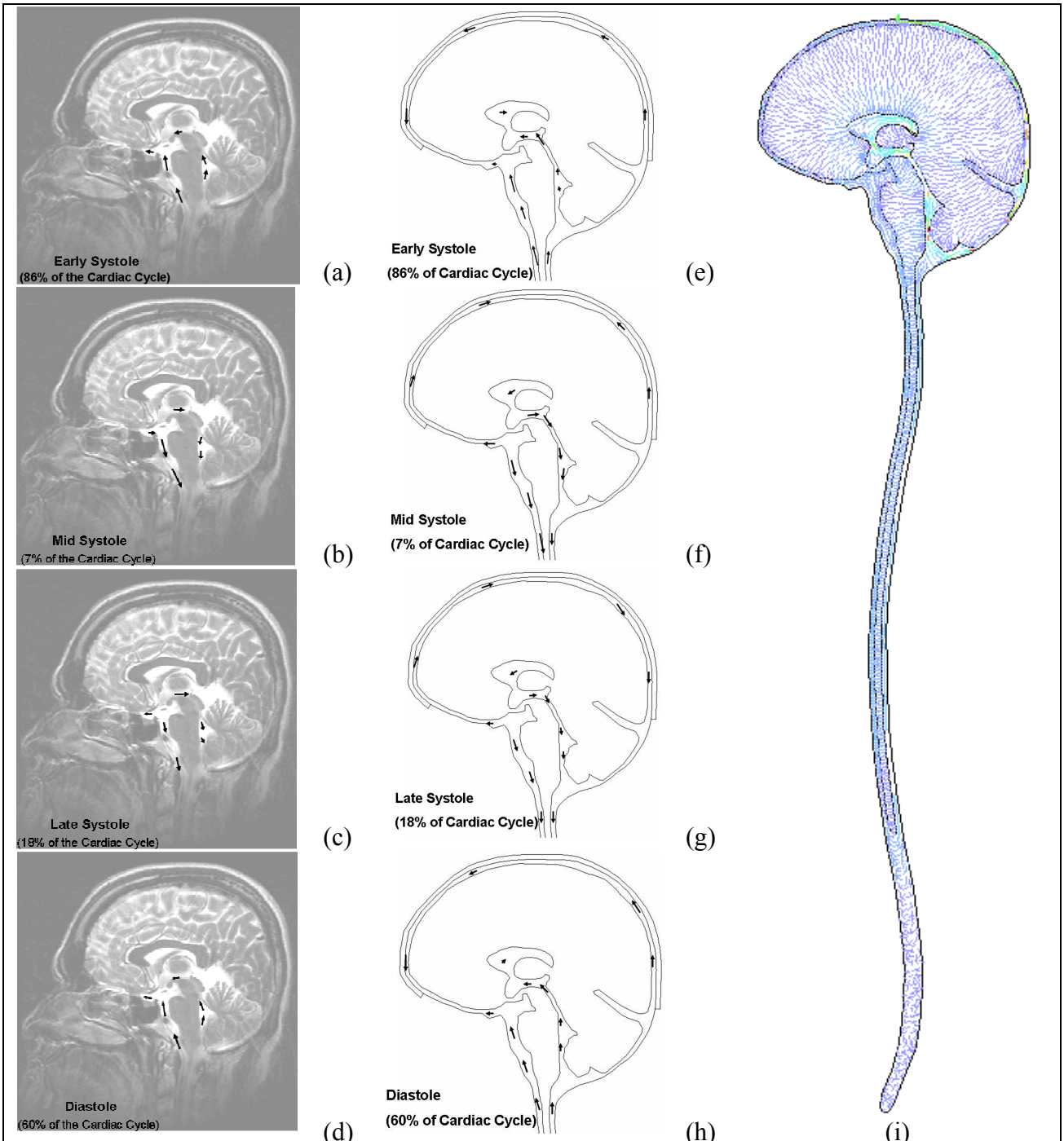

Figure 16. Measured (CINE-MRI; frames a-d) and calculated (CFD; frames e-h) CSF flow in a normal brain during one cardiac cycle; relative magnitude depicted by arrow length. The model CSF flow predictions are in good agreement with CINE-MRI measurements—in timing, direction, and magnitude. (i) CSF flow field throughout the cranio-spinal system at 18% of the cardiac cycle.

The reference time of the cardiac cycle is based on the signal of the basilar arterial blood flow given in Figure 15a, b. The measured direction and relative magnitude of CSF flow occurring at early systole, mid-systole, late systole, and diastole is shown in frames a through d of Figure 16. Frame a shows the latter stages of inferior-superior flow of CSF from the spinal canal to the cranium in early systole. This flow pattern is in good agreement with the measurement of the lateral ventricle size change shown in Figure 15. At this point in time, the lateral ventricles are just beginning to decrease in volume. During systole, the cerebral vasculature expands. The increase of the cerebral blood lumen causes stress to the parenchyma which in turn compresses the lateral ventricles simultaneously. The CSF volume inside the lateral ventricles is also diminished by the expanding choroid plexus. A compression of the lateral ventricles at the same time as the expansion of the choroid plexus results in displacement of CSF out of the ventricular system as seen in frames b and c. CSF is further discharged from the cranial subarachnoidal space into the spinal canal. Thus, CSF flow is superior-inferior, entering the spinal canal during mid and late stages of systole. The arterial pressure decreases in diastole of frame d. The blood lumen diminishes again, and CSF flows back from the spinal canal into the cranial subarachnoidal space. This backflow is also reversing the flow in the aqueduct. The complex flow patterns and the predicted CSF velocities throughout the cranium of a normal subject during the course of one cardiac cycle are provided in frames e-h of Figure 16. The predicted results agree closely with CINE-MRI data in direction, magnitude, and timing. The CSF velocity field throughout the cranio-spinal system at 18% of the cardiac cycle is shown in Figure 16i.

The overall sequence of pulsatile CSF flow patterns in the hydrocephalic case is similar to the normal. However, the total CSF displacement through the ventricular system is larger in

hydrocephalus than in the normal case. In healthy brains, N=6, the average peak CSF velocity at the junction of the aqueduct and the fourth ventricle is about 3.82±2.12 mm/s. In hydrocephalus, N=5, the velocity magnitude is 3.4 times higher with peak velocity of 13.14±2.64 mm/s as in Figure 17. The CSF stroke volume through the ventricular system in the normal case is 0.028 ml; in hydrocephalus it is 0.222 ml, about eight times greater, shown in Figure 18. Predicted ventricular CSF stroke volumes for both the normal and hydrocephalic case are in good agreement with CINE-MRI CSF ventricular stroke volume measurements.

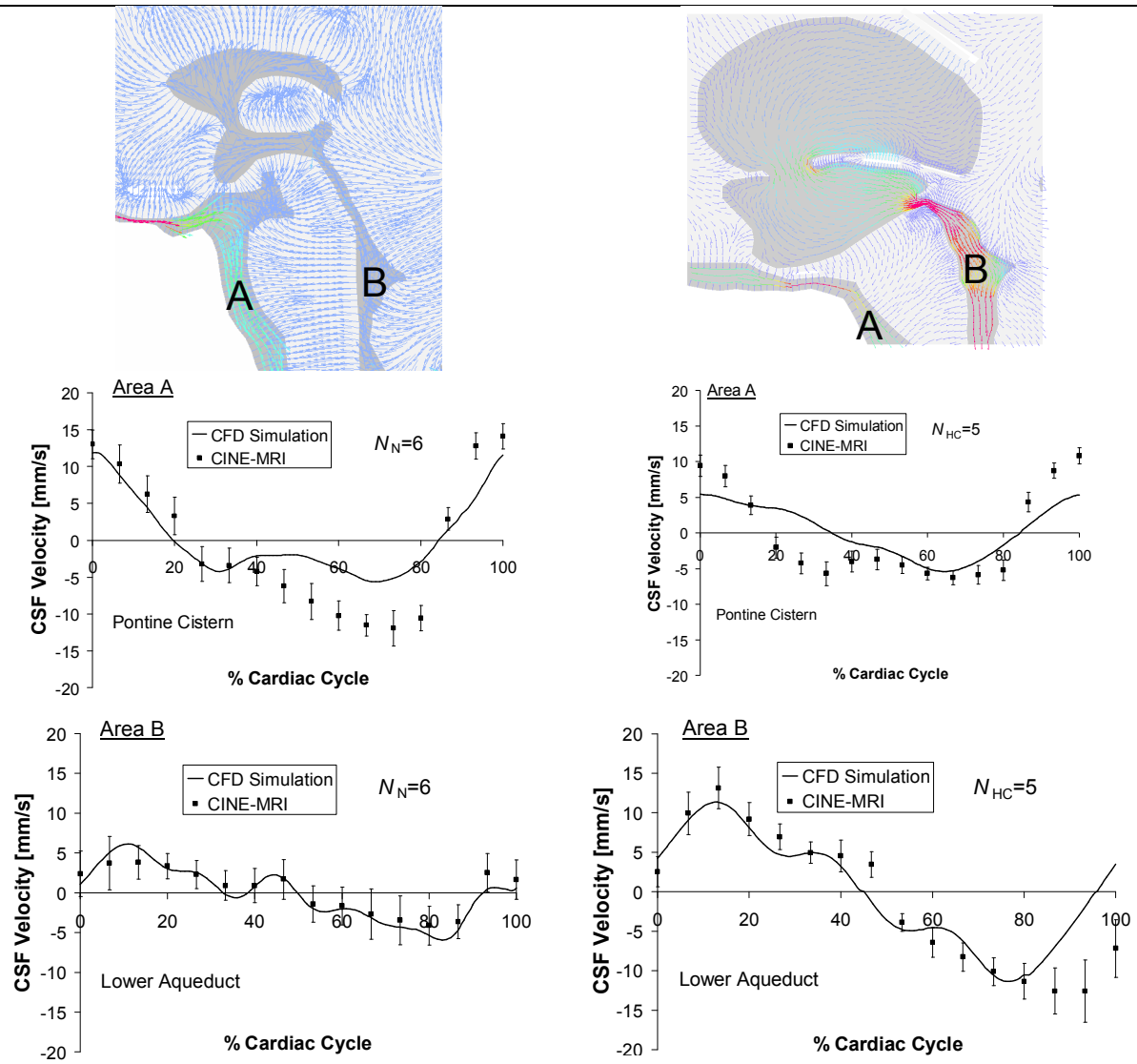

Normal subject **Communicating hydrocephalus patient**

Figure 17. Changes in pontine cistern and aqueduct flow patterns. In normal brains the average peak velocity in the pontine cistern is about 13.9 mm/s. Average peak velocity in the pontine cistern for the communicating hydrocephalic patients was 10.8 mm/s. In normal brains the average peak velocity at the junction of the aqueduct and the fourth ventricle is 3.8 mm/s. In the hydrocephalic case, the velocity magnitude is 3.4 times higher with peak velocity 13.1 mm/s. Velocity measurements based on 6 normal and 5 communicating hydrocephalic subjects; CFD results shown in solid lines. (Note: positive values correspond to S-I flow; negative values to I-S flow.)

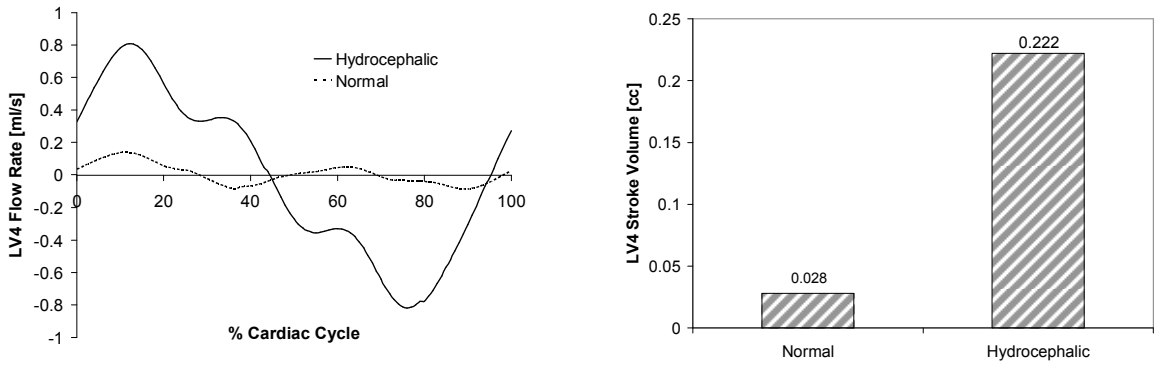

(a) (b)

Figure 18. Comparison of predicted CSF flow rate (a) and stroke volume (b) through lower fourth ventricle (LV4) in the normal versus communicating hydrocephalic case. Flow rate was calculated by multiplying LV4 velocity measurements (over the course of the cardiac cycle) by the cross sectional area of LV4 (circular cross section assumed). Stroke volume calculated by calculating the positive area under the curve (S-I flow) of (a).

In normals, the CSF velocity is higher in the pontine cistern compared to the hydrocephalic case. As displayed in Figure 17, in healthy brains, the average peak velocity in the pontine cistern is about 13.93±9.97 mm/s, N=6. Peak velocity in the pontine cistern for the hydrocephalic patients we tested, N=5, was only 10.82±1.16 mm/s on average. This value is about 30% lower than the normal subjects. We calculated the ratios of aqueduct to pontine velocity magnitudes, A/P. For the normal subject $(A/P)_N$ is about 0.3. In hydrocephalus this ratio is 1.2, approximately *four times greater* than normal. This increase in the velocity magnitude ratio is indicative of a reduced flow in the pontine cistern together with an increased flow through the aqueduct under hydrocephalic conditions, quantified in Figure 19.

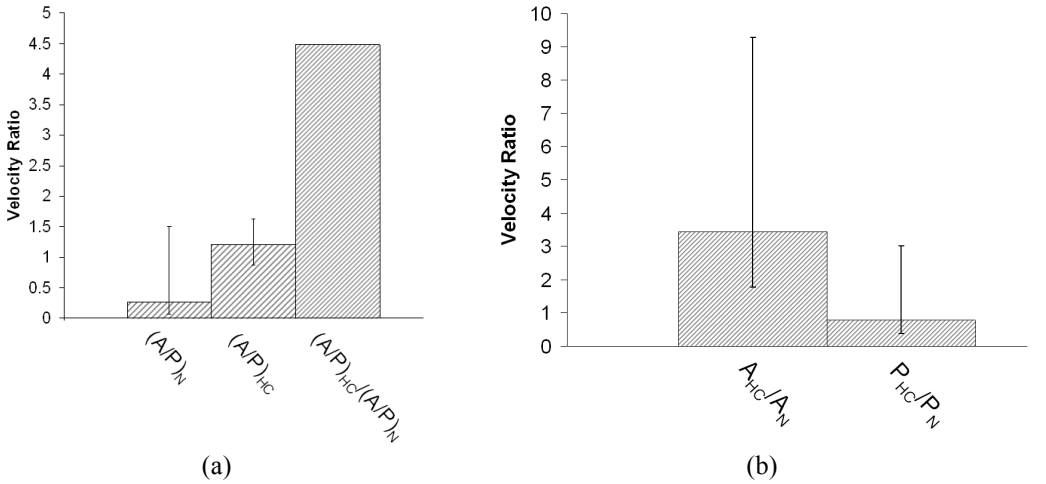

(a) (b)

Figure 19. CINE-MRI data from Figure 17 is revisited here to more clearly show the marked changes in CSF flow dynamics between normal subjects and communicating hydrocephalic patients. Due to the standard deviation of the measurements, a range of ratio values has been plotted. Frame (a) shows that in the normal case the aqueduct to pontine cistern CSF velocity is small compared to the same ratio in hydrocephalic patients. The ratio of the aqueduct to the pontine cistern velocity may on average be 4.5 times larger in the hydrocephalic case. (b) There is a significant increase in aqueductal flow velocity and marked decrease in pontine cistern flow velocity in the communicating hydrocephalic case. (A_N=3.82±2.12, P_N=13.93±9.97, A_{HC}=13.14±2.64, P_{HC}=10.82±1.16)

Qualitative differences in the CSF flow patterns between the normal and hydrocephalic case are displayed in Figure 20. At mid systole, the pontine CSF flow is larger in the normal case, but the aqueductal CSF flow is larger in the hydrocephalic case.

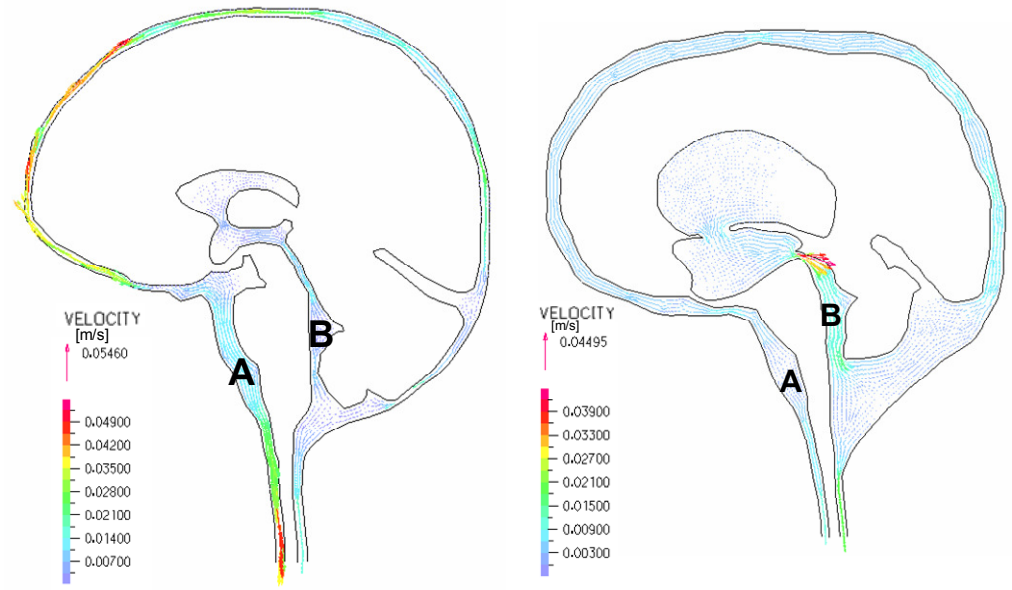

Figure 20. Simulated CSF flow pattern changes in the pontine cistern (A) and aqueduct (B) for normal (left) and hydrocephalic (right) subjects. CSF pontine flow is more pronounced in the normal case, whereas CSF flow is higher in the aqueduct and ventricular pathways under hydrocephalic conditions.

4.4.2. Intracranial Pressure Dynamics

For both normal and hydrocephalic subjects, the ICP peaks during systole. The timing of the ICP wave follows the blood pressure wave. We believe this lag indicates that CSF motion is induced by the expanding and receding vasculature. As shown in Figure 21, our simulations predict an ICP amplitude in the lateral ventricles for the normal subject of about 84 Pa; in the hydrocephalic patient it is almost twice that amount—161 Pa. This predicted increase in pulsatility matches ample clinical evidence of increased ICP amplitudes in hydrocephalus (Pettorossi, Di Rocco et al. 1978; Gonzalez-Darder and Barcia-Salorio 1989). The transmantle pressure gradient, defined as the difference between the subarachnoidal space and the lateral ventricle pressure, stays always small in both normal (45 Pa) as well as hydrocephalic (22 Pa) subjects. The lack of large transmantle pressure differences corroborates earlier findings (Stephensen, Tisell et al. 2002; Penn, Lee et al. 2005; Linninger, Xenos et al. 2007).

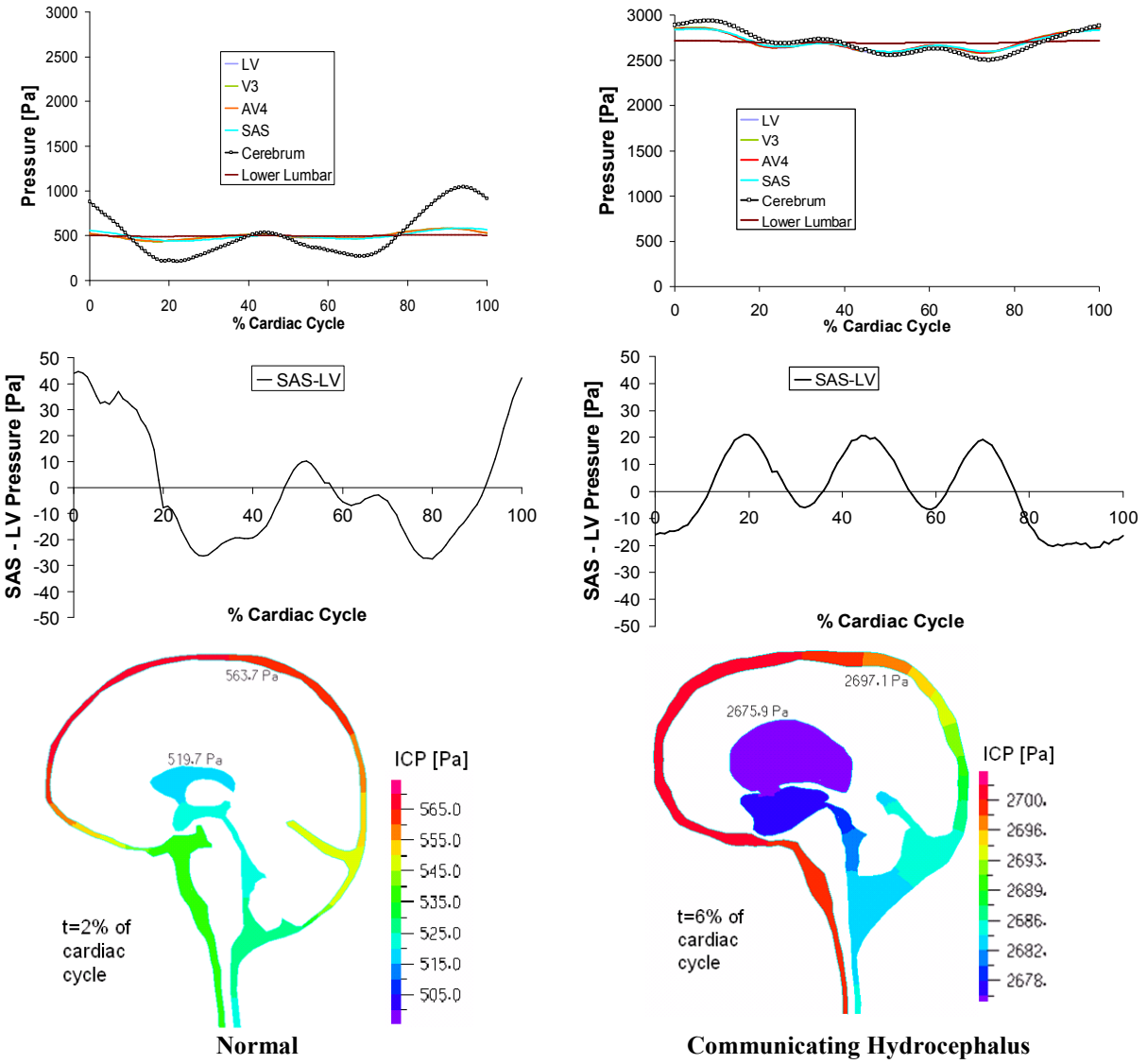

Figure 21. Simulations of intracranial pressure (ICP) dynamics. Normal subject (left); hydrocephalic patient (right). Top: Pressures in the ventricular system (Lateral ventricle (LV), third ventricle (V3), and junction of aqueduct and fourth ventricle (AV4)), the subarachnoidal space (SAS), cerebrum, and lower lumbar region. Middle: Despite elevated ICP in hydrocephalus, the *transmantle pressure* gradient, defined as the pressure difference between SAS and LV, does not exceed 45 Pa for the normal subject, 22 Pa for the hydrocephalic patient. Bottom: Two-dimensional visualization of the pressure field throughout the ventricular system and SAS when the transmantle pressure gradient is a maximum.

Pressure fields within the aqueduct for both normal and hydrocephalic cases are shown in Figure 22. Pressure gradients of only 1.4 Pa (normal) and 0.9 Pa (hydrocephalic) produce maximum velocities of 18 mm/s (normal) and 45 mm/s (hydrocephalic), respectively. These

predicted pressure differences for the normal subject is in agreement with both experimental and other earlier computational findings (Jacobson, Fletcher et al. 1996; Jacobson, Fletcher et al. 1999; Fin and Grebe 2003; Linninger, Tsakiris et al. 2005).

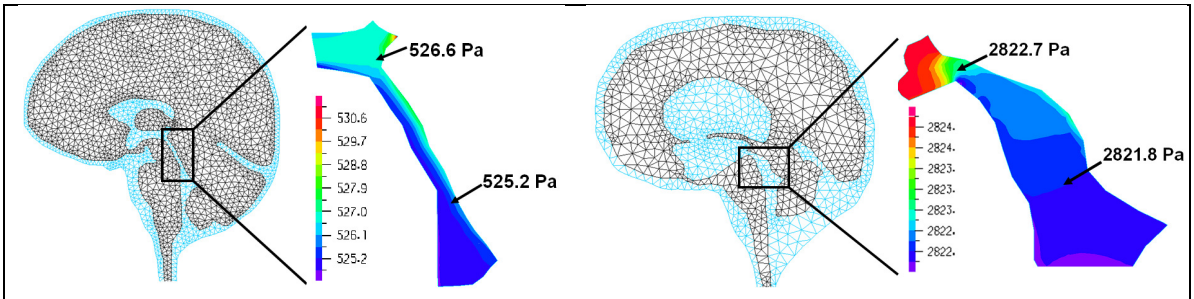

Normal **Communicating Hydrocephalus**

Figure 22. Pressure gradients across the aqueduct of Sylvius for normal subject (left) and patient with communicating hydrocephalus (right) when CSF velocity is a maximum through this structure. Pressure gradient: normal=1.4 Pa; hydrocephalic=0.9 Pa. The pressure difference in the aqueduct for the normal subject is on the order of other published values (Jacobson, Fletcher et al. 1996; Jacobson, Fletcher et al. 1999; Fin and Grebe 2003; Linninger, Tsakiris et al. 2005).

A summary of tissue stresses and CSF flow velocities at 13% of the cardiac cycle for the communicating hydrocephalus patient is given in Figure 23. Detail A provides a partial view of the parenchyma stress and CSF velocity fields in the lateral and third ventricles. Detail B shows stresses on the spinal dura wall in the prepontine area and CSF velocity in lower cranial subarachnoidal space. Detail C displays the stresses on the distensible mid portion of the spinal dura and a snapshot of CSF velocities in the spinal canal. These computations suggest that as fluid flows into the spinal canal, the spinal dura is compressed.

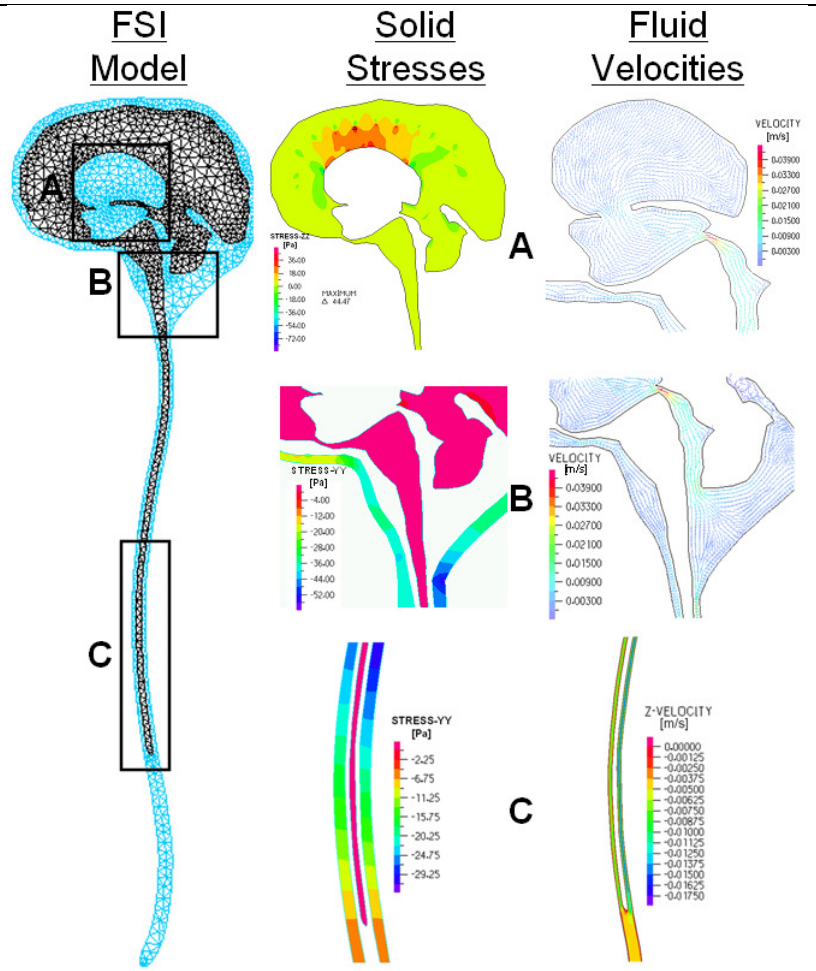

Figure 23. Summary of stresses and CSF velocities at 13% of the cardiac cycle, communicating hydrocephalus patient. Zone A: parenchyma stress and CSF velocity within the ventricular system. Zone B: stress on the spinal dura wall; CSF velocity in lower cranial SAS. Zone C: stress on mid portion of spinal dura wall and CSF velocity magnitude in the superior-inferior direction.

4.4.3. Prediction of Acute Hydrocephalic Conditions

We changed the reabsorption resistance in our model and observed dynamically which changes would occur in response to drastically increasing the reabsorption resistance. Without any further changes to the model we observed that the ventricles grew. In response to an incremental increase in CSF outflow resistance through the sagittal sinus, the lateral ventricular pressure also increases as shown in Figure 24.

(a)

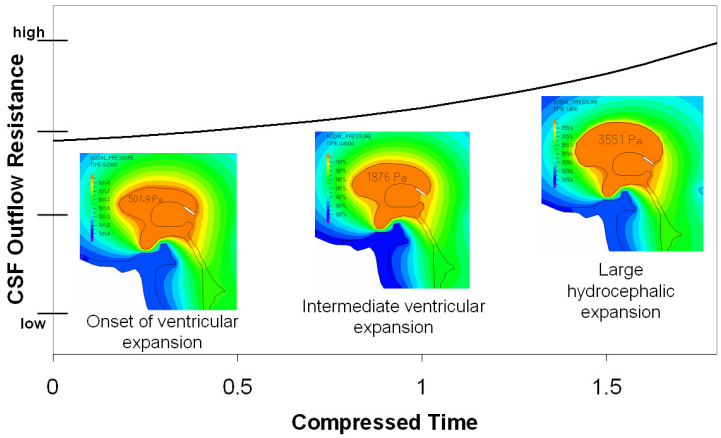

(b)

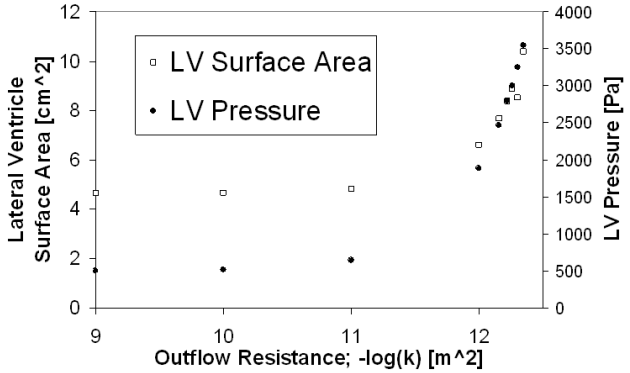

Figure 24. Predicted hydrocephalus model. (a) The resistance to CSF flow out of the cranium was increased incrementally. The negative log of permeability versus time has been plotted for ease of presentation. The size of the lateral ventricles increases substantially as the outflow resistance of our model is increased. (b) Quantitative results showing the surface area and pressure of the lateral ventricles as the resistance is increased. k=permeability

Three stages of ventricular growth have been plotted to show how the ventricles enlarge with increasing fluid pressure. The first image, in which the outflow resistance has not increased substantially, shows minimal enlargement of the lateral ventricle as well as an intraventricular pressure near the baseline ICP (500 Pa) prescribed in the model. There is noticeable ventricular expansion in the second image, in which higher outflow resistance results in intraventricular pressure of 1876 Pa, or three times the baseline value. In the third image there is substantial expansion of the lateral ventricle as well as an intraventricular pressure seven times larger than baseline. Figure 24b shows quantitatively the extent of lateral ventricle expansion and pressure

rise as outflow resistance is increased. The lateral ventricle surface area increases from 4.64 cm^2 to 10.38 cm^2, an increase of 223%; intraventricular pressure increases to 3708 Pa, approximately seven times greater than normal. The stress field for the largest ventricular expansion is shown in Figure 25. Tensile stresses are highest in the anterior and posterior horns. This pattern has also been noted clinically and computationally (Zimmerman, Fleming et al. 1986; Pena, Bolton et al. 1999; Taylor and Miller 2004). Large tensile stresses in the posterior and anterior horns in the hydrocephalic case imply that the tissue is stretched, and this may lead to periventricular edema associated with tissue damage (Ulug, Truong et al. 2003). Compressive stresses over the middle section may be responsible for fluid content change known to occur in hydrocephalus (Penn and Bacus 1984). The CSF seepage pathways inside the parenchyma is shown in Figure 25b. CSF flows through the ventricular system as well as seeps into the cerebrum toward the sagittal sinus where CSF is reabsorbed.

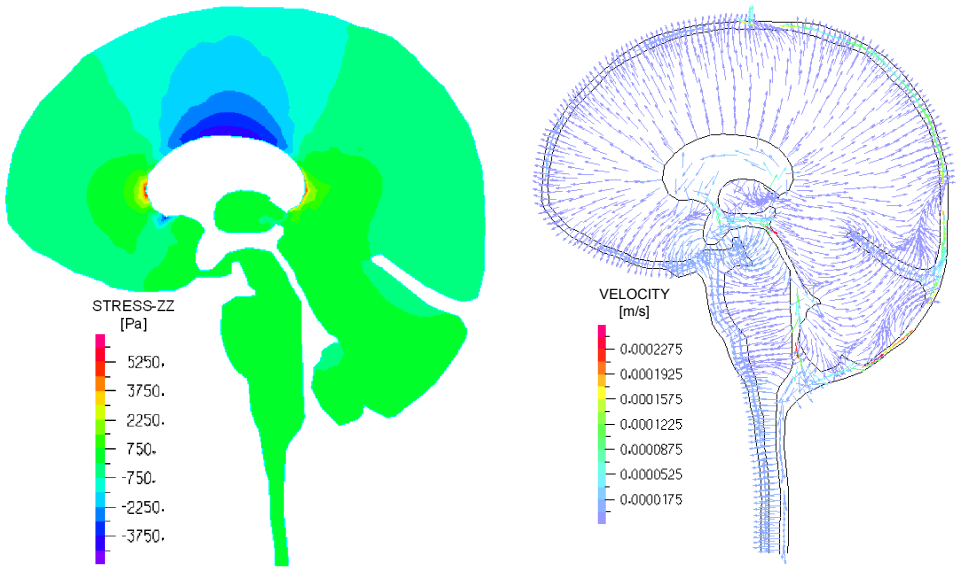

(a) (b)

Figure 25. Solid stresses and fluid flow in simulated communicating hydrocephalus. (a) Stress in the cerebrum under conditions of large ventricular expansion. Tensile stresses (red) occur near the anterior and posterior horns of the ventricles. Compressive stresses (blue) are prominent at and superior to the midsection of the lateral ventricle wall. (b) CSF flow field under identical conditions as in (a). CSF flows through the ventricular system as well as seeps through the cerebrum. The CSF is reabsorbed through the sagittal sinus.

4.5. Discussion

4.5.1. CSF Flow through the Pontine Cistern

The fluid-tissue interaction model proposed here advances the work of Linninger, et al. (Linninger, Xenos et al. 2007), by incorporating a deformable poroelastic medium. In contrast to earlier work where for the normal case we could not validate CSF velocity in the area of the pontine cistern, this work suggests that the expansion of arteries surrounding the cortex and the base of the brain (Circle of Willis) contribute significantly to the CSF velocity in the pontine cistern and ultimately to the CSF stroke volume into the spinal canal. Using a compartmental model, our group has determined that the reduction of CSF flow into the spinal canal in hydrocephalus may be due to a stiffening cerebrospinal system (in production). The soft tissue surrounding the spinal canal is compliant up to a particular threshold. An increase in ICP,

perhaps caused by a decrease in CSF uptake through the sagittal sinus, may push the spinal canal to its threshold, limiting the amount of CSF that may be displaced into the canal, and thereby lowering the flow rate through the pontine cistern.

4.5.2. Pressures throughout the Ventricular System

We have reproduced experimental findings that show a doubling of the pressure amplitude of the lateral ventricle in hydrocephalic patients (Czosnyka, Czosnyka et al. 2004). We have shown also that only a small pressure gradient is needed for maximum velocity through the aqueduct of Sylvius. Our predicted result of 1.4 Pa is in excellent agreement with other independent findings (Jacobson, Fletcher et al. 1996; Jacobson, Fletcher et al. 1999; Fin and Grebe 2003; Linninger, Tsakiris et al. 2005). We also predict a smaller value of 0.9 Pa for the hydrocephalic case, indicative of the change in geometry of the deformed ventricular system.

4.5.3. Changes to CSF Outflow Resistance

Our model used only basic conservation laws for mass and momentum transport and a small set of physical properties given in Table 5 to reproduce all known measurements of pressures and flow fields consistently in normal as well as in hydrocephalic patients. Given this satisfactory match between predictions and measurements, can the mathematical model also predict the transition from the normal to hydrocephalic state? An answer to this question would also provide a basic physical understanding of the causes of hydrocephalus. The next paragraph shows evidence in support of a theory for the creation of hydrocephalus.

A majority of researchers agree that hydrocephalus is associated with changes in the reabsorption of CSF into the sagittal sinus through the subarachnoid villi. Such obstruction causing hydrocephalus in animal models (Dandy 1919; Linninger, Tsakiris et al. 2005) is bound to increase the reabsorption resistance of CSF into the venous system. Thus, we implemented in the model a gradual increase of the outflow resistance. After a short delay, an increase in the

stresses in the horns of the lateral ventricles was noticed. As the reabsorption resistance is increased further the ventricular space enlarges thus reducing the space available for the parenchyma. Simultaneously the fluid water content of the parenchyma is reduced by discharging extracellular CSF. In effect the lateral ventricle increases and the size of the parenchyma is diminished consistent with the pathophysiology of hydrocephalus.

According to the Kellie-Monro doctrine, the cranium is a closed system. Therefore, when CSF accumulates due to constant production but increased outflow resistance, the deformation also goes along with an increase of ICP. Nevertheless, in our simulation of acute communicating hydrocephalus no large transmantle pressure gradients were observed remaining approximately at only 1 Pa. In fact, the only condition needed for ventricular enlargement was the overall increase in intraventricular pressure. In many cases of hydrocephalus it is believed that reabsorption through the arachnoid granulations is diminished. The mechanical model proposed here fits the current understanding of the pathophysiology of acute communicating hydrocephalus.

This model supports the notion of the significance of reabsorption resistance in the onset of acute hydrocephalus. This model does not prove hydrocephalus occurs in this manner nor does it explain all forms of the hydrocephalus syndrome. Specifically, normal pressure hydrocephalus requires the understanding about why the intracranial pressures, which might have been initially high, return to lower levels. We believe that biomechanical relaxation of tissues or changes to the tissue properties might be responsible for the normal pressure hydrocephalus phenomenon, but definitive answers require more research and are too early to be made from this study focusing on the onset of acute hydrocephalus. Nevertheless, the qualitative agreement of changes induced in this comprehensive model by reducing the reabsorption constant leading to intracranial

pressure rise as well as the enlargement of the ventricles are very encouraging. While these simulation results do not confirm the onset of acute hydrocephalus in reality, the first principles physics model adopted here supports the notion of the significance of reabsorption in the development of hydrocephalus.

4.6. Model Limitations and Future Work

This chapter presents CSF flow field predictions in two and three dimensions, and advances our compartmental model (Linninger, Tsakiris et al. 2005) which accounted for the interaction between CSF and the choroid plexus. Some limitations of this current model need to be mentioned. First, even though the MRI reconstruction of geometry and physiological spaces in the brain was performed in three dimensions, many of the comparisons between normal and hydrocephalic simulation experiments were conducted with mid-sagittal two-dimensional simulations. This choice shortened the simulation time since the main objective in this publication was to describe the timing and the relationship between variables. Some results of the three-dimensional analysis have been reported in Figure 14, like the flow fields in the ventricular spaces, but a full display of three-dimensional results was omitted. Second, in the current model we predicted the effect of expanding vasculature as input on the parenchyma and the CSF flow as output. However, we did not fully create a spatially accurate model of the cerebral vasculature. In the simulations for normal and hydrocephalic brain dynamics, the amplitudes in the prepontine region are smaller than ones observed in CINE-MRI measurements. We attribute that to the simplified model of cerebral vasculature which in reality may add more pulsatility due to the interaction with the basilar artery. In the future, a fully coupled cerebral vasculature model interacting with the CSF and parenchyma will be developed. This future model will compute all forces and pressures that occur inside the central nervous system only as functions of the arterial and venous pressures. All internal force interactions and mass transfer

between vasculature, CSF, and parenchyma will be resolved by momentum and species transport equations.

5. THREE-DIMENSIONAL COMPUTATIONAL ANALYSIS OF CSF FLOW IN THE BRAIN

5.1. Summary

A three-dimensional model of the human cerebrospinal fluid (CSF) spaces is presented. Patient-specific brain geometries were reconstructed from magnetic resonance images. The model was validated by comparing the predicted flow rates with Cine phase-contrast MRI measurements. The model predicts the complex CSF flow patterns and pressures in the ventricular system and subarachnoid space of a normal subject. The predicted maximum rostral to caudal CSF flow in the pontine cistern precedes the maximum rostral to caudal flow in the ventricles by about 10% of the cardiac cycle. This prediction is in excellent agreement with the subject-specific flow data. The computational results quantify normal intracranial dynamics and provide a basis for analyzing diseased intracranial dynamics.

5.2. Introduction

CSF, a clear plasma-like fluid surrounding the cerebrum and spinal cord, is produced mainly by the choroid plexus and flows through the ventricles to the subarachnoid space where it is absorbed into the blood stream via the sagittal sinus (Nolte and Sundsten 2002). Disturbances in the natural CSF flow patterns are often associated with diseases like hydrocephalus, syringomyelia, or Chiari malformation (Milhorat, Chou et al. 1999; Koyanagi, Iwasaki et al. 2005). The modeling approach presented here provides a basis for creating a quantitative understanding of changes in flow patterns associated with the diseased brain. By incorporating subject-specific geometric data into our model, the CSF flow and pressure gradients in the brain can be quantified. Through rigorous modeling, we intend to reproduce the dynamic mechanical behavior of an individual human brain, and by doing so, we aim to explain quantitative relationships between cerebral blood flow, CSF pressures, and flow rates.

Previously, we have devoted much effort to reconstructing the CSF flow in two-dimensions (Linninger, Xenos et al. 2007; Linninger, Sweetman et al. 2009). However, a two-dimensional approach has the disadvantage that it does not render the volume relationships accurately. For instance, when considering only a two-dimensional cross-section along the longitudinal fissure of the brain, one either misses the cerebral ventricles completely or does not correctly render the space between the two hemispheres. Moreover, the spatial relationship between the pontine cistern and the ventricular space can not be properly rendered in a two-dimensional model. The correct relationship between all fluid spaces in the cranium can only be studied properly when using a three-dimensional model.

Several three-dimensional models of cerebrospinal fluid flow have been reported in the literature. Jacobson et al. have studied the flow and pressure dynamics of the cerebral aqueduct (Jacobson, Fletcher et al. 1996; Jacobson, Fletcher et al. 1999). More advanced aqueductal models accounted for the aqueduct's deformability (Fin and Grebe 2003). Three-dimensional CSF flow studies inside the third ventricle have also been reported (Kurtcuoglu, Soellinger et al. 2007; Cheng, Tan et al. 2010). Gupta et al. investigated the CSF flow in the lower region of the subarachnoid space, caudal to the lateral and third ventricles (Gupta, Soellinger et al. 2009). More recently, Linge et al. proposed a three-dimensional CSF flow model of the lower subarachnoid space and cervical region of the spinal canal (Linge, Haughton et al. 2010). However, none of the prior models described the CSF flow in the entire ventricular system and the subarachnoidal spaces.

The models described above were developed to increase knowledge about normal and diseased CSF dynamics. We agree with those researchers who point out that computational modeling of the CSF spaces is needed for improving shunt design for hydrocephalic patients and

for improving methods of intraventricular and intrathecal drug delivery (Kurtcuoglu, Soellinger et al. 2007; Gupta, Soellinger et al. 2009). To this end, this article presents a three-dimensional flow model of the human cranial fluid space. As an advancement of the prior models mentioned above, the current model includes the *entire* cranial subarachnoid space as well as the entire ventricular system. The model is used to predict the CSF flow field and intracranial pressures resulting from brain tissue displacement.

The next section describes our methodology and presents the governing equations and boundary conditions used in our simulations. The Results section presents model predictions of CSF flow rates and intracranial pressures for a subject with average-sized ventricles and a patient with enlarged cerebral ventricles. This report closes with a discussion of our findings as well as a critical assessment of the current model.

5.3. Methods

5.3.1. CSF and Blood Flow Measurements

Cine phase-contrast magnetic resonance imaging (CINE-MRI) was used to measure cranial CSF velocities in a normal subject and a patient diagnosed with communicating hydrocephalus. Additional measurements included change in lateral ventricle size, CSF flow rate in the third ventricle and at the junction of the aqueduct and fourth ventricle, and the blood flow rate in the basilar artery. The participants signed consent forms approved by the Institutional Review Board. Detailed flow results and data acquisition methods were described previously (Zhu, Xenos et al. 2006; Linninger, Xenos et al. 2007; Linninger, Sweetman et al. 2009).

5.3.2. Image Reconstruction and Model Development

T_2-weighted MR images of the cranium were manually segmented using image reconstruction software, Mimics 12.11 (Materialise, Belgium). The manual segmentation process resulted in patient-specific, three-dimensional triangulated surface meshes of a normal subject

and a patient with communicating hydrocephalus. The crude image displayed in the left panel of Figure 26 displays the actual reconstruction of the ventricular and cranial subarachnoid spaces obtained from the T_2 images for the normal subject.

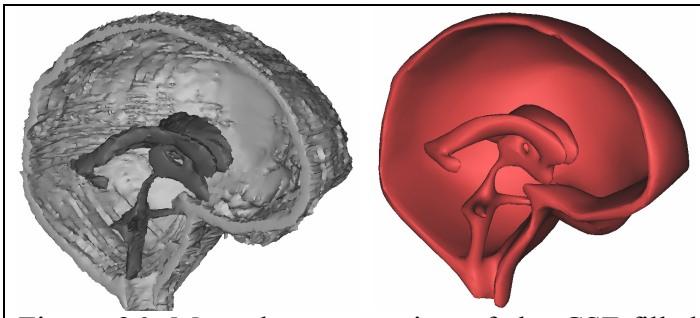

Figure 26. Manual segmentation of the CSF-filled spaces of the cranium resulted in the initially crude surface shown on the left. Advanced filtering techniques such as surface smoothing and triangle reduction resulted in the improved, more realistic surface displayed on the right.

Because of the finite resolution of the MRI data, the crude reconstruction has rough surfaces with many discontinuous faces. The coarse surface may cause artificial flow effects along uneven interfaces. In an effort to overcome this deficiency, the rough surfaces were removed using Laplacian smoothing (Hansen, Douglass et al. 2005). During the smoothing process, the quantity of triangular faces defining the surface mesh was reduced and the surface quality improved by normalizing the triangles' height to base ratio. These filtering techniques were provided by Mimics to obtain the improved surface reconstruction shown on the right in Figure 26. After improving the reconstructed brain and ventricular surfaces, the surface meshes were imported into ADINA-FSI 8.6. In ADINA-FSI the meshes were discretized using Delaunay triangulation for the inner domain and the advancing front algorithm for the domain boundary. The normal brain shown in Figure 27 required 765,062 tetrahedral fluid elements and 486,542 tetrahedral solid elements. The three-dimensional model and a summary of boundary conditions

are shown in Figure 27. Material parameters and a list of boundary conditions are given in Table 6.

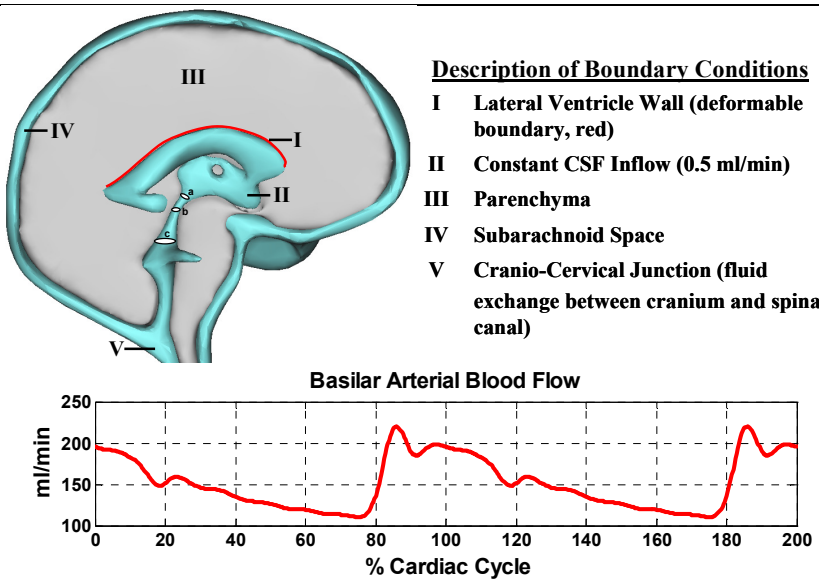

Figure 27. Three-dimensional model of the human cranium. Deformation occurs along the upper surface of the lateral ventricle wall, highlighted in red. The blood flow waveform in the basilar artery, bottom graph, was used as a boundary condition for pulsatile CSF flow; described in Methods section. Circular cross sections *a*, *b*, and *c* in the ventricular system indicate locations where the Womersley numbers were calculated. Mean value, c_0 and coefficients a_k, and b_k of the Fourier series in eq. (1-23) are 169.7760, 27.9791, 12.3427, 14.9403, -5.3310, -5.4838, -1.6638, 2.2920, 4.5670, 9.5584, -6.9098, -6.8080, -0.6282, 3.7181, 4.2953, 1.6978, -0.1358, respectively.

Table 6. List of boundary conditions and material parameters.

Location	Boundary Condition	Material parameters
Lateral & 3rd Ventricle	CSF inflow, 0.5 ml/min	-
Upper subarachnoid space	Pressure, 500 Pa	-
Arachnoid layer	no slip, u=v=w=0	-
CSF pathways	divergence free	density, 998.2 kg/m^3; viscosity, 0.001003 kgm^{-1}s^{-1}
Brain tissue	fluid structure interaction along lateral ventricle wall and near pontine cistern	Young's modulus, 10 kPa; Shear modulus, 3.4 kPa; Poisson ratio, 0.45

5.3.3. Fluid-Solid Boundary Conditions

The mathematical models adopt physiologically relevant boundary conditions accounting for CSF production and pulsatility. The total CSF production, S_f, is a fluid generation term

matching experimental data for average CSF production in adult humans, approximately 0.5 ml/min (Segal 2001). CSF is treated as a Newtonian fluid with viscosity and density similar to water. Assuming fluid incompressibility, continuity for CSF flow in the ventricles is written,

$$\rho_f \left(\vec{\nabla} \cdot \vec{u} \right) = S_f \tag{1-21}$$

Outside the ventricles no CSF is produced; accordingly the continuity equation reduces to $\nabla \cdot \vec{u} = 0$. CSF motion inside the fluid-filled spaces is governed by the Navier-Stokes equations given in eq. (1-22), written in vector form.

$$\rho_f \left(\frac{\partial \vec{u}}{\partial t} + \vec{u} \cdot \vec{\nabla} \vec{u} \right) = -\vec{\nabla} p + \mu \vec{\nabla}^2 \vec{u} \tag{1-22}$$

In eqs. (1-21) and (1-22), ρ_f is CSF density; $\vec{u}$ is CSF velocity; $\vec{\nabla} p$ is the pressure gradient; μ is fluid viscosity.

Pulsating cerebral blood flow drives pulsatile CSF flow within the central nervous system (CNS). The process is driven by blood supply to the brain causing compliant arteries and arterioles to expand. Vascular expansion causes brain tissue stresses and displacements. In our model, tissue displacement compresses the lateral ventricles, forcing CSF into the subarachnoid space. Because the cranial volume remains constant, the total vascular expansion is matched by the sum of the CSF stroke volume expelled into the distensible spinal canal and the blood which leaves the cranium through the venous sinuses (Greitz 2004). As the cerebral vasculature returns to its diastolic resting lumen, CSF expelled during cardiac systole flows back from the spinal canal to the cranial subarachnoid space.

To account for the blood-CSF interaction in our model, volumetric expansion terms embedded in the parenchyma mimic arterial expansion and contraction. These volumetric expansions, S_V, are transmitted to the CSF-filled spaces. The magnitude and timing of the source terms, S_V, follow the measured cerebral blood flow wave pattern shown in Figure 27. The signal

was discretized with a Fourier series, eq. (1-23), where $i = \sqrt{-1}$, $c_k = (a_k \pm ib_k)/2$. The sign of the complex part, ib_k, is taken as plus when *k* is positive, and negative when *k* is negative. The value index zero, c_0, and coefficients a_k, b_k are given in Figure 27.

$$S_V(t) = \sum_{k=-8}^{8} c_k e^{2ik\pi t} \tag{1-23}$$

Seventeen terms were used to reconstruct the blood flow waveform measured at the basilar artery. We found that seventeen terms are a sufficient number of coefficients to reproduce the waveform accurately. The use of additional Fourier coefficients did not further improve the quality of the reconstructed waveform. Tissue displacement and ventricular wall movement is governed by eq. (1-24), where ρ_s is the density of the solid phase, $\vec{d}$ is the displacement vector of the solid cell matrix, G is the shear modulus, ν is the Poisson ratio, and ε_v is the volumetric strain.

$$\rho_s \frac{\partial^2 \vec{d}}{\partial t^2} = G\nabla^2 \vec{d} + \frac{G}{1-2\nu}\nabla\varepsilon_v \text{ with } \varepsilon_v = \vec{\nabla}\cdot\vec{d} \text{ and } \dot{\vec{d}} = \vec{u}_s \tag{1-24}$$

Fluid-structure interaction constraints are applied along the upper wall of the lateral ventricle. These constraints ensure equal displacement of solid and fluid elements along the ventricular surface as well as equal but opposite forces normal to the fluid-solid interface. At non-deformable interfaces, *no-slip* boundary conditions apply for the fluid.

5.3.4. Fluid Pressure Boundary Conditions

Normal intracranial pressure (ICP) is about 500 Pa (4 mmHg above venous pressure). Accordingly, we set a baseline ICP of 500 Pa. For the pathological case, we set the baseline ICP at 2700 Pa (Linninger, Xenos et al. 2007). These baseline pressures were applied at the sagittal sinus. The sagittal sinus represents as a porous structure surrounding the cranial subarachnoid space through which CSF reabsorption occurs.

5.3.5. Grid Independence Studies

To ensure accurate solutions of the fluid flow simulations, mesh independence studies were conducted. The velocity magnitude in three locations was compared across three computational grids: a *coarse* mesh with 543,903 elements, a *medium* mesh with 765,062 elements, and a *fine* mesh containing 1,599,412 elements. As shown in Figure 28, the percent error between the medium and fine meshes is less than 0.6% for the three areas of interest. This small change justifies the choice of the medium size grid for subsequent simulations. A fully implicit Euler scheme, using ADINA, with a step-size of 0.01 seconds was adequate to capture the CSF dynamics sufficiently; computer experiments with smaller step sizes showed no differences in the simulation results.

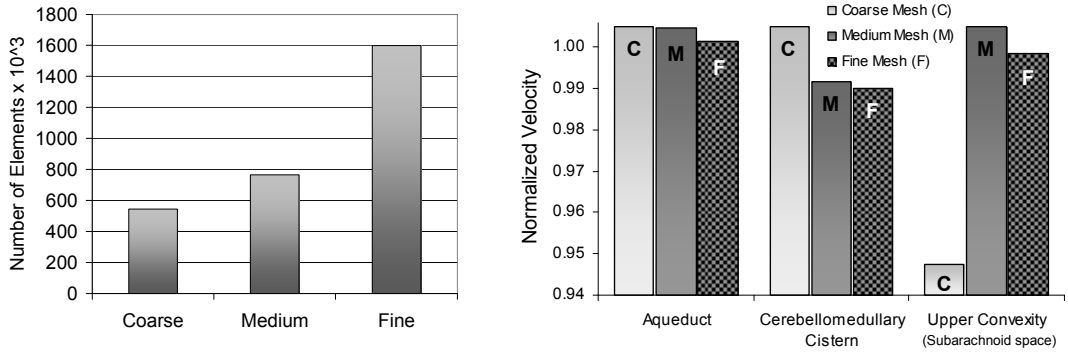

Figure 28. Frame A: the three grid sizes used in the mesh independence study. Frame B: comparison of the predicted maximum velocity magnitude in the aqueduct, cerebellomedullary cistern, and upper convexity of the subarachnoid space for the three grids. Percent error between the medium grid and fine grid is less than 0.6% for the three locations. Velocity values were obtained at mid-systole and normalized with respect to the maximum velocity at each location.

5.4. Results

5.4.1. Geometrical Properties of Normal and Diseased Brains

Table 7 summarizes the geometrical dimensions of the normal and hydrocephalic brains obtained from the image reconstruction technique. Although the main brain dimensions were similar for the normal and hydrocephalic case, the lateral ventricle volume was almost 18 times larger in the hydrocephalic case. This difference in ventricular size corresponds to a much

smaller parenchyma volume in the hydrocephalic case compared to normal: 1120 ml hydrocephalic, 1388 ml normal. Because this patient was diagnosed with communicating hydrocephalus, we conjecture that the decrease in brain tissue volume was due to tissue compression coupled with decreased brain water content. This process occurring in hydrocephalus is different from ventricular enlargement due to brain atrophy (Charney and Nestler 2004). The brain model cortical surface area is also given in Table 7. The values of the computational meshes are smaller than those typically reported for the brain cortical surface area, which can range from 1,500cm^2 to 2,500cm^2 (Blinkov and Glezer 1968; Peters and Jones 1984; Tramo, Loftus et al. 1995; Hutsler, Loftus et al. 1998). The significance of this discrepancy will be addressed in the Discussion section.

Table 7. Geometric details of three-dimensional reconstructed normal and diseased brains.

		Normal		**Hydrocephalic**	
Dimension [mm]	Crnm	163.1	*AP*	170.6	*AP*
		157.0	*SI*	168.2	*SI*
		150.3	*RL*	160.0	*RL*
	LV	73.3	*AP*[a]	103.4	*AP*[a]
		59.9	*RL*[b]	48.6	*RL*[b]
Volume [mL]	BT	1388.0		1120.3	
	SAS	101.1		104.0	
	LV	16.5		290.1	
	3V	4.5		9.9	
	4V	7.2		6.2	
Surface area [cm^2]	CS	783.8		851.9	
	VS	108.7		317.4	
Womersley number	A-V3	5.0		10.7	
	AS	4.2		9.2	
	A-4V	8.0		35.2	

AP[a] measured from the left posterior horn to the left anterior horn; *RL*[b] measured from left posterior horn to right posterior horn; Crnm, cranium; AP, anterior to posterior length; SI, superior to inferior length; RL, length from right to left; LV, lateral ventricle; BT, brain tissue; SAS, subarachnoid space; 3V, third ventricle; 4V, fourth ventricle; CS, cortical surface; VS, ventricular surface; A-V3, junction of aqueduct and third ventricle; AS, aqueduct of Sylvius; A-4V, junction of aqueduct and fourth ventricle

5.4.2. Model Predictions of CSF Flow and Pressures

Figure 29 compares the predicted CSF flow rate with CINE-MRI measurements obtained from a mid-coronal cross section in the third ventricle. The model predictions are in close agreement with the *in vivo* flow measurements. Computing the positive area under the curve in Figure 29 yielded a CSF stroke volume of 0.028 ml.

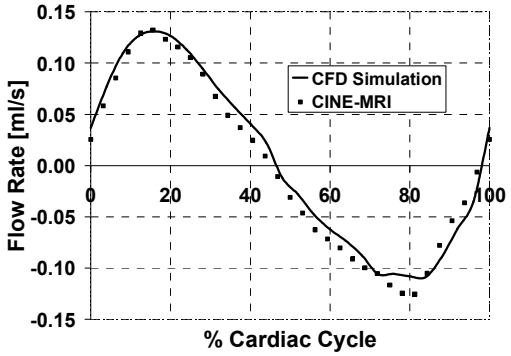

Figure 29. Simulated and measured CSF flow rates in the third ventricle of a normal subject. The model predictions (solid line) agree closely with the patient-specific data (squares).

Figure 30 shows early systolic, mid-systolic, and diastolic pressure and velocity profiles. The model predicts that velocity magnitude is largest in the aqueduct of Sylvius and at mid-systole reaches a maximum of 25 mm/s. The pressure contours indicate a reversal in the pressure gradient during the course of the cardiac cycle. This pressure sign change corresponds to a reversal of CSF flow, from caudal to rostral, seen in Details A-C.

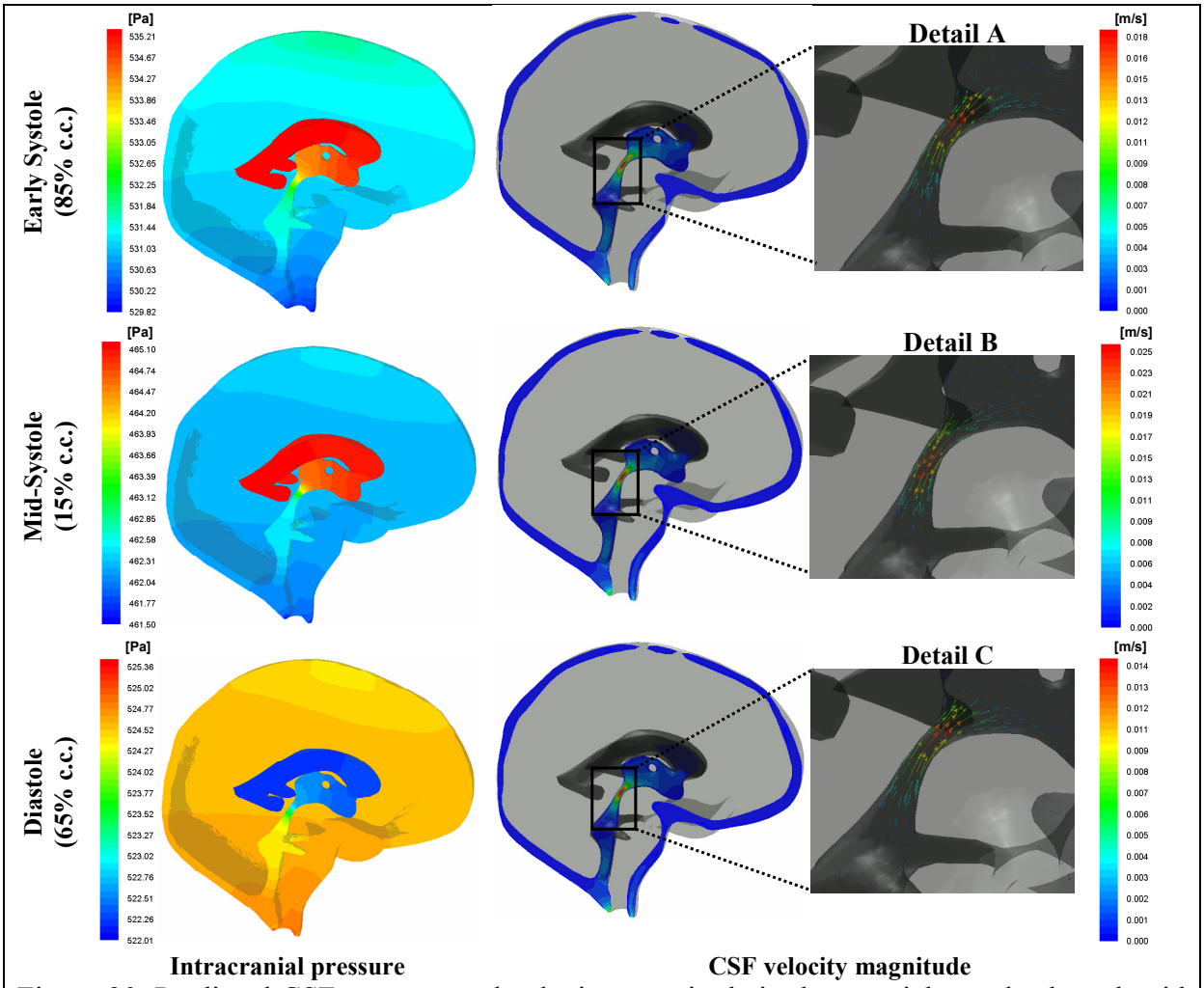

Figure 30. Predicted CSF pressure and velocity magnitude in the ventricles and subarachnoid space. Left panel shows the pressure contours at 15%, 65%, and 85% of the cardiac cycle. Pressure is highest in the ventricles at early systole with flow in the rostral direction shown in Detail A. Flow rate reaches a maximum in mid-systole with flow **out of the ventricles** shown in Detail B. During diastole, the pressure gradient reverses, being higher in the subarachnoid space compared to the ventricles. Accordingly, CSF flows back to the ventricles as shown in Detail C.

Velocity magnitude in the pontine cistern and in three points in the ventricular system is plotted over one cardiac cycle in Figure 31. Peak caudal CSF velocity magnitude slightly exceeds peak rostral CSF velocity magnitude. This difference reflects the small net flow due to constant CSF production. Figure 31 also shows that CSF flow in the pontine cistern becomes caudal before ventricular flow becomes caudal. The phase difference is about 10% of the cardiac cycle.

Pressure levels in the lateral ventricle and the upper convexity of the subarachnoid space are shown in the lower panel of Figure 31. The difference in pressure between the lateral ventricles and the upper convexity of the subarachnoid space is called the transmantle pressure gradient; the transmantle pressure gradient does not exceed 4 Pa at any point in the cardiac cycle. The pressure profile shows two time instances during the cardiac cycle in which the pressure gradient between the lateral ventricles and the subarachnoid space reverses. These events occur at about 23% and 82% of the cardiac cycle and are indicated by open circles in the figure. The simulations predict that when the pressure gradient reverses, that is when lateral ventricle pressure begins to exceed subarachnoid pressure, CSF flow does not immediately change from rostral to caudal. For example, at 82% of the cardiac cycle lateral ventricle pressure surpasses the subarachnoid pressure, but CSF flow does not become entirely caudal until 98% of the cardiac cycle. Thus, the change in predominant flow direction lags 58 degrees behind the transmantle pressure sign reversal.

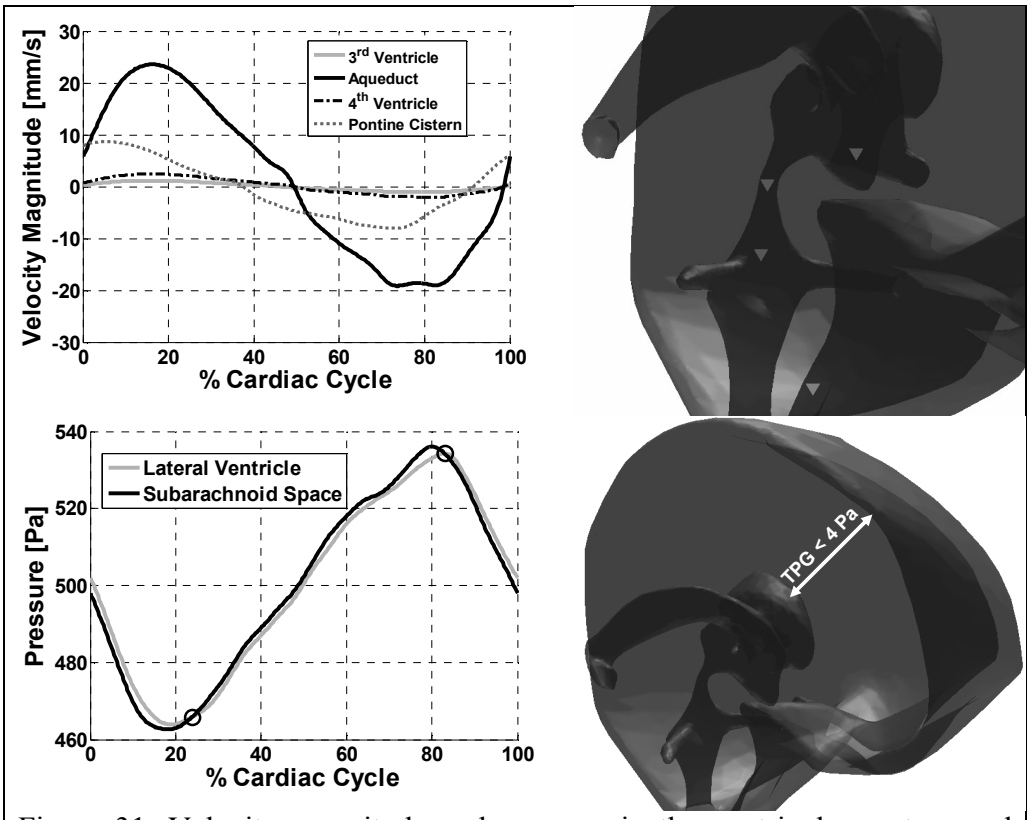

Figure 31. Velocity magnitude and pressure in the ventricular system and subarachnoid space. Velocity magnitude in third ventricle, cerebral aqueduct, fourth ventricle, and pontine cistern (downward pointing triangles, upper figure right) is plotted. Positive values correspond to caudal flow; negative values rostral. Bottom graph: pressure trajectories in the lateral ventricle and subarachnoid space.

5.4.3. Disease Simulation

The analysis of velocity and pressure dynamics can also be performed for abnormal intracranial dynamics. The brain geometry of a 50 year old hydrocephalic patient was reconstructed. As indicated in Table 7, the ventricular space was eleven times larger than normal. Snapshots of the pressure and velocity fields at 15% of the cardiac cycle are shown in Figure 32, Frames A and B. Peak caudal CSF velocity in the aqueduct was 41.3 mm/s in systole; peak rostral CSF velocity was 39.9 mm/s in diastole. Intracranial pressure trajectories in the lateral ventricle and the upper convexity of the subarachnoid space, Frame C, reveal that the transmantle pressure gradient in the hydrocephalic case remains small throughout the cardiac

cycle, not exceeding 11 Pa in this subject. The predicted pressure amplitude in the lateral ventricles is 69 Pa. This pressure amplitude is almost twice the normal case. Frame D shows the excellent agreement between the measured and predicted CSF flow rates in the third ventricle. The CSF stroke volume in the ventricles (for this particular patient) is about eight times larger compared to the normal case we studied.

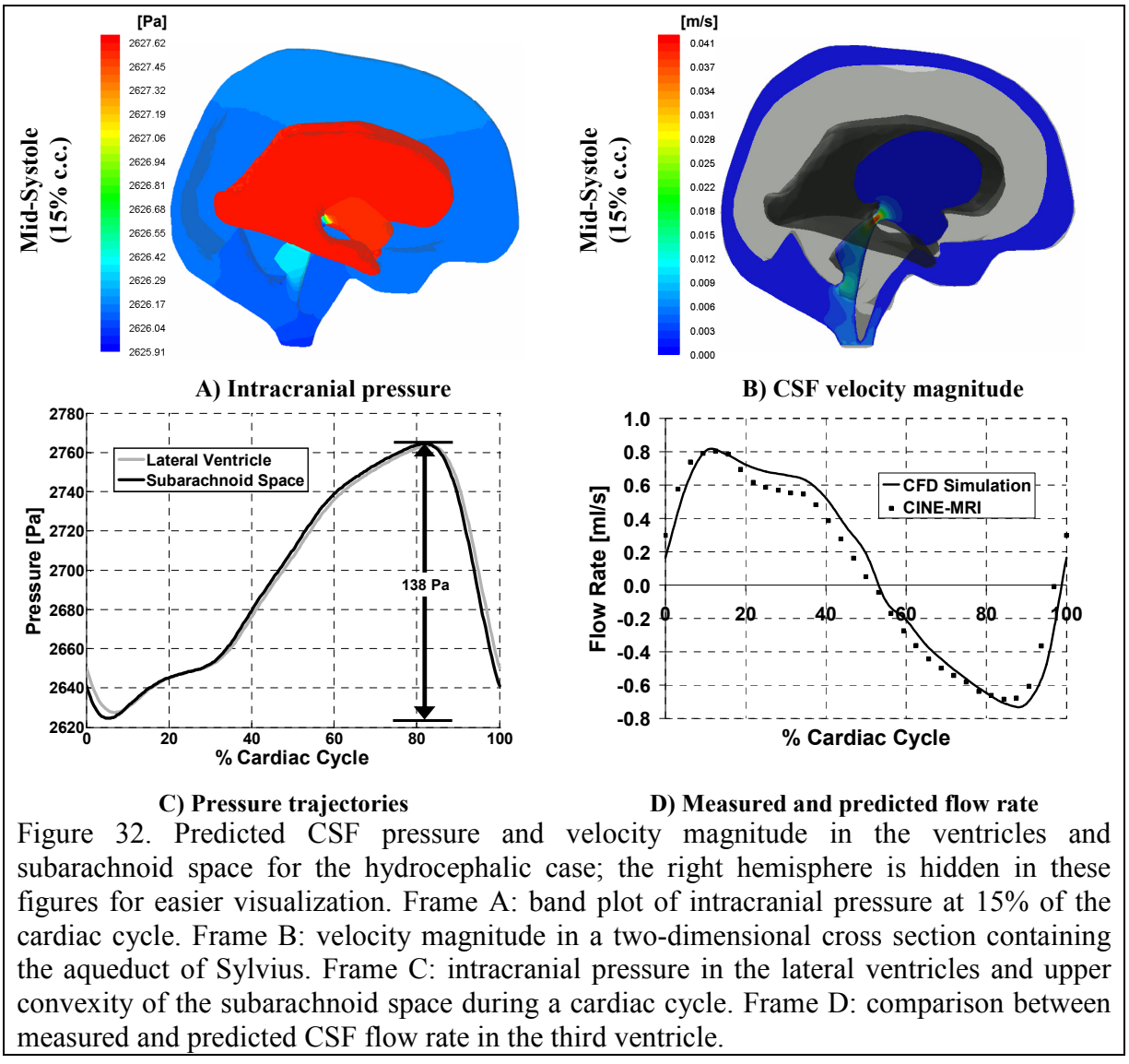

Figure 32. Predicted CSF pressure and velocity magnitude in the ventricles and subarachnoid space for the hydrocephalic case; the right hemisphere is hidden in these figures for easier visualization. Frame A: band plot of intracranial pressure at 15% of the cardiac cycle. Frame B: velocity magnitude in a two-dimensional cross section containing the aqueduct of Sylvius. Frame C: intracranial pressure in the lateral ventricles and upper convexity of the subarachnoid space during a cardiac cycle. Frame D: comparison between measured and predicted CSF flow rate in the third ventricle.

5.5. Discussion

5.5.1. CSF Flow Patterns and Pressure Dynamics

Figure 31 displayed the CSF velocity magnitude in the ventricular system and pontine cistern over the course of the cardiac cycle. The maximum velocity magnitude in the pontine cistern precedes the maximum velocity magnitudes in the ventricles by about 10% of the cardiac cycle. This finding is in good agreement with recent clinical measurements also showing a phase lag of 10% between maximum pontine flow and ventricular flow (Enzmann and Pelc 1991; Baledent, Henry-Feugeas et al. 2001; Zhu, Xenos et al. 2006; Gupta, Soellinger et al. 2009). In the human brain, blood traverses the Circle of Willis at the base of the brain before reaching the microvasculature. Because the Circle of Willis is near the pontine cistern, large arterial expansion in this region is likely to displace CSF out of the subarachnoid space before microvasculature expansion in the brain tissue causes CSF flow out of the ventricles. This explanation is consistent with *in vivo* CSF flow measurements indicating extracerebral expansion precedes brain expansion by about 8% of the cardiac cycle (Greitz, Franck et al. 1993; Greitz 2004). Cerebral vasculature relaxation leading to volumetric contraction of the large arterial vessels causes CSF flow reversal about mid-way into the cardiac cycle. Simultaneously, CSF refills the lateral ventricles to make up for the contracting parenchyma volume in the diastole.

5.5.2. Non-Dimensional Analysis of the Navier-Stokes Equations

When the lateral ventricle pressure exceeds subarachnoid pressure, CSF flows out of the ventricles into the subarachnoid space. The flow reverses when subarachnoid pressure exceeds ventricular pressure. The change in flow direction is not directly in phase with the pressure sign change. Figure 31 shows a transmantle pressure sign reversal at about 82% of the cardiac cycle where lateral ventricular pressure begins to exceed the pressure in the subarachnoid space. CSF however, begins to flow out of the ventricles only at about 98% of the cardiac cycle. We

conclude that this is a delayed flow response with a phase lag of 58 degrees. The phase lag can be explained in terms of the Womersley number, a non-dimensional number derived from the unsteady Navier-Stokes equations.

The Womersley number, abbreviated Wo, relates flow pulsatility (unsteady or inertial forces) to fluid viscosity (viscous forces), and has been used to characterize flow and pressure dynamics in blood vessels and the cranial fluid space (Ku 1997; Gupta, Soellinger et al. 2009). Experimental and theoretical studies have shown that when viscous forces are much larger than inertial forces the flow profile is parabolic and its direction immediately follows the instantaneous pressure gradient. In this case the flow is well represented by the Hagen–Poiseuille equation (Womersley 1955). When inertial forces dominate viscous forces the flow profile is flat or plug-like. In this case, the flow direction is also governed by the pressure gradient, but some time is required to overcome the inertial forces and for the fluid direction to align with the instantaneous pressure gradient. In general, for $Wo < 1$, the fluid velocity profile is parabolic and the flow is in phase with the pressure gradient. The fluid profile loses its parabolic shape when $Wo > 1$, and a phase lag between pressure and flow becomes more pronounced as Wo reaches ten or more (Womersley 1955; Loudon and Tordesillas 1998). Womersley numbers were calculated using eq. (1-25) in which ω is the pressure pulsation frequency, v is the kinematic fluid viscosity, and R is characteristic length.

$$Wo = R\sqrt{\frac{\omega}{v}} \tag{1-25}$$

For a cylindrical fluid domain, the parameter R is simply the tube radius. For more complex geometry such as the brain ventricles, the characteristic length needs to be defined locally. Accordingly, local Womersley numbers were computed at three locations in the ventricular system as shown in Figure 27. At these locations, the characteristic length, R, is the average

radius of a circular cross section, the pressure pulsation frequency is $2\pi/T$ (with $T=1$ s), and the kinematic viscosity is $v=10^{-6}$ m^{2}s^{-1}. Table 7 lists the Womersley numbers for the aqueduct-third ventricle junction, aqueduct, and aqueduct-fourth ventricle junction. The aqueductal Womersley number of our model differs by about 12% from the value reported in (Gupta, Soellinger et al. 2009), indicating slight anatomical variations between normal subjects. All sites analyzed in the ventricular system had Womersley values greater than one. Our computational results show that as a consequence, noticeable phase separation is observed between the pressure gradient and the flow response. In summary, the phase lag can be attributed to highly pulsatile CSF flow within the ventricles where the Womersley numbers are much greater than unity.

5.5.3. Specific Contributions

Early in this report, prior three-dimensional flow studies of the CSF spaces were reported. The premise of this and prior studies were that by studying the flow dynamics in the human brain diseases like hydrocephalus can be better understood, and perhaps better treatments for this disease can be devised. To this end, this report presents our most recent advancement in computational fluid flow analysis of the human brain. The main contributions from this particular study are the following:

1. The fluid motion in the entire subarachnoid space and ventricular system was modeled.
2. The pulsating CSF flow was set in motion by deforming tissue boundaries.
3. The three-dimensional analysis of normal dynamics was extended to a pathological case.

We believe these three contributions constitute a significant advancement over previous work. The first main contribution reflects our continued progress toward more complete and spatially accurate computational models of the central nervous system. The second main contribution stems from a concerted effort in our group to make system wide CSF models physiologically consistent. Clinical evidence points to the cerebral vasculature expansion as the

driving force for CSF motion. Rather than imposing CSF motion directly as an inflow boundary condition, our model allows for fluid and tissue boundary interaction. Tissue boundary motion deforms the CSF space and drives CSF motion in a pulsatile, cyclical fashion. Finally, the third major contribution is the analysis of the CSF motion in a patient with communicating hydrocephalus. There is still a need for improving the diagnosis of hydrocephalus (Greitz 2004). Improvements in diagnosing hydrocephalus may be possible once the differences between normal and hydrocephalic CSF flow patterns are satisfactorily quantified. The computational fluid dynamics results reported in this article foster a better fundamental understanding of flow principles, which will eventually lead to better diagnosis.

5.5.4. Model Limitations and Future Model Refinement

In this extensive, yet preliminary investigation, some details of the cranial fluid space were not addressed. For example, the gyrated cortical surface was not resolved and the resistance posed by the arachnoid trabeculae was neglected. However, in view of the small pressure drops that occur in the CSF spaces, we believe these omissions will not significantly affect the flow field. The trabeculae may increase the flow resistance, but the large cortical surface area will decrease the resistance. Overall, resolving aspects of the geometric domain for which there is little data available does not yet seem to be warranted.

Also, lacking in our current model of intracranial dynamics is an accurate implementation for brain tissue stress. More research of brain tissue properties, and in particular tissue stiffness, is needed before mathematical models of the brain can provide accurate stress predictions. Recently, researchers have used magnetic resonance elastography (MRE) to measure brain tissue stiffness non-invasively (Green, Bilston et al. 2008; Kruse, Rose et al. 2008; Sack, Beierbach et al. 2008). To calculate the tissue shear modulus, Kruse et al. assume a Hookean, linear elastic relationship between stress and strain (Kruse, Rose et al. 2008). Green et al. (Green, Bilston et al.

2008) and Sack et al. (Sack, Beierbach et al. 2008) have used MRE to derive shear and shear-viscosity moduli to fit their proposed viscoelastic model of brain tissue. In the study conducted by Green et al., differences in white and gray matter are accounted for, whereas in the Sack et al. study, the tissue is assumed homogenous. Unfortunately, MRE is highly dependent on these underlying tissue property assumptions, and as such the literature values are often inconsistent qualitatively and quantitatively. For example, Kruse et al. report that white matter shear stiffness is higher than that of gray matter—13.6 kPa and 5.22 kPa, respectively. Conversely, Green et al. find that gray matter is stiffer than white matter—3.1 kPa and 2.7 kPa, respectively. Sack et al. does not differentiate between white and gray matter in their study, and is difficult to compare quantitatively. However, their overall tissue shear stiffness, ~1.2 kPa is closer to the value reported by Green et al. Complicating all these findings is the fact that shear stiffness is dependent on the excitation frequency applied to the tissue; typically anywhere between 25Hz to 100Hz. How the findings derived from high level excitations can be extrapolated for much smaller frequencies which naturally occur in the brain (~1Hz) has not been quantified. However, the MRE results seem to suggest a trend in the overall magnitude of the shear modulus. Thus, our implemented value of 3.4 kPa is on the same order of magnitude as that reported in the literature.

As a final note, accurate prediction of pathological brain dynamics will require model refinement. For the prediction of hydrocephalus, we propose to treat the brain tissue as poroelastic. This treatment will allow prediction of fluid transport in the brain as well as predict more accurately brain tissue stress induced by vasculature expansion or ventricular dilation. Modeling normal and diseased CSF dynamics may even be improved with the inclusion of the spinal canal because the tissues surrounding the spinal subarachnoid space provide the greatest

region of compliance in the entire CNS. Although including the spinal canal in this three-dimensional model was beyond the scope of this study, we have addressed the impact on brain dynamics due to a compliant spinal canal in previous publications using a physiological compartmental model (Linninger, Xenos et al. 2009). More advanced models accounting for the spinal canal are expected to elucidate the pressure-volume relationship and compensatory mechanisms of the CSF system, which has received much attention in hydrocephalus research (Meier and Bartels 2002; Czosnyka, Cieslicki et al. 2005).

5.6. Conclusions

In this study, experimental data was obtained from a normal subject and compared with a three-dimensional computational model of intracranial dynamics. Developed from subject-specific MR images, and using physiological boundary conditions as input, the model reproduces pulsatile CSF motion and predicts intracranial pressures and flow rates. CSF flow predictions agreed quantitatively with actual human CINE-MRI measurements. Small pressure gradients and amplitudes were predicted by the model. Based on the close match between model and experimental measurements, we conclude that the predicted pressure gradients and CSF flow fields are representative of those in the human brain.

5.7. Summary of Equations Used in the Model

This section summarizes the equations in vector form and boundary conditions for the solution of the fluid-structure interaction problem of intracranial dynamics.

CSF flow

$$\rho_f\left(\vec{\nabla}\cdot\vec{u}\right)=S_f, \qquad \text{continuity in ventricles,}$$
$$\vec{\nabla}\cdot\vec{u}=0, \qquad \text{continuity outside the ventricles,} \tag{A1}$$
$$\rho_f\left(\frac{\partial\vec{u}}{\partial t}+\vec{u}\cdot\vec{\nabla}\vec{u}\right)=-\vec{\nabla}p+\mu\vec{\nabla}^2\vec{u}, \qquad \text{fluid momentum.} \tag{A2}$$

CSF boundary, and interface conditions and source terms

On non-deformable interfaces a no-slip boundary condition is applied for the fluid

$$\vec{u}_f=0, \qquad \text{no-slip on non-deformable faces.} \tag{A3}$$

A baseline ICP pressure is applied on the upper subarachnoid space:

$$\begin{aligned} p_{upper\ SAS} &= 500 \text{ Pa (4 mmHg)}, && \text{for normal subject,} \\ p_{upper\ SAS} &= 2{,}700 \text{ Pa (20 mmHg)}, && \text{for pathological case.} \end{aligned} \tag{A4}$$

Fluid-structure interaction constraints are applied along the upper wall of the lateral ventricle to ensure: (i) displacements of the fluid and solid domain are compatible; (ii) stresses at this boundary are at equilibrium, and (iii) no-slip condition for the fluid.

$$\vec{d}_s = \vec{d}_f \tag{A5}$$

$$\boldsymbol{\sigma}_s \cdot \vec{n} = \boldsymbol{\sigma}_f \cdot \vec{n} \tag{A6}$$

$$\vec{u}_s = \vec{u}_f \tag{A7}$$

where $\boldsymbol{\sigma}$, $\vec{d}, \vec{u}, \vec{n}$ are the stress tensor, the vector of displacement, the velocity vector and the normal vector on the boundary (Valencia, Morales et al. 2008).

$S_f = 0.5$ ml/min, CSF constant production in the lateral, 3rd and 4th ventricles. (A8)

Tissue displacement

$$\rho_s \frac{\partial^2 \vec{d}_s}{\partial t^2} = G\vec{\nabla}^2 \vec{d}_s + \frac{G}{1-2\nu}\vec{\nabla}\varepsilon_v \text{ with } \varepsilon_v = \vec{\nabla} \cdot \vec{d}_s \text{ and } \dot{\vec{d}}_s = \vec{u}_s . \tag{A9}$$

Tissue boundary conditions and source terms

$S_V(t) = \sum_{k=-8}^{8} c_k e^{2ik\pi t}$, k = 1, 2, …, volumetric tissue expansion. (A10)

The subscripts s, f indicate the solid and the fluid.

6. CEREBROSPINAL FLUID FLOW DYNAMICS IN THE CENTRAL NERVOUS SYSTEM

6.1. Summary

Cine-phase-contrast-MRI was used to measure the three-dimensional cerebrospinal fluid (CSF) flow field inside the central nervous system (CNS) of a healthy subject. Image reconstruction and grid generation tools were then used to develop a three-dimensional fluid-structure interaction model of the CSF flow inside the CNS. The CSF spaces were discretized using the finite element method and the constitutive equations for fluid and solid motion solved in ADINA-FSI 8.6. Model predictions of CSF velocity magnitude and stroke volume were found to be in excellent agreement with the experimental data. CSF pressure gradients and amplitudes were computed in all regions of the CNS. The computed pressure gradients and amplitudes closely match values obtained clinically. The highest pressure amplitude of 77 Pa was predicted to occur in the lateral ventricles. The pressure gradient between the lateral ventricles and lumbar region of the spinal canal did not exceed 132 Pa (~ 1 mmHg) at any time during the cardiac cycle. The pressure wave speed in the spinal canal was predicted and found to agree closely with values previously reported in the literature. Finally, the forward and backward motion of the CSF in the ventricles was visualized, revealing the complex mixing patterns in the CSF spaces. The mathematical model presented in this article is a prerequisite for developing a mechanistic understanding of the relationships between vasculature pulsations, CSF flow, and CSF pressure waves in the CNS.

6.2. Introduction

Cine-phase-contrast-MRI (CINE-MRI) has been used to quantify CSF flow in humans (Enzmann and Pelc 1991; Greitz, Franck et al. 1993; Zhu, Xenos et al. 2006). Computational fluid dynamics has been used to complement CINE-MRI measurements by calculating the CSF

pressure and velocity fields in the cranial subarachnoid space and cerebral ventricles (Jacobson, Fletcher et al. 1996; Fin and Grebe 2003; Gupta, Soellinger et al. 2009; Linninger, Sweetman et al. 2009; Cheng, Tan et al. 2010). These computational studies predict and explain complex fluid flow patterns in the CSF spaces, an outcome difficult to establish with CINE-MRI alone. As a measuring device for some regions of interest in the CSF space, CINE-MRI is not apt to explain the complex dynamics inside the CNS. However, CINE-MRI is the basis for developing computational fluid dynamic models that help quantify intracranial dynamics of the human brain. Using CINE-MRI and image processing tools, CSF velocities can be calculated in several areas of interest in the cranial space. These experimental measurements may then be used to develop and validate computational models.

The advantage of developing a computational model from CINE-MRI is that the computational model reproduces the three-dimensional flow field in all regions of interest in the entire CSF filled spaces of the CNS. Moreover, once the model is validated, studies can be conducted on a computer to assess if particular deviations from normal physiology may be responsible for significant changes in flow patterns (Levine 1999; Pena, Harris et al. 2002). Conclusions may then be drawn or clinical experiments devised to improve clinicians' understanding of disease onset or progression. In effect, computational CSF flow studies are a valuable tool for developing a mechanistic understanding of normal and pathological CNS dynamics.

Previous computational studies deployed simplified models of the CSF spaces. These studies focused on two-dimensional cross sections or partial aspects of the CSF space (Pena, Bolton et al. 1999; Fin and Grebe 2003; Linninger, Xenos et al. 2007; Gupta, Soellinger et al. 2009; Linninger, Sweetman et al. 2009). To date, there are no three-dimensional fluid-structure

interaction models of CSF motion inside the entire CNS. A physiological CSF model should account for the cranial CSF space as well as the spinal canal. Computer models that include the spinal canal are needed for improving our understanding of many diseases of the CNS including hydrocephalus, Chiari malformation, or benign intracranial hypertension (Czosnyka, Czosnyka et al. 2004). Furthermore, a craniospinal model of the CNS may help evaluate modern drug delivery methods like intrathecal drug administration by accurately predicting therapeutic drug distribution in the CSF spaces and brain tissue (Saltzman and Olbricht 2002; LaVan, McGuire et al. 2003). Predicting drug distribution with computer models is possible by numerically solving the governing equations for drug diffusion coupled with convective species transport through the CSF (Linninger, Somayaji et al. 2008). This article presents a three-dimensional fluid dynamics model of the CNS which accurately resolves the geometry of the fluid-filled spaces in the cranium and spinal canal. The objective is to develop a computational model that quantifies the interactions between pulsating vasculature, CSF flow, and deformable brain tissue. By doing so, we hope to render a more detailed picture of CSF dynamics in the human CNS.

The article is organized as follows: In the next section we describe methods. The results section compares *in vivo* data with computer simulations and provides a detailed analysis of CSF flow and pressure dynamics in the cranium and spinal canal. The article closes with a discussion and suggestions for future advancements in computational fluid mechanics of the CNS.

6.3. Methods

6.3.1. Process Overview: From Measurement to Computation

The modeling approach described here proceeds in four phases illustrated in Figure 33. First, CINE-MRI imaging (3T GE Signa; GE Medical Systems, Milwaukee, WI) is used to extract actual patient's brain geometry and to measure CSF flow velocities *in vivo*. Second, image reconstruction software (Materialise, Belgium) is used to create accurate geometrical

representations of the human ventricular system, subarachnoid spaces and brain parenchyma. The image reconstruction process delineates the boundaries between cerebrospinal fluid spaces and soft brain tissue. By connecting the pixel information from each MRI slice with adjacent slices, a three-dimensional representation of the individual's brain geometry is generated. In the third phase, the fluid-filled spaces bounded by the reconstructed surfaces are divided into small tetrahedral balance envelopes via grid generation software (Gambit 2.4). Finally, in phase four, physiological boundary conditions are assigned to the model, and governing equations for fluid flow and solid motion are solved numerically using finite element methods. Computational predictions are then compared to the *in vivo* measurements.

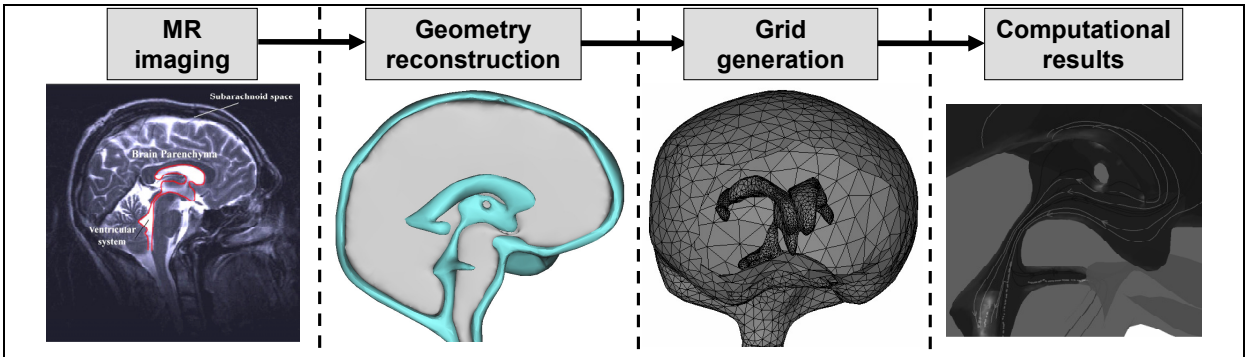

Figure 33. Workflow for developing a computational model of the central nervous system. The first step is the collection of medical images from magnetic resonance imaging. Then, geometry reconstruction is used to detect sharp boundaries of functional regions inside the brain to generate three-dimensional surfaces. Third, grid generation partitions the surfaces into tetrahedral elements for the solution of transport equations. Finally, computational analysis solves transport equations to predict fluid velocities and pressures as well as solid strains and stresses.

Details related to CSF flow measurements have been discussed in our prior publications (Zhu, Xenos et al. 2006; Linninger, Xenos et al. 2007), but for completeness will be repeated briefly. The CINE-MRI technique was used to collect CSF flow data from eight healthy subjects and three patients with hydrocephalus. The scans were performed in a 3T GE Signa system (GE Medical Systems, Milwaukee, WI, USA) equipped with a standard quadrature birdcage head

coil. Study participants signed the consent forms approved by the Institutional Review Board at the University of Chicago and the University of Illinois at Chicago. Images at 16 equidistant time frames were collected at a mid-sagittal cross-section and an axial slice across the middle of the lateral ventricle. Images at 32 equidistant time frames were collected at: 1) an axial slice across the junction between the aqueduct of Sylvius and the fourth ventricle to measure CSF flow rate; 2) a mid-coronal slice at the third ventricle to measure CSF flow rate; and 3) an axial slice perpendicular to the basilar artery in the prepontine region to measure blood flow rate. For CSF flow measurement, a velocity encoding value (V_{ENC}) of 5 cm/s was chosen; for blood flow measurement in the basilar artery, V_{ENC} was set to 100 cm/s. Additional acquisition parameters were: echo time = 8.4 msec; repetition time = 18 msec; flip angle = 20°; field of view = 24 cm; slice thickness = 5 mm; matrix size = 256x192, 75% phase field of view to achieve an effective matrix resolution of 256x256. Total acquisition time was about one hour. The measured velocity at a particular point of interest on the MR image is averaged over 180 cardiac cycles. The comparison between simulated results and experimental measurements is made point to point; averaged velocities from CINE-MRI are compared with simulated velocities from our computational model. The computational results provide velocity data at mesh nodes, the location of which is matched with the pixel location of the CINE-MRI CSF velocity measurement. To compute flow rates, the velocity vector field is integrated over a cross sectional area in the model corresponding to the area of interest used in the CINE-MRI measurements.

6.3.2. Model Boundary Conditions and Governing Equations

Meaningful CSF flow and pressure predictions require physiologically consistent boundary conditions. CSF production, CSF reabsorption, and effects of pulsatile vasculature expansion were incorporated into the computer model. Constant CSF production is due to active secretion from the choroid plexus as well as diffuse production in the brain parenchyma. In the model,

CSF is constantly produced from the lateral ventricles at a rate of 0.4 ml/min. This value is in the range of several clinical studies (Lorenzo, Page et al. 1970; Segal 2001; Silverberg, Heit et al. 2001; Huang, Chung et al. 2004). The constant production of CSF is governed by eq. (1-26) which assumes fluid incompressibility and Newtonian rheological behavior. The fluid velocity vector is $\vec{u}$, and constant CSF production is represented as S_f.

$$\nabla \cdot \vec{u} = S_f \tag{1-26}$$

There are many clinical studies supporting the thesis that CSF is mainly reabsorbed into the circulatory system through the arachnoid villi (Ellington and Margolis 1969; Davson 1984; Upton and Weller 1985). To mimic the actual CSF uptake through the arachnoid villi, in the model CSF reabsorption occurs via a porous region superior to the upper convexity of the subarachnoid space (Linninger, Sweetman et al. 2009). Although some researchers believe a small amount of CSF is reabsorbed in the spinal canal, we choose to neglect spinal CSF reabsorption in this study. The assumption of negligible reabsorption in the spinal cavity is also supported by CINE-MRI measurements showing undetectable levels of CSF elimination in the spinal canal (Alperin, Vikingstad et al. 1996; Loth, Yardimci et al. 2001).

Transient changes in vasculature lumen throughout the cardiac cycle cause local deformation of brain tissue. Tissue deformation, in turn, compresses the fluid-filled extracellular space in the parenchyma and causes compression of the lateral ventricles. The subsequent change in lateral ventricular volume results in CSF flow out of the ventricles (White, Wilson et al. 1979). This chain of events leads to the hypothesis that CSF motion in the CNS is mainly caused by vasculature expansion in the cranium (Bhadelia, Bogdan et al. 1997; Baledent, Henry-Feugeas et al. 2001; Greitz 2004). To mimic the effects of vascular pulsations and tissue boundary motion near the lateral ventricles, we have imposed moving parenchyma boundaries in the model that

pulsate in accordance with the physiological blood flow waveform measured *in vivo*. The measured blood flow waveform was reconstructed with a Fourier series, $f(t)$, with seventeen coefficients as shown in eq. (1-27).

$$f(t) = \sum_{k=-8}^{8} c_k e^{2ik\pi t} \tag{1-27}$$

In (1-27), $i = \sqrt{-1}$, $c_k = (a_k \pm ib_k)/2$. The sign of the complex part, ib_k, is taken as plus when *k* is positive, and negative when *k* is negative. The values for c_0, a_k, and b_k were provided in an earlier chapter. The signal was further normalized and then scaled in order to apply an explicit displacement boundary condition along the upper walls of the lateral ventricles. This boundary condition mimics the effects of the tissue deformation that is transmitted to the moving lateral ventricle walls. Pulsatile volume changes in the subarachnoid space near the basilar artery and Circle of Willis are also accounted for in the model. These displacements are also due to expanding vasculature. Overall, the expansion of the intracranial vasculature decreases the space available to the cranial CSF by about 1.5 ml (Greitz 2004). Because the skull is rigid and all fluids are incompressible, CSF is necessarily pushed into the spinal canal due to mass conservation. In our model, the CSF motion is governed by the Navier-Stokes equations provided in eq. (1-28), where $\vec{\nabla} p$ is the pressure gradient, μ the fluid viscosity, ρ_f the fluid density, and $\vec{u}$ the CSF velocity.

$$\rho_f \left(\frac{\partial \vec{u}}{\partial t} + \vec{u} \cdot \vec{\nabla} \vec{u} \right) = -\vec{\nabla} p + \mu \vec{\nabla}^2 \vec{u} \tag{1-28}$$

CSF exchange between the cranial and spinal subarachnoid space is possible because the spinal canal boundaries are not as rigid as the bony cranium. The extent of spinal canal volume change is a measure of its *compliance*. This compliance is believed to be due to several factors: (1) the venous plexi (which may displace venous blood) in the lumbar and epidural spaces,

(2) ligamentum flava, and (3) nerve sheaths (Nieuwenhuys, Voogd et al. 1988; Thron, Rossberg et al. 1988; Yaksh 1999; Bateman 2000; Henry-Feugeas, Idy-Peretti et al. 2000; Czosnyka, Czosnyka et al. 2004; Barshes, Demopoulos et al. 2005). CSF cranial-spinal exchange maintains proper pressure–volume compensation within the entire CNS. Without this fluid exchange, intracranial pressures could rise to dangerous levels, in effect immediately reducing cerebral blood flow to critical levels (Czosnyka, Czosnyka et al. 2004). Spinal compliance is accounted for in the model by incorporating a deformable region that surrounds the spinal fluid. Because experimental data suggests the upper region of the canal is less compliant than lower regions, the compliance in our model is high in the lumbar region (Martins, Wiley et al. 1972; Enzmann and Pelc 1991; Baledent, Henry-Feugeas et al. 2001; Yallapragada and Alperin 2004; Wagshul, Chen et al. 2006). The membrane boundary may deform in response to changes in fluid pressure along the fluid-membrane interface. As pressure increases in the lower lumbar region, the membrane distends. Fluid expelled from the cranium then occupies the additional volume of the spinal canal (Baledent, Henry-Feugeas et al. 2001). The deformation of the lumbar area and motion of the spinal fluid must obey to specific force balances enforced along the fluid-structure interface. To ensure equal stresses and equal displacements along the fluid-structure interface, kinematic and dynamic boundary conditions were imposed. The kinematic boundary condition, eq. (1-29), states that the fluid displacement, $\vec{d}_f$, equals the solid displacement, $\vec{d}_s$, along the interface. Dynamic boundary condition, eq. (1-30) states that the fluid and solid stresses normal to the interface are equivalent. In (1-30) $\boldsymbol{\sigma}_f$ and $\boldsymbol{\sigma}_s$ are the fluid and solid stresses respectively, and $\vec{n}$ is the normal vector to the boundary interface.

$$\vec{d}_f = \vec{d}_s \tag{1-29}$$

$$\vec{n} \cdot \boldsymbol{\sigma}_f = \vec{n} \cdot \boldsymbol{\sigma}_s \tag{1-30}$$

The deformable membrane, representing the compliance of the epidural space, was modeled as a neo-Hookean material; the neo-Hookean material formulation is an extension of the isotropic linear Hooke's law to large nonlinear deformations. This choice was motivated by clinical observations that the pressure-volume relationship in the central nervous system is nonlinear (Czosnyka, Czosnyka et al. 2004). The neo-Hookean material response is governed by eq. (1-31).

$$W = \frac{1}{2}\mu(I_1 - 3) \tag{1-31}$$

In (1-31), W is the strain energy density, μ is the shear modulus, and I_1 is the sum of the diagonal elements of the Cauchy-Green deformation tensor (Belytschko, Liu et al. 2000). In the model, the shear modulus of the deformable membrane is set to 4kPa. The Young's modulus, E is related to the shear modulus through the Poisson ratio, v as in eq. (1-32).

$$E = 2\mu(1 + v) \tag{1-32}$$

For the incompressible, neo-Hookean material formulation, the Poisson ratio is nearly 0.5; accordingly eq. (1-32) yields a corresponding Young's modulus of 12kPa. To our knowledge, the exact mechanical properties of the epidural space have not yet been determined experimentally. Nevertheless, the material stiffness assigned to the deformable membrane lies in the reported stiffness range for soft biological tissues (Fung 1993). The model was implemented in the fluid-structure interaction module of ADINA 8.6 (Adina R&D Inc., Watertown MA, USA). A more thorough treatment of the theory behind fluid-structure interaction problems can be found elsewhere (Bathe 1996). In addition, the solution procedure for nonlinear, large deformation materials implemented in the ADINA program is fully discussed elsewhere (Sussman and Bathe 1987; Bathe 1996). The cranial and spinal canal domains were typically composed of 871,358 tetrahedral fluid elements and the deformable membrane contained 4,792 tetrahedral solid

elements; more refined meshes were used for mesh independence studies. Simulations were analyzed for *grid* and *time-step* size independence by successively refining the computational mesh and decreasing the time-step size until a stable result of the numerical solution was reached. Table 8 shows that the predicted velocities and pressures at select locations were independent of the mesh resolutions and time-steps used in the CFD simulation. Tabular values show velocity magnitude and pressure in the aqueduct at 20% of the cardiac cycle as a function of approximate mesh size ($x10^3$ elements) and time-step size. The numerical solution was convergent with about 850,000 elements and a time-step size of 0.01s. Shaded values show small changes with further grid and time-step size refinement. Velocity magnitude and pressure in the lateral ventricle, pontine cistern, and lower spinal canal showed similar convergence trends.

Table 8. Solution convergence study for mesh and time-step independence.

	Velocity magnitude [m/s]					**Pressure [Pa]**				
Time step [s]	**230**	**460**	**750**	**870**	**1,230**	**230**	**460**	**750**	**870**	**1,230**
0.025	18.1	19.2	20.7	22.4	22.5	519.5	522.2	524.1	526.5	528.3
0.020	19.3	20.4	21.5	22.5	22.5	519.7	522.5	526.2	527.5	529.5
0.015	20.8	21.8	22.3	22.5	22.5	520.0	523.0	527.8	528.5	529.5
0.010	21.8	22.4	22.6	22.6	22.6	521.1	523.2	530.7	530.7	530.7
0.005	21.8	22.4	22.6	22.6	22.6	521.3	523.5	530.7	530.7	530.7

A schematic of the computational model of the CNS is shown in Figure 34. Table 9 also summarizes a summary of the boundary conditions and material properties used in the model.

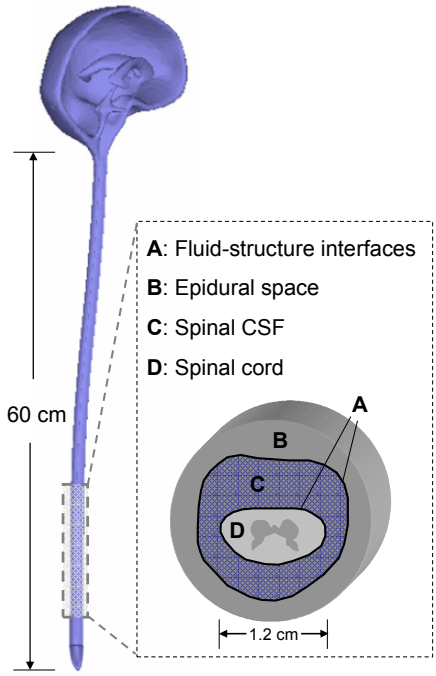

Figure 34. Computer model of the central nervous system. The model consists of the cranial fluid space and spinal canal. Shown in detail is a representative cross section of the spinal canal. Expansion of the spinal fluid space is possible by deforming a surrounding flexible epidural region, labeled B in the diagram.

Table 9. List of boundary conditions and material parameters. Available published data is also provided.

Location	Boundary Condition	Material parameters
Lateral Ventricles	CSF inflow, 0.4 ml min^{-1} (Silverberg, Heit et al. 2001)	Volume, 16.5 ml
Upper subarachnoid space	Pressure, 500 Pa (Jacobson, Fletcher et al. 1996)	-
Arachnoid and pia layer	no slip, u=v=w=0	rigid wall
CSF pathways	divergence free	ρ : 998.2 kg m^{-3}; μ , 0.001 $kgm^{-1}s^{-1}$
Deformable membrane	fluid structure interaction	Neo-Hookean model; Young's modulus, 12 kPa

ρ :density; μ :viscosity

6.4. Results

The computed three-dimensional fluid velocities and pressures in the cranium are presented first. The direction and magnitude of CSF flow in the third and fourth ventricles, aqueduct of Sylvius, and pontine cistern are then quantified. Next, the fluid-mixing occurring in the CSF spaces is demonstrated by visualizing the fluid pathlines in the ventricles. Finally, a description

of the flow patterns in the spinal canal is presented along with methods for quantifying fluid pressures and visualizing the flow field.

6.4.1. 3D Simulation of CSF Velocity and Pressure Fields in the CNS

The left frame of Figure 35 shows the comparison between model predictions and experimental data for the CSF flow rate measured at the third ventricle for an individual healthy subject. The predicted flow rate and waveform match experimental measurements closely. Integrating the positive area under the curve yields a predicted CSF stroke volume from the ventricular spaces into the subarachnoid space of 0.032 ml per cardiac cycle. The right frame of Figure 35 compares the predicted and experimental velocity magnitudes in the pontine cistern. Though the predicted and experimental results do not match in all instances of the cardiac cycle, the overall trends in frequency and amplitudes are in excellent agreement. Table 10 summarizes the computed and experimental velocity magnitudes in the ventricles, pontine cistern, and cranio-cervical junction. Flow data obtained by Greitz (Greitz, Hannerz et al. 1994) and Zhu *et al* (Zhu, Xenos et al. 2006) from several normal subjects show similar flow patterns. Similar trends include larger CSF stroke volumes at the cranio-cervical junction compared with smaller stroke volumes through the ventricles.

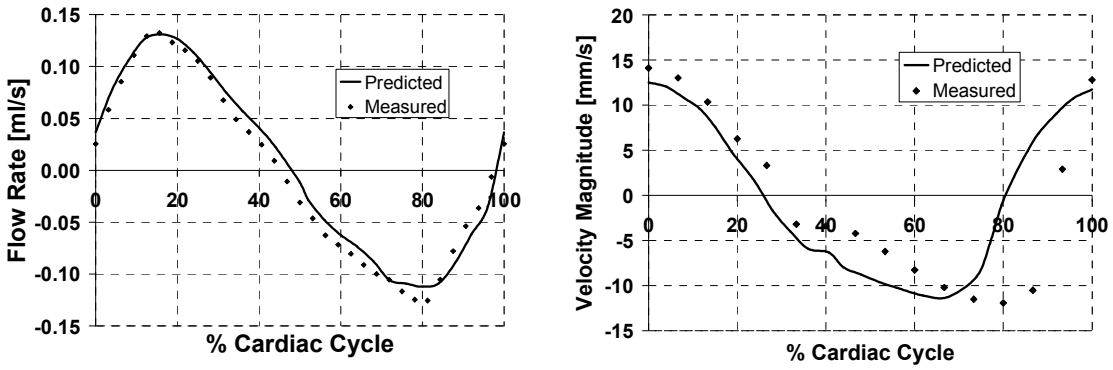

Flow at 3rd ventricle **CSF velocity in pontine cistern**

Figure 35. Left: Comparison of predicted and measured CSF flow rate at the level of the third ventricle for a normal subject. Right: Comparison of predicted and measured CSF velocity in the pontine cistern. By convention, positive values represent cranial to caudal flow, whereas negative values represent caudal to cranial flow. The overall temporal pattern of predicted velocities is in excellent agreement with *in vivo* measurements.

Table 10. Experimental and predicted CSF flow quantities. Published clinical data is also provided.

Location	**Computational fluid dynamics** *Max Velocity [mm/s]*	**CINE-MRI** *Max Velocity [mm/s]*
Third ventricle	4.5	3.7±1.5 (Zhu, Xenos et al. 2006)
Aqueduct	24	-
Lower fourth ventricle	2.9	3.8±2.1 (Zhu, Xenos et al. 2006)
Pontine cistern	12.5	13.9±9.9 (Zhu, Xenos et al. 2006)
Plane with L1 vertebra	1.9	-

Location	**Computational fluid dynamics** *Stroke volume [ml]*	**CINE-MRI** *Stroke volume [ml]*
Ventricles	0.032	0.0289±0.0161 (Zhu, Xenos et al. 2006)
Cranio-cervical junction	0.8	0.96±0.16 (Greitz, Hannerz et al. 1994)

Figure 36 shows the predicted CSF velocity magnitude at equally spaced cross sections in the cranial fluid space at mid systole. High CSF velocities occur in the ventricles and are maximal in the aqueduct of Sylvius. The computational model predicted a maximum velocity magnitude in the aqueduct of 24 mm/s. Figure 36 also shows the changes in CSF velocity magnitude throughout the cardiac cycle at four locations in the cranium: third ventricle, aqueduct of Sylvius,

fourth ventricle, and pontine cistern. Caudal flow predominates in the pontine cistern earlier than in the ventricles; the phase lag is about 10% of the cardiac cycle.

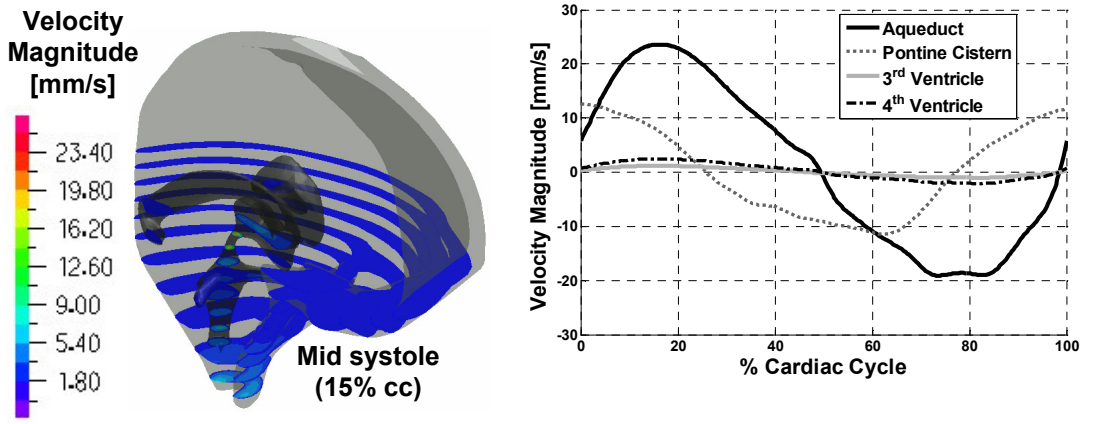

Figure 36. Computed CSF velocity magnitude at mid systole shown at equally spaced cross sections in the cranial fluid space (left). Predicted CSF velocity magnitude at four regions of interest in the cranium throughout the cardiac cycle (right). Positive values correspond to predominantly caudal (from cranium to spinal canal) CSF flow. Negative values reflect CSF returning to the cranium. Velocity magnitude: $\|\vec{u}\| = \sqrt{u_x^2 + u_y^2 + u_z^2}$.

The cranial fluid pressure field at mid systole is shown in Figure 37. The model predicts relatively flat intracranial pressure wave amplitude over the course of a cardiac cycle. The peak pressures at any given location do not fluctuate from their average value by more than 96 Pa. These predictions agree well with clinical studies showing small pulse amplitudes throughout the cardiac cycle (Czosnyka, Czosnyka et al. 2004). Changes in cranial CSF pressure are small, less than 1 mmHg, despite large pressure differences, about 40 mmHg, in cranial blood throughout the cardiac cycle (Sherwood 1995; Silbernagl and Despopoulos 2009). The CSF pressure stabilization is due to the availability of the compliant spinal canal to receive CSF. The model supports the theory of the spinal canal's role to attenuate CSF pressure amplitudes.

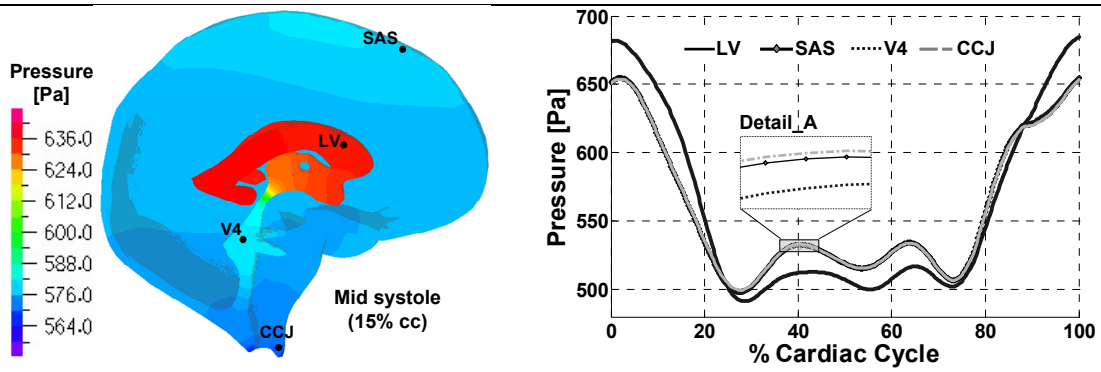

Figure 37. CSF pressure at mid systole in the cranial fluid space (left). The graph on the right depicts the predicted CSF pressure throughout the cardiac cycle in the lateral ventricles (LV), fourth ventricle (V4), upper convexity of the subarachnoid space (SAS), and cranio-cervical junction (CCJ). Detail_A shows that very small pressure gradients exist between SAS, V4, and CCJ throughout the cardiac cycle.

6.4.2. Fluid Pathlines in the Ventricular System

Knowledge of CSF flow patterns is significant for possible drug administration; the CSF spaces provide a vehicle for administering drugs directly into the CNS by bypassing the blood-brain-barrier. To illustrate these flow patterns more clearly, Figure 38 shows the fluid pathlines in the lateral ventricles, third ventricle, and aqueduct of Sylvius. As shown in the figure, CSF flow in systole is in the cranial to caudal direction. In diastole, flow reverses to become dominantly cranial, again filling the lateral ventricles.

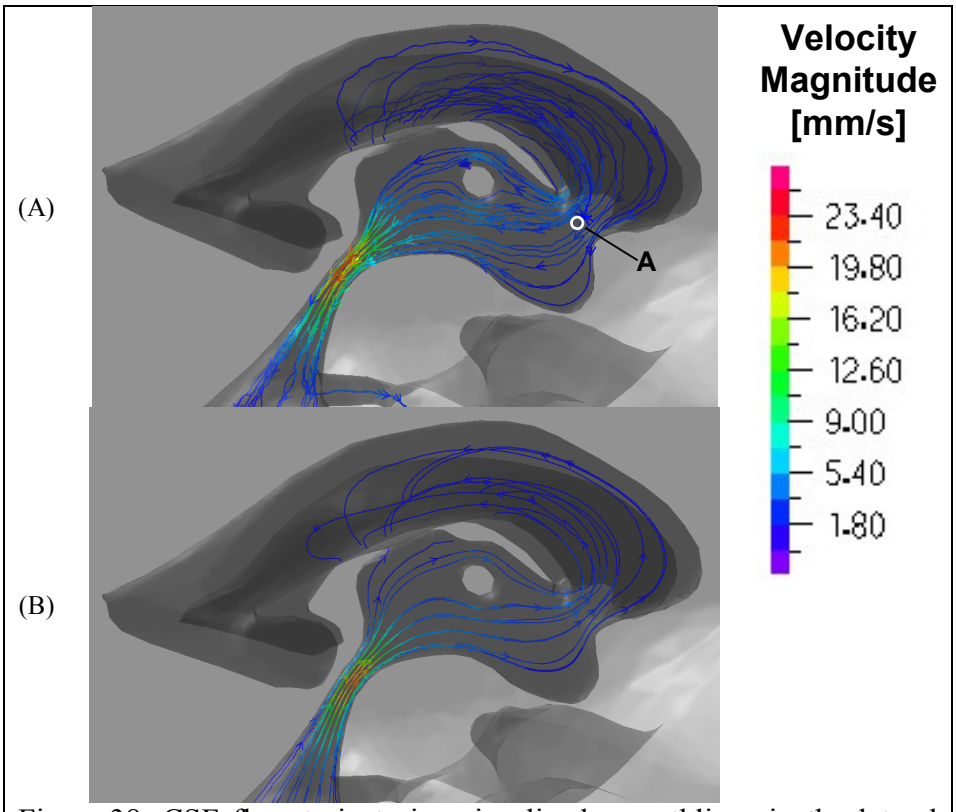

Figure 38. CSF flow trajectories visualized as pathlines in the lateral ventricles, third ventricle, and aqueduct of Sylvius. The top and bottom frames show the flow direction and velocity magnitude at 20% and 80% of the cardiac cycle, respectively. At each location the CSF flow exhibits flow reversal with pulsatile forward and backward motion. The velocity profile for location A in the top frame is plotted in Figure 39 The net CSF flow during the cardiac cycle is cranial to caudal with a stroke volume of 0.032 ml.

Figure 39 plots the velocity profile of location A labeled in Figure 38. As indicted by the shaded areas in Figure 39, there is a net forward flow due to the CSF production, but the peculiar forward and backward stroke volume induces a complex mixing pattern. When administering drugs or nanoparticles into the spinal CSF, they would be affected by these mixing patterns and carried with the fluid so that the apparent transport is expected to be much faster than by diffusion alone. Although an analysis of drug transport in the CSF spaces is beyond the scope of this article, we suspect the pulsatile cranial-caudal motion can contribute significantly to the wider distribution of drugs administered intrathecally or intraventricularly. Actually, such

favorable transport in intrathecal delivery has been reported previously and can now be studied with the detailed computational fluid mechanic models of this article (Kroin, Ali et al. 1993).

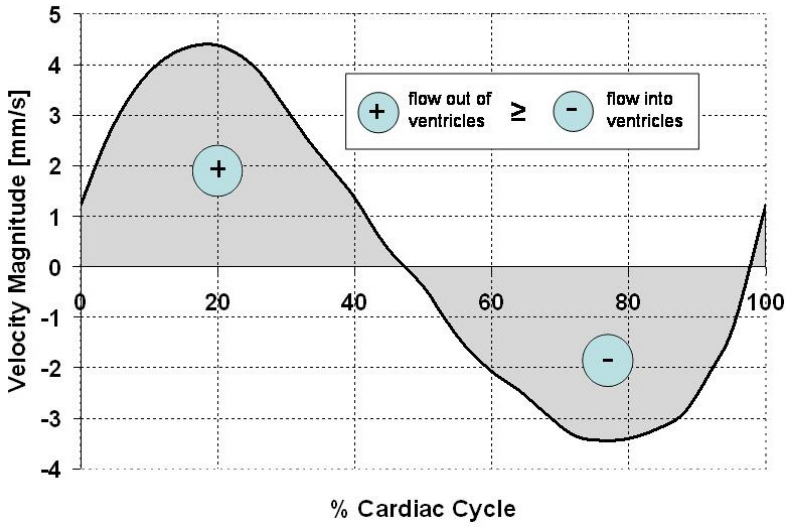

Figure 39. Velocity data plotted for location A of Figure 38. The flow in the ventricles changes direction during the cardiac cycle as indicated by the shaded regions. Due to the constant production of CSF in the lateral ventricles, volumetric flow out of the ventricles slightly exceeds volumetric flow returning to the ventricles during each cardiac cycle.

6.4.3. CSF Pressure in the Cranio-Spinal System

Figure 40 shows the pressures in the cranium and spinal canal at four time points in the cardiac cycle. During early systole, pressure is highest in the ventricles, while lower pressures are found near the base of the spinal canal. As fluid continues to exit the cranium during mid systole, ventricular pressure reaches its peak, while the pressure in the spinal canal also rises. In late systole the pressure in the spinal canal exceeds the pressure in the lateral ventricles. At this point in the cardiac cycle fluid flow begins to reverse from predominantly caudal to rostral direction. Finally, in diastole the spinal canal pressure is higher than the ventricular pressure. At this point in the cardiac cycle, CSF flow is also predominantly rostral, refilling the ventricles as they return to normal size.

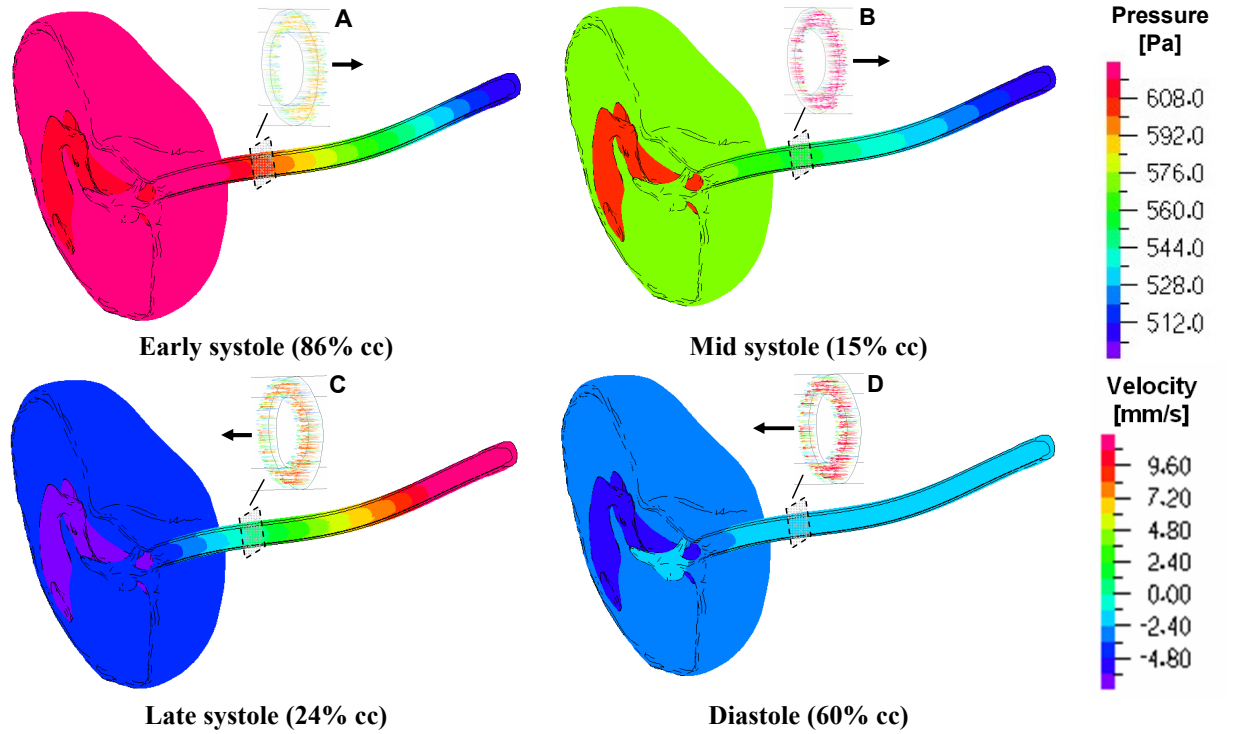

Figure 40. Half section of the brain and spinal canal showing calculated pressure evolution and CSF flow direction at four time points in the cardiac cycle (cc). In the systole pressure is higher in the cranium than in the spinal canal. The pressure difference reverses in diastole; in effect CSF flow is predominantly rostral toward the cranium in the diastolic phase of the cardiac cycle. Details A-D show the computed velocity vectors in a representative cross section of the spinal canal. Black arrows indicate the dominant flow direction, which is mainly caudal in the systole and reverses in the diastole.

6.4.4. Pressure Wave Speed in the Spinal Canal

Figure 41 shows detailed pressure and flow predictions at three locations in the spinal canal: upper (I), middle (II), and lower (III) regions. The pressure amplitude is highest in the superior-most portion of the spinal canal, 77 Pa. The pressure amplitude is 57% lower in the middle section, and 83% lower in the lumbar region.

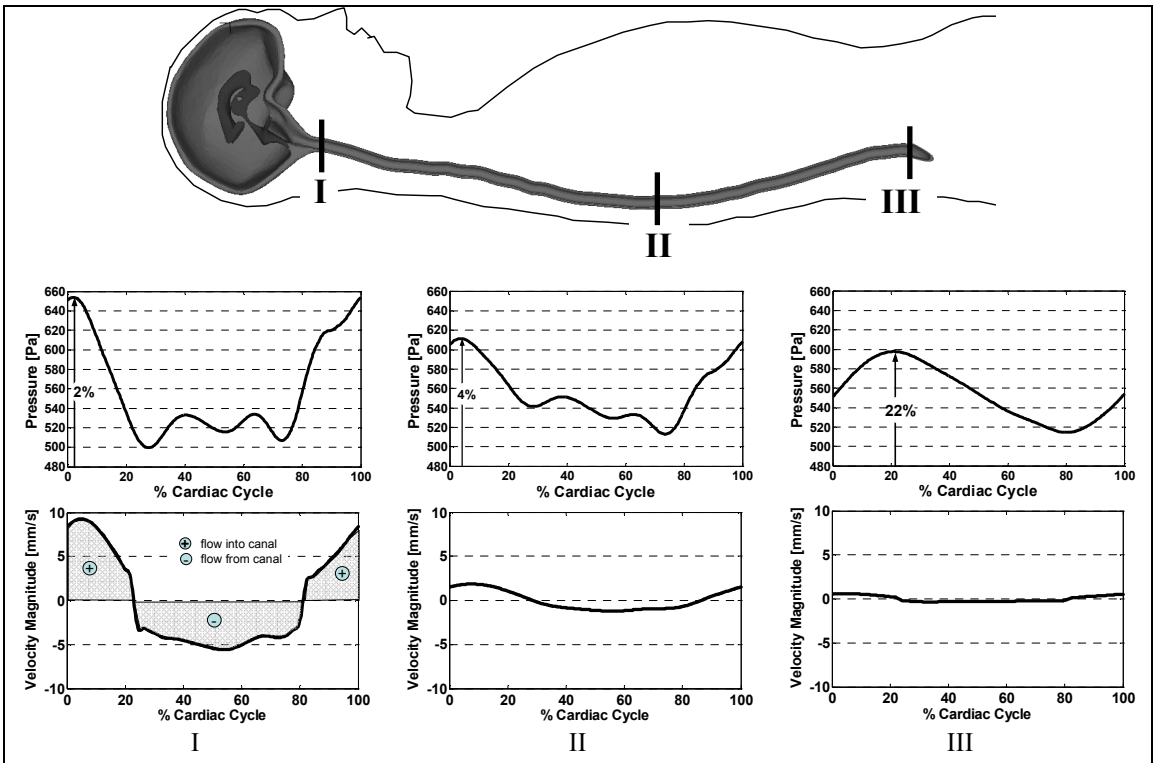

Figure 41. Detailed predictions of pressure and CSF flow profiles at three locations in the spinal canal throughout the cardiac cycle. Peak pressure in upper (I), middle (II), and lower (III) sections occur at 2%, 4%, and 22% of the cardiac cycle, respectively. Pressure amplitude of 77 Pa in the superior-most section of the spinal canal is 57% higher than the middle section, and 83% higher than the lower section of the canal. The second row of plots shows CSF flowing much faster at the cranio-cervical junction (section I) compared to other regions of the canal. Note: positive velocity values indicate the flow direction is from cranium to lower lumbar region (caudal flow). The opposite holds true for negative values: flow occurs toward the cranium (rostral flow).

Our simulations also permit an estimation of the pressure wave speed, a phenomenon that has recently received much attention in the MRI community. Some researchers claim that the pressure wave speed in the spinal canal may be an indicator of pathological changes in the CNS (Greitz, Ericson et al. 1999; Carpenter, Berkouk et al. 2003; Kalata, Martin et al. 2009). The wave speed was calculated by first noting the time at which peak pressures occur in three different locations of the spinal canal. Figure 41 shows that the peak pressure in the upper region occurs at 2% of the cardiac cycle and that peak pressures in the middle and lower regions occur

at 4% and 22%, respectively. Taking the cardiac cycle to be 1 second and the length of the spinal canal as 60 cm, the pressure wave speed in the canal was found to be 3 m/s (60 cm/0.20 s).

6.4.5. CSF Flow Predictions in the Spinal Canal and Summary of Central Nervous System Dynamics

CSF flow predictions in Figure 41 show that velocity is highest near the cranio-cervical junction and diminishes further down the canal. Because the spinal canal expands, CSF flux decreases as a function of distance from the cranio-cervical junction (Loth, Yardimci et al. 2001). Lower predicted CSF velocity in the inferior regions of the canal is due to the expansion of the deformable region in the model.

Pressures and velocities in the cranium and spinal canal are compared in Figure 42. The pressure and velocity profiles of Figure 41 have been superimposed to allow for a direct comparison. According to model predictions, 96 Pa is the highest pressure amplitude in the CNS and occurs in the ventricles. Pressure gradients are small throughout the CNS. The pressure difference between the lateral ventricles and lower lumber region does not exceed 132 Pa at any time during the cardiac cycle. This value is close to 1 mmHg, which is below the detection limit of current *in vivo* pressure sensors. Table 11 provides detailed pressure gradients between the lateral ventricles, subarachnoid spaces, and spinal canal during the cardiac cycle. The data shows that pressures gradients and pressure amplitudes in the central nervous system are small, and that there is a sign change in the pressure gradient. This sign change occurs when CSF flow direction changes from caudal to rostral.

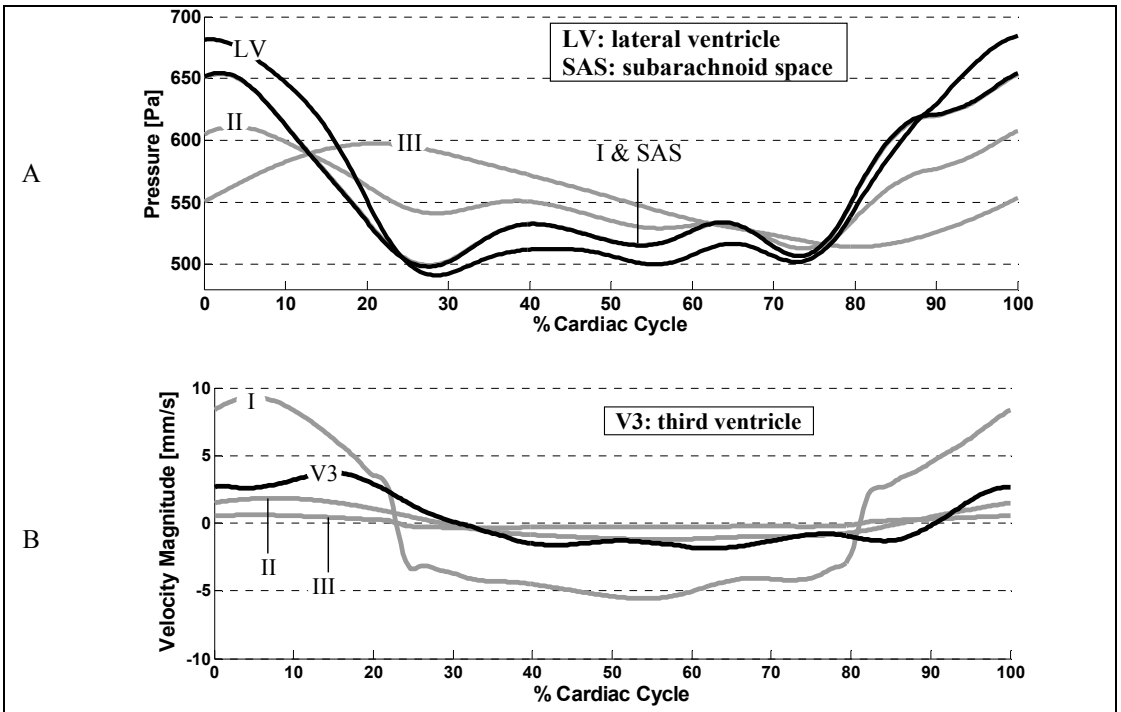

Figure 42. Summary of the pressures and CSF flow patterns in the spinal canal and cranium as indicated by the pressure and velocity trajectories in five regions of interest. Black lines correspond to cranial data. Grey lines refer to spinal canal data (see Figure 41 for locations I, II, III). Frame A: computer model predicts that the intracranial pressure amplitude (based on LV curve) is about 96 Pa. Also, the pressure difference between the lateral ventricles and position III (lower lumbar region) in the spinal canal does not exceed 132 Pa (~ 1 mmHg) at any time during the cardiac cycle. Curves I and SAS are indistinguishable. Frame B: positive values correspond to CSF flow out of the cranium toward the lower lumbar region of the spinal canal. Flow becomes caudal first in the pontine and cerebellomedullary cisterns as well as in the spinal canal; this specific flow pattern is due to large arterial expansion near the base of the brain. Flow out of the ventricles (data for third ventricle shown, V3) then follows when the lateral ventricles compress slightly due to brain capillary and arteriole expansion.

Figure 42b shows the relative flow direction and magnitude in the ventricles and spinal canal. Caudal flow in the spinal canal precedes caudal flow in the ventricles by about 10% of the cardiac cycle. We attribute this phase lag to the temporal distribution of vasculature expansion throughout the cranium. As blood flows into the brain, compliant arteries near the base of the brain expand, decreasing the available cranial CSF volume. Downstream arterioles and capillaries in the brain parenchyma dilate soon after, causing local tissue displacement and slight

compression of the lateral ventricles. The earlier expansion at the base of the brain causes the initial caudal flow into the spinal canal. The second wave of vasculature expansion in the brain tissue leads to caudal flow in the ventricles.

Table 11. Temporal pressure gradients between the lateral ventricles (LV), three points in the spinal canal (I, II, III), and upper convexity of the subarachnoid space (SAS) as a function of time (% cardiac cycle).

	Pressure Difference [Pa]				
% cc	**LV-I**	**LV-II**	**LV-III**	**LV-SAS**	**SAS-I**
0	30.57	76.22	130.39	29.69	0.88
10	34.10	47.99	64.08	34.47	-0.37
20	16.09	-11.76	-45.75	17.27	-1.18
30	-10.36	-49.28	-96.34	-9.51	-0.85
40	-20.82	-38.77	-60.12	-20.66	-0.16
50	-12.03	-28.36	-47.27	-11.83	-0.20
60	-19.50	-23.97	-28.70	-19.72	0.22
70	-7.97	-12.39	-16.96	-7.91	-0.06
80	-10.63	8.12	30.92	-11.52	0.89
90	9.27	51.93	103.08	8.26	1.01
100	30.58	76.24	130.42	29.70	0.88

6.5. Discussion

A three-dimensional physiological model of intracranial dynamics of CSF flow in the central nervous system has been presented. The model included the cranial CSF spaces and the spinal canal. Rather than modeling the brain parenchyma, or calculating its distributed stress and strain field directly, we have applied physiological boundary conditions like constant CSF production, CSF reabsorption in the sagittal sinus, and vasculature expansion. The effects of vasculature expansion were implemented as moving parenchyma boundaries near the lateral ventricles and base of the brain. In this particular study, fluid motion in the porous brain parenchyma was not modeled because the main intent was to study in detail the fluid motion in the cranial and spinal subarachnoid spaces. Despite this simplification, the model predictions of CSF flow throughout the central nervous system are in excellent agreement with clinical findings both in velocity magnitude and stroke volume at several locations in the craniospinal system. Although the stresses in brain parenchyma were not computed explicitly, we believe the impact on the

predicted results were minimal because, as we have shown in prior studies, the CSF velocity and pressure gradients in the brain parenchyma are several orders of magnitude less than those observed in the free CSF spaces (Penn, Lee et al. 2005; Linninger, Xenos et al. 2007; Linninger, Sweetman et al. 2009).

CSF flow was predicted everywhere in the three-dimensional fluid space of the craniospinal system. Pulsatile flow patterns throughout the cardiac cycle were shown for four locations in the cranial space and three locations in the spinal canal. The model predictions support clinical findings that caudal flow occurs sooner in the pontine cistern than in the ventricles (Greitz 2004). We attribute the 10% predicted phase lag to an early vasculature expansion occurring near the base of the brain, later followed by dilation of the capillaries and arterioles embedded in the brain parenchyma. The early expansion compresses the cranial subarachnoid space, whereas the later expansion compresses the CSF space of the lateral ventricles. Both events cause CSF to displace caudally toward the compliant spinal canal.

Fluid pressure fields in the ventricles, subarachnoid space, and spinal canal were quantified. However, absolute pressures could not be verified in the model because absolute pressure measurements were not available for the normal subjects we tested. Nevertheless, relative pressures (or pressure gradients) predicted in the model follow naturally from the Navier-Stokes equations and are in excellent agreement with previous findings (Jacobson, Fletcher et al. 1996; Linninger, Xenos et al. 2007; Linninger, Sweetman et al. 2009). The model predicts a complex pattern of small fluid pressure fluctuations distributed in space and time throughout the CNS. The pressure amplitude is a measure of these fluctuations; it was found to be highest in the lateral ventricles, but did not exceed 96 Pa. The pressure difference between the lateral ventricles and lowest region of the spinal canal was less than 132 Pa throughout the entire cardiac cycle.

These differences are very small, less than 1 mmHg, and would be difficult to measure directly with most *in vivo* pressure monitors.

A pressure wave speed of 3 m/s in the spinal canal was calculated. This value matches other published values of wave speeds in the spinal canal. A summary of six independent studies of wave speed measurements was recently published by Kalata (2009). Half of the studies reported a wave speed in the spinal canal of about 4 m/s. As discussed by these authors, in studies reporting values higher than 4 m/s there may have been significant experimental errors. Also, in a recent study by Bertram et al. in which a wave speed of 12.2 m/s was predicted, the elastic modulus assumed for the surrounding dura of the spinal canal appears too large (Bertram, Brodbelt et al. 2005); stiffer systems yield higher pressure wave speeds (Zhang and Greenleaf 2006). In our study, the deformable region at the base of the spinal canal was modeled as a nonlinear neo-Hookean material with Young's modulus set to 12kPa. The choice of a nonlinear material model is consistent with clinical observations which show a nonlinear trend between fluid volume and fluid pressure in the central nervous system. In those studies, bolus injections into the central nervous system gave rise to a nonlinear pressure response as seen in compliance curves relating intracranial pressure and fluid volume (Czosnyka, Czosnyka et al. 2004). The Young's modulus chosen for the deformable membrane is within the range of stiffness values for biological soft tissues reported by Fung(Fung 1993). Based on the match between simulated and measured CSF flow patterns, the supporting literature for biological soft tissues, and the consistency between compliance studies and our chosen material model, the model parameters selected for this study appear to be satisfactory.

More research is needed to fully assess the mechanical function of the epidural space in maintaining homeostasis of the cranio-spinal system. Prior experimental data cited in this article

suggests a compensatory role of the epidural space in maintaining a healthy level of CNS system compliance. Until mechanical properties and stress responses of the epidural space are determined experimentally, we chose a simple neo-Hookean model. Limited precision of the material properties, however, should not alter the major conclusions drawn from this study, which seeks to understand the overall dynamics of blood flow, CSF motion, and CSF pressure. As additional experimental compliance data of the spinal cavity becomes available, our models can and should easily be updated.

6.6. Conclusion

We have presented a mathematical model for developing a mechanistic understanding of the relationships between vasculature pulsations, CSF flow, and CSF pressure waves in the CNS. CSF flow data and geometry of a healthy human subject were used to construct a physiological model of the central nervous system. The model was validated by comparing the experimental CSF velocity and flow rates with the simulated results. Model predictions were in excellent agreement with the CINE-MRI measurements. The complex CSF flow patterns and pressure profiles were resolved by graphing their predicted waveforms as a function of space and time. According to the model, the complex pulsatile CSF flow pattern in the CNS is realized with pressure gradients below 1 mmHg. The model was useful in estimating the pressure wave speed in the spinal canal and found to be about 3 m/s. This value closely matches other theoretical studies by independent researchers. Backward and forward CSF mixing in the ventricles was visualized. Quantifying these mixing patterns throughout the craniospinal system is of clinical interest for intrathecal and intraventricular drug delivery. Future work will apply this current three-dimensional model to predicting therapeutic drug transport in the CSF spaces and be used as an analysis tool for designing drug delivery methods to the CNS.

7. A NOVEL METHOD FOR MULTI-SCALE MODELING OF BIOMECHANICAL INTERACTIONS IN THE BRAIN

7.1. Background and Motivation

CSF flow rates and velocities can be measured using advanced imaging modalities such as CINE-MRI, but the driving forces behind CSF motion are not fully understood. Recent clinical measurements suggests there is a cause and effect relationship between cerebral blood flow dynamics and pulsatile CSF flow, but there are no computational methods capable of quantifying the dynamic force balances between the expanding cerebral vasculature, the soft deformable brain tissue matrix, and the displaceable CSF (Henry-Feugeas, Idy-Peretti et al. 2000; Baledent, Henry-Feugeas et al. 2001; Baledent, Gondry-Jouet et al. 2004; Kim, Thacker et al. 2007). This computational deficit stems from three major challenges: generating an anatomically consistent model of cerebral vasculature, quantifying the force interactions between vasculature and brain tissue, and quantifying the force interactions between brain tissue and CSF.

In the previous chapters of this dissertation, I have presented first principles models of the craniospinal system as a valuable tool for quantifying CSF dynamics. In our models, CSF motion was induced by one of two methods. First, hollow spheres (rectangles in 2d) representing large clusters of cerebral vessels were forced to expand and contract according to the cardiac pressure waveform. The expansion and contraction of these spheres caused the brain tissue to deform and accelerate the surrounding CSF. In a second approach, the CSF domain was deformed explicitly via an applied boundary motion along the lateral ventricle wall and pontine cistern. In both cases, CSF was accelerated toward the spinal canal during cardiac systole, and in diastole, CSF flowed back to the cranium and lateral ventricles. Regardless of the approach used to deform the CSF space, the predicted CSF flow field was in good agreement with our CSF flow measurements

(Zhu, Xenos et al. 2006), suggesting that brain motion and its interaction with the CSF space is the driving force of CSF motion.

Beyond explaining the CSF flow field as a function of the pulsating vasculature, a detailed representation of the cerebral vasculature may provide greater insight into several poorly understood phenomena in the human brain. For example, besides quantifying the interactions between blood, brain, and CSF, the vasculature-brain-CSF model could have potential for clinical applications such as analysis and prediction of blood flow changes due to ventricular enlargement in hydrocephalus (Momjian, Owler et al. 2004; Owler, Momjian et al. 2004; Owler, Pena et al. 2004), analysis and planning of surgical interventions for aneurysm and vessel occlusion (Charbel, Gonzales-Portillo et al. 1999; Charbel, Guppy et al. 2001; Charbel, Zhao et al. 2004; Amin-Hanjani, Alaraj et al. 2010), or improved prediction of therapeutic drug delivery to the central nervous system.

These potential clinical applications require a quantitative tool to analyze cerebral blood flow, CSF flow, and biomechanical interactions between vasculature, brain tissue, and CSF. However, the development of such a tool requires knowledge of several disciplines including medical imaging/image processing, computer science, computational fluid dynamics, and solid mechanics. For this reason, we believe the development of a comprehensive model of blood, CSF, and brain dynamics has not yet been satisfactorily addressed by the medical or engineering community. Therefore, to bridge the gap between experimental measurements of blood and CSF flow and quantitative analysis, this final chapter offers a multi-step process for quantifying the interactions between expanding vasculature, brain tissue, and CSF.

7.2. Limitation of Conventional Computational Fluid Dynamics

Steps toward quantifying these interactions will require the development of a computational fluid dynamics (CFD) program. In most CFD applications, a physical domain is divided into small balance envelopes (or control volumes) over which the fluid flow equations are solved. (Readers unfamiliar with computational fluid dynamics may consult (Fox, McDonald et al. 2009) and (Versteeg and Malalasekera 2007) for an excellent overview). In some cases, the physical domain of interest can be discretized using a *structured* grid approach. In structured grids, each boundary (or face) of a balance envelope is aligned with one of the axes of the global coordinate system. Structured grid discretization is limited to primitive shapes such as rectangles, rectangular prisms, cylinders, cones, and spheres. In contrast, in order to represent brain geometry accurately, one needs to adopt an unstructured grid approach. In unstructured grids, the control volume boundaries are generally not aligned with the global coordinate system. These arbitrary face orientations in unstructured grids require writing the governing equations of solid and fluid motion in terms of local coordinate systems defined by each control volume face.

Though fluid dynamics can be predicted in geometrically complex biological domains using unstructured grids, advanced technology is still required to develop a comprehensive model of vasculature, brain tissue, and CSF. In conventional fluid-structure interaction approaches, interacting domains require mesh compatibility at the interface. In the brain-vasculature interaction problem, the computational cells on the boundary of each vessel will cause the computational cells of the brain mesh to be several orders of magnitude smaller than its overall length scale, which is approximately 15 cm. In other words, the size of the smallest control volumes in the brain mesh would have to be on the same order of magnitude as the control volumes of an embedded cerebral vessel. It is very likely that this situation makes the entire problem intractable even with state-of-the-art computational resources.

7.3. Overview of Proposed Method

To overcome the intractability of the brain-vasculature-CSF interaction problem, we propose a novel method in which the CSF and brain domains are discretized with quadrilateral (2d) or tetrahedral (3d) elements while the vasculature domain is discretized into several thousand cylinders, each representing individual vessel segments of the arterial network. To be precise, the finite volume method is used to govern brain and CSF motion and a network-based model is used to govern vasculature dynamics.

Computational domains of the brain, CSF, and cerebral arteries were derived from medical images using manual segmentation (Materialise Inc 2008). Due to the finite resolution of the medical images, the microvasculature computational domain could not be derived using manual segmentation. Instead, the microvasculature domain was generated using sophisticated growth and optimization algorithms based on natural flow laws (Schreiner and Buxbaum 1993; Karch, Neumann et al. 1999; Schreiner, Karch et al. 2006; Sweetman, Linninger et al. 2010).

The vessel growth algorithm idealizes each blood vessel as a cylinder. By treating individual blood vessels as cylinders, blood flow and pressures as well as changes in vessel diameter can be computed analytically. Changes in vessel diameter were governed by a linear elastic model that accommodates vessel expansion or contraction due to pressure differences between the vessel lumen and surrounding brain tissue. Changes in vessel caliber were then transmitted to an associated brain mesh control volume as a volumetric strain (positive volumetric strain for vessel expansion, negative volumetric strain for vessel contraction). The association between a vessel and a brain mesh control volume was then established via a search algorithm, details of which are provided later in this chapter. Brain tissue displacement induced by dynamic changes in volumetric strain was governed by a steady-state momentum balance with an underlying linear elastic constitutive model.

Data from MRI suggests displacements in the brain tissue cause compression of the CSF-filled lateral ventricles (Zhu, Xenos et al. 2006). We hypothesize this motion along the brain-CSF interface contributes to the pulsatile CSF flow field. The SIMPLE algorithm was used to solve the CSF flow field in the deforming fluid space of the lateral ventricles and subarachnoid space. In a deformable fluid domain, a relative velocity occurs between the fluid and the computational grid. As such, the Navier-Stokes equations were written in an Arbitrary-Lagrangian-Eulerian (ALE) reference frame. To maintain the integrity of the fluid mesh due to grid deformation, a mesh displacement scheme was developed and implemented. For this extensive initial undertaking which seeks to model vasculature, brain tissue, and CSF interactions, we have limited the study to a two-dimensional mid-sagittal cross section of the human brain.

This chapter is divided into six sections. The first four sections describe the mathematical framework that supports the brain-vasculature-CSF model. Dividing this complex problem into small self-contained sections will elucidate the physics of each sub-problem as well as serve as a guideline for creating one's own computer program. The fifth section summarizes the methods and results of the model. The sixth section discusses the model results and future applications.

7.4. Fluid Motion: Solution of the Navier-Stokes Equations Using the SIMPLE Algorithm

7.4.1. Section Overview

This section describes how to solve the governing equations of fluid motion, the Navier-Stokes equations, using the SIMPLE (semi-implicit method for pressure-linked equations) method. The SIMPLE algorithm, introduced by Patankar (1980), is prevalent in CFD literature and used in many CFD codes. Two excellent references for learning about the SIMPLE algorithm are (Patankar 1980; Versteeg and Malalasekera 1995). Other texts and articles which may be useful are (Date 1993; Date 1996; Davidson 1996; Date 1998; de Foy and Dawes 2000;

Lien 2000; Date 2005; Versteeg and Malalasekera 2007). Before describing the details of the SIMPLE algorithm, the governing equations of fluid motion are presented. The concept of the unstructured grid is also presented to prepare the reader for the details of how to discretize the governing fluid equations. These prerequisites then lead naturally to the presentation of the SIMPLE algorithm. The section closes with a fluid flow simulation in the brain's lateral ventricle in which our results are compared to the commercial CFD tool, Fluent 6.3.

7.4.2. The Governing Equations for Fluid Motion

The governing equations for fluid motion are derived from three conservation laws:

- Conservation of Mass (Continuity Equation)
- Conservation of Momentum (Momentum Equation)
- Conservation of Energy (Energy Equation)

The energy equation is included when the physical system is subject to changes in temperature. In this dissertation, the fluid and tissue interactions are quantified. Since these systems experience negligible change in temperature, our discussion of the energy equation ceases here. Assuming fluid incompressibility, the continuity and momentum equations are written:

$$\text{Continuity} \qquad \nabla \cdot \vec{u} = 0 \tag{1-33}$$

$$\text{Momentum} \qquad \underbrace{\rho \frac{\partial \vec{u}}{\partial t}}_{\text{Local Acceleration}} = \underbrace{-\nabla p}_{\text{Pressure Gradient}} - \underbrace{\rho \vec{u} \cdot \nabla \vec{u}}_{\text{Convective Acceleration}} + \underbrace{\mu \nabla \cdot \left(\nabla \vec{u} \right)}_{\text{Diffusion Term}} \tag{1-34}$$

In (1-33) through (1-34), $\vec{u}$ is the fluid velocity, ρ is the fluid density, and μ is the fluid viscosity. The momentum equation consists of four main contributions: a local acceleration term, a pressure gradient term, a convective acceleration term, and a diffusion term. In a two-dimensional analysis, the *x* and *y* momentum equations are:

x momentum:
$$\rho\frac{\partial u}{\partial t} = -\nabla_x p \; - \; \rho \; \vec{u} \; \cdot \; \overbrace{\nabla u}^{\substack{u \\ \text{component} \\ \text{only}}} \; + \mu \; \nabla \cdot \overbrace{\left(\nabla u\right)}^{\substack{u \\ \text{component} \\ \text{only}}} \tag{1-35}$$

y momentum:
$$\rho\frac{\partial v}{\partial t} = -\nabla_y p \; - \; \rho \; \vec{u} \; \cdot \; \overbrace{\nabla v}^{\substack{v \\ \text{component} \\ \text{only}}} \; + \mu \; \nabla \cdot \overbrace{\left(\nabla v\right)}^{\substack{v \\ \text{component} \\ \text{only}}} \tag{1-36}$$

In (1-35) and (1-36), the notation, $\nabla_x p$, indicates that the derivative is with respect to x only ($\partial p / \partial x$). Similarly, $\nabla_y p$ is equivalent to ($\partial p / \partial y$). Let us keep the following goal in mind. We would like to predict fluid flow in a complex domain (such as the lateral ventricles of the brain). To do so, we need to discretize that domain into several control volumes (or balance envelopes) as shown in Figure 43. The computational domain in Figure 43 is an example of an unstructured grid. As previously mentioned, the faces of each balance envelope are generally not aligned with a global coordinate system (x, y as shown).

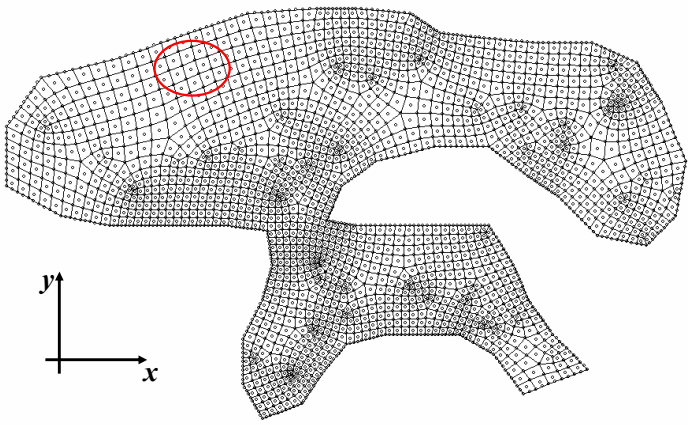

Figure 43. Complex physical domain (the brain's lateral ventricle—2D cross section) subdivided into approximately 1,600 balance envelopes. The red circled region is used to illustrate face fluxes in Figure 44.

The fluid motion must adhere to mass and momentum balances. The momentum balance in the x-direction is enforced over each balance envelope (control volume, cv) by integrating each term of eq. (1-35) over the volume (area in 2d) of the balance envelope, and over a finite period of time, Δt. The same procedure is applied to eq. (1-36) for the momentum balance in the y-

direction. The integration is explicitly shown in eq. (1-37), using the *x*-momentum as an example.

$$\rho \int_{t}^{t+\Delta t} \int_{cv} \frac{\partial u}{\partial t} dV dt = - \int_{t}^{t+\Delta t} \int_{cv} \nabla_x p \, dV dt - \rho \int_{t}^{t+\Delta t} \int_{cv} \vec{u} \cdot \nabla u \, dV dt + \mu \int_{t}^{t+\Delta t} \int_{cv} \nabla \cdot (\nabla u) \, dV dt \qquad (1\text{-}37)$$

It will be shown in section 7.4.3 how the integration of the terms in eq. (1-37) leads to the discretized version of the momentum equation. Before describing the integration of each term, some geometrical definitions and conventions must be described. First, let us keep in mind that the momentum balances will be written for each control volume. Figure 44 shows a typical control volume in the center of the grid with its geometrical center point labeled ϕ_0. ϕ_0's West, North, East, and South neighbors labeled ϕ_1 in Frames A, B, C, and D, respectively. The vector pointing in the direction from ϕ_1 to ϕ_0 is labeled $\vec{e}_\xi$. The red vector, $\vec{e}_\eta$, is always defined on the face adjacent to ϕ_0 and ϕ_1. The magnitude of $\vec{e}_\eta$ is equal to the length of the face. The key question is: In which direction should this vector point? In my derivations, the direction of $\vec{e}_\eta$ is such that the cross product, $\vec{e}_\xi \times \vec{e}_\eta$, follows the right-hand rule (your thumb will point up when you curl $\vec{e}_\xi$ into $\vec{e}_\eta$). A section of the computational grid from Figure 43 is used to show four possible orientations of the $\vec{e}_\xi$ and $\vec{e}_\eta$ vectors in Figure 44.

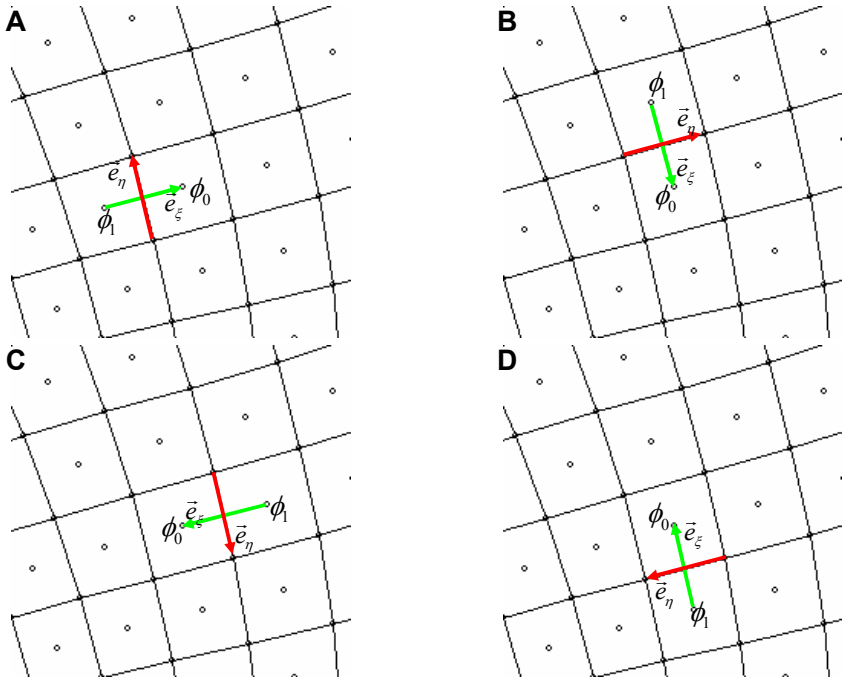

Figure 44. A section of the computational grid from the lateral ventricle (see Figure 43) is used to illustrate how the face vectors $\vec{e}_\xi$ and $\vec{e}_\eta$ are oriented. $\vec{e}_\xi$ is always directed from ϕ_1 to ϕ_0. The direction of $\vec{e}_\eta$ is such that $\vec{e}_\xi \times \vec{e}_\eta$ follows the right hand rule.

In our discussion of discretization which follows, when we apply Gauss theorem we will need the unit normal vector directed outward from the control volume. Consider Frame A of Figure 44. Since $\vec{e}_\eta$ is defined as $\vec{e}_\eta = (x_\eta, y_\eta)$, a perpendicular vector to $\vec{e}_\eta$ can be written as either $\vec{e}_{\eta\perp A} = (y_\eta, -x_\eta)$ or $\vec{e}_{\eta\perp B} = (-y_\eta, x_\eta)$. We need to determine which one of those normal vectors is directed out of the volume. This can be determined by performing the following cross product:

$$\vec{e}_{\eta\perp A} \times \vec{e}_\eta = \begin{vmatrix} i & j & k \\ y_\eta & -x_\eta & 0 \\ x_\eta & y_\eta & 0 \end{vmatrix} = 0\hat{i} - 0\hat{j} + (y_\eta^2 + x_\eta^2)\hat{k}$$

Because the $\hat{k}$ component is positive, $\vec{e}_{\eta\perp A} \times \vec{e}_\eta$ is defined by the right hand rule, and consequently, $\vec{e}_{\eta\perp A}$ is directed into the control volume, as shown in Figure 45. Since we require

the outward normal, $\vec{e}_{\eta\perp B} = (-y_\eta, x_\eta)$, we can write the outward normal as $\vec{n} = -(y_\eta, -x_\eta)$ and the unit outward normal to be used in Gauss theorem is:

$$\hat{\vec{n}} = -(y_\eta, -x_\eta) / \sqrt{x_\eta^2 + y_\eta^2}$$

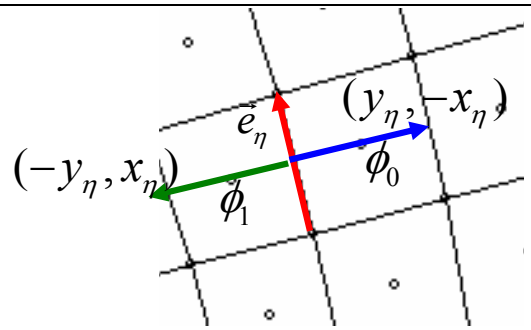

Figure 45. Frame A of Figure 44 revisited. The blue and green vectors are both perpendicular to the $\vec{e}_\eta$ vector. The blue vector is directed into control volume ϕ_0. The green vector is directed out of control volume ϕ_0.

7.4.3. Discretization of the Fluid Equations

We are now ready to describe the discretization of the momentum equations. However, to simplify the following discussion, only steady-state conditions are considered. Consequently, each term of the momentum equation is integrated over a control volume only; the time integration is postponed until section 7.5. Eq. (1-35) will be used as an example.

Pressure Gradient Term

$$-\int_{cv} \nabla p \, dV \quad \overset{\text{Apply Gauss Theorem}}{\Rightarrow} \quad -\oint_{face} p \, \hat{\vec{n}} \, dA$$

Because the integral $\oint_{face} dA$ is the length of the control volume face, that is, $\oint_{face} dA = \sqrt{x_\eta^2 + y_\eta^2}$, we have:

$$-\sum_{f=1}^{\#\text{ of faces}} p(-1)\begin{pmatrix} y_\eta \\ -x_\eta \end{pmatrix} = \sum_{f=1}^{\#\text{ of faces}} p\begin{pmatrix} y_\eta \\ -x_\eta \end{pmatrix}$$

For the *x*-momentum, the pressure gradient term is written as:

$$\sum_{f=1}^{\#\text{ of faces}} p\, y_\eta \Big|^f$$

For the *y*-momentum, the pressure gradient term is written:

$$\sum_{f=1}^{\#\text{ of faces}} p\left(-x_\eta\right)\Big|^f$$

Special Note: We use a collocated grid approach which solves for pressure and velocities at the center of each control volume. Since the discretized equation requires pressure at the control volume face, the value of pressure on the face is taken as the average pressure value between two adjacent cells (ϕ_0 and ϕ_1).

Convective Acceleration Term

This term causes the Navier-Stokes equations to be nonlinear. To circumvent this problem, we will provide an initial guess ($\vec{u}$, given) for the fluid velocity, such that the momentum equation takes the following form:

$$0 = -\int_{cv} \nabla_x p \, dV - \rho \int_{cv} \underbrace{\vec{u}}_{\text{given}} \cdot \overbrace{\nabla u}^{\text{solution variable}} \, dV + \mu \int_{cv} \nabla \cdot \overbrace{\nabla u}^{\text{solution variable}} \, dV$$

This arrangement is the basis of the SIMPLE algorithm in which $\vec{u}$ is provided via a guess or an earlier iteration. The velocity field resulting from the *x* and *y* momentum equations are then used to correct the pressure field; this will be discussed later. Since $\vec{u} = (u, v)$ is known from a previous iteration, we can take it out of the integral. We will append the superscript *i*-1 to the velocity vector $\vec{u}$ (denoting its value is known from a previous iteration) and append an asterisk to the solution variable, *u*.

$$-\rho \int_{cv} \vec{u} \cdot \nabla u \, dV = -\rho \left(u^{i-1} \quad v^{i-1} \right) \int_{cv} \nabla u^* dV$$

We now apply Gauss theorem:

$$-\rho \left(u^{i-1} \quad v^{i-1} \right) \int_{cv} \nabla u^* dV = -\rho \left(u^{i-1} \quad v^{i-1} \right) \int_{face} u^* \, \hat{\vec{n}} \, dA,$$

Assuming u^* is constant along the face, dA, and noting that $\hat{\vec{n}} = -\left(y_\eta, -x_\eta\right) / \oint_{face} dA$, we have:

$$-\rho\begin{pmatrix} u^{i-1} & v^{i-1}\end{pmatrix}\int_{\text{face}} u^*\,\hat{\vec{n}}\,dA = \rho\sum_{f=1}^{\#\text{ of faces}}\begin{pmatrix} u^{i-1} & v^{i-1}\end{pmatrix}\begin{pmatrix} y_\eta \\ -x_\eta\end{pmatrix}u^*\Big|^f$$

For the *x*-momentum, the convective term is written:

$$\rho\sum_{f=1}^{\#\text{ of faces}}\left(u^{i-1}y_\eta - v^{i-1}x_\eta\right)u^*\Big|^f$$

For the *y*-momentum, the convective term is written:

$$\rho\sum_{f=1}^{\#\text{ of faces}}\left(u^{i-1}y_\eta - v^{i-1}x_\eta\right)v^*\Big|^f$$

The discretization invokes u^* and v^* at the face. To obtain u^* (or v^*) at a face which is adjacent to two control volumes, we take the average value of u^* (or v^*) in those respective control volumes.

Diffusion Term

$$\mu\int_{\text{cv}}\nabla\cdot\left(\nabla u^*\right)dV \overbrace{\qquad=\qquad}^{\text{Gauss Theorm Applied}} \mu\oint_{\text{face}}\nabla u^*\cdot\hat{\vec{n}}\,dA$$

Note that $\nabla u^* = \begin{pmatrix}\dfrac{\partial u^*}{\partial x}\\ \dfrac{\partial u^*}{\partial y}\end{pmatrix} = \begin{pmatrix}\dfrac{\partial\xi}{\partial x}\dfrac{\partial u^*}{\partial\xi}+\dfrac{\partial\eta}{\partial x}\dfrac{\partial u^*}{\partial\eta}\\ \dfrac{\partial\xi}{\partial y}\dfrac{\partial u^*}{\partial\xi}+\dfrac{\partial\eta}{\partial y}\dfrac{\partial u^*}{\partial\eta}\end{pmatrix} = \begin{pmatrix}\xi_x\Delta u_\xi+\eta_x\Delta u_\eta\\ \xi_y\Delta u_\xi+\eta_y\Delta u_\eta\end{pmatrix}$

$$\Rightarrow\begin{pmatrix}\xi_x\Delta u_\xi+\eta_x\Delta u_\eta\\ \xi_y\Delta u_\xi+\eta_y\Delta u_\eta\end{pmatrix} = \begin{pmatrix}\dfrac{y_\eta}{\left|J^{-1}\right|}\left(u_0^*-u_1^*\right)-\dfrac{y_\xi}{\left|J^{-1}\right|}\left(u_N^*-u_S^*\right)\\ -\dfrac{x_\eta}{\left|J^{-1}\right|}\left(u_0^*-u_1^*\right)+\dfrac{x_\xi}{\left|J^{-1}\right|}\left(u_N^*-u_S^*\right)\end{pmatrix}$$

Thus, we have,

$$\mu\int_{\text{face}}\left(\frac{y_\eta}{\left|J^{-1}\right|}\left(u_0^*-u_1^*\right)-\frac{y_\xi}{\left|J^{-1}\right|}\left(u_N^*-u_S^*\right),\quad -\frac{x_\eta}{\left|J^{-1}\right|}\left(u_0^*-u_1^*\right)+\frac{x_\xi}{\left|J^{-1}\right|}\left(u_N^*-u_S^*\right)\right)\cdot(-1)\begin{pmatrix}y_\eta\\ -x_\eta\end{pmatrix}/\sqrt{x_\eta^2+y_\eta^2}\,dA$$

$$\Rightarrow -\mu\sum_{f=1}^{\#\text{ of faces}}\left(\frac{y_\eta^2}{\left|J^{-1}\right|}\left(u_0^*-u_1^*\right)-\frac{y_\eta y_\xi}{\left|J^{-1}\right|}\left(u_N^*-u_S^*\right)+\frac{x_\eta^2}{\left|J^{-1}\right|}\left(u_0^*-u_1^*\right)-\frac{x_\eta x_\xi}{\left|J^{-1}\right|}\left(u_N^*-u_S^*\right)\right)$$

$$\Rightarrow -\mu\sum_{f=1}^{\#\text{ of faces}}\left(\frac{y_\eta^2+x_\eta^2}{\left|J^{-1}\right|}\left(u_0^*-u_1^*\right)-\frac{x_\eta x_\xi+y_\eta y_\xi}{\left|J^{-1}\right|}\left(u_N^*-u_S^*\right)\right)$$

$$\Rightarrow -\mu \sum_{f=1}^{\#\text{ of faces}} \left[\frac{q_1}{\left|J^{-1}\right|}\left(u_0^* - u_1^*\right) - \frac{q_2}{\left|J^{-1}\right|}\left(u_N^* - u_S^*\right) \right]^f \qquad (1\text{-}38)$$

The following formula provides an excellent approximation to the diffusion term of the *x*-momentum (1-38); details provided in the Appendix.

$$\Rightarrow -\mu \sum_{f=1}^{\#\text{ of faces}} \left[\frac{u_0^* - u_1^*}{q_3}\left|J^{-1}\right| \right]^f \text{, where } \begin{array}{l} q_3 = x_\xi^2 + y_\xi^2 \\ \left|J^{-1}\right| = x_\xi y_\eta - x_\eta y_\xi \end{array}$$

For the *y*-momentum, the diffusion term is written:

$$\Rightarrow -\mu \sum_{f=1}^{\#\text{ of faces}} \left[\frac{v_0^* - v_1^*}{q_3}\left|J^{-1}\right| \right]^f$$

To summarize, eq. (1-37) in its discretized form can be written (for *x*-momentum):

$$0 = \sum_{f=1}^{\#\text{ of faces}} p\, y_\eta \Big|^f + \rho \sum_{f=1}^{\#\text{ of faces}} \left(u^{i-1} y_\eta - v^{i-1} x_\eta\right) u^* \Big|^f - \mu \sum_{f=1}^{\#\text{ of faces}} \left[\frac{u_0^* - u_1^*}{q_3}\left|J^{-1}\right| \right]^f \qquad (1\text{-}39)$$

7.4.4. The SIMPLE Algorithm: A Pressure and Velocity Correction Scheme

Overview. Instead of simultaneously solving the momentum and continuity equations to obtain the velocity and pressure fields, we decouple the equations so that the pressure and velocity fields are solved independently. How can this be accomplished? The first step is to assume a pressure field, p^{i-1}, as well as an *x* and *y* velocity field, u^{i-1} and v^{i-1}. Using these "known" fields, we solve for the u^* component of the $\vec{u}^*$ velocity field with the help of the *x* momentum equation and solve for the v^* component of the $\vec{u}^*$ velocity field with the help of the *y* momentum equation.

The next step involves computing a pressure correction p'. The equation for p' is derived by implementing a Darcy-like flow assumption on the velocity correction. This gives rise to a pure diffusion equation for the pressure correction, which serves to drive the system toward conserving mass; see continuity equation, eq. (1-33). This iterative procedure is repeated

successively until the entire flow field satisfies continuity. As an additional check for solution convergence, the calculated velocities must change only slightly from a previous iteration to a current one. For example, one may set the velocity change tolerance to 0.1%, which is the default convergence criteria used in the commercial CFD tool Fluent.

Implementation: Solution of the x and y momentum equations. The first step in the SIMPLE algorithm is to solve the following momentum equations (assuming steady-state for simplicity):

$$x\text{-momentum: } 0 = -\int_{cv} \nabla_x p^{i-1}\, dV - \rho \int_{cv} \vec{u}^{i-1} \cdot \left(\nabla u^*\right) dV + \mu \int_{cv} \nabla \cdot \left(\nabla u^*\right) dV \qquad (1\text{-}40)$$

$$y\text{-momentum: } 0 = -\int_{cv} \nabla_y p^{i-1}\, dV - \rho \int_{cv} \vec{u}^{i-1} \cdot \left(\nabla v^*\right) dV + \mu \int_{cv} \nabla \cdot \left(\nabla v^*\right) dV \qquad (1\text{-}41)$$

As stated above, two fields are provided *a priori*: the pressure field, p^{i-1} and the velocity field, $\vec{u}^{i-1}$, where *i*-1 indicates initial guess or value from previous iteration. On the first iteration, *i* equals 1, so the initial guess, u^0 is given. Equations (1-40) and (1-41) will lead to two independent systems of equations. One system will yield solution u^*; the other will yield v^*.

Implementation: Velocity correction. Since the initial guess may be far off from the actual solution, $\left(u^* \quad v^*\right)$ will likely not equal $\left(u^{i-1} \quad v^{i-1}\right)$. Thus, we devise an equation for the velocity correction, $\vec{u}'$. As documented in (Patankar 1980; Versteeg and Malalasekera 1995), it may be assumed that the velocity correction at a control volume face (boundary) is proportional to the pressure gradient across that same face. The proportionality constant is a conglomerate of fluid viscosity, density, and sizes of neighboring control volumes (see eqs. 6.19-6.23 of (Versteeg and Malalasekera 1995)). In the SIMPLE algorithm, some of the contributions to the velocity correction from the neighboring cells are ignored (compare eqs. 6.19 and 6.21 of (Versteeg and Malalasekera 1995)). Thus, the velocity correction does not need to be derived rigorously from the governing equations. (Dropping the contributions from the neighbor cells is quite an arbitrary

choice). The authors contend that "The omission of terms such as $\sum a_{nb}u'_{nb}$ in the derivation does not affect the final solution because the pressure correction and velocity corrections will all be zero in a converged solution…" (pg. 145, (Versteeg and Malalasekera 1995)). Based on this argument, we propose the following form for the velocity correction:

$$\vec{u}' = -\frac{\kappa}{\mu}\nabla p' \tag{1-42}$$

Equation (1-42) is similar in form to Darcy's Law. μ and κ account for the diffusion and convective contributions to the velocity correction, respectively. Whereas μ is always set to the actual value of the fluid viscosity, κ is an adjustable constant needed for improving convergence speed. For example, when the viscosity is $1\text{Pa}\cdot\text{s}$, setting κ to 0.01 accelerates convergence speed by about 20 times (compared to when κ is set to 1). For a viscosity value of $0.001\text{Pa}\cdot\text{s}$, κ should be set to 1e-6. To account for generalized coordinates, (1-42) is written:

$$\begin{pmatrix} u' \\ v' \end{pmatrix} = -\frac{\kappa}{\mu}\begin{pmatrix} \frac{\partial p'}{\partial x} \\ \frac{\partial p'}{\partial y} \end{pmatrix} \text{ with } \begin{aligned} \frac{\partial p'}{\partial x} &= \frac{\partial p'}{\partial \xi}\frac{\partial \xi}{\partial x} + \frac{\partial p'}{\partial \eta}\frac{\partial \eta}{\partial x} = \xi_x \frac{\partial p'}{\partial \xi} + \eta_x \frac{\partial p'}{\partial \eta} \\ \frac{\partial p'}{\partial y} &= \frac{\partial p'}{\partial \xi}\frac{\partial \xi}{\partial y} + \frac{\partial p'}{\partial \eta}\frac{\partial \eta}{\partial y} = \xi_y \frac{\partial p'}{\partial \xi} + \eta_y \frac{\partial p'}{\partial \eta} \end{aligned}$$

Recall the metrics of transformation:

$$\xi_x = \frac{y_\eta}{\left|J^{-1}\right|};\ \eta_x = -\frac{y_\xi}{\left|J^{-1}\right|};\ \xi_y = -\frac{x_\eta}{\left|J^{-1}\right|};\ \eta_y = \frac{x_\xi}{\left|J^{-1}\right|}$$

So that we have:

$$u' = -\frac{\kappa}{\mu\left|J^{-1}\right|}\left[y_\eta \frac{\partial p'}{\partial \xi} - y_\xi \frac{\partial p'}{\partial \eta}\right]; \qquad v' = -\frac{\kappa}{\mu\left|J^{-1}\right|}\left[-x_\eta \frac{\partial p'}{\partial \xi} + x_\xi \frac{\partial p'}{\partial \eta}\right]$$

From (Linninger 2011) we have that $\frac{\partial p'}{\partial \xi} = \Delta p'_\xi = p'_0 - p'_1$ and $\frac{\partial p'}{\partial \eta} = \Delta p'_\eta = p'_N - p'_S$. This leads to the final form for the velocity correction:

$$u' = -\frac{\kappa}{\mu\left|J^{-1}\right|}\left[y_\eta\left(p'_0 - p'_1\right) - y_\xi\left(p'_N - p'_S\right)\right]$$
$$v' = -\frac{\kappa}{\mu\left|J^{-1}\right|}\left[-x_\eta\left(p'_0 - p'_1\right) + x_\xi\left(p'_N - p'_S\right)\right] \tag{1-43}$$

Implementation: Corrected velocity. The velocity correction, $\vec{u}'$ will be used to calculate the corrected velocity, $\vec{u}$. The velocity correction, $\vec{u}'$ is the difference between the corrected velocity, and the solution variable, $\begin{pmatrix} u^* & v^* \end{pmatrix}$:

$$\begin{pmatrix} u' \\ v' \end{pmatrix} = \begin{pmatrix} u \\ v \end{pmatrix} - \begin{pmatrix} u^* \\ v^* \end{pmatrix}$$

After rearranging the above expression, eq. (1-44) emerges:

$$\begin{pmatrix} u \\ v \end{pmatrix} = \begin{pmatrix} u^* \\ v^* \end{pmatrix} + \begin{pmatrix} u' \\ v' \end{pmatrix} \tag{1-44}$$

Substituting eq. (1-43) into eq. (1-44) leads to two equations that represent the corrected velocity components, u and v.

$$u = u^* - \frac{\kappa}{\mu\left|J^{-1}\right|}\left[y_\eta\left(p'_0 - p'_1\right) - y_\xi\left(p'_N - p'_S\right)\right] \tag{1-45}$$

$$v = v^* - \frac{\kappa}{\mu\left|J^{-1}\right|}\left[-x_\eta\left(p'_0 - p'_1\right) + x_\xi\left(p'_N - p'_S\right)\right] \tag{1-46}$$

Equations (1-45) and (1-46) require some discussion. First, eqs. (1-45) and (1-46) are used to obtain u and v at the faces of each control volume. Thus, to obtain u (and v) at the cell center, eqs. (1-47) and (1-48) are used:

$$u_{\text{Average}} = \frac{1}{\#\text{ of faces}} \sum_{f=1}^{\#\text{ of faces}} \left\{ u^*\Big|^f - \frac{\kappa}{\mu\left|J^{-1}\right|}\left[y_\eta\left(p'_0 - p'_1\right) - y_\xi\left(p'_N - p'_S\right)\right]\Big|^f \right\} \tag{1-47}$$

$$v_{\text{Average}} = \frac{1}{\#\text{ of faces}} \sum_{f=1}^{\#\text{of faces}} \left\{ v^*\Big|^f - \frac{\kappa}{\mu\left|J^{-1}\right|}\left[-x_\eta\left(p'_0 - p'_1\right) + x_\xi\left(p'_N - p'_S\right)\right]\Big|^f \right\} \tag{1-48}$$

Equations (1-47) and (1-48) return the average corrected velocity component (at the cell center) based on the corrected velocities computed at the cell center's faces. Second, since u^* is computed at the cell center, $u^*\big|^f$ is computed using $u^*\big|^f = (u^*_{v1} + u^*_{v2})/2$, where u^*_{v1} and u^*_{v2} are known values from cells adjacent to face, *f*.

Implementation: Pressure correction equation. If the corrected velocity components, *u* and *v*, were the correct velocity, we should expect these velocity components to satisfy the continuity equation:

$$\int_{cv} \nabla \cdot \vec{u}\, dV = q \Rightarrow \oint_{face} \vec{u} \cdot \hat{\vec{n}}\, dA = q$$

Note, q is zero for an incompressible fluid in an undeformable fluid domain. With the relation, $\oint_{face} dA = \sqrt{x_\eta^2 + y_\eta^2}$, the above can be cast into

$$q = \sum_{f=1}^{\#\text{of faces}} \begin{pmatrix} u & v \end{pmatrix} \cdot (-1) \begin{pmatrix} y_\eta \\ -x_\eta \end{pmatrix}\Bigg|^f$$

Therefore, the total mass balance is:

$$q = -\sum_{f=1}^{\#\text{of faces}} \left(u y_\eta - v x_\eta \right)\Big|^f \tag{1-49}$$

For a given face, we can substitute eq. (1-45) into (1-49) and rewrite continuity as:

$$q^f = -1 \left[\begin{array}{l} y_\eta \left\{ u^* - \dfrac{\kappa}{\mu \left| J^{-1} \right|} \left[y_\eta \left(p'_0 - p'_1 \right) - y_\xi \left(p'_N - p'_S \right) \right] \right\} \\ -x_\eta \left\{ v^* - \dfrac{\kappa}{\mu \left| J^{-1} \right|} \left[-x_\eta \left(p'_0 - p'_1 \right) + x_\xi \left(p'_N - p'_S \right) \right] \right\} \end{array} \right]$$

This simplifies to:

$$q^f = -1 \left[y_\eta u^* - x_\eta v^* - \frac{\kappa}{\mu} \frac{\left(y_\eta^2 + x_\eta^2 \right)}{\left| J^{-1} \right|} \left(p'_0 - p'_1 \right) + \frac{\kappa}{\mu} \frac{\left(y_\xi y_\eta + x_\xi x_\eta \right)}{\left| J^{-1} \right|} \left(p'_N - p'_S \right) \right]$$

Or more simply as:

$$q^f = -1\left\{ y_\eta u^* - x_\eta v^* - \frac{\kappa}{\mu}\left[\frac{q_1}{\left|J^{-1}\right|}\left(p'_0 - p'_1\right) - \frac{q_2}{\left|J^{-1}\right|}\left(p'_N - p'_S\right) \right] \right\}$$

We can again use the approximation for the diffusion term introduced earlier to rewrite the above expression as:

$$q^f = -1\left\{ y_\eta u^* - x_\eta v^* - \frac{\kappa}{\mu}\left[\frac{\left(p'_0 - p'_1\right)}{q_3}\left|J^{-1}\right| \right] \right\}, \quad \text{where} \quad \begin{aligned} q_3 &= x_\xi^2 + y_\xi^2 \\ \left|J^{-1}\right| &= x_\xi y_\eta - x_\eta y_\xi \end{aligned} \qquad (1\text{-}50)$$

Assuming q to be zero for an incompressible fluid in an undeformable fluid domain, the complete equation which takes into account the contributions from all faces of a control volume is:

$$\sum_{f=1}^{\#\text{ of faces}} \left\{ -y_\eta u^* + x_\eta v^* + \frac{\kappa}{\mu}\left[\frac{\left(p'_0 - p'_1\right)}{q_3}\left|J^{-1}\right| \right] \right\}\Bigg|^f = 0.$$

This leads to the pressure correction equation for p':

$$\underbrace{\sum_{f=1}^{\#\text{ of faces}} \frac{\kappa}{\mu}\left[\frac{\left(p'_0 - p'_1\right)}{q_3}\left|J^{-1}\right| \right]\Bigg|^f}_{\text{Deviation from Continuity}} = \sum_{f=1}^{\#\text{ of faces}} \underbrace{y_\eta u^* - x_\eta v^*\Big|^f}_{\text{Continuity}} \qquad (1\text{-}51)$$

Note about eq. (1-51): First, it should be emphasized that p' is the pressure correction, not the actual pressure. Second, the right-hand-side of eq. (1-51) is continuity (see eq. (1-49)). The left-hand-side seems to describe the deviation from satisfying continuity. If solving the system of equations for the pressure correction, p' leads to p' being zero everywhere, then u^* and v^* satisfy continuity—the left-hand-side will be zero and hence $y_\eta u^* - x_\eta v^* = 0$. Thus, at convergence the current velocity field, u^* and v^* satisfies continuity and p' is zero (or sufficiently close to zero) everywhere.

Implementation: Pressure and velocity update. If convergence has not been reached, we apply the relation, $p = p^{i-1} + p'$ to improve the quality of the pressure field. p^{i-1} is the pressure value at the previous iteration—the value used in (1-40) and (1-41). Actually, the improved pressure value will be calculated via under-relaxation:

$$p^{new} = p^{i-1} + \alpha_p p', \quad \text{where} \quad 0 < \alpha_p < 1$$

For the second iteration, p^{i-1} will be set equal to p^{new}; this updated p^{i-1} will be used as the new pressure guess in eqs. (1-40) and (1-41). The velocities are also updated with under-relaxation ($0 < \alpha_u < 1$ and $0 < \alpha_v < 1$); the velocity components that will be used in eqs. (1-40) and (1-41) for the next iteration are:

$$u^{new} = \alpha_u u + (1 - \alpha_u) u^{i-1}$$
$$v^{new} = \alpha_v v + (1 - \alpha_v) v^{i-1}$$

From eq. (1-45)

A flow diagram of the proposed method is given in Figure 46.

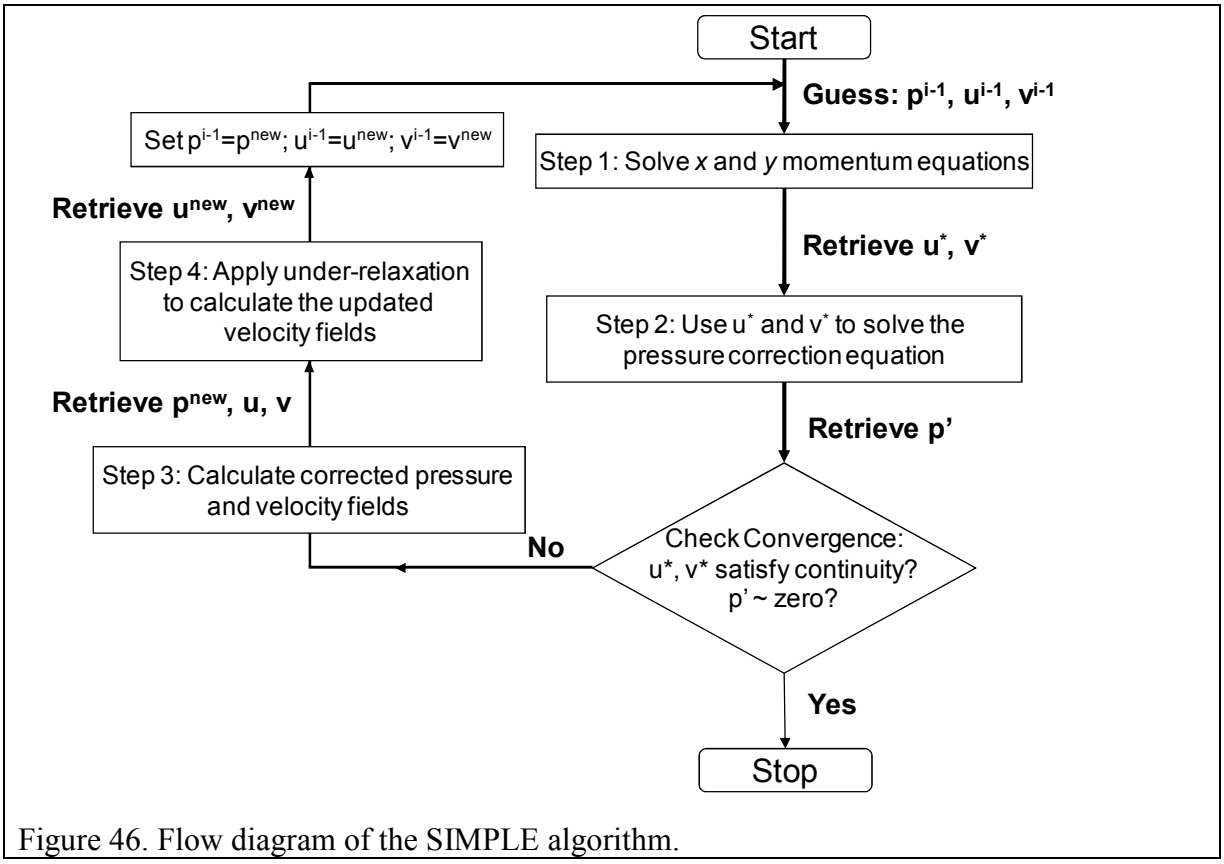

Figure 46. Flow diagram of the SIMPLE algorithm.

7.4.5. Program Validation of Steady-State Fluid Flow Prediction

The methodology described in the previous sections has been implemented as an object-oriented finite volume computer program in Delphi 7. Fluid flow simulations using our program were compared with results obtained using the commercial CFD tool, Fluent 6.3. Both structured and unstructured grids were used in the validation study.

Figure 47 shows a structured grid case study with dimensions, height 0.0764m and width 0.44m. The fluid domain was subdivided into 1,000 rectangular control volumes. A fluid velocity of 0.05m/s was specified at the left boundary and an outlet pressure of 0.001 Pa was specified at the right boundary. As shown in the figure, there is good agreement between the simulations obtained using our program and those obtained using Fluent.

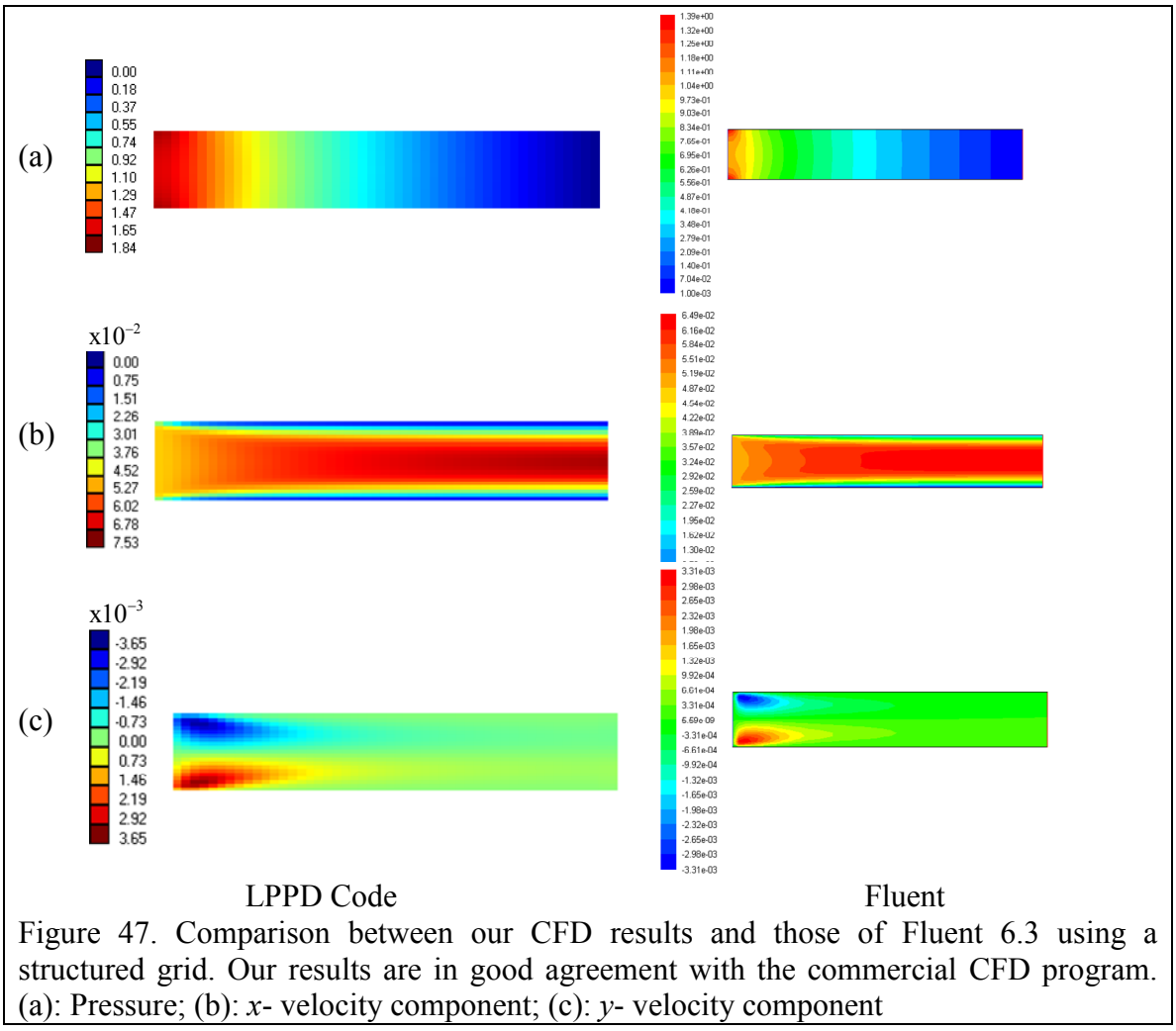

Figure 47. Comparison between our CFD results and those of Fluent 6.3 using a structured grid. Our results are in good agreement with the commercial CFD program. (a): Pressure; (b): *x*- velocity component; (c): *y*- velocity component

To validate our unstructured discretization scheme, Figure 48 compares our program results with those of Fluent in a cross section of a human brain's ventricular system. 1,180 control volumes were used in the simulation. In the study, an inflow of 0.003m/s in the negative *y*-direction was applied at the top o the lateral ventricle. An outlet pressure of 0.001 Pa was applied as indicated in the figure. The results for pressure and velocity closely match the results obtained using Fluent.

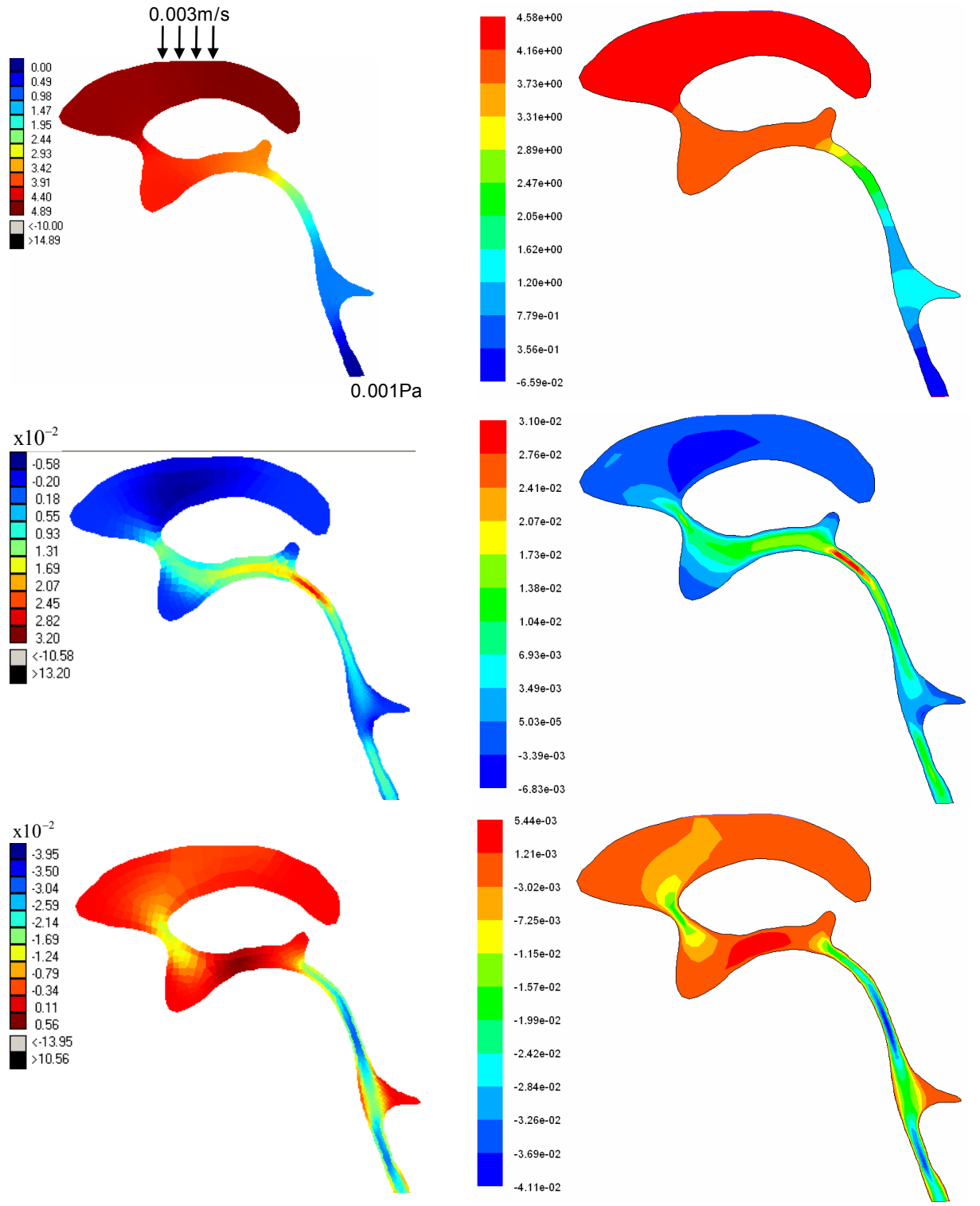

LPPD Code Fluent

Figure 48. CFD results of flow in the brain's lateral ventricle. Our implementation compares well with results obtained using the commercial CFD program, Fluent. Top row: Pressure; Middle row: *x*-velocity component; Bottom row: *y*-velocity component

7.5. The Arbitrary Lagrangian-Eulerian Method for Fluid Flow

7.5.1. Motivation and Overview of Section

An Eulerian reference frame is a reference frame in which the quantity of interest (fluid motion for example) is observed by a fixed observer. When the observer moves with the quantity of interest, the reference frame is referred to as Lagrangian. When a fluid grid is stationary, the governing fluid flow equations introduced in section 7.4.2 are applicable and are said to be written in an Eulerian reference frame. When the boundary of the fluid grid is displaced explicitly or implicitly (an implicit displacement of the fluid grid could be due to the displacement of a solid body along the solid-fluid interface) the internal structure of the fluid grid is also set in motion to accommodate the motion at the boundary.

At a moving boundary, the fluid grid and the fluid move at the same rate. The mathematical treatment at the moving boundary is said to be Lagrangian because the observer (an imaginary observer sitting on the fluid grid boundary) moves at the same rate as the fluid. Internal fluid grid points which are not on the moving boundary may move according to some overall governing scheme such that all control volumes in the fluid grid remain viable. For example, if a particular control volume in the computational domain were to collapse due to grid deformation, the continuum would break down and one could no longer compute the velocity or pressures for that particular control volume. Instituting a scheme for grid motion and coupling that motion with the underlying fluid dynamics leads to what many researchers call an Arbitrary Lagrangian-Eulerian (ALE) mathematical framework. In ALE, with the exception of the grid boundary, the fluid grid moves at a different speed than the fluid. Thus the governing flow equations are modified to account for the difference between the convective flux of the fluid with respect to the convective flux of the fluid grid.

Two key points regarding problems involving moving boundaries must be emphasized:

- The local time derivative in the momentum equations must be accounted for
- A zero (no-slip) velocity along the moving wall is not appropriate

The first point is due to the fact that the volume (or area in 2D) of the control volumes is changing; the local time derivative accounts for this change as will be shown in section 7.5.3. We must account for this volume change to properly balance the change in momentum of a given control volume. The second point is due to the fact that there can be no material separation along the solid-fluid interface. This condition is often referred to as a kinematic boundary condition for the solid-fluid interface. Mathematically it is written,

$$\vec{u}_f = \dot{\vec{d}}$$

where $\vec{u}_f$ is the fluid velocity at the wall and $\dot{\vec{d}}$ is the wall velocity.

The ALE governing equations and implementation will be introduced in this section. The derivation of the modified governing equations for a moving reference frame can be found in (Fox, McDonald et al. 2009) and will not be repeated here. The Space Conservation Law (SCL), which is introduced in (Demirdzic and Peric 1988), is a law which seeks to maintain volume conservation of the fluid grid. CFD codes in which the SCL is not accounted for may lead to spurious results. If the SCL is not implemented, the grid motion usually leads to an undesirable mass source as documented in (Ferziger and Peric 2002). In this section, the SCL will briefly be explained and supported by a specific example. After introducing the modified governing equations in the ALE reference frame, the importance and inner workings of the SCL will be explained.

7.5.2. Governing Equations in the ALE Reference Frame

The governing flow equations for an incompressible fluid written in the ALE reference frame (see (Demirdzic and Peric 1988; Demirdzic and Peric 1990) for example) are:

SCL
$$\frac{d}{dt}\int_{\text{cv}} dV - \oint_{face} \vec{u}_g \cdot \hat{\vec{n}}\, dA = 0 \tag{1-52}$$

Continuity
$$\frac{d}{dt}\int_{\text{cv}} dV + \oint_{face} (\vec{u}_f - \vec{u}_g) \cdot \hat{\vec{n}}\, dA = 0 \tag{1-53}$$

Momentum
$$\rho\int_{\text{cv}} \frac{\partial \vec{u}}{\partial t} dV = -\int_{\text{cv}} \nabla p^{i-1}\, dV - \rho\int_{\text{cv}} \left(\vec{u}_f^{\,i-1} - \vec{u}_g\right)\cdot\left(\nabla \vec{u}^{\,*}\right) dV + \mu\int_{\text{cv}} \nabla\cdot\left(\nabla \vec{u}^{\,*}\right) dV \tag{1-54}$$

In eqs. (1-52) through (1-54), $\vec{u}_g$ is introduced as the grid velocity (defined at a control volume face). The SCL is an auxiliary equation by virtue that $\vec{u}_g$ should be computed such that (1-52) is satisfied. Methods to compute $\vec{u}_g$ are given in section 7.5.4. Eq. (1-53) will be used to derive a modified pressure correction equation in a similar manner as described in section 7.4.4 for stationary grids. Before discussing the SCL and the modified pressure correction, the next section presents the discretized forms of the momentum equations in the ALE reference frame.

7.5.3. Discretization of the ALE Equations

We present in eq. (1-55) the unsteady form of the *x*-momentum equation, which was first introduced in eq. (1-35). Each term in eq. (1-55) is integrated in space and time to arrive at the discretized form of the unsteady *x*-momentum equation.

$$\rho\int_{t}^{t+\Delta t}\int_{\text{cv}} \frac{\partial u}{\partial t} dV dt = -\int_{t}^{t+\Delta t}\int_{\text{cv}} \nabla_x p\, dV dt - \rho\int_{t}^{t+\Delta t}\int_{\text{cv}} \vec{u}\cdot\nabla u\, dV dt + \mu\int_{t}^{t+\Delta t}\int_{\text{cv}} \nabla\cdot\left(\nabla u\right) dV dt \tag{1-55}$$

This section will describe the integration/discretization of each term in eq. (1-55).

Local Acceleration Term. The discretizated form of the local acceleration term in the unsteady *x*-momentum equation is derived as follows. To handle the integral, we will assume that u (the *x* component of the velocity vector) is a function of time but not a function of V (the volume/area of a control volume at an instance in time). We will further assume that V is a function of time only. With these assumptions, we rewrite the double integral in eq. (1-55) as,

$$\rho \int_t^{t+\Delta t} \int_{cv} \frac{\partial u}{\partial t} dV dt = \rho \int_t^{t+\Delta t} \frac{\partial u}{\partial t} \int_{cv} dV \, dt \,,$$

which ultimately leads to

$$\rho \int_t^{t+\Delta t} \frac{\partial u}{\partial t} \int_{cv} dV \, dt = \rho \int_t^{t+\Delta t} \frac{\partial u}{\partial t} V \, dt \Rightarrow \rho \left[(uV)^{t+\Delta t} - (uV)^t \right] \tag{1-56}$$

Pressure Gradient Term. The discretizated form of the pressure gradient term in the unsteady *x*-momentum equation is derived as follows. From section 7.4.3, integration over the control volume led to:

$$-\int_{cv} \nabla_x p \, dV = \sum_{f=1}^{\#\text{ of faces}} p \, y_\eta \Big|^f$$

Thus, we have for the time integration:

$$\int_t^{t+\Delta t} \left(\sum_{f=1}^{\#\text{ of faces}} p \, y_\eta \Big|^f \right) dt \tag{1-57}$$

Let us recall that the SIMPLE algorithm stands for semi-implicit method for pressure-linked equations. Since the method is semi-implicit, some terms can be treated implicitly while others treated explicitly. We have chosen to treat the pressure term as explicit and the velocity term as implicit. Consequently, in the first iteration of a given time step, we use the converged value of p from the previous time step. Thus, we can remove p from the time integral and rewrite eq. (1-57) as:

$$\sum_{f=1}^{\#\text{ of faces}} p \, y_\eta \Big|^f \int_t^{t+\Delta t} dt \,,$$

which leads to:

$$\sum_{f=1}^{\#\text{ of faces}} p \, y_\eta \Big|^f \Delta t$$

Convective Acceleration Term. The convective term in the ALE reference frame was introduced in eq. (1-54). The convective term associated with the *x*-momentum is given in eq. (1-58).

$$-\rho\left(\vec{u}_f^{\,i-1}-\vec{u}_g\right)\cdot\left(\nabla u^*\right) \tag{1-58}$$

$\vec{u}_f^{\,i-1}$ and $\vec{u}_g$ are the fluid velocity and fluid grid velocity, respectively, calculated at a control volume face. To aid the derivation, we introduce the relative velocity vector, $\vec{\hat{u}}_r$ with components $\hat{u}_r$ and $\hat{v}_r$. $\vec{\hat{u}}_r$, $\hat{u}_r$, and $\hat{v}_r$ are defined as:

$$\begin{aligned}\vec{\hat{u}}_r &= \vec{u}_f^{\,i-1}-\vec{u}_g\\ \hat{u}_r &= u_f^{i-1}-u_g\\ \hat{v}_r &= v_f^{i-1}-v_g\end{aligned} \tag{1-59}$$

By substituting eq. (1-59) into eq. (1-58) and integrating over a control volume, cv we have:

$$-\rho\int_{\text{cv}}\vec{\hat{u}}_r\cdot\left(\nabla u^*\right)dV$$

Using the same arguments for the integral as in section 7.4.3, we eventually arrive at:

$$\rho\sum_{f=1}^{\#\text{ of faces}}\left(\hat{u}_r y_\eta-\hat{v}_r x_\eta\right)u^*\Big|^f$$

Thus, we have for the time integration:

$$\rho\int_t^{t+\Delta t}\left(\sum_{f=1}^{\#\text{ of faces}}\left(\hat{u}_r y_\eta-\hat{v}_r x_\eta\right)u^*\Big|^f\right)dt$$

The relative velocity contribution can be removed from the time integral leading to:

$$\rho\sum_{f=1}^{\#\text{ of faces}}\left[\left(\hat{u}_r y_\eta-\hat{v}_r x_\eta\right)\int_t^{t+\Delta t}u^*dt\right]\Bigg|^f$$

As stated in (Patankar 1980) (page 55), we need an assumption for how the unknown, u^* varies with time from *t* to $t+\Delta t$. One may propose

$$\int_t^{t+\Delta t}u^*dt=\left[f\,u^{*,new}+\left(1-f\right)u^{*,old}\right]\Delta t$$

where f is a weighting factor between 0 and 1. Setting f equal to one leads to an implicit time integration; setting f equal to zero, leads to explicit time integration. Since implicit time integration is unconditionally stable, we set f to 1. In this chapter u^* has always been assumed to be at the new time level. Thus we write the discretized convective term as

$$\rho \sum_{f=1}^{\#\text{ of faces}} \left[\left(\hat{u}_r y_\eta - \hat{v}_r x_\eta \right) u^* \right]^f \Delta t$$

Diffusion Term. The discretized diffusion term requires no special treatment other than appending it with Δt as was done in the pressure gradient term and the convective term. From section 7.4.3, integration over the control volume led to:

$$-\mu \sum_{f=1}^{\#\text{ of faces}} \left[\frac{u_0^* - u_1^*}{q_3} \left| J^{-1} \right| \right]^f$$

Thus, we have for time integration,

$$-\mu \int_t^{t+\Delta t} \left(\sum_{f=1}^{\#\text{ of faces}} \left[\frac{u_0^* - u_1^*}{q_3} \left| J^{-1} \right| \right]^f \right) dt = -\mu \sum_{f=1}^{\#\text{ of faces}} \left[\frac{u_0^* - u_1^*}{q_3} \left| J^{-1} \right| \right]^f \Delta t$$

Complete Discretized Forms of the Unsteady Momentum Equations. Since Δt is common to the pressure gradient, convective, and diffusion terms, both sides of the momentum equation are divided by Δt, and the discretized x and y-momentum equations are written:

x-momentum

$$\frac{\rho \left[(uV)^{t+\Delta t} - (uV)^t \right]}{\Delta t} = \sum_{f=1}^{\#\text{ of faces}} p\, y_\eta \Big|^f + \rho \sum_{f=1}^{\#\text{ of faces}} \left[\left(\hat{u}_r y_\eta - \hat{v}_r x_\eta \right) u^* \right]^f - \mu \sum_{f=1}^{\#\text{ of faces}} \left[\frac{u_0^* - u_1^*}{q_3} \left| J^{-1} \right| \right]^f$$

y-momentum

$$\frac{\rho \left[(vV)^{t+\Delta t} - (vV)^t \right]}{\Delta t} = -\sum_{f=1}^{\#\text{ of faces}} p\, x_\eta \Big|^f + \rho \sum_{f=1}^{\#\text{ of faces}} \left(\hat{u}_r y_\eta - \hat{v}_r x_\eta \right) v^* \Big|^f - \mu \sum_{f=1}^{\#\text{ of faces}} \left[\frac{v_0^* - v_1^*}{q_3} \left| J^{-1} \right| \right]^f$$

Ultimately, a linear algebra problem will be solved to compute u^* and v^*. The transition from discrete equations to a linear set of equations is clearer when we bring the unknown variables to

the left side and the constants to the right side. In the equations below, u^* and v^* have been rewritten as $u^{t+\Delta t}$ and $v^{t+\Delta t}$. According to the derivation, it seems u^t and v^t should be the values of the velocity components from the previous time step. However, the ALE program is more stable when u^t and v^t are the values of the velocity components from the previous iteration within a given time step. Therefore u^t and v^t will be rewritten as u^{i-1} and v^{i-1}. The pressure term, p^{i-1} is the value of the pressure from the previous iteration within a given time step. V^t is the volume (area in 2d) of a control volume from the previous time step; $V^{t+\Delta t}$ is the known volume (area in 2d) of a control volume at the current time.

x-momentum

$$\frac{\rho V^{t+\Delta t}}{\Delta t}u_0^{t+\Delta t} - \rho\sum_{f=1}^{\#\text{ of faces}}\left[\left(\hat{u}_r y_\eta - \hat{v}_r x_\eta\right)u^{t+\Delta t}\right]\Big|^f + \mu\sum_{f=1}^{\#\text{ of faces}}\left[\frac{u_0^{t+\Delta t}-u_1^{t+\Delta t}}{q_3}\left|J^{-1}\right|\right]\Big|^f = \sum_{f=1}^{\#\text{ of faces}} p^{i-1}\,y_\eta\Big|^f + \frac{\rho V^t}{\Delta t}u_0^{i-1}$$

y-momentum

$$\frac{\rho V^{t+\Delta t}}{\Delta t}v_0^{t+\Delta t} - \rho\sum_{f=1}^{\#\text{ of faces}}\left[\left(\hat{u}_r y_\eta - \hat{v}_r x_\eta\right)v^{t+\Delta t}\right]\Big|^f + \mu\sum_{f=1}^{\#\text{ of faces}}\left[\frac{v_0^{t+\Delta t}-v_1^{t+\Delta t}}{q_3}\left|J^{-1}\right|\right]\Big|^f = -\sum_{f=1}^{\#\text{ of faces}} p^{i-1}\,x_\eta\Big|^f + \frac{\rho V^t}{\Delta t}v_0^{i-1}$$

7.5.4. Space Conservation Law: Calculating the Grid Velocities

As stated in section 7.5.2, eq. (1-52) is not explicitly included in the equation set. Nevertheless, the grid velocity $\vec{u}_g$ should satisfy the SCL, eq. (1-52). Using a specific example, this section aims to describe how the grid velocities at each face are computed. To compute the face velocities, we need two items:

- A perpendicular vector to the face
- The distance vector of the face center

Finding the Perpendicular to the Face

To find the perpendicular vector to the face, we will first need to construct a vector from the face. This face vector will be given the label η^0 in the initial configuration, and the label η^n at the new time level. The direction of this vector is not important. However, it is important that the

direction we choose be the same for the initial configuration and the new time step. The vector perpendicular to η^0 (η^n in the new time level) will be labeled $\vec{S}_f^o$ ($\vec{S}_f^n$ in the new time level). Given that η^0 is defined as $\eta^0 = (x_{\eta^0}, y_{\eta^0})$, $\vec{S}_f^o$ will be defined as $\vec{S}_f^o = (y_{\eta^0}, -x_{\eta^0})$.

Finding the Distance Vector of the Face Center

To find the distance vector of the face center, one should subtract the coordinates of the face center in the initial configuration from the coordinates of the face center in the new configuration. Specifically, one would have,

$$\delta\vec{r}_f = \vec{r}_f^n - \vec{r}_f^0$$

where $\vec{r}_f^n$ is a position vector in the new configuration and $\vec{r}_f^0$ is a position vector in the initial configuration. Once these items have been computed, the equations for calculating the grid velocities can be invoked. The specific equations which are derived in (Demirdzic and Peric 1988), are as follows:

u component of grid velocity $$u_{g,f} = \frac{S_{x,f}^o + S_{x,f}^n}{2S_{x,f}^n}\frac{\delta x_f}{\Delta t} \qquad (1\text{-}60)$$

v component of grid velocity $$v_{g,f} = \frac{S_{y,f}^o + S_{y,f}^n}{2S_{y,f}^n}\frac{\delta y_f}{\Delta t} \qquad (1\text{-}61)$$

The symbols used in (1-60) through (1-61) as well as those used in the example which follows are defined in Table 1. Figure 49 shows the physical interpretation of all variables used to calculate the grid velocity. The example will clarify all above concepts and demonstrate how to successfully use eqs. (1-60) and (1-61).

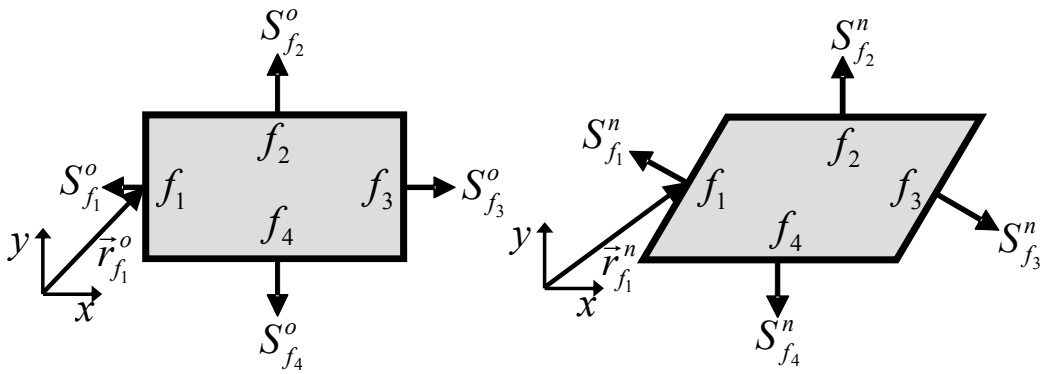

Figure 49. Physical interpretation of S^o_f, S^n_f, $\vec{r}^{\,o}_f$ and $\vec{r}^{\,n}_f$ used to calculate $u_{g,f}$ and $v_{g,f}$

Table 12: Definition of symbols used in the SCL calculations.

Symbol	Description
η^0, η^n	Face vector in initial and new configuration, respectively
$\vec{S}^o_f$, $\vec{S}^n_f$	Vector that is perpendicular to the face vector (initial and new configuration, respectively)
$S^o_{x,f}$, $S^o_{y,f}$	The x and y components of the perpendicular vector (initial configuration shown only)
$\delta\vec{r}_f$	A distance vector that arises when the position of a face center moves to a new point in space in a given time period
δx_f, δy_f	The x and y components of the distance vector, $\delta\vec{r}_f$
Δt	Time step size

Example Problem: Calculating Grid Velocities Using the SCL

Consider the grid shown in Figure 50. Initially, cells V1 and V2 have an equal area of 15 units. During a one second interval, f3 is moved two units to the left. V1 has a final area of 9 and V2 has a final area of 21. In this example, the calculation of all face velocities will be demonstrated. Since only f3 moves in this example, intuitively, we can guess that the only face with a velocity value will be f3.

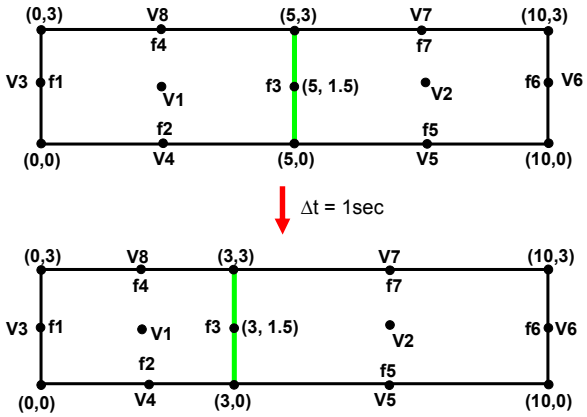

Cell Areas in Initial Configuration

$A_{V1}^{0} = (5)(3) = 15$

$A_{V2}^{0} = (5)(3) = 15$

Cell Areas at New Time Level

$A_{V1}^{n} = (3)(3) = 9$

$A_{V2}^{n} = (7)(3) = 21$

Figure 50. Case study of a grid undergoing internal deformation. Face 3 (f3), highlighted in green, is moved two units to the left in a time span of 1 second ($\Delta t = 1\,\text{sec}$).

The velocities will be computed for each face.

Face 1

The first component of the face 1 vector is calculated by subtracting the *x*-coordinate of one endpoint of face 1 from the *x*-coordinate of the other endpoint of face 1. The second component arises by repeating the procedure for the *y*-coordinates:

$$\eta_{f_1}^{0} = (x_\eta, y_\eta) = (0-0, 3-0) = (0,3)$$

The vector perpendicular to $\eta_{f_1}^{0}$ is obtained using the formula,

$$\vec{S}_{f_1}^{o} = (y_\eta, -x_\eta) = (3,0)$$

Since the face remains stationary during the time interval, the face vector and perpendicular vector in the new configuration have the same values as in the initial configuration. Note the change in notation below on these vectors in the new configuration:

$$\eta_{f_1}^n = (x_\eta, y_\eta) = (0-0, 3-0) = (0,3)$$
$$\vec{S}_{f_1}^n = (y_\eta, -x_\eta) = (3,0)$$

The distance vector arising from a change in the position of the face 1 center is computed as:

$$\delta\vec{r}_{f_1} = \vec{r}_{f_1}^n - \vec{r}_{f_1}^0 = (0,1.5) - (0,1.5) = (0,0)$$

Having all required items, we are now ready to invoke eqs. (1-60) and (1-61) to compute the face velocity.

$$u_{g,f} = \frac{S_{x,f}^o + S_{x,f}^n}{2S_{x,f}^n}\frac{\delta x_f}{\Delta t} = \frac{3+3}{2(3)}\frac{0}{1} = 0\,; \quad v_{g,f} = \frac{S_{y,f}^o + S_{y,f}^n}{2S_{y,f}^n}\frac{\delta y_f}{\Delta t} = \frac{0+0}{2(0)}\frac{0}{1} = 0$$

We must be careful when coding so that the denominator does not become zero as it has in this simple example. If it does, simply make that velocity component zero.

For face 1, $u_{g,f_1} = 0$; $v_{g,f_1} = 0$. This face has zero velocity.

Face 2

$\eta^0 = (5-0, 0-0) = (5,0) \Rightarrow \vec{S}_{f_2}^o = (0,-5)$

$\eta^n = (3-0, 0-0) = (3,0) \Rightarrow \vec{S}_{f_2}^n = (0,-3)$

$\delta\vec{r}_{f2} = \vec{r}_{f2}^n - \vec{r}_{f2}^0 = (1.5-2.5, 0-0) = (-1,0)$

Let's review: $\vec{S}_{f_2}^o = (0,-5)$ $\vec{S}_{f_2}^n = (0,-3)$ $\delta\vec{r}_{f_2} = (-1,0)$

$$u_{g,f_2} = \frac{0+0}{2(0)}\left(\frac{-1}{1}\right) = 0\,; \qquad v_{g,f_2} = \frac{-5+-3}{2(-3)}\left(\frac{0}{1}\right) = 0$$

Though the size of face 2 shrunk, both the *u* and *v* components of the velocity vector of face 2 are zero. The face velocity is based on how the face moves in the direction of the normal vector. From the diagram, we can see that the face did not move in the direction of $\vec{S}_{f_2}$.

Face 3

$\eta^0 = (0,3) \Rightarrow \vec{S}_{f_3}^o = (3,0)$

$\eta^n = (0,3) \Rightarrow \vec{S}_{f_3}^n = (3,0)$

$\delta\vec{r}_{f_3} = \vec{r}_{f_3}^n - \vec{r}_{f_3}^0 = (3-5, 1.5-1.5) = (-2,0)$

Let's review: $\vec{S}_{f_3}^o = (3,0)$ $\vec{S}_{f_3}^n = (3,0)$ $\delta\vec{r}_{f_3} = (-2,0)$

$$u_{g,f_3} = \frac{3+3}{2(3)}\begin{pmatrix}-2\\1\end{pmatrix} = -2 \qquad v_{g,f_3} = \frac{0+0}{2(0)}\begin{pmatrix}0\\1\end{pmatrix} = 0$$

Velocity of f_3 = (-2,0)

Based on our findings for f1 and f2, we can conclude that all other faces should have a velocity of zero.

Check the Solution

We can check our results by calculating the fluid continuity for both control volumes. For an incompressible fluid, continuity is written as

$$\nabla \cdot \vec{u} = q\,,$$

where $\nabla \cdot \vec{u}$ is the divergence of the velocity field and q is a measure of volume change in the control volume. Integrating both sides of the equation over a control volume yields

$$\int_{CV} \nabla \cdot \vec{u}\, dV = \int_{CV} q\, dV$$

$$\Rightarrow \int_{CV} \nabla \cdot \vec{u}\, dV \Rightarrow \oint_S \vec{u} \cdot \hat{\vec{n}}\, dS \Rightarrow \sum_{f=1}^{\#\text{ of faces}} \begin{pmatrix}u & v\end{pmatrix}\begin{pmatrix}n_x\\n_y\end{pmatrix} \qquad (1\text{-}62)$$

where $(n_x, n_y)^T$ is normal vector to the face directed out of the control volume. Equation (1-62) should be evaluated for all faces. However, since f3 is the only face that had a velocity, the computation is:

Volume 1 (V1)

$\vec{u} = (-2,0)\,;\ \vec{n} = (3,0)$

$$\vec{u} \cdot \vec{n} = \begin{pmatrix}-2 & 0\end{pmatrix}\begin{pmatrix}3\\0\end{pmatrix} = -6$$

Volume 2 (V2)

$\vec{u} = (-2,0)\,;\ \vec{n} = (-3,0)$

$$\vec{u} \cdot \vec{n} = \begin{pmatrix}-2 & 0\end{pmatrix}\begin{pmatrix}-3\\0\end{pmatrix} = 6$$

This matches the change in area experienced by the volumes. V1 decreased by 6 and V2 increased by 6; compare A_{V1}^0 to A_{V1}^n and A_{V2}^0 to A_{V2}^n.

Additional case studies invoking the SCL are given in the Appendix.

7.5.5. Pressure Correction in the ALE Framework

The overall solution approach for solving fluid flow in an ALE reference frame is,

- Compute the grid velocities
- Solve the *x* and *y* momentum equations using the relative velocity
- Solve the pressure correction equation

Having demonstrated how to calculate the grid velocities, and having presented the momentum equations written in an ALE reference frame, we are now in a position to address how the pressure correction equation is modified in the ALE reference frame. To derive a modified pressure correction let us compare the continuity equation written in the Eulerian reference frame to the continuity equation written in the ALE reference frame.

Continuity Equation

Eulerian Reference Frame

$$\oint_A \underbrace{\vec{u}_f}_{\substack{\text{"Correct"} \\ \text{Velocity}}} \cdot \hat{\vec{n}}\, dA = 0 \qquad (1\text{-}63)$$

ALE Reference Frame

$$\frac{d}{dt}\int_{CV} dV + \oint_A \underbrace{(\vec{u}_f - \vec{u}_g)}_{\substack{\text{"Correct"} \\ \text{Velocity}}} \cdot \hat{\vec{n}}\, dA = 0 \qquad (1\text{-}64)$$

Let us also recall the expression for the "correct" velocity, $\vec{u}_f$, defined in section 7.4.4 and repeated here for convenience:

$$\vec{u}_f = \vec{u}_f^{\,*} + \vec{u}_f\,' \qquad (1\text{-}65)$$

where the subscript *f* has been appended to each term to indicate fluid velocities (as opposed to grid velocities). The velocity entity used in the continuity eq. (1-49) was indeed $\vec{u}_f$. Therefore, to obtain the "correct" velocity in the ALE reference frame, we simply subtract the grid velocity, $\vec{u}_g$ from the fluid velocity, $\vec{u}_f$:

$$\hat{\vec{u}}_r = \vec{u}_f - \vec{u}_g = \vec{u}_f^{\,*} + \vec{u}_f\,' - \vec{u}_g$$

The correct velocity in the ALE reference frame has been given the notation $\vec{\hat{u}}_r$, where *r* indicates relative velocity between the fluid and the grid. With the help of eq. (1-43), the new components of the correct velocity field are:

$$\hat{u}_r = u_f^* - \frac{\kappa}{\mu\left|J^{-1}\right|}\left[y_\eta\left(p'_0 - p'_1\right) - y_\xi\left(p'_N - p'_S\right)\right] - u_g \tag{1-66}$$

$$\hat{v}_r = v_f^* - \frac{\kappa}{\mu\left|J^{-1}\right|}\left[-x_\eta\left(p'_0 - p'_1\right) + x_\xi\left(p'_N - p'_S\right)\right] - v_g \tag{1-67}$$

When the grid velocity is zero everywhere, u_g and v_g are zero, and hence the original formula for the correct velocity is preserved. These components of the correct velocity can now be substituted into eq. (1-64). First, let us rewrite the second term of eq. (1-64) as:

$$\int_A \vec{\hat{u}}_r \cdot \hat{\vec{n}}\, dA$$

Substituting the components in eqs. (1-66) and (1-67) into the above expression yields:

$$\oint_A \begin{pmatrix}\hat{u}_r & \hat{v}_r\end{pmatrix} \cdot (-1) \begin{pmatrix} y_\eta \\ -x_\eta \end{pmatrix} / \sqrt{x_\eta^2 + y_\eta^2}\, dA$$

Which eventually leads to

$$q = -\sum_{f=1}^{\#\text{ of faces}} \left(\hat{u}_r y_\eta - \hat{v}_r x_\eta\right)\Big|^f \tag{1-68}$$

Of note, eq. (1-68) is completely analogous to eq. (1-49). Substituting (1-66) and (1-67) into eq. (1-68) eventually yields:

$$q = -\sum_{f=1}^{\#\text{ of faces}} \left\{ y_\eta\left(u_f^* - u_g\right) - x_\eta\left(v_f^* - v_g\right) - \frac{\kappa}{\mu}\left[\frac{p'_0 - p'_1}{q_3}\left|J^{-1}\right|\right]\right\}\Bigg|^f \tag{1-69}$$

To complete the formulation for the pressure correction equation in the ALE reference frame, we need to address the first term in eq. (1-64). $\frac{d}{dt}\int_{\text{CV}} dV$ will be discretized as follows:

$$\frac{d}{dt}\int_{CV} dV \Rightarrow \frac{V^n - V^0}{\Delta t} \tag{1-70}$$

V^n and V^0 are the current and old volumes, respectively, of a particular control volume. In two-dimensions, V is the area of the control volume. Δt is the time step. The final form of the pressure correction equation in the ALE reference frame can therefore be written as:

Pressure Correction Equation in the ALE Reference Frame

$$\frac{V^n - V^0}{\Delta t} - \sum_{f=1}^{\#\text{ of faces}} \left\{ y_\eta \left(u_f^* - u_g \right) - x_\eta \left(v_f^* - v_g \right) - \frac{\kappa}{\mu} \left[\frac{p'_0 - p'_1}{q_3} \left| J^{-1} \right| \right] \right\}^f = 0 \tag{1-71}$$

By isolating the unknown variable p' on the left side of the equation, and bringing known variables to the right, eq. (1-71) can be rewritten as:

$$\sum_{f=1}^{\#\text{ of faces}} \frac{\kappa}{\mu} \left[\frac{p'_0 - p'_1}{q_3} \left| J^{-1} \right| \right]^f = \sum_{f=1}^{\#\text{ of faces}} \left[y_\eta \left(u_f^* - u_g \right) - x_\eta \left(v_f^* - v_g \right) \right] - \frac{V^n - V^0}{\Delta t}$$

The overall solution strategy for solving fluid motion in a deformable grid is given in Figure 51.

ALE Solution Strategy

Objective: To solve fluid flow problems in a moving grid.

Required Steps:

1. Solve flow field on undeformed grid
2. Compute boundary deformation and fluid grid displacement to solve S_f^0 and S_f^n
3. Calculate cell face velocities, $\vec{u}_g$ using eq. 20 of (Demirdzic and Peric 1988):

$$u_{g,f} = \frac{S_{x,f}^o + S_{x,f}^n}{2S_{x,f}^n}\frac{\delta x_f}{\Delta t}\ ; \quad v_{g,f} = \frac{S_{y,f}^o + S_{y,f}^n}{2S_{y,f}^n}\frac{\delta y_f}{\Delta t}$$

4. Solve the *x* and *y* momentum equations for u^* and v^* using the current value of $\vec{u}_f$ (where $\vec{u}_f$ is the fluid velocity) and pressure as well as $\vec{u}_g$ from above.

x-momentum:

$$\rho\int_{cv}\frac{\partial u}{\partial t}dV = -\int_{cv}\nabla_x p^{i-1}\,dV - \rho\int_{cv}\left(\vec{u}_f^{\,i-1} - \vec{u}_g\right)\cdot\left(\nabla u^*\right)dV + \mu\int_{cv}\nabla\cdot\left(\nabla u^*\right)dV$$

y-momentum:

$$\rho\int_{cv}\frac{\partial v}{\partial t}dV = -\int_{cv}\nabla_y p^{i-1}\,dV - \rho\int_{cv}\left(\vec{u}_f^{\,i-1} - \vec{u}_g\right)\cdot\left(\nabla v^*\right)dV + \mu\int_{cv}\nabla\cdot\left(\nabla v^*\right)dV$$

5. Solve the pressure correction equation for p':

$$\sum_{f=1}^{\#\text{ of faces}}\frac{\kappa}{\mu}\left[\frac{p'_0 - p'_1}{q_3}\left|J^{-1}\right|\right]\Bigg|^f = \sum_{f=1}^{\#\text{ of faces}}\left[y_\eta\left(u_f^* - u_g\right) - x_\eta\left(v_f^* - v_g\right)\right] - \frac{V^n - V^0}{\Delta t}$$

6. Update pressure and velocity fields
7. Repeat steps 4 through 6 until convergence
8. Repeat steps 2 through 7 for all deformation steps

Figure 51. Overview of the ALE solution strategy

The appendix includes a validation study of my ALE program by presenting my results alongside results obtained in Fluent. Also in the appendix is a step by step example of the ALE method in a one-cell grid.

7.6. Mesh/Grid Motion for a Fluid Domain

7.6.1. Overview and Motivation

A mesh (computational grid) will deform if one or more of its boundaries are set in motion. In the brain model, the fluid boundary will move due to brain tissue motion along the fluid-tissue interface. In our discussion of ALE, it was implicit that a particular method governed the internal motion of the fluid grid. This section describes the actual method used to govern fluid mesh

motion. Several methods for fluid grid motion have been proposed (Hughes, Liu et al. 1981; Nomura and Hughes 1992; Nitikitpaiboon and Bathe 1993; Blom 2000; Cao, Huang et al. 2002; Zhao and Forhad 2003; Tan, Tang et al. 2006). Some of these methods utilize distance functions while others incorporate spring-based stiffness functions to maintain fluid grid integrity. These methods are well suited when applied to Cartesian or curvilinear grids. However, unstructured meshes (as encountered exclusively in this dissertation) present a limitation to these methods, requiring a more general formulation. For example, Souli and Zolesio (2001) proposed an elasticity model to govern fluid mesh motion. Similar to Souli and Zolesio's method, our formulation uses solid elasticity equations to govern fluid mesh motion. Our method results in a favorable distribution of fluid mesh displacement such that deformations occurring at the brain-CSF interface do not lead to significant mesh distortion or element collapse. The governing equation for fluid mesh motion is given in (1-72).

$$0 = G\nabla^2\vec{d} + (\lambda + G)\nabla\left(\nabla\cdot\vec{d}\right) \tag{1-72}$$

In a two-dimensional analysis, eq. (1-72) takes the following form:

$$\begin{aligned} 0 &= G\nabla^2\alpha + (\lambda + G)\nabla\left(\frac{\partial\alpha}{\partial x} + \frac{\partial\beta}{\partial y}\right) \\ 0 &= G\nabla^2\beta + (\lambda + G)\nabla\left(\frac{\partial\alpha}{\partial x} + \frac{\partial\beta}{\partial y}\right) \end{aligned} \tag{1-73}$$

In eq. (1-72) and (1-73), G and λ are Lame constants and $\vec{d}$ is the displacement vector. In 2d, $\vec{d}$ has two components, α and β, as indicated in eq. (1-73). With relation (1-74)

$$\varepsilon_v = \nabla\cdot\vec{d} = \frac{\partial\alpha}{\partial x} + \frac{\partial\beta}{\partial y}, \tag{1-74}$$

eq. (1-72) is equivalent to

$$0 = G\nabla^2\vec{d} + (\lambda + G)\nabla\varepsilon_v, \tag{1-75}$$

where ε_v is the volumetric strain. The value of G affects the shearing motion of the internal fluid grid, whereas λ affects the compressibility of the fluid control volumes. For the fluid grid, G is set to 1,000 N/m^2. λ can be determined from G and the Poisson ratio, v (set to 0.3 for the fluid grid) as shown in eq. (1-76).

$$\lambda = \frac{2Gv}{1-2v} \tag{1-76}$$

The discretized form of eq. (1-75) is described next.

7.6.2. Discretization of Governing Equations

The discretized form of eq. (1-75) is obtained by integrating each term over a control volume. In eq. (1-77), G and λ are assumed constant and removed from the integral.

$$0 = G\int_{CV} \nabla^2 \vec{d}\, dV + (\lambda + G)\int_{CV} \nabla \bar{\varepsilon}_v\, dV \tag{1-77}$$

Because a collocated discretization scheme is adopted, $\vec{d}$ and ε_v are calculated at the control volume center. However, the discretization will invoke the displacements (and hence contributions to the volumetric strain) at the face of a control volume. Therefore, the bar over the volumetric strain term in eq. (1-77) indicates that the average displacement at each face will be used to calculate the volumetric strain for a given control volume. As illustrated in Figure 52, the displacements of adjacent cell centers are averaged to calculate the displacement at the face.

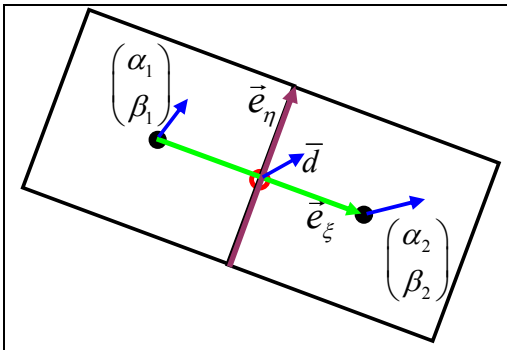

$$\vec{\bar{d}} = \begin{pmatrix}\bar{\alpha}\\ \bar{\beta}\end{pmatrix} = \begin{pmatrix}\dfrac{\alpha_1+\alpha_2}{2}\\ \dfrac{\beta_1+\beta_2}{2}\end{pmatrix}$$

Figure 52. Illustration and mathematical formula for calculating the displacement at the face of a control volume.

Gauss theorem is applied to rewrite eq. (1-77) as:

$$0 = G\oint_A \nabla\vec{d}\cdot\hat{\vec{n}}\,dA + (\lambda+G)\oint_A \bar{\varepsilon}_v\cdot\hat{\vec{n}}\,dA \qquad (1\text{-}78)$$

$\hat{\vec{n}}$ is a unit vector perpendicular to a control volume face and directed **out of** the control volume. When using the outward normal in Gauss theorem, we imply that material is flowing out of a domain. If a solid control volume decreases in size, its volumetric strain is defined as negative; we can think of the solid material as leaving the domain. Thus, in the derivations to follow, $\bar{\varepsilon}_v$ is assumed to be a negative value. We will now examine each term in eq. (1-78).

The Volumetric Strain Term

The average volumetric strain (the contribution to the volumetric strain at a face), $\bar{\varepsilon}_v$ can be written

$$\bar{\varepsilon}_v = \frac{\partial\bar{\alpha}}{\partial x} + \frac{\partial\bar{\beta}}{\partial y} = \nabla\cdot\vec{\bar{d}}$$

The average displacement vector $\vec{\bar{d}}$ is calculated as in Figure 52. The change in size of a control volume is governed by the following relation:

$$\varepsilon_v = \int_{cv} \nabla\cdot\vec{d}\,dV \qquad (1\text{-}79)$$

Performing Gauss theorem on (1-79) and using the relation $\hat{\vec{n}} = -(y_\eta, -x_\eta)/\oint_{face} dA$ leads to:

$$\bar{\varepsilon}_{\mathrm{v}} = \oint_{face} \vec{\bar{d}} \cdot \hat{\vec{n}}\, dA = \sum_{f=1}^{\#\text{ of faces}} \vec{\bar{d}} \cdot \vec{n}\Big|^{f}, \quad \text{where } \vec{\bar{d}} = \begin{pmatrix} \bar{\alpha} \\ \bar{\beta} \end{pmatrix}; \quad \vec{n} = -\begin{pmatrix} y_\eta \\ -x_\eta \end{pmatrix} \tag{1-80}$$

Here again, the bars have been introduced to indicate average values are calculated at the face. Carrying out the inner product (dot product) in eq. (1-80), we have:

$$-\sum_{f=1}^{\#\text{ of faces}} \begin{pmatrix} \bar{\alpha} & \bar{\beta} \end{pmatrix} \cdot \begin{pmatrix} y_\eta \\ -x_\eta \end{pmatrix} \Rightarrow \bar{\varepsilon}_{\mathrm{v}} = -\sum_{f=1}^{\#\text{ of faces}} \bar{\alpha} y_\eta - \bar{\beta} x_\eta \tag{1-81}$$

According to eq. (1-77), we need the gradient of the volumetric strain, ε_{v}. We apply Gauss theorem and obtain:

$$\int_{\mathrm{cv}} \nabla \bar{\varepsilon}_{\mathrm{v}} dV = \oint_{Face} \bar{\varepsilon}_{\mathrm{v}}\, \hat{\vec{n}}\, dA,$$

Because we are assuming $\bar{\varepsilon}_{\mathrm{v}}$ to be negative, in what follows, we will use the opposite value specified in (1-81). Again using the relation, $\hat{\vec{n}} = -\left(y_\eta, -x_\eta\right) / \oint_{face} dA$, we have for a given face:

$$\bar{\varepsilon}_{\mathrm{v}} (-1) \begin{pmatrix} y_\eta \\ -x_\eta \end{pmatrix} = \left(\bar{\alpha} y_\eta - \bar{\beta} x_\eta\right)(-1) \begin{pmatrix} y_\eta \\ -x_\eta \end{pmatrix} = \left(\bar{\alpha} y_\eta - \bar{\beta} x_\eta\right) \begin{pmatrix} -y_\eta \\ x_\eta \end{pmatrix} = \begin{pmatrix} -y_\eta \left[\bar{\alpha} y_\eta - \bar{\beta} x_\eta\right] \\ x_\eta \left[\bar{\alpha} y_\eta - \bar{\beta} x_\eta\right] \end{pmatrix}$$

The Diffusion Term, $G\nabla^2 d$

The discretized form of the diffusion term was derived in section 7.4.3:

$$-G \sum_{f=1}^{\#\text{ of faces}} \left[\frac{q_1}{\left|J^{-1}\right|} \Delta\phi_\xi - \frac{q_2}{\left|J^{-1}\right|} \Delta\phi_\eta \right]^{f},$$

where $q_1 = x_\xi + y_\xi$ and $q_2 = x_\xi x_\eta + y_\xi y_\eta$. Substituting the above relation with the approximated diffusion term, the final discretized form of the solid deformation equations are:

$$0 = -G \sum_{f=1}^{\#\text{ of faces}} \left[\frac{\left(\alpha_0 - \alpha_1\right)}{q_3} \left|J^{-1}\right| \right]^{f} - \left(\lambda + G\right) \sum_{f=1}^{\#\text{ of faces}} y_\eta \left(\bar{\alpha} y_\eta - \bar{\beta}\, x_\eta\right)\Big|^{f} \tag{1-82}$$

$$0 = -G \sum_{f=1}^{\#\text{ of faces}} \left[\frac{\left(\beta_0 - \beta_1\right)}{q_3} \left|J^{-1}\right| \right]^{f} + \left(\lambda + G\right) \sum_{f=1}^{\#\text{ of faces}} x_\eta \left(\bar{\alpha} y_\eta - \bar{\beta}\, x_\eta\right)\Big|^{f} \tag{1-83}$$

However, it is more convenient for programming to rewrite eqs. (1-82)-(1-83) with opposite signs. This is easily accomplished by multiplying each term by -1:

$$0 = G \sum_{f=1}^{\#\text{ of faces}} \left[\frac{(\alpha_0 - \alpha_1)}{q_3} \left| J^{-1} \right|^f \right] + (\lambda + G) \sum_{f=1}^{\#\text{ of faces}} y_\eta \left(\bar{\alpha} y_\eta - \bar{\beta}\ x_\eta \right)^f \tag{1-84}$$

$$0 = G \sum_{f=1}^{\#\text{ of faces}} \left[\frac{(\beta_0 - \beta_1)}{q_3} \left| J^{-1} \right|^f \right] - (\lambda + G) \sum_{f=1}^{\#\text{ of faces}} x_\eta \left(\bar{\alpha} y_\eta - \bar{\beta}\ x_\eta \right)^f \tag{1-85}$$

We can write eqs. (1-84) and (1-85) more explicitly:

$$0 = G \sum_{f=1}^{\#\text{ of faces}} \left[\frac{(\alpha_0 - \alpha_1)}{q_3} \left| J^{-1} \right|^f \right] + (\lambda + G) \sum_{f=1}^{\#\text{ of faces}} \left\{ 0.5 y_\eta^2 [\alpha_1] + 0.5 y_\eta^2 [\alpha_2] - 0.5 x_\eta y_\eta [\beta_1] - 0.5 x_\eta y_\eta [\beta_2] \right\} \tag{1-86}$$

$$0 = G \sum_{f=1}^{\#\text{ of faces}} \left[\frac{(\beta_0 - \beta_1)}{q_3} \left| J^{-1} \right|^f \right] + (\lambda + G) \sum_{f=1}^{\#\text{ of faces}} \left\{ -0.5 x_\eta y_\eta [\alpha_1] - 0.5 x_\eta y_\eta [\alpha_2] + 0.5 x_\eta^2 [\beta_1] + 0.5 x_\eta^2 [\beta_2] \right\} \tag{1-87}$$

In eqs. (1-86) and (1-87), the average values, $\bar{\alpha}$ and $\bar{\beta}$, have been replaced by the relations given in Figure 52. Equations (1-86) and (1-87) lead to a linear algebra problem which computes the displacement of each control volume. The new grid positions are then updated by averaging the displacements of neighboring cell centers.

7.7. Volumetric Strain as an Input/Boundary Condition for Solid Mechanics

7.7.1. Overview and Motivation

Typically, solid mechanics problems utilize displacement, force, or pressure conditions on the boundary of the solid body. For the vasculature-brain tissue interaction problem, we implement a volumetric strain boundary condition to simulate the effect of expanding cerebral vessels on the deformation of the surrounding brain tissue. To demonstrate the blood vessel-brain tissue interaction problem, consider a distensible tube surrounded by a deformable solid body with

pressure, p_{Solid} as in Figure 53. As fluid (or blood) pressure, p_{Tube} in the tube increases relative to p_{Solid}, the tube expands. In turn, the surrounding solid body deforms. One may therefore ask: To what extent is the solid body deformed, and how does one go about computing the deformation? This section seeks to address this question by presenting the governing equations for vessel dynamics and brain tissue motion.

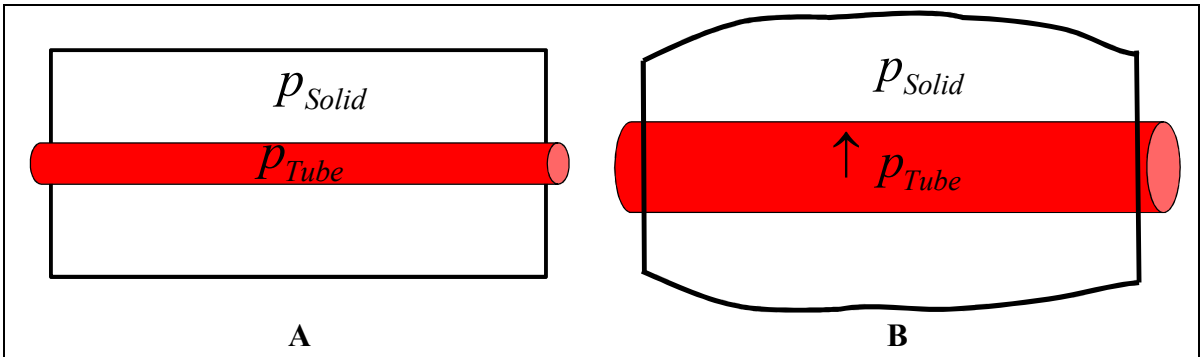

Figure 53. Frame A: Tube is at resting state and there is no solid body deformation. Frame B: Differences between fluid (or blood) pressure and surrounding increases and the tube expands. The tube expansion causes the surrounding solid body at pressure p_{Solid} to deform.

7.7.2. Blood Flow and Vessel Expansion Formulation

In our model of cerebral vasculature, each vessel is represented as a cylinder with a fixed length. Given these assumptions, eqs. (1-88)-(1-90) are applied to the model to compute blood pressure, blood flow, and vessel cross-sectional area at discrete time points during the cardiac cycle. Equation (1-88) is a mass conservation equation. Equation (1-89) is a simplified momentum balance for the vessel, and eq. (1-90) governs vessel expansion. The description of each symbol in eqs. (1-88)-(1-90) is provided in Table 13.

$$l_{vessel}\frac{A_{vessel}^{n}-A_{vessel}^{n-1}}{\Delta t}=f_{in}-f_{out} \tag{1-88}$$

$$p_{in}-p_{out}=\frac{8\pi\mu l_{vessel}}{\left(A_{vessel}^{n-1}\right)^{2}}f_{out} \tag{1-89}$$

$$p_{vessel} - p_{brain} = E_{vessel}\left(\frac{A^{n}_{vessel} - A^{o}_{vessel}}{A^{o}_{vessel}}\right) \tag{1-90}$$

Table 13: Definition of symbols in eqs. (1-88)-(1-90)

Symbol	Meaning
l_{vessel}	Vessel length
$A^{n}_{vessel}, A^{n-1}_{vessel}$	Vessel cross-sectional area at current time and previous time, respectively
A^{o}_{vessel}	Vessel cross-sectional area at zero transmural pressure
Δt	Time step size
f_{in}, f_{out}	Flow into and out of a given tube, respectively
p_{in}, p_{out}	Pressure at the inlet and outlet of a given tube, respectively
μ	Blood viscosity
p_{brain}	Brain tissue pressure
p_{vessel}	Vessel lumen pressure; defined by the average of p_{in} and p_{out}
E_{vessel}	Vessel stiffness

To illustrate how these equations can be applied to a vasculature network, consider the small vessel network shown in Figure 54. Labels P1, P2, and P3 stand for pressures at nodes 1, 2, and 3, respectively. Labels v1, v2, and v3 refer to specific segments (or vessels) of the network. In such a system, choices can be made regarding the boundary conditions. For example, one could choose to set the inflow at P1 and the pressures at P3 and P4. Alternatively, one could specify the inlet and outlet pressures and solve for all flows in the network. The latter is chosen for the example to follow.

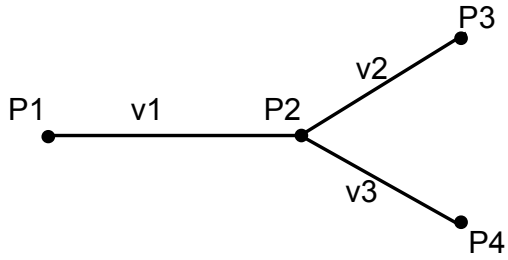

Figure 54. Small network to demonstrate blood flow and vessel expansion methodology.

For the example to follow, $p_{vessel} = \frac{p_{in} + p_{out}}{2} = 0.5p_{in} + 0.5p_{out}$

Example

In Figure 54, blood enters at P1 and exits the network at P3 and P4. The pressures are specified at P1, P3, and P4. In this example, there are 10 unknowns: A_{v1}^n, A_{v2}^n, A_{v3}^n, f_{in_v1}, f_{out_v1}, f_{in_v2}, f_{out_v2}, f_{in_v3}, f_{in_v3}, p_2. The constants, material parameters, boundary conditions, and initial conditions are:

Constants

Length of vessel 1: l_v1=0.02m
Length of vessel 2: l_v2=0.015m
Length of vessel 3: l_v3=0.015m

Material parameters

Blood viscosity: mu=0.003 kg/ms
Young's Modulus of blood vessel: E=1.6e6 N/m^2

Boundary conditions

P_{brain}=10,000 N/m^2
P1=16,000 N/m^2 (~120 mmHg)
P3=13,333 N/m^2 (~100 mmHg)
P4=13,333 N/m^2 (~100 mmHg)

Initial conditions

Cross-sectional area of tube 1: A_v1 = $\pi(0.005m)^2 \cong 7.854e-5$
Cross-sectional area of tube 2: A_v2 = $\pi(0.004m)^2 \cong 5.027e-5$
Cross-sectional area of tube 3: A_v3 = $\pi(0.004m)^2 = 5.027e-5$

The equations are set up as follows (unknowns have been brought to the left hand side; known values are on the right hand side):

Vessel 1

$$\frac{l_{v1}}{\Delta t} A_{v1}^n - f_{in\_v1} + f_{out\_v1} = \frac{l_{v1}}{\Delta t} A_{v1}^{n-1}$$

$$-\frac{8\pi\mu l_{v1}}{\left(A_{v1}^{n-1}\right)^2} f_{out\_v1} - p_2 = -p_1$$

$$-\frac{E}{A_{v1}^o} A_{v1}^n + 0.5 p_2 = -0.5 p_1 + p_{brain} - E$$

Vessel 2

$$\frac{l_{v2}}{\Delta t} A_{v2}^n - f_{in\_v2} + f_{out\_v2} = \frac{l_{v2}}{\Delta t} A_{v2}^{n-1}$$

$$-\frac{8\pi\mu l_{v2}}{\left(A_{v2}^{n-1}\right)^2} f_{out\_v2} + p_2 = p_3$$

$$-\frac{E}{A_{v2}^{o}} A_{v2}^{n} + 0.5 p_2 = -0.5 p_3 + p_{brain} - E$$

Vessel 3

$$\frac{l_{v3}}{\Delta t} A_{v3}^{n} - f_{in\_v3} + f_{out\_v3} = \frac{l_{v3}}{\Delta t} A_{v3}^{n-1}$$

$$-\frac{8\pi\mu l_{v3}}{\left(A_{v3}^{n-1}\right)^2} f_{out\_v3} + p_2 = p_4$$

$$-\frac{E}{A_{v3}^{o}} A_{v3}^{n} + 0.5 p_2 = -0.5 p_4 + p_{brain} - E$$

As one can see, there are only 9 equations above. However, we previously stated that there are 10 unknowns. Therefore, we need an additional equation. It is the tube junction law equation:

$$f_{out\_v1} = f_{in\_v2} + f_{in\_v3} \Rightarrow f_{out\_v1} - f_{in\_v2} - f_{in\_v3} = 0$$

This equation states that the flux out of vessel 1 is equal to the combined flux entering vessels 2 and 3. The equations can be put into matrix format and solved in Matlab. The Matlab script and the results for the parameters listed in the Matlab file are given below.

```
clc
clear all
format long e

l_v1=0.02; %[m]
l_v2=0.015; %[m]
l_v3=0.015; %[m]
mu=0.003; %[kg/(m*s)]
E = 1.6e6;%[N/(m^2)]
A_v1= pi*(0.005^2); %[m^2]
A_v2= pi*(0.004^2); %[m^2]
A_v3= pi*(0.004^2); %[m^2]
p_star = 10000; %[N/(m^2)]
deltaT = 0.25;
p1 = 16000;
p3 = 13333;
p4 = 13333;

Matrix = [l_v1/deltaT 0 0 -1 1 0 0 0 0 0
           0 0 0 0 -8*pi*mu*l_v1/((A_v1)^2) 0 0 0 0  -1
          -E/A_v1 0 0 0 0 0 0 0 0 0.5
          0 l_v2/deltaT 0 0 0 -1 1 0 0 0
          0 0 0 0 0 0 -8*pi*mu*l_v2/((A_v2)^2) 0 0    1
          0 -E/A_v2 0 0 0 0 0 0 0 0.5
          0 0 l_v3/deltaT 0 0 0 0 -1 1 0
          0 0 0 0 0 0 0 0 -8*pi*mu*l_v3/((A_v3)^2)    1
```

```
          0 0 -E/A_v3 0 0 0 0 0 0  0.5
          0   0  0  0 1 -1 0 -1 0 0];

TargetVector = [l_v1*A_v1/deltaT; -p1; -0.5*p1+p_star-E; l_v2*A_v2/deltaT; p3; -
0.5*p3+p_star-E; l_v3*A_v3/deltaT; p4; -0.5*p4+p_star-E; 0];

Result = Matrix\TargetVector
```

A_{v1}^{n} = 7.880016828035806e-005

A_{v2}^{n} =5.039021456139354e-005

A_{v3}^{n} = 5.039021456139354e-005

f_{in_v1} = 5.695415938288823e-003

f_{out_v1} = 5.695395110133574e-003

f_{in_v2} =2.847697555066784e-003

f_{out_v2} = 2.847690071140546e-003

f_{in_v3} =2.847697555066784e-003

f_{out_v3} = 2.847690071140546e-003

p_2 = 1.460769236279424e+004

These results are reasonable. All vessels expanded slightly, and as a result all outflow values for a given tube are a little less than what flowed into that tube. If the vessel stiffness were decreased, the expansion of the tubes would be larger and the outflow of each vessel would decrease.

7.7.3. The Relationship between a Vessel and a Brain Tissue Control Volume

Because the vessel lengths are constant throughout the simulation, the change in volume of a particular vessel, ΔV_{vessel}, is:

$$\Delta V_{vessel} = l\left(A^{n} - A^{n-1}\right) \tag{1-91}$$

The vessel volume change is then used to compute the volumetric strain of a particular control volume of the brain mesh using eq. (1-92):

$$\varepsilon_{\mathrm{v}}[\text{b.c.v.}] = \frac{\Delta V_{vessel}}{\text{Volume}[\text{b.c.v.}]} \tag{1-92}$$

b.c.v. stands for brain control volume. In a 2d application, Volume[b.c.v.] is the cell area. In general, the volume change of several vessels contributes to a particular brain control volume. As such, the equation above is placed in a program loop to accommodate contributions from all vessels contained in a given control volume. The general formula is given below.

$$\varepsilon_v[\text{b.c.v.}] = \varepsilon_v[\text{b.c.v.}] + \frac{\Delta V_{vessel}}{\text{Volume[b.c.v.]}}$$

The volume change of a given blood vessel will contribute to the volumetric strain of a particular brain control volume if the center of the vessel lies in that particular control volume. In other words, if the center of vessel *i* lies in the space defined by control volume *j*, then the volume change of vessel *i* will contribute to the volumetric strain of control volume *j*. To better illustrate, Figure 55 considers a case in which the center of a blood vessel lies in one of the brain tissue control volumes. Since there is only one blood vessel in V5, and the center of the vessel lies within V5, the volume change of the vessel will lead to volumetric strain in V5.

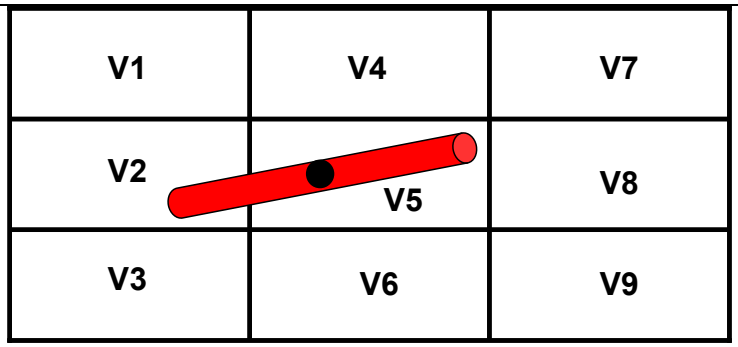

Figure 55. A computational mesh which contains one blood vessel. The center of the vessel (black dot) lies in the control volume labeled V5. Thus, when the vessel expands, its volume change will contribute to the volumetric strain of V5.

7.7.4. Linking the Vasculature Mesh with the Brain Mesh

Because the meshes are developed separately from one another, the vasculature mesh is completely independent of the brain mesh. To associate the volume change of a vessel with a particular brain control volume, a search algorithm was developed to link individual vessels with

brain control volumes in which the vessel's center resided. Equation (1-93) was used to calculate the vessel's center with vessel begin point (x_1, y_1) and end point (x_2, y_2):

$$\text{Vessel Center} = \left(\frac{x_1 + x_2}{2}, \frac{y_1 + y_2}{2} \right) \tag{1-93}$$

A search was then performed over all brain control volumes to determine whether the vessel's center resided in the currently tested brain control volume. The control volumes are labeled 1 through *high*, where *high* is the total number of internal control volumes. The center of vessel 1 is tested first to see whether it lies in control volume 1 of the brain mesh. To accomplish this, the control volume was divided into upper and lower triangles as shown in Figure 56.

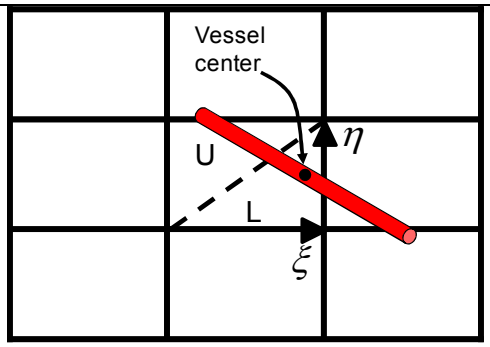

Figure 56. A sample quadrilateral control volume (center cell) that has been divided into an upper (U) and a lower (L) triangle. If the vessel center lies in the control volume, ξ and η will be greater or equal to zero, and the sum of ξ and η will be less than or equal to one. Incidentally, if the brain mesh were to contain triangular elements as opposed to quadrilaterals the search would be easier because the search space would be a triangle at the outset.

If the vessel center did not lie in the upper triangle, the lower triangle was then tested. If it was determined that the vessel center did not lie in either the upper or lower triangle, the vessel center was tested in the next higher labeled brain control volume. This search algorithm uses the same math used to generate random points in the vasculature generation algorithm. The math is thoroughly described in (Sweetman, Linninger et al. 2010) but also provided in the Appendix for

ease of reference. In the search algorithm, instead of specifying ξ and η to generate a random point within a given control volume, we solve for ξ and η. The algorithm begins by setting one of the control volume vertices as the origin while the other two points are used to establish two vectors which are parameterized in ξ and η. If the vessel center lies in the control volume, ξ and η will be greater or equal to zero, and the sum of ξ and η will be less than or equal to one. This method requires a linear algebra problem with the following components:

$$\text{Target Vector}=\begin{pmatrix} x \text{ Coordinate of Vessel Center} - x \text{ Coordinate of Origin} \\ y \text{ Coordinate of Vessel Center} - y \text{ Coordinate of Origin} \end{pmatrix}$$

$$\text{Jacobian} = \begin{pmatrix} V_{1x} & V_{2x} \\ V_{1y} & V_{2y} \end{pmatrix}$$

7.7.5. Computing the Deformation of the Grid with Volumetric Strain as Input

This section includes an example of how to calculate brain tissue displacement when the volumetric strains in all control volumes are known. Before introducing the example problem, the governing equation for solid body motion due to volumetric strain input is presented.

The governing equation for volumetric strain input is similar to that used in section 7.6. We begin by reintroducing eq. (1-75), written again here for convenience.

$$0 = G\nabla^2\vec{d} + (\lambda + G)\nabla\varepsilon_{\mathrm{v}} \tag{1-94}$$

Integrating each term over a control volume we have:

$$0 = G\int_{CV} \nabla^2\vec{d}\, dV + (\lambda + G)\int_{CV} \nabla\varepsilon_{\mathrm{v}}\, dV \tag{1-95}$$

Applying Gauss theorem leads to:

$$0 = G\int_{A} \nabla\vec{d}\cdot\hat{\vec{n}}\, dA + (\lambda + G)\int_{A} \varepsilon_{\mathrm{v}}\,\hat{\vec{n}}\, dA \tag{1-96}$$

As in section 7.6, ε_v is treated as a negative-valued scalar in the derivation. Let us therefore replace ε_v with $-|\varepsilon_v|$ Eq. (1-96) leads to two equations for the 2D case:

$$0 = G\int_A \nabla\alpha\cdot(-1)\begin{pmatrix} y_\eta \\ -x_\eta \end{pmatrix} / \sqrt{x_\eta^2 + y_\eta^2}\, dA + (\lambda + G)\int_A -|\varepsilon_v|(-y_\eta) / \sqrt{x_\eta^2 + y_\eta^2}\, dA \tag{1-97}$$

$$0 = G\int_A \nabla\beta\cdot(-1)\begin{pmatrix} y_\eta \\ -x_\eta \end{pmatrix} / \sqrt{x_\eta^2 + y_\eta^2}\, dA + (\lambda + G)\int_A -|\varepsilon_v|(x_\eta) / \sqrt{x_\eta^2 + y_\eta^2}\, dA \tag{1-98}$$

We can distribute the minus sign out of the integral to arrive at:

$$0 = -G\int_A \nabla\alpha\cdot\begin{pmatrix} y_\eta \\ -x_\eta \end{pmatrix} / \sqrt{x_\eta^2 + y_\eta^2}\, dA + (\lambda + G)\int_A |\varepsilon_v|(y_\eta) / \sqrt{x_\eta^2 + y_\eta^2}\, dA \tag{1-99}$$

$$0 = -G\int_A \nabla\beta\cdot\begin{pmatrix} y_\eta \\ -x_\eta \end{pmatrix} / \sqrt{x_\eta^2 + y_\eta^2}\, dA - (\lambda + G)\int_A |\varepsilon_v|(x_\eta) / \sqrt{x_\eta^2 + y_\eta^2}\, dA \tag{1-100}$$

For the example that follows, it is easier to rewrite eqs. (1-99) and (1-100) as:

$$0 = G\int_A \nabla\alpha\cdot\begin{pmatrix} y_\eta \\ -x_\eta \end{pmatrix} / \sqrt{x_\eta^2 + y_\eta^2}\, dA - (\lambda + G)\int_A \varepsilon_v(y_\eta) / \sqrt{x_\eta^2 + y_\eta^2}\, dA \tag{1-101}$$

$$0 = G\int_A \nabla\beta\cdot\begin{pmatrix} y_\eta \\ -x_\eta \end{pmatrix} / \sqrt{x_\eta^2 + y_\eta^2}\, dA + (\lambda + G)\int_A \varepsilon_v(x_\eta) / \sqrt{x_\eta^2 + y_\eta^2}\, dA \tag{1-102}$$

Finally, in generalized coordinates, the discretized equations are:

$$0 = G\sum_{f=1}^{\#\text{ of faces}} \frac{\alpha_0 - \alpha_1}{q_3}\left|J^{-1}\right|^f - (\lambda + G)\sum_{f=1}^{\#\text{ of faces}} \varepsilon_v(y_\eta)\Big|^f \tag{1-103}$$

$$0 = G\sum_{f=1}^{\#\text{ of faces}} \frac{\beta_0 - \beta_1}{q_3}\left|J^{-1}\right|^f + (\lambda + G)\sum_{f=1}^{\#\text{ of faces}} \varepsilon_v(x_\eta)\Big|^f \tag{1-104}$$

Example

This example shows how to calculate solid body deformation due to volumetric strain input. Figure 57 shows the computational grid.

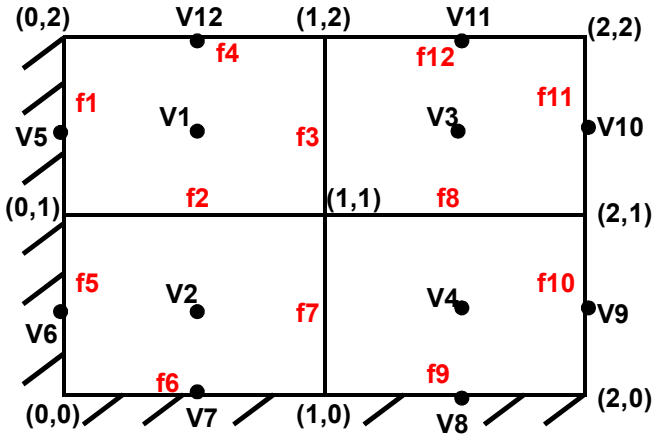

Figure 57. Computational grid used for calculating solid body deformation due to volumetric strain input. The control volumes are labeled V1 through V12 with the control volume center indicated by a black dot. Grid faces are labeled in red, f1 through f12. The diagonal lines along f1, f5, f6, and f9 indicate the body is fixed on those faces.

Description of Boundary Conditions

- Faces 1, 5, 6, and 9 are fixed. As a consequence, the displacement vector for volumes 5, 6, 7, and 8 are set to zero (see boundary equations later on in this example).

- Faces 4, 12, 11, and 10 are free to be displaced. The displacement vector for volumes 12, 11, 10, and 9 will be set as follows:

  The displacement vector of volume 12 is set equal to the displacement vector of volume 1.

  The displacement vector of volume 11 and volume 10 are set equal to the displacement vector of volume 3.

  The displacement vector of volume 9 is set equal to the displacement vector of volume 4.

  Though different choices could be made regarding the displacement of vols 12, 11, 10, and 9, I believe this is probably the simplest choice.

- In this problem, only volume 3 will have a volumetric strain input—its value is 0.4. All other volumes will have zero volumetric strain input.

Metrics Table

It is convenient to set-up a table that includes the face and cell metrics. Recall that $q_3 = x_\xi^2 + y_\xi^2$ and $\left|J^{-1}\right| = x_\xi y_\eta - x_\eta y_\xi$.

Volume	Face	x_ξ	y_ξ	x_η	y_η	q_3	$\left\|J^{-1}\right\|$
1	f1	0.5	0	0	1	0.25	0.5
	f2	0	1	-1	0	1	1
	f3	-1	0	0	-1	1	1
	f4	0	-0.5	1	0	0.25	0.5
2	f5	0.5	0	0	1	0.25	0.5
	f6	0	0.5	-1	0	0.25	0.5
	f7	-1	0	0	-1	1	1
	f2	0	-1	1	0	1	1
3	f3	1	0	0	1	1	1
	f8	0	1	-1	0	1	1
	f11	-0.5	0	0	-1	0.25	0.5
	f12	0	-0.5	1	0	0.25	0.5
4	f7	1	0	0	1	1	1
	f9	0	0.5	-1	0	0.25	0.5
	f10	-0.5	0	0	-1	0.25	0.5
	f8	0	-1	1	0	1	1

Important Note for Equation Set-up Below: Since the volumetric strain is required at the face, averages are used to obtain the face value. Note also, that for boundaries, the face value is provided as a boundary condition. Thus, instead of using an average for the boundary faces, the value at the face (provided from the boundary condition) is used.

Equations

Volume 1, α

$$G\left[\frac{\alpha_1-\alpha_5}{0.25}(0.5)+\frac{\alpha_1-\alpha_2}{1}(1)+\frac{\alpha_1-\alpha_3}{1}(1)+\frac{\alpha_1-\alpha_{12}}{0.25}(0.5)\right]...$$

$$-(\lambda+G)\left[\varepsilon_{v5}(1)+\frac{\varepsilon_{v1}+\varepsilon_{v2}}{2}(0)+\frac{\varepsilon_{v1}+\varepsilon_{v3}}{2}(-1)+\varepsilon_{v12}(0)\right]$$

Volume 1, β

$$G\left[\frac{\beta_1-\beta_5}{0.25}(0.5)+\frac{\beta_1-\beta_2}{1}(1)+\frac{\beta_1-\beta_3}{1}(1)+\frac{\beta_1-\beta_{12}}{0.25}(0.5)\right]...$$

$$+(\lambda+G)\left[\varepsilon_{v5}(0)+\frac{\varepsilon_{v1}+\varepsilon_{v2}}{2}(-1)+\frac{\varepsilon_{v1}+\varepsilon_{v3}}{2}(0)+\varepsilon_{v12}(1)\right]$$

Volume 2, α

$$G\left[\frac{\alpha_2-\alpha_6}{0.25}(0.5)+\frac{\alpha_2-\alpha_7}{0.25}(0.5)+\frac{\alpha_2-\alpha_4}{1}(1)+\frac{\alpha_2-\alpha_1}{1}(1)\right]...$$

$$-(\lambda+G)\left[\varepsilon_{v6}(1)+\varepsilon_{v7}(0)+\frac{\varepsilon_{v2}+\varepsilon_{v4}}{2}(-1)+\frac{\varepsilon_{v2}+\varepsilon_{v1}}{2}(0)\right]$$

Volume 2, β

$$G\left[\frac{\beta_2-\beta_6}{0.25}(0.5)+\frac{\beta_2-\beta_7}{0.25}(0.5)+\frac{\beta_2-\beta_4}{1}(1)+\frac{\beta_2-\beta_1}{1}(1)\right]...$$

$$+\left(\lambda+G\right)\left[\varepsilon_{v6}(0)+\varepsilon_{v7}(-1)+\frac{\varepsilon_{v2}+\varepsilon_{v4}}{2}(0)+\frac{\varepsilon_{v2}+\varepsilon_{v1}}{2}(1)\right]$$

Volume 3, α

$$G\left[\frac{\alpha_3-\alpha_1}{1}(1)+\frac{\alpha_3-\alpha_4}{1}(1)+\frac{\alpha_3-\alpha_{10}}{0.25}(0.5)+\frac{\alpha_3-\alpha_{11}}{0.25}(0.5)\right]...$$

$$-\left(\lambda+G\right)\left[\frac{\varepsilon_{v3}+\varepsilon_{v1}}{2}(1)+\frac{\varepsilon_{v3}+\varepsilon_{v4}}{2}(0)+\frac{\varepsilon_{v3}+\varepsilon_{v10}}{2}(-1)+\frac{\varepsilon_{v3}+\varepsilon_{v11}}{2}(0)\right]$$

Volume 3, β

$$G\left[\frac{\beta_3-\beta_1}{1}(1)+\frac{\beta_3-\beta_4}{1}(1)+\frac{\beta_3-\beta_{10}}{0.25}(0.5)+\frac{\beta_3-\beta_{11}}{0.25}(0.5)\right]...$$

$$+\left(\lambda+G\right)\left[\frac{\varepsilon_{v3}+\varepsilon_{v1}}{2}(0)+\frac{\varepsilon_{v3}+\varepsilon_{v4}}{2}(-1)+\frac{\varepsilon_{v3}+\varepsilon_{v10}}{2}(0)+\frac{\varepsilon_{v3}+\varepsilon_{v11}}{2}(1)\right]$$

Volume 4, α

$$G\left[\frac{\alpha_4-\alpha_2}{1}(1)+\frac{\alpha_4-\alpha_8}{0.25}(0.5)+\frac{\alpha_4-\alpha_9}{0.25}(0.5)+\frac{\alpha_4-\alpha_3}{1}(1)\right]...$$

$$-\left(\lambda+G\right)\left[\frac{\varepsilon_{v4}+\varepsilon_{v2}}{2}(1)+\frac{\varepsilon_{v4}+\varepsilon_{v8}}{2}(0)+\frac{\varepsilon_{v4}+\varepsilon_{v9}}{2}(-1)+\frac{\varepsilon_{v4}+\varepsilon_{v3}}{2}(0)\right]$$

Volume 4, β

$$G\left[\frac{\beta_4-\beta_2}{1}(1)+\frac{\beta_4-\beta_8}{0.25}(0.5)+\frac{\beta_4-\beta_9}{0.25}(0.5)+\frac{\beta_4-\beta_3}{1}(1)\right]...$$

$$+\left(\lambda+G\right)\left[\frac{\varepsilon_{v4}+\varepsilon_{v2}}{2}(0)+\frac{\varepsilon_{v4}+\varepsilon_{v8}}{2}(-1)+\frac{\varepsilon_{v4}+\varepsilon_{v9}}{2}(0)+\frac{\varepsilon_{v4}+\varepsilon_{v3}}{2}(1)\right]$$

Boundary Equations, α

$\alpha_5=0;\ \alpha_6=0;\ \alpha_7=0;\ \alpha_8=0;$

$\alpha_9=\alpha_4;\ \alpha_{10}=\alpha_3;\ \alpha_{11}=\alpha_3;\ \alpha_{12}=\alpha_1$

Boundary Equations, β

$\beta_5=0;\ \beta_6=0;\ \beta_7=0;\ \beta_8=0;$

$\beta_9=\beta_4;\ \beta_{10}=\beta_3;\ \beta_{11}=\beta_3;\ \beta_{12}=\beta_1$

The equations for volumes 1-4 will now be put in a more transparent form

Volume 1, α

$$G\left[2\left(\alpha_1-\alpha_5\right)+\alpha_1-\alpha_2+\alpha_1-\alpha_3+2\left(\alpha_1-\alpha_{12}\right)\right]-\left(\lambda+G\right)\left[-0.2\right]=0$$

$$\Rightarrow 6G\alpha_1-G\alpha_2-G\alpha_3-2G\alpha_5-2G\alpha_{12}=-192.308$$

Volume 1, β

$$G\left[2\left(\beta_1-\beta_5\right)+\beta_1-\beta_2+\beta_1-\beta_3+2\left(\beta_1-\beta_{12}\right)\right]=0$$

$$\Rightarrow 6G\beta_1-G\beta_2-G\beta_3-2G\beta_5-2G\beta_{12}=0$$

Volume 2, α

$$G\left[2\left(\alpha_2-\alpha_6\right)+2\left(\alpha_2-\alpha_7\right)+\alpha_2-\alpha_4+\alpha_2-\alpha_1\right]=0$$

$$\Rightarrow -G\alpha_1+6G\alpha_2-G\alpha_4-2G\alpha_6-2G\alpha_7=0$$

Volume 2, β

$$G\left[2\left(\beta_2-\beta_6\right)+2\left(\beta_2-\beta_7\right)+\beta_2-\beta_4+\beta_2-\beta_1\right]=0$$

$$\Rightarrow -G\beta_1+6G\beta_2-G\beta_4-2G\beta_6-2G\beta_7=0$$

Volume 3, α

$$G\left[\alpha_3-\alpha_1+\alpha_3-\alpha_4+2\left(\alpha_3-\alpha_{10}\right)+2\left(\alpha_3-\alpha_{11}\right)\right]=0$$

$$\Rightarrow -G\alpha_1+6G\alpha_3-G\alpha_4-2G\alpha_{10}-2G\alpha_{11}=0$$

Volume 3, β

$$G\left[\beta_3-\beta_1+\beta_3-\beta_4+2\left(\beta_3-\beta_{10}\right)+2\left(\beta_3-\beta_{11}\right)\right]=0$$

$$\Rightarrow -G\beta_1+6G\beta_3-G\beta_4-2G\beta_{10}-2G\beta_{11}=0$$

Volume 4, α

$$G\left[\alpha_4-\alpha_2+2\left(\alpha_4-\alpha_8\right)+2\left(\alpha_4-\alpha_9\right)+\alpha_4-\alpha_3\right]=0$$

$$\Rightarrow -G\alpha_2-G\alpha_3+6G\alpha_4-2G\alpha_8-2G\alpha_9=0$$

Volume 4, β

$$G\left[\beta_4-\beta_2+2\left(\beta_4-\beta_8\right)+2\left(\beta_4-\beta_9\right)+\beta_4-\beta_3\right]+\left(\lambda+G\right)\left[0.2\right]=0$$

$$\Rightarrow -G\beta_2-G\beta_3+6G\beta_4-2G\beta_8-2G\beta_9=-192.308$$

Let's Review. We have the following set of equations:

$$6G\alpha_1 - G\alpha_2 - G\alpha_3 - 2G\alpha_5 - 2G\alpha_{12} = -192.308$$
$$-G\alpha_1 + 6G\alpha_2 - G\alpha_4 - 2G\alpha_6 - 2G\alpha_7 = 0$$
$$-G\alpha_1 + 6G\alpha_3 - G\alpha_4 - 2G\alpha_{10} - 2G\alpha_{11} = 0$$
$$-G\alpha_2 - G\alpha_3 + 6G\alpha_4 - 2G\alpha_8 - 2G\alpha_9 = 0$$
$$\alpha_5 = 0$$
$$\alpha_6 = 0$$
$$\alpha_7 = 0$$
$$\alpha_8 = 0$$
$$\alpha_9 - \alpha_4 = 0$$
$$\alpha_{10} - \alpha_3 = 0$$
$$\alpha_{11} - \alpha_3 = 0$$
$$\alpha_{12} - \alpha_1 = 0$$
$$6G\beta_1 - G\beta_2 - G\beta_3 - 2G\beta_5 - 2G\beta_{12} = 0$$
$$-G\beta_1 + 6G\beta_2 - G\beta_4 - 2G\beta_6 - 2G\beta_7 = 0$$
$$-G\beta_1 + 6G\beta_3 - G\beta_4 - 2G\beta_{10} - 2G\beta_{11} = 0$$
$$-G\beta_2 - G\beta_3 + 6G\beta_4 - 2G\beta_8 - 2G\beta_9 = -192.308$$
$$\beta_5 = 0$$
$$\beta_6 = 0$$
$$\beta_7 = 0$$
$$\beta_8 = 0$$
$$\beta_9 - \beta_4 = 0$$
$$\beta_{10} - \beta_3 = 0$$
$$\beta_{11} - \beta_3 = 0$$
$$\beta_{12} - \beta_1 = 0$$

The equations for α can be rewritten in matrix format as:

$$\begin{bmatrix} 6G & -G & -G & 0 & -2G & 0 & 0 & 0 & 0 & 0 & 0 & -2G \\ -G & 6G & 0 & -G & 0 & -2G & -2G & 0 & 0 & 0 & 0 & 0 \\ -G & 0 & 6G & -G & 0 & 0 & 0 & 0 & 0 & -2G & -2G & 0 \\ 0 & -G & -G & 6G & 0 & 0 & 0 & -2G & -2G & 0 & 0 & 0 \\ 0 & 0 & 0 & 0 & 1 & 0 & 0 & 0 & 0 & 0 & 0 & 0 \\ 0 & 0 & 0 & 0 & 0 & 1 & 0 & 0 & 0 & 0 & 0 & 0 \\ 0 & 0 & 0 & 0 & 0 & 0 & 1 & 0 & 0 & 0 & 0 & 0 \\ 0 & 0 & 0 & 0 & 0 & 0 & 0 & 1 & 0 & 0 & 0 & 0 \\ 0 & 0 & 0 & -1 & 0 & 0 & 0 & 0 & 1 & 0 & 0 & 0 \\ 0 & 0 & -1 & 0 & 0 & 0 & 0 & 0 & 0 & 1 & 0 & 0 \\ 0 & 0 & -1 & 0 & 0 & 0 & 0 & 0 & 0 & 0 & 1 & 0 \\ -1 & 0 & 0 & 0 & 0 & 0 & 0 & 0 & 0 & 0 & 0 & 1 \end{bmatrix} \begin{pmatrix} \alpha_1 \\ \alpha_2 \\ \alpha_3 \\ \alpha_4 \\ \alpha_5 \\ \alpha_6 \\ \alpha_7 \\ \alpha_8 \\ \alpha_9 \\ \alpha_{10} \\ \alpha_{11} \\ \alpha_{12} \end{pmatrix} = \begin{pmatrix} -192.308 \\ 0 \\ 0 \\ 0 \\ 0 \\ 0 \\ 0 \\ 0 \\ 0 \\ 0 \\ 0 \\ 0 \end{pmatrix}$$

Similarly, the equations for β can be rewritten in matrix format as:

$$\begin{bmatrix} 6G & -G & -G & 0 & -2G & 0 & 0 & 0 & 0 & 0 & 0 & -2G \\ -G & 6G & 0 & -G & 0 & -2G & -2G & 0 & 0 & 0 & 0 & 0 \\ -G & 0 & 6G & -G & 0 & 0 & 0 & 0 & 0 & -2G & -2G & 0 \\ 0 & -G & -G & 6G & 0 & 0 & 0 & -2G & -2G & 0 & 0 & 0 \\ 0 & 0 & 0 & 0 & 1 & 0 & 0 & 0 & 0 & 0 & 0 & 0 \\ 0 & 0 & 0 & 0 & 0 & 1 & 0 & 0 & 0 & 0 & 0 & 0 \\ 0 & 0 & 0 & 0 & 0 & 0 & 1 & 0 & 0 & 0 & 0 & 0 \\ 0 & 0 & 0 & 0 & 0 & 0 & 0 & 1 & 0 & 0 & 0 & 0 \\ 0 & 0 & 0 & -1 & 0 & 0 & 0 & 0 & 1 & 0 & 0 & 0 \\ 0 & 0 & -1 & 0 & 0 & 0 & 0 & 0 & 0 & 1 & 0 & 0 \\ 0 & 0 & -1 & 0 & 0 & 0 & 0 & 0 & 0 & 0 & 1 & 0 \\ -1 & 0 & 0 & 0 & 0 & 0 & 0 & 0 & 0 & 0 & 0 & 1 \end{bmatrix} \begin{pmatrix} \beta_1 \\ \beta_2 \\ \beta_3 \\ \beta_4 \\ \beta_5 \\ \beta_6 \\ \beta_7 \\ \beta_8 \\ \beta_9 \\ \beta_{10} \\ \beta_{11} \\ \beta_{12} \end{pmatrix} = \begin{pmatrix} 0 \\ 0 \\ 0 \\ -192.308 \\ 0 \\ 0 \\ 0 \\ 0 \\ 0 \\ 0 \\ 0 \\ 0 \end{pmatrix}$$

Important Note: In the official implementation, one should not break up the alpha and beta equations into two separate matrices. It happens to work in this case because alpha and beta are decoupled—the grid is completely orthogonal. Once the grid deforms, the grid is no longer orthogonal and as a consequence, alpha and beta unknowns would appear together in a single equation.

This Concludes the Example Problem.

7.8. Summary of Methods and Computational Results for the Comprehensive Vasculature-Brain-CSF Model

7.8.1. Methods

This section provides an overview of model development, governing equations, boundary conditions, initial conditions, and material properties of vasculature, brain tissue, and CSF. The required steps for obtaining the brain and CSF computational domains are presented first. Next, boundary conditions and governing equations of CSF and brain tissue motion are described. Finally, the process of obtaining the computational domain of cerebral vasculature is explained, followed by a description of the governing equations and boundary conditions for vessel-tissue interaction. The section concludes with a summary of the overall solution strategy.

Development of Brain and CSF Computational Domains. The brain and CSF domains were obtained by selecting a domain of interest from an artery atlas of the human brain (Salamon and Corbaz 1971). An image from the atlas, shown in Figure 58A, was chosen so that major regions of the CSF pathway could be included in the study, such as the ventricles, aqueduct of Sylvius, pontine cistern, and subarachnoid space (SAS).

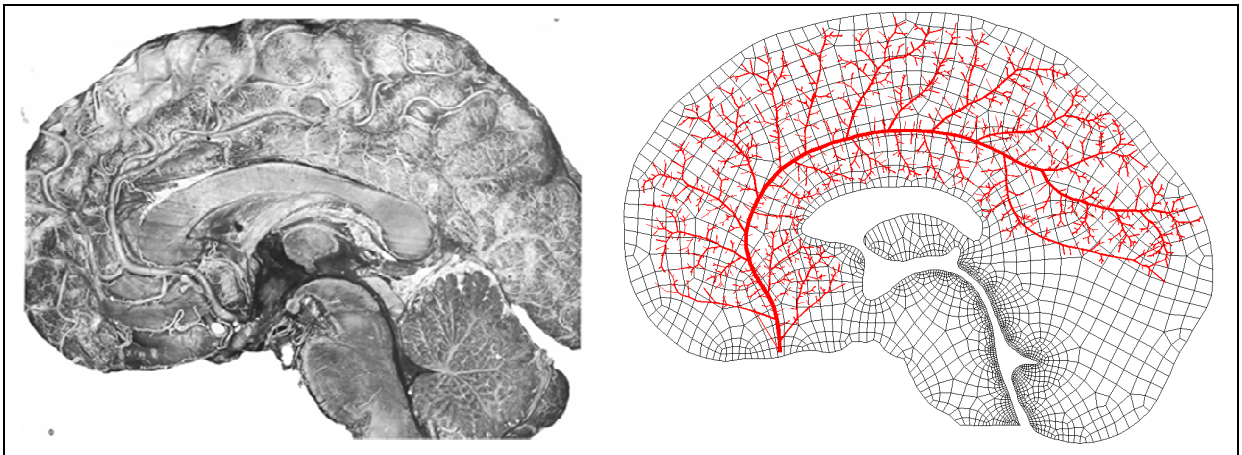

A **B**

Figure 58. (A) Mid-sagittal histological image of the human brain used to develop the two-dimensional model of brain, vasculature, and CSF interaction (Salamon and Corbaz 1971). (B) Computer-generated model of a simplified cerebral vasculature network.

The image was imported into Image J (http://rsbweb.nih.gov/ij/), where points that delineated the brain tissue and CSF spaces were selected. These points were then imported into grid generation software, Gambit 2.4.6. In Gambit, the surface points were connected using a combination of non-uniform rational basis splines (NURBS) and straight edges. After creating all edges, two logically connected and closed regions representing brain tissue and CSF were generated. The two regions were then discretized into quadrilateral control volumes using an unstructured grid meshing algorithm in Gambit. The computational domains of brain tissue and CSF are shown in Figure 59.

CSF and Brain Tissue Boundary Conditions. After meshing the CSF and brain domains, boundary conditions were applied to the model. For the fluid, a zero velocity (*no-slip*) boundary condition was applied to fixed walls and a kinematic boundary condition was applied to boundaries in which motion was possible along brain-CSF interfaces. The kinematic boundary condition is represented mathematically in eq. (1-105).

$$\vec{u}_{CSF} = \dot{\vec{d}}_{Brain} \tag{1-105}$$

Equation (1-105) states that the CSF velocity, $\vec{u}_{CSF}$, at a moving boundary is equal to the velocity of the moving boundary. The velocity of the moving boundary is represented by the time derivative of the brain tissue displacement, $\dot{\vec{d}}_{Brain}$. As indicated in Figure 59B, a Neumann boundary condition for the velocity, $\partial\vec{u} / \partial\vec{n} = 0$, was applied at the outlet of the CSF domain. This boundary condition sets the velocity at the boundary equal to the velocity at the adjacent interior control volume. Also at the outlet, a Dirichlet boundary condition for the pressure was applied and set to 500 Pa (Linninger, Sweetman et al. 2009). Along all other fluid boundaries, Neumann boundary conditions for pressure, $\partial p / \partial\vec{n} = 0$, were applied.

For the brain tissue, Neumann boundary conditions for tissue displacement were applied along the upper wall of the lateral ventricle and at the base of the brain near the pontine cistern. These locations constituted boundaries at which motion could occur along the brain-CSF interface. The Neumann boundary condition for displacement, $\partial\vec{d} / \partial\vec{n} = 0$, sets the brain tissue displacement at the boundary equal to the displacement at the adjacent interior control volume. Our choice of where to place Neumann boundary conditions in the brain tissue was based on prior research which indicates that ventricular wall motion and large arterial expansion near the base of the brain drives pulsatile CSF flow (Linninger, Sweetman et al. 2009; Sweetman and Linninger 2011; Sweetman, Xenos et al. 2011). Along all other brain boundaries, Dirichlet boundary conditions of $\vec{d}(t) = 0$ were applied.

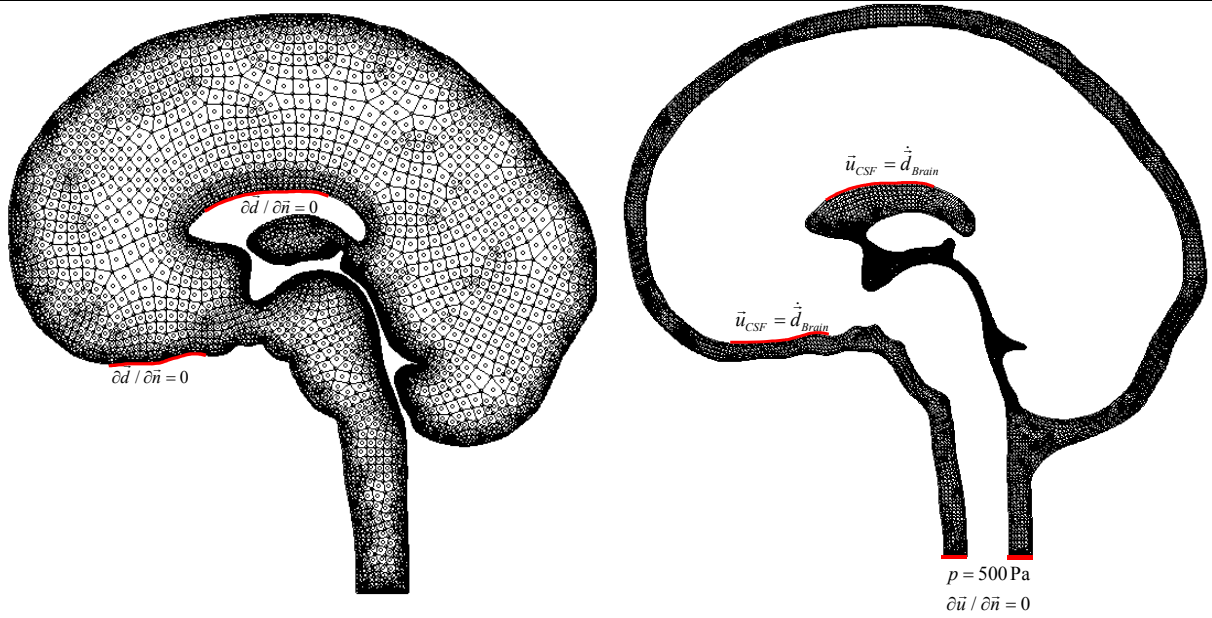

Figure 59. Computational domains of brain tissue and CSF. (A) Neumann boundary conditions for tissue displacement are indicated at the top of the lateral ventricle and near the pontine cistern. All other boundaries of the brain domain are fixed in space throughout the simulation. (B) In the fluid domain, kinematic boundary conditions are specified at the top of the lateral ventricle and near the pontine cistern. A Neumann boundary condition for fluid velocity and a Dirichlet boundary condition for fluid pressure are specified at the outlet of the CSF domain. All other fluid boundaries were given a *no-slip* condition for velocity and a Neumann boundary condition for pressure.

CSF Material Properties and Governing Equations. CSF was modeled as an incompressible, Newtonian fluid. Since CSF is mainly water with the exception of a small percentage of plasma proteins, we have set the density and viscosity of CSF to 1,000kg/m^3 and 0.001Pa$\cdot$s, respectively. In a non-deformable fluid domain, fluid motion is governed by the Navier-Stokes equations written in an Eulerian reference frame, as in eqs. (1-106) and (1-107).

$$\textit{Continuity} \qquad \nabla \cdot \vec{u} = 0 \qquad (1\text{-}106)$$

$$\textit{Momentum} \qquad \rho \frac{\partial \vec{u}}{\partial t} = -\nabla p - \rho \vec{u} \cdot \nabla \vec{u} + \mu \nabla \cdot \left(\nabla \vec{u} \right) \qquad (1\text{-}107)$$

In (1-106) and (1-107), $\vec{u}$, ρ, p, and μ are the fluid velocity, density, pressure, and viscosity, respectively. In the real brain, the CSF space deforms due to displacement along the brain-CSF

interface. To account for the relative motion of CSF and the underlying CSF mesh, the governing flow equations are recast in an Arbitrary-Lagrangian-Eulerian (ALE) reference frame.

Continuity-ALE
$$\frac{d}{dt}\int_V dV + \int_A (\vec{u} - \vec{u}_g)\, d\vec{A} = 0 \tag{1-108}$$

Momentum-ALE
$$\rho\int_V \frac{\partial \vec{u}}{\partial t} dV = -\int_V \nabla p\, dV - \rho\int_V \left(\vec{u} - \vec{u}_g\right)\cdot\left(\nabla \vec{u}\right) dV + \mu\int_V \nabla\cdot\left(\nabla \vec{u}\right) dV \tag{1-109}$$

The new symbol introduced in eqs. (1-108)-(1-109) is $\vec{u}_g$, the grid velocity. The grid velocity was calculated using the formula derived in (Demirdzic and Peric 1990), which ensures that the Space Conservation Law (SCL) is satisfied. The SCL prevents grid motion from leading to artificial mass sources (Demirdzic and Peric 1988; Demirdzic and Peric 1990; Ferziger and Peric 2002). The mathematical representation of the SCL is given in eq. (1-110).

Space Conservation Law
$$\frac{d}{dt}\int_V dV - \int_A \vec{u}_g \cdot d\vec{A} = 0 \tag{1-110}$$

Equation (1-110) states that for a given control volume in a given time interval, the divergence of the grid velocity must equal the volume change of that control volume.

Equations (1-108)-(1-110) imply the existence of an underlying fluid mesh motion scheme. We govern fluid mesh motion with the steady-state equations of solid body displacement given in eq. (1-111). This technique follows the same strategy proposed by (Souli and Zolesio 2001). However, we implement a linear elastic model and use a finite volume spatial discretization technique.

$$0 = G_f \nabla^2 \vec{d}_f + \left(\lambda_f + G_f\right)\nabla\left(\nabla\cdot\vec{d}_f\right) \tag{1-111}$$

In eq. (1-111), G_f and λ_f are Lame constants and $\vec{d}_f$ is the fluid grid displacement. The value of G_f affects the shearing motion of the internal fluid grid, whereas λ_f affects the compressibility of the fluid control volumes. For the fluid grid, G_f is set to 1,000 N/m^2. λ_f can be determined from eq. (1-112) using G_f and the Poisson ratio, v which was set to 0.3. The values of G_f and v were determined empirically.

$$\lambda_f = \frac{2Gv}{1-2v} \tag{1-112}$$

Brain Tissue Material Properties and Governing Equations. Brain tissue displacement is also governed through eq. (1-111), which is written in terms of tissue displacement, $\vec{d}_{Brain}$, tissue volumetric strain, ε_{Brain}, and tissue material properties G_{Brain} and λ_{Brain} to form eq. (1-113).

$$0 = G_{Brain}\nabla^2\vec{d}_{Brain} + \left(\lambda_{Brain} + G_{Brain}\right)\nabla\varepsilon_{Brain}, \quad \text{where } \varepsilon_{Brain} = \nabla\cdot\vec{d}_{Brain} \tag{1-113}$$

Based on (Taylor and Miller 2004), G_{Brain} was set to 500 Pa. v was set at 0.48 to represent nearly incompressible brain tissue (Nagashima, Shirakuni et al. 1990). Accordingly, the Young's modulus was 1,480 Pa. λ_{Brain} was calculated using eq. (1-112).

Development of Cerebral Vasculature Computational Domain. The two-dimensional vasculature model was developed by first importing the image in Figure 58A into an "in-house" vasculature reconstruction program. In the program, a user creates and connects points along major arteries of the histological image until the basic structure of the large arteries is represented on the computer. An automatic vessel growth algorithm is then applied to the base arterial structure so that small arteries and arterioles are generated within the brain tissue domain. The simplified vasculature network displayed in Figure 58B consisted of approximately 3,000

vessel segments. The details of the vessel growth algorithm are fully described elsewhere (Schreiner and Buxbaum 1993; Karch, Neumann et al. 1999; Schreiner, Karch et al. 2006).

Governing Equations for Vasculature. Each blood vessel in our model is cylindrical with a fixed length. With these physical assumptions, eqs. (1-114)-(1-116) are applied to the vasculature model to compute blood pressure, blood flow, and vessel cross-sectional area at discrete time points during the cardiac cycle.

Continuity-Blood
$$l_{vessel}\frac{A_{vessel}^{n}-A_{vessel}^{n-1}}{\Delta t}=f_{in}-f_{out} \tag{1-114}$$

Momentum-Blood
$$p_{in}-p_{out}=\frac{8\pi\mu l_{vessel}}{\left(A_{vessel}^{n-1}\right)^{2}}f_{in} \tag{1-115}$$

Vessel Distensibility
$$p_{vessel}-p_{brain}=E_{vessel}\left(\frac{A_{vessel}^{n}-A_{vessel}^{o}}{A_{vessel}^{o}}\right) \tag{1-116}$$

Equation (1-114) is a mass balance represented by the vessel length, l_{vessel}, the vessel cross-sectional area at time *n* and $n-1$, A_{vessel}^{n} and A_{vessel}^{n-1} respectively, the flow into and out of the vessel, f_{in} and f_{out} respectively, and the time step, Δt. Equation (1-115) is a simplified momentum balance represented by the vessel inlet and outlet pressure, p_{in} and p_{out} respectively, the blood viscosity, μ, the vessel length, the vessel cross-sectional area at the previous time step, and the flow into the vessel. Equation (1-116) governs vessel distensibility via the pressure difference between vessel lumen and surrounding brain tissue, p_{vessel} and p_{brain} respectively, vessel stiffness, E_{vessel}, the vessel cross-sectional area at time *n*, and the vessel cross-sectional area at zero transmural pressure (when $p_{vessel}=p_{brain}$), A_{vessel}^{o}. Equations (1-114)-(1-116) lead to a large system of linear equations in which the vessel cross section, vessel inflow and outflow, and vessel inlet and outlet pressures are solved simultaneously.

Boundary Conditions for Blood Flow. Blood flow and vasculature expansion were calculated as a function of the cardiac cycle. Though there is constant blood supply to the brain throughout the cardiac cycle, there is an increased amount of blood flow during cardiac systole when the cerebral blood pressure rises. In diastole, blood flow to the brain decreases with a simultaneous decrease in blood pressure. In the past, we have reconstructed the pressure waveform using a 17 coefficient Fourier series (Linninger, Sweetman et al. 2009; Linninger, Xenos et al. 2009; Sweetman and Linninger 2011; Sweetman, Xenos et al. 2011). However, for this initial conceptual model of brain, vasculature, and CSF we employ a sinusoidal pressure function as given in eq. (1-117) and displayed in Figure 60.

$$p_{\text{inlet}}(t) = 13,000 + 3,000\sin[2\pi(t-0.25)] \qquad (1\text{-}117)$$

p_{inlet} is applied to the inlet vessel of the arterial network. The waveform has a mean pressure of 13,000Pa (97.5mmHg) and pressure amplitude of 3,000Pa (22.5mmHg). Currently, the vasculature model terminates at the arteriolar level. Each terminating blood vessel is assigned an outlet pressure of 40mmHg, commensurate with values found in (Knezevic 1988).

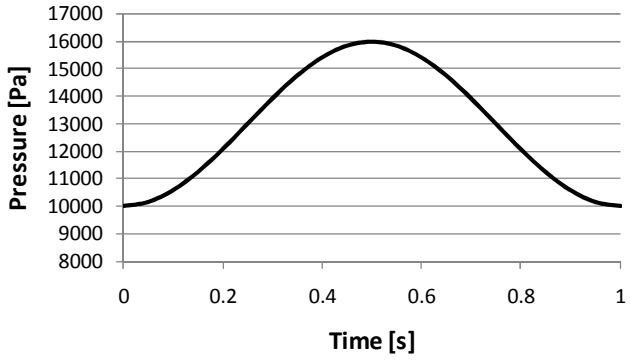

Figure 60. Blood pressure waveform. The pressure was applied to the inlet vessel of the brain-vasculature-CSF model to induce brain tissue motion and CSF flow dynamics.

Boundary Conditions for Vasculature-Tissue Interaction. Vessel expansion and brain tissue deformation is initiated through eq. (1-116). As p_{vessel} increases during cardiac systole the

vessels expand. During cardiac diastole, p_{vessel} decreases, and the vessels contract to their pre-systolic cross-sectional area. For each vessel, p_{vessel} is taken to be the mean of the vessel inlet and outlet pressure; p_{brain} is set to 1,000 Pa (Johanson, Duncan et al. 2008).

The expansion or contraction of a vessel in a given time step, Δt, is represented by the change in vessel cross-sectional area. Because each vessel is modeled as a cylinder with fixed length, the change in volume of a particular vessel, ΔV_{vessel}, is given by eq. (1-118).

$$\Delta V_{vessel} = l_{vessel}\left(A_{vessel}^{n} - A_{vessel}^{n-1}\right) \tag{1-118}$$

The vessel volume change is then used to compute the volumetric strain, $\varepsilon_{\text{b.c.v.}}$, of a particular control volume of the brain mesh using eq. (1-119).

$$\varepsilon_{\text{b.c.v.}} = \frac{\Delta V_{vessel}}{V_{\text{b.c.v.}}} \tag{1-119}$$

The subscript, b.c.v., stands for *brain control volume*. In a two-dimensional application, $V_{\text{b.c.v.}}$ is the area of <u>one</u> control volume. In our model, we assume the volume change of a given blood vessel contributes to the volumetric strain of a particular brain control volume if the center of the vessel lies in that particular control volume. In other words, if the center of vessel *i* lies in the space defined by control volume *j*, then the volume change of vessel *i* will contribute to the volumetric strain of control volume *j*. Because the center of several vessels may reside within the same brain mesh control volume, the volume change of several neighboring vessels may contribute to the overall volumetric strain of a particular brain control volume. After calculating $\varepsilon_{\text{b.c.v.}}$ via (1-119) for all brain control volumes, eq. (1-113) is applied to the brain mesh using $\varepsilon_{\text{b.c.v.}}$ as an internal boundary condition. During vessel expansion, $\varepsilon_{\text{b.c.v.}}$ is positive, the brain tissue expands, and the CSF space is compressed. When the vessels constrict, $\varepsilon_{\text{b.c.v.}}$ is negative,

the brain tissue returns to an undeformed state, and the CSF space recovers to its initial volume. In summary, the cyclical expansion and relaxation of the cerebral vessels deforms the surrounding brain tissue and CSF space and leads to the pulsatile CSF flow patterns.

Solution Strategy. The model simulations were performed over an entire cardiac cycle. The cardiac cycle was assumed to be one second and was divided into 0.01s time intervals. All time derivatives in eqs. (1-108)-(1-110) and (1-114) were discretized using implicit Euler integration. The finite volume method was used to spatially discretize the governing brain tissue displacement and fluid flow equations. The brain-vasculature-CSF interaction program was implemented in Delphi 7.0; all linear algebraic systems were written in a sparse matrix format and solved using HSL_MA48 (http://www.hsl.rl.ac.uk/). A flow diagram of the overall solution strategy is provided in Figure 61.

As indicated in Figure 61, the CSF flow field is initialized under steady-state conditions. Next, with an increment in Δt, a new pressure value is calculated from eq. (1-117) and applied to the first vessel in the vasculature network. Equations (1-114)-(1-116) are then solved to recover for each vessel the updated cross-sectional area, inlet and outlet pressures as well as inlet and outlet flows. Changes in vessel volume are then used to compute volumetric strains in the brain mesh. Next, the volumetric strains are used in eq. (1-113) to calculate brain deformation and displacements along the brain-CSF interface. Finally, the CSF flow field governed by eqs. (1-108)-(1-109) is solved using the SIMPLE algorithm (Patankar 1980; Versteeg and Malalasekera 1995). In our implementation of the SIMPLE algorithm, we have set the pressure and velocity under-relaxation parameters to 0.5. Two convergence criteria were used in the SIMPLE algorithm. The first, eq. (1-120), is a percent difference formula that corresponds to a 0.1% change in the velocity field from the previous iteration, $\vec{u}^{i-1}$, to the current iteration, $\vec{u}^{i}$.

The second, eq. (1-121), corresponds to a sufficiently small pressure correction, p'. When eqs. (1-120) and (1-121) are satisfied, the pressure and velocity fields are accepted and the simulation advances to the next time step or terminates if the end of the cardiac cycle has been reached.

Convergence-Velocity $$\left|\frac{\vec{u}^{\,i}-\vec{u}^{\,i-1}}{\text{mean}(\vec{u}^{\,i},\vec{u}^{\,i-1})}\right| \le 0.001 \qquad \text{(1-120)}$$

Convergence-Pressure Correction $$p' \le 1e-5 \qquad \text{(1-121)}$$

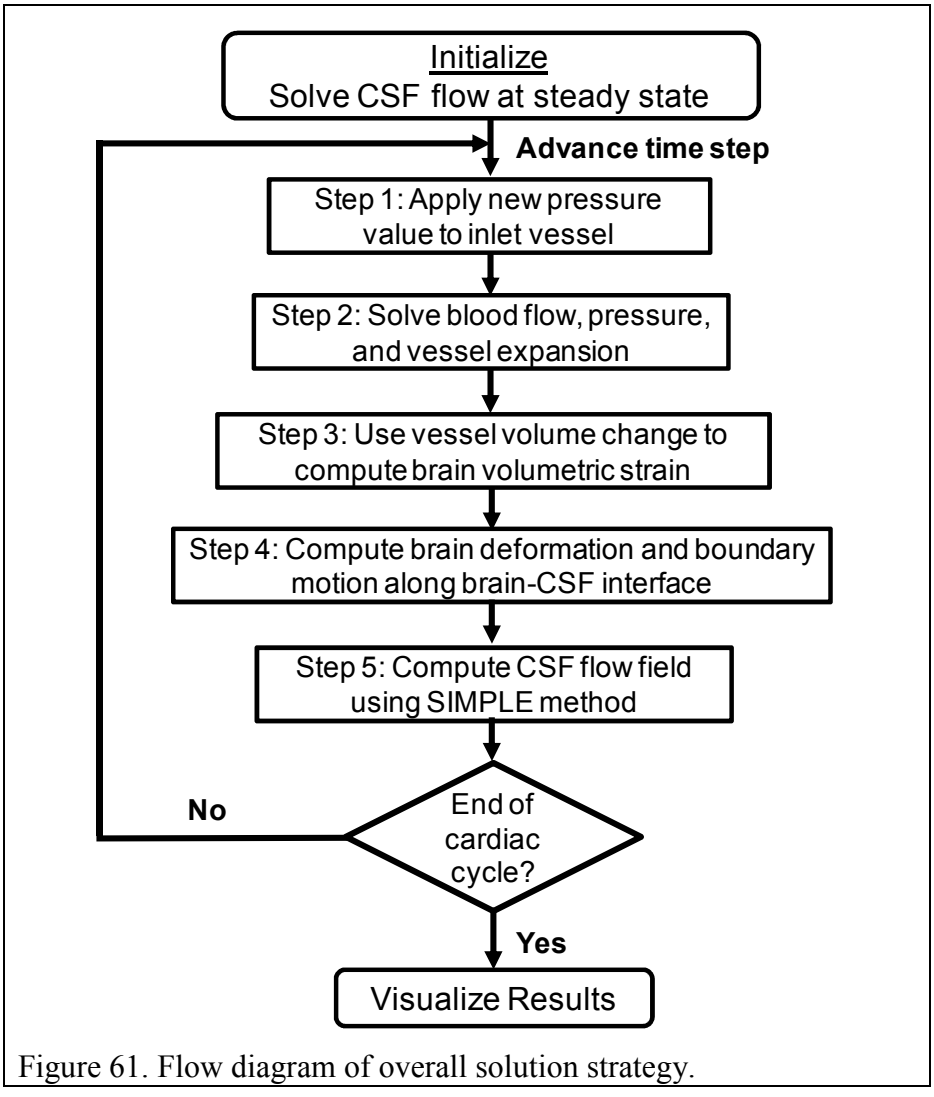

Figure 61. Flow diagram of overall solution strategy.

7.8.2. Results

Figure 62A shows a simplified cerebral vasculature network used to induce brain deformation and CSF motion. The inlet vessel, indicated by an arrow, had the largest radius of 0.001m. The smallest vessel radius was 0.000208919m. Equation (1-122), which relates vessel radius, R to vessel stiffness was derived using values reported in (Zagzoule and Marc-Vergnes 1986). The elastance distribution for the 235 vessels in the network is given in Figure 62B.

$$\text{Vessel Stiffness} = -17,435\ln(R) + 153,063 \qquad (1\text{-}122)$$

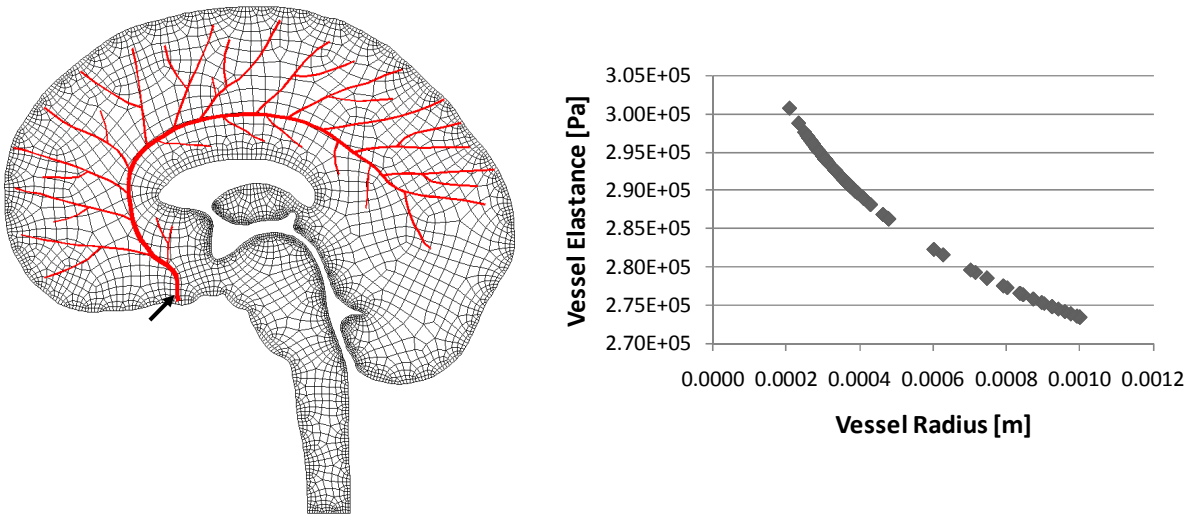

A **B**

Figure 62. A) Conceptual model of the cerebral vasculature—inlet vessel indicated by arrow. B) Vessel radius and associated elastance distribution.

Brain Tissue Displacement. Figure 63 shows the vessel pressure and brain tissue displacement at mid systole (30% of the cardiac cycle) and diastole (70% of the cardiac cycle). According to eq. (1-117) and Figure 60, the pressure applied to the inlet vessel at mid systole and diastole is equal. Thus, it follows that the pressure distribution at mid systole and diastole shown in Figure 63 are the same. However, the x and y brain tissue displacements differ at mid systole and diastole in the following way. At mid systole, the vessels are expanding. As a result, near the pontine cistern, the x-displacement is predominantly negative on the left side of the vessels and positive on the right side of the vessels. Because the tissue is free to deform into the CSF space

near the pontine cistern and along the lateral ventricle walls, the *y*-displacement is negative in these regions. When the vessels constrict during diastole, the brain begins to relax to its undeformed state. Hence, *x*-displacement becomes positive on the left side of the vessels and negative on the right side of the vessels. The *y*-displacement is positive in both the pontine cistern and lateral ventricle regions because the brain tissue is moving upward as it is restored to its undeformed state.

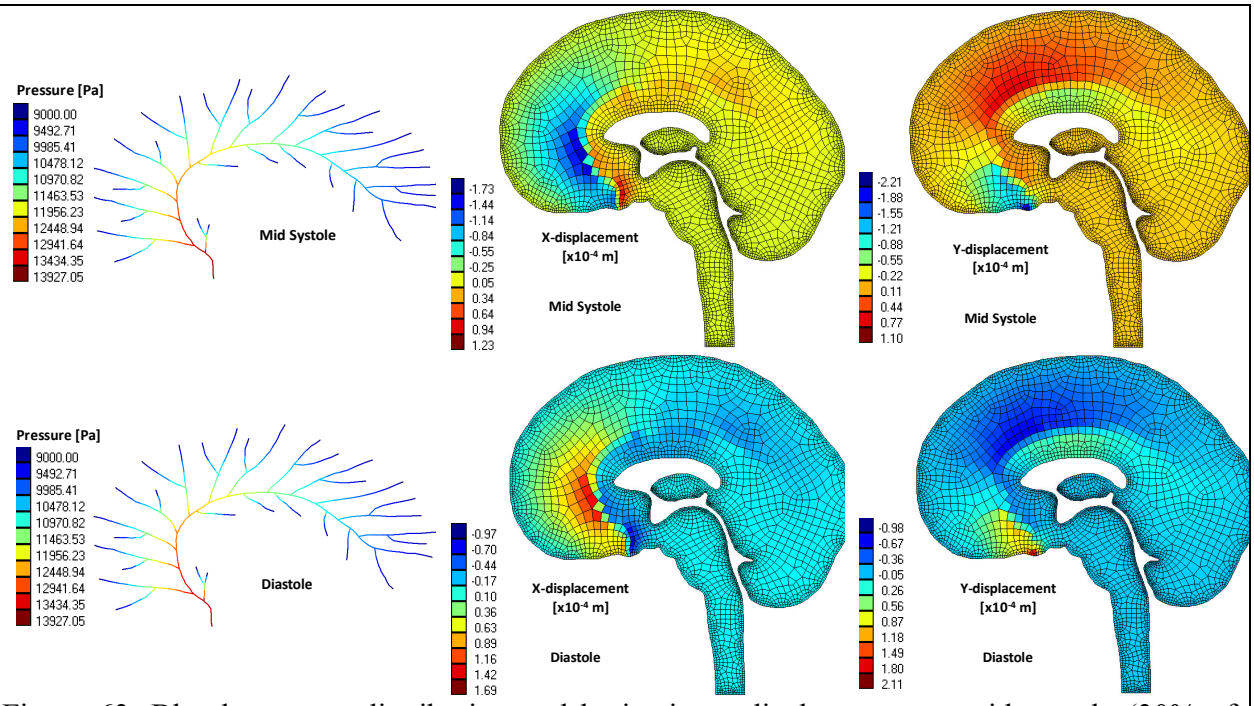

Figure 63. Blood pressure distribution and brain tissue displacement at mid systole (30% of cardiac cycle) and diastole (70% of cardiac cycle).

CSF flow and pressure dynamics. Figure 64 displays the CSF velocity and pressure field at early systole, mid systole, and diastole. At early systole, the vasculature begins to expand as it fills with blood. In turn, the brain parenchyma yields to the expanding vasculature and compresses the CSF space. As a result, the CSF is accelerated, directed toward the spinal canal and upper cranial subarachnoid space. The CSF pressure is highest in the pontine cistern and lateral ventricles, where brain tissue displacement along the brain-CSF interface is greatest. At 30% of the cardiac cycle, the rate of vasculature expansion reaches a maximum. In turn, the rate

of displacement along the brain-CSF interface is also highest. Consequently, superior-inferior CSF speed near the pontine cistern reaches its maximum value of 8.6mm/s and superior-inferior speed in the aqueduct is 16.9mm/s. During diastole, the inlet blood pressure is decreasing at its maximum rate. In turn, vessel diameter and brain parenchyma size decrease at their maximum rate. Consequently, the CSF inferior-superior speed reaches its maximum value of 18.5mm/s.

During systole the pressure is high in the ventricles and low at the base of the cranial CSF space. During diastole, the pressure gradient reverses, and the pressure is lower in the ventricles. According to the simulation, the largest pressure gradient in the cranial CSF space is less than 2.5Pa. Also, the pressure difference across the cerebral aqueduct varies from about 1Pa to 2Pa at any given time during the cardiac cycle. These values are in excellent agreement with our previous computational studies (Linninger, Sweetman et al. 2009).

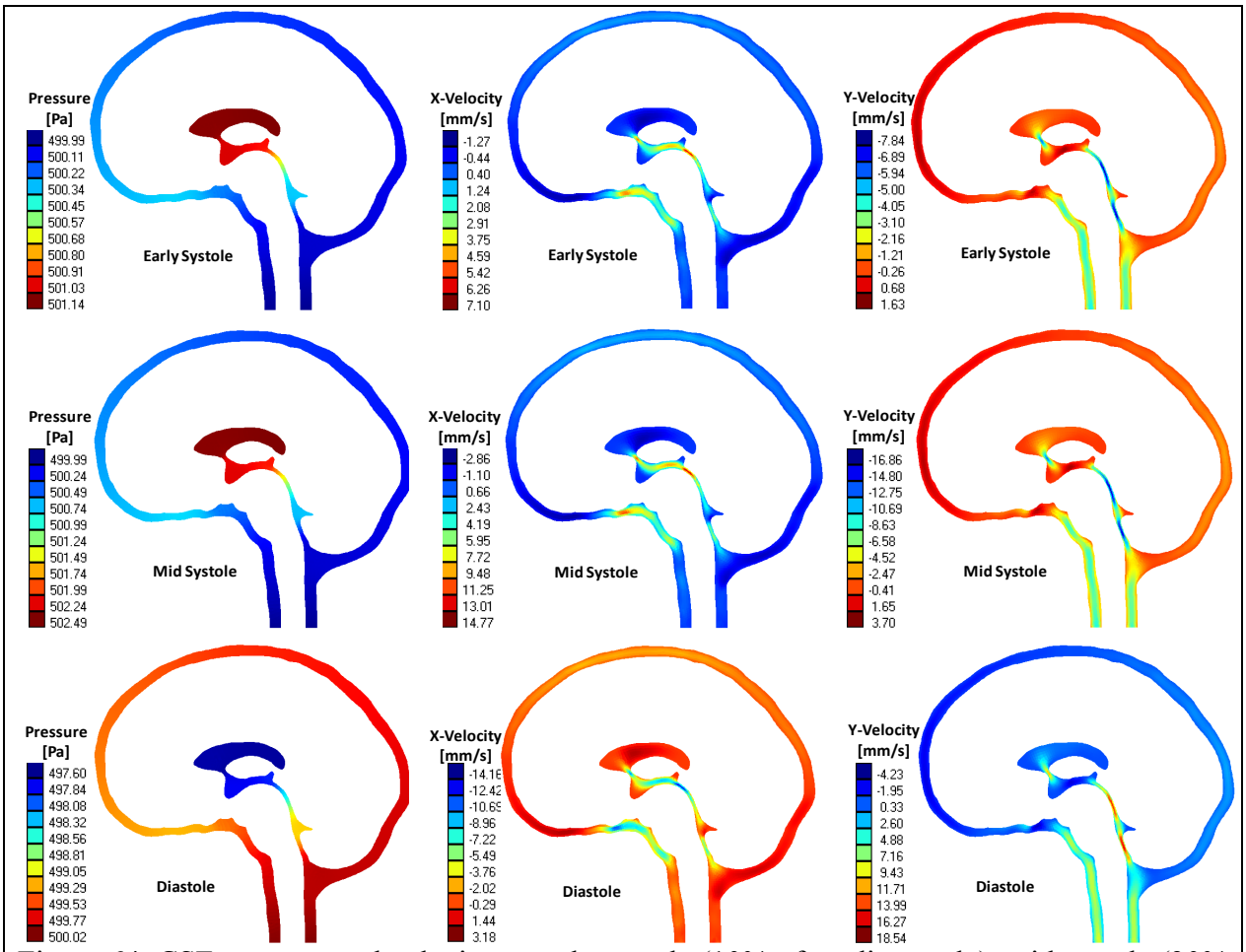

Figure 64. CSF pressure and velocity at early systole (10% of cardiac cycle), mid systole (30% of cardiac cycle), and diastole (70% of cardiac cycle). In early systole and mid systole, large motion along the brain-CSF interface near the pontine cistern and lateral ventricles causes compression of the CSF space and acceleration of CSF toward the spinal canal. The superior-inferior flow reaches its maximum value at mid systole. During diastole, the brain returns to its undeformed state and in turn the CSF is accelerated back toward the cranium.

Vessel stiffness and changes in CSF flow. Arteriosclerosis of the cerebral vasculature is found in a large percentage of the adult and elderly population. The hardening of arteries associated with arteriosclerosis is hypothesized to change the overall CSF flow dynamics (Greitz 2004). To test the impact of stiff vessels on intracranial dynamics, the larger vessels in the network were assigned an elastance value five times higher than typically observed in healthy subjects. The vessels were assigned stiffness values according to eq. (1-123).

$$\text{Vessel Stiffness [Pa]} = 196,784e^{2,031.1 \cdot R} \qquad (1\text{-}123)$$

The elastance distribution for the 235 vessels in the network for this case study is given in Figure 65.

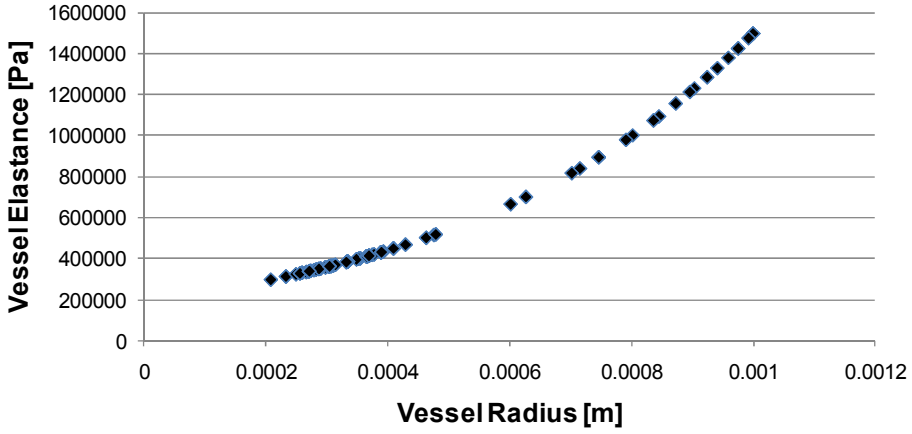

Figure 65. Vessel radius and elastance distribution for a case study of stiff arteries.

Figure 66 shows the CSF flow and pressure field at mid systole with stiff large vessels. Overall, the pressure gradient throughout the cranial CSF space is reduced compared to the normal case. In addition, the CSF velocity is decreased in the aqueduct and pontine cistern. We can gain greater insight into the effect of stiff vessels by comparing the aqueduct to pontine cistern velocity ratios between the two cases. In the normal case, the aqueduct to pontine cistern velocity ratio was 1.96 (16.9/8.6). In the stiff vessel case, the aqueduct to pontine cistern velocity ratio is higher at 3.18 (7/2.2). Though the total flow is decreased in the stiff vessel case, the flow is more diminished in the pontine cistern than in the aqueduct. Though we are cautious to draw conclusions based on this preliminary study, Greitz has hypothesized that stiff arteries would decrease flow in the pontine cistern and through the cervical junction (Greitz 2004). A more detailed vasculature network may prove or disprove this hypothesis and lead to greater knowledge about how vasculature compliance affects intracranial dynamics.

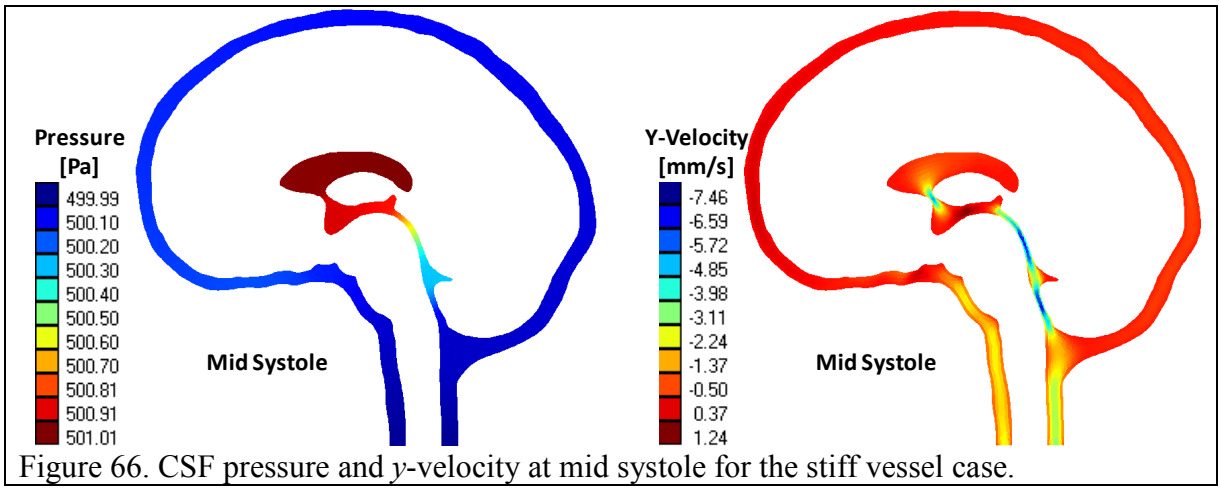

Figure 66. CSF pressure and *y*-velocity at mid systole for the stiff vessel case.

Results of fluid grid deformation. This results section closes with a short presentation of the fluid grid deformation scheme we have implemented. Figure 67 shows the fluid grid near the pontine cistern at the beginning of the simulation (before brain tissue deformation) and at 0.5s, when brain tissue deformation is greatest. One can see from the figure that even with relatively large fluid grid deformation, the mesh motion algorithm controls the mesh displacement well.

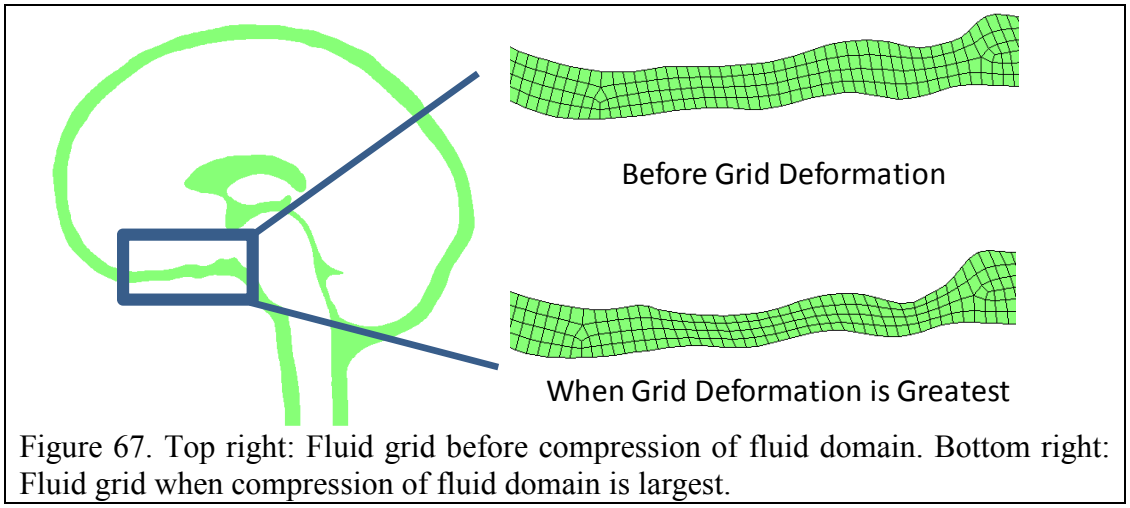

Figure 67. Top right: Fluid grid before compression of fluid domain. Bottom right: Fluid grid when compression of fluid domain is largest.

7.9. Discussion

This chapter has presented a novel approach for integrating a detailed cerebral vasculature network in a biomechanical model of brain tissue motion and CSF flow. The vasculature model was developed using a combination of manual segmentation and an automatic vessel growth

algorithm. The governing equations of tissue displacement and fluid motion were discretized using the finite volume method and solved over realistic domains of brain and CSF spaces. The dynamic expansion and contraction of the vasculature network led to deformation of brain tissue and the CSF spaces. Brain tissue displacement along the brain-CSF interface led to pulsatile CSF motion throughout the cardiac cycle.

From 2d to 3d. To arrive at this fully integrated model of vasculature, brain tissue, and CSF, particular geometrical and physical assumptions were adopted. For example, the study has been confined to a two-dimensional mid-sagittal cross section of the human brain. Despite this simplification, we have been able to capture the fluid dynamics in the CSF spaces; the current model predictions are in good agreement with our previously published results (Linninger, Sweetman et al. 2009). Overall, this 2d model serves as a proof of concept for a future 3d model of vasculature, brain tissue, and CSF dynamics. The progression to 3d will require a 3d vasculature model as a well as 3d brain and CSF spaces. Our recent efforts in 3d modeling of the entire CSF space indicate this objective can be achieved. In addition, significant progress has been made toward the development of a 3d vasculature computer model. Figure 68 shows our current 3d vasculature model, which was obtained through a combination of advanced manual segmentation techniques developed in our lab with an automatic vessel growth algorithm. The model includes major arterial structures such as the carotid arteries, vertebral arteries, and Circle of Willis as well as automatically generated microvasculature. Steady-state blood pressure simulations over the course of a cardiac cycle were conducted. Figure 68 shows the systolic and diastolic pressure distribution throughout the network.

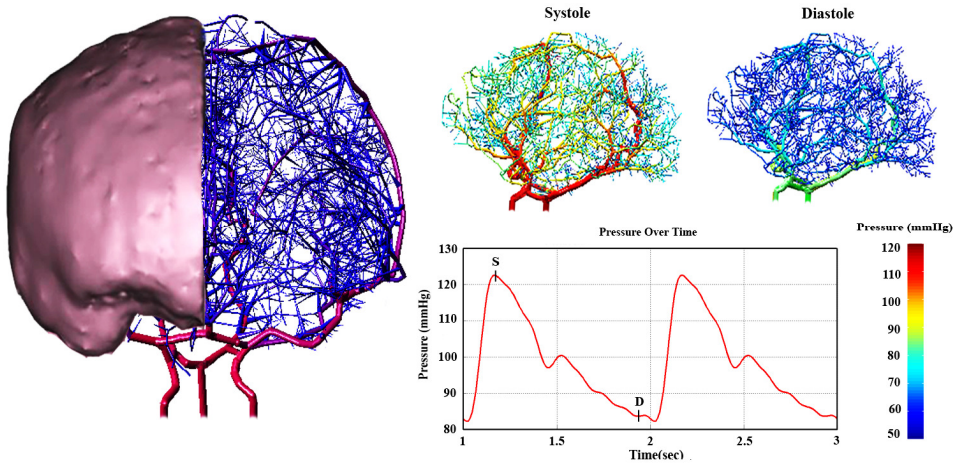

Figure 68. A surface mesh of the brain was constructed from MRI data and a vascular network was grown using the automatic growth algorithm. Blood pressure simulations of the generated vasculature network are shown for systole (cardiac contraction) and diastole (cardiac recoil). Systolic input (S) and diastolic input (D) are indicated on the pressure waveform.

A fully integrated 3d model of vasculature, brain tissue, and CSF may also require a new method for controlling boundary motion along the brain-CSF interface. In 2d, the kinematic boundary condition is applied to line segments. In 3d, the kinematic boundary condition must be applied to planes. More work is needed to assess whether our current method of controlling boundary motion can be extended to 3d without major modification.

An additional consideration for a 3d model is the calculation of the fluid grid velocity, $\vec{u}_g$. Because the current approach for computing $\vec{u}_g$ is specific for the 2d case, the progression to a 3d model will require a new method for calculating $\vec{u}_g$. Demirdzic and Peric state that the calculation of $\vec{u}_g$ can be extended to 3d, but proposed no specific method (Demirdzic and Peric 1988; Demirdzic and Peric 1990). However, since $\vec{u}_g$ in 2d is a function of how much area is swept by a line segment in a given period of time, one could imagine that $\vec{u}_g$ in 3d will be a function of how much volume is swept be a two-dimensional face in a given period of time.

A final note on the progression to 3d is the issue of computational resources. The 2d model for brain, vasculature, and CSF contained about 10,000 control volumes for brain and CSF combined, and about 3,000 vessel segments. This resolution translates to approximately 35,000 equations, which was manageable on a standard PC using sparse solver techniques. A 3d model will require several million control volumes for combined brain and CSF and also several million vessel segments. Though still to be determined, the model may need to be represented by at least 500 million equations.

Two-way coupling between brain tissue and CSF. In its current stage, the model takes into account only kinematic boundary conditions along the CSF-brain tissue interface. Essentially, the brain tissue displaces, and the velocity of the moving boundary is used as a velocity boundary condition for the fluid. A more advanced treatment of the interacting forces between CSF and brain tissue would be to also implement a dynamic boundary condition. The dynamic boundary would require that the forces along the CSF-brain tissue interface are equal. The dynamic boundary condition is very advanced and beyond the scope of this dissertation. To begin thinking about implementing this condition, one would have to realize that the dynamic boundary condition would involve iterative coupling between the solid and fluid. When the brain tissue displacement drives CSF motion, the coupling scheme might proceed as follows:

1. Guess tissue displacement everywhere in brain domain and along CSF-brain tissue boundary
2. Compute fluid velocity and pressure field using SIMPLE
3. Check if solid stress/pressure is equal to the fluid pressure computed from SIMPLE
4. If solid and fluid pressures are not equal, provide a better guess for the brain tissue displacement and repeat steps 2 and 3.

The two-way coupling between fluid and solid domains is still an active area of research. Some articles that may be useful to the LPPD lab in the future are (Yu 1986; Nitikitpaiboon and Bathe 1993; Crolet and Ohayon 1994; Morand and Ohayon 1995; Heil 1998; Bathe, Zhang et al. 1999; Le Tallec and Mouro 2001; Rugonyi and Bathe 2001; Dervieux 2003; Zhao and Forhad 2003; Heil 2004; Lohner, Cebral et al. 2004; Khurram 2005; Le Tallec, Gerbeau et al. 2005; Bungartz and Schäfer 2006; Kanchi 2006; Matthies, Niekamp et al. 2006; Fernandez, Gerbeau et al. 2007; Vierendeels, Lanoye et al. 2007; Heil, Hazel et al. 2008; Sternel, Schafer et al. 2008; Xia and Lin 2008; Badia, Quaini et al. 2009; Brebbia 2009; Roszak, Posadzy et al. 2009; Wang and Belytschko 2009; Kuttler, Gee et al. 2010; Souli and Benson 2010).

Two-way coupling between brain tissue and cerebral vasculature. In its current stage, there is only one-way coupling between the vasculature and brain tissue. Effectively, the vasculature expands due to a pressure difference between the dynamically changing lumen pressure and the statically set tissue pressure. A more rigorous and significantly advanced treatment of interactions between brain tissue and vasculature would be to implement a two-way coupling scheme between the vasculature and brain tissue. Implementation of two-way coupling is a very ambition task. Currently, I cannot provide the best advice for future implementation. However, I can provide some words of caution. Currently, the change in vessel volume is used as a boundary condition in the brain mesh as a volumetric strain. (The change in vessel volume is computed based on a set tissue pressure.) When the brain deforms due to the volumetric strain input, it assumes a different pressure state than the static pressure value used to compute the vessel volume change. This implies that (similar to the CSF-brain interface two-way coupling strategy), an iterative approach is needed between the vessels and the brain tissue. The expansion of the vessels would have to be guessed, the tissue pressure would have to be computed, and then the

solution would have to converge at a state in which the tissue pressure used to compute the vessel expansion is equal to the tissue pressure computed from the tissue displacement. Furthermore, one would have to be sure that the tissue pressures being computed are physiologically reasonable. In other words, since we are currently using a linear elastic model, it is possible that the pressures computed in a linear elastic model would be different than what would be computed in a poroelastic, viscoelastic, or hyperelastic model.

Present vasculature model and thoughts for future improvements. The current vasculature model only considers arteries and arterioles. The model terminates before the capillary network. This omission is acceptable for the current aim of this model, which was to generate CSF flow as a function of the cerebral vasculature expansion. In comparison to the arterial network, the capillaries and venous do not expand as much if at all. Thus, there is little contribution lost from not modeling the capillary or venous system. In future work, our lab may be interested in investigating CSF production and reabsorption via the capillary network of the brain parenchyma. To that end, we have already begun work to develop a capillary model.

One major assumption of this current model is that the arteries are expanding within the brain tissue. This may be true for the small arterioles, but in fact large arteries are found within the CSF space. Future work will be focused on learning how the expansion of the large arteries can be transferred to the CSF space directly as opposed to causing deformation in the brain tissue which eventually causes CSF space deformation.

Brain tissue properties and disease assessment. Over several decades, researchers have modeled the material response of the brain as linear elastic, poroelastic, porous-undeformable, viscoelastic-nonporous, viscoelastic-porous, and hyperelastic. Since the main objective of this study was to quantify CSF motion as a function of the pulsating cerebral vasculature, the main

interest was the deformation of the brain tissue along the brain-CSF interfaces and the effect this has on the CSF flow field. Thus, for this initial work, the brain parenchyma was idealized as a linear elastic material.

In our lab, we are also studying the porous properties of the brain, especially as it relates to hydrocephalus. As the ventricles enlarge in hydrocephalus, the porosity of the brain tissue decreases. Methods to quantify the extent of porosity change under hydrocephalic conditions are still underdeveloped. We envision mathematical models with realistic geometry and accurate material properties will someday provide better means for quantifying porosity changes. To accomplish this goal, our future work includes treating the brain as a poroelastic material.

Further refinement of the vasculature bed is also needed to better understand hydrocephalus. For example, clinicians have not yet determined whether the capillaries or venous system serve as alternate CSF reabsorption pathways in hydrocephalic conditions. In the future, we will modify our existing model to allow fluid exchange across the endothelial layer of the capillaries and venules. As the current model terminates at the arteriolar level, we are developing new vessel growth algorithms to generate the capillary and venous system. Because there are over one billion capillaries in the brain, we do not propose to model capillaries as discrete segments, but instead will adopt a porous network model as has been reported in the literature (Baish, Netti et al. 1997).

A final remark regarding the model's application for hydrocephalus is related to blood flow in the brain. Clinicians have observed that expansion of the lateral ventricles and accompanying compression of the brain parenchyma leads to significant changes in cerebral blood flow. For example, Momjian et al. (2004) have found that cerebral blood flow decreases by about 14% in the periventricular white matter in patients with enlarged ventricles. We foresee our

mathematical model being used as an additional tool for quantifying these changes and for developing treatment strategies based on improved predictions.

7.10. Conclusion

In this first fully integrated vasculature, brain tissue, CSF intracranial dynamic model, we have computed the CSF flow field as a function of the interaction between pulsating cerebral vasculature and deformable brain tissue. The brain and CSF computational domains were derived from a 2d mid-sagittal histological image containing the cerebral ventricles, aqueduct of Sylvius, and subarachnoid space. The vasculature model was developed using a combination of manual segmentation and an automatic vessel growth algorithm. Computer predictions of blood flows and pressures as well as vessel distensibility were used to induce brain tissue motion and brain-CSF interaction along the lateral ventricles and the base of the brain near the pontine cistern. The predicted CSF flow field was in good agreement with previously published results (Linninger, Sweetman et al. 2009), and therefore provide a proof of concept for future work in advancing the model to three-dimensions to predict the entire CSF flow field as a function of the pulsating vasculature.

CITED LITERATURE

Abbott, N. J. (2004). "Evidence for bulk flow of brain interstitial fluid: significance for physiology and pathology." Neurochem Int **45**(4): 545-552.

Alperin, N., E. M. Vikingstad, et al. (1996). "Hemodynamically independent analysis of cerebrospinal fluid and brain motion observed with dynamic phase contrast MRI." Magn Reson Med **35**(5): 741-754.

Amin-Hanjani, S., A. Alaraj, et al. (2010). "Flow replacement bypass for aneurysms: decision-making using intraoperative blood flow measurements." Acta Neurochir (Wien) **152**(6): 1021-1032; discussion 1032.

Badia, S., A. Quaini, et al. (2009). "Coupling Biot and Navier-Stokes equations for modelling fluid-poroelastic media interaction." Journal of Computational Physics **228**(21): 7986-8014.

Baish, J. W., P. A. Netti, et al. (1997). "Transmural coupling of fluid flow in microcirculatory network and interstitium in tumors." Microvasc Res **53**(2): 128-141.

Baledent, O., C. Gondry-Jouet, et al. (2004). "Relationship between cerebrospinal fluid and blood dynamics in healthy volunteers and patients with communicating hydrocephalus." Invest Radiol **39**(1): 45-55.

Baledent, O., M. C. Henry-Feugeas, et al. (2001). "Cerebrospinal fluid dynamics and relation with blood flow: a magnetic resonance study with semiautomated cerebrospinal fluid segmentation." Invest Radiol **36**(7): 368-377.

Barshes, N., A. Demopoulos, et al. (2005). Anatomy and Physiology of the Leptomeninges and CSF Space. Leptomeningeal Metastases. L. E. Abrey, M. C. Chamberlain and H. H. Engelhard, Springer US. **125:** 1-16.

Bateman, G. A. (2000). "Vascular compliance in normal pressure hydrocephalus." AJNR Am J Neuroradiol **21**(9): 1574-1585.

Bathe, K. J. (1996). Finite Element Procedures. Upper Saddle River, Prentice Hall.

Bathe, K. J., H. Zhang, et al. (1999). "Finite element analysis of fluid flows fully coupled with structural interactions." Computers & Structures **72**(1-3): 1-16.

Belytschko, T., W. K. Liu, et al. (2000). Nonlinear finite elements for continua and structures. Chichester; New York, Wiley.

Bering, E. A., Jr. (1962). "Circulation of the cerebrospinal fluid. Demonstration of the choroid plexuses as the generator of the force for flow of fluid and ventricular enlargement." J Neurosurg **19**: 405-413.

Bertram, C. D., A. R. Brodbelt, et al. (2005). "The origins of syringomyelia: numerical models of fluid/structure interactions in the spinal cord." J Biomech Eng **127**(7): 1099-1109.

Bhadelia, R. A., A. R. Bogdan, et al. (1997). "Cerebrospinal fluid pulsation amplitude and its quantitative relationship to cerebral blood flow pulsations: a phase-contrast MR flow imaging study." Neuroradiology **39**(4): 258-264.

Biot, M. A. (1941). "General theory of three-dimensional consolidation." J Appl Phys **12**: 155-164.

Biot, M. A. (1955). "Theory of elasticity and consolidation for a porous anisotropic solid." J Appl Phys **26**: 182-185.

Blinkov, S. M. and I. I. Glezer (1968). The human brain in figures and tables; a quantitative handbook. New York, Basic Books.

Blom, F. J. (2000). "Considerations on the spring analogy." International Journal for Numerical Methods in Fluids **32**(6): 647-668.

Brebbia, C. A. (2009). Fluid structure interaction V. Southampton ; Boston, WIT Press.

Brown, P. D., S. L. Davies, et al. (2004). "Molecular mechanisms of cerebrospinal fluid production." Neuroscience **129**(4): 957-970.

Bungartz, H. J. and M. Schäfer (2006). Fluid-structure interaction : modelling, simulation, optimisation. Berlin, Springer-Verlag.

Cao, W. M., W. Z. Huang, et al. (2002). "A moving mesh method based on the geometric conservation law." Siam Journal on Scientific Computing **24**(1): 118-142.

Carpenter, P. W., K. Berkouk, et al. (2003). "Pressure wave propagation in fluid-filled co-axial elastic tubes. Part 2: Mechanisms for the pathogenesis of syringomyelia." J Biomech Eng **125**(6): 857-863.

Charbel, F. T., G. Gonzales-Portillo, et al. (1999). "Quantitative assessment of vessel flow integrity for aneurysm surgery. Technical note." J Neurosurg **91**(6): 1050-1054.

Charbel, F. T., K. H. Guppy, et al. (2001). "Computerized hemodynamic evaluation of the cerebral circulation for bypass." Neurosurg Clin N Am **12**(3): 499-508, viii.

Charbel, F. T., M. Zhao, et al. (2004). "A patient-specific computer model to predict outcomes of the balloon occlusion test." J Neurosurg **101**(6): 977-988.

Charney, D. S. and E. J. Nestler (2004). Neurobiology of mental illness. New York, Oxford University Press.

Cheng, S., K. Tan, et al. (2010). "The effects of the interthalamic adhesion position on cerebrospinal fluid dynamics in the cerebral ventricles." J Biomech **43**: 579-582.

Chiang, W. W., C. G. Takoudis, et al. (2009). "Relationship between ventricular morphology and aqueductal cerebrospinal fluid flow in healthy and communicating hydrocephalus." Invest Radiol **44**(4): 192-199.

Crolet, J. M. and R. Ohayon (1994). Computational methods for fluid-structure interaction. Harlow, Essex, Eng., New York, Longman Scientific & Technical; Wiley.

Czosnyka, M., Z. Czosnyka, et al. (2004). "Cerebrospinal fluid dynamics." Physiol Meas **25**(5): R51-76.

Czosnyka, Z., M. Czosnyka, et al. (2002). "Laboratory testing of hydrocephalus shunts -- conclusion of the U.K. Shunt evaluation programme." Acta Neurochir (Wien) **144**(6): 525-538; discussion 538.

Czosnyka, Z. H., K. Cieslicki, et al. (2005). "Hydrocephalus shunts and waves of intracranial pressure." Medical & Biological Engineering & Computing **43**(1): 71-77.

Dandy, W. E. (1919). "Experimental Hydrocephalus." Ann Surg **70**(2): 129-142.

Date, A. W. (1993). "Solution of Navier-Stokes Equations on Non-Staggered Grid." International Journal of Heat and Mass Transfer **36**(7): 1913-1922.

Date, A. W. (1996). "Complete pressure correction algorithm for solution of incompressible Navier-Stokes equations on a nonstaggered grid." Numerical Heat Transfer Part B-Fundamentals **29**(4): 441-458.

Date, A. W. (1998). "Solution of Navier-Stokes equations on nonstaggered grid at all speeds." Numerical Heat Transfer Part B-Fundamentals **33**(4): 451-467.

Date, A. W. (2005). Introduction to computational fluid dynamics. New York, NY, Cambridge University Press.

Davidson, L. (1996). "A pressure correction method for unstructured meshes with arbitrary control volumes." International Journal for Numerical Methods in Fluids **22**(4): 265-281.

Davson, H. (1984). Formation and drainage of the cerebrospinal fluid. Hydrocephalus. K. Shapiro, A. Marmarou and H. Portnoy. New York, Raven Press**:** 3-40.

Davson, H. and M. B. Segal (1996). Physiology of the CSF and blood-brain barriers. Boca Raton, CRC Press.

De Boor, C. (2000). A practical guide to splines. New York, Springer.

de Foy, B. and W. Dawes (2000). "Unstructured pressure-correction solver based on a consistent discretization of the Poisson equation." International Journal for Numerical Methods in Fluids **34**(6): 463-478.

Del Bigio, M. R. and J. E. Bruni (1988). "Changes in periventricular vasculature of rabbit brain following induction of hydrocephalus and after shunting." J Neurosurg **69**(1): 115-120.

Demirdzic, I. and M. Peric (1988). "Space Conservation Law in Finite Volume Calculations of Fluid-Flow." International Journal for Numerical Methods in Fluids **8**(9): 1037-1050.

Demirdzic, I. and M. Peric (1990). "Finite Volume Method for Prediction of Fluid-Flow in Arbitrarily Shaped Domains with Moving Boundaries." International Journal for Numerical Methods in Fluids **10**(7): 771-790.

Dervieux, A. (2003). Fluid-structure interaction. London ; Sterling, VA, Kogan Page Science.

Dumoulin, C. L., S. P. Souza, et al. (1988). "Time-resolved magnetic resonance angiography." Magn Reson Med **6**(3): 275-286.

Egnor, M., L. Zheng, et al. (2002). "A model of pulsations in communicating hydrocephalus." Pediatr Neurosurg **36**(6): 281-303.

Eide, P. K. (2008). "Demonstration of uneven distribution of intracranial pulsatility in hydrocephalus patients." J Neurosurg **109**(5): 912-917.

Eklund, A., P. Smielewski, et al. (2007). "Assessment of cerebrospinal fluid outflow resistance." Med Biol Eng Comput **45**(8): 719-735.

Ellington, E. and G. Margolis (1969). "Block of arachnoid villus by subarachnoid hemorrhage." J Neurosurg **30**(6): 651-657.

Enzmann, D. R. and N. J. Pelc (1991). "Normal flow patterns of intracranial and spinal cerebrospinal fluid defined with phase-contrast cine MR imaging." Radiology **178**(2): 467-474.

Fernandez, M. A., J. F. Gerbeau, et al. (2007). "A projection semi-implicit scheme for the coupling of an elastic structure with an incompressible fluid." International Journal for Numerical Methods in Engineering **69**(4): 794-821.

Ferziger, J. H. and M. Peric (2002). Computational methods for fluid dynamics. Berlin ; New York, Springer.

Fin, L. and R. Grebe (2003). "Three dimensional modeling of the cerebrospinal fluid dynamics and brain interactions in the aqueduct of sylvius." Comput Method Biomec **6**(3): 163-170.

Fishman, R. A. (1980). Cerebrospinal fluid in diseases of the nervous system. Philadelphia, Saunders.

Fox, R. W., A. T. McDonald, et al. (2009). Introduction to fluid mechanics. Hoboken, N.J., Wiley.

Fung, Y. C. (1993). Biomechanics: Mechanical Properties of Living Tissues. New York, Springer-Verlag.

Gjerris, F. and S. E. Borgesen (1992). "Current concepts of measurement of cerebrospinal fluid absorption and biomechanics of hydrocephalus." Adv Tech Stand Neurosurg **19**: 145-177.

Gonzalez-Darder, J. M. and J. L. Barcia-Salorio (1989). "Pulse amplitude and volume-pressure relationships in experimental hydrocephalus." Acta Neurochir (Wien) **97**(3-4): 166-170.

Gosling, R. G. and D. H. King (1974). "Arterial assessment by Doppler-shift ultrasound." Proc R Soc Med **67**(6 Pt 1): 447-449.

Green, M. A., L. E. Bilston, et al. (2008). "In vivo brain viscoelastic properties measured by magnetic resonance elastography." NMR Biomed **21**(7): 755-764.

Greitz, D. (2004). "Radiological assessment of hydrocephalus: new theories and implications for therapy." Neurosurg Rev **27**(3): 145-167.

Greitz, D. (2006). "Unraveling the riddle of syringomyelia." Neurosurg Rev **29**(4): 251-263; discussion 264.

Greitz, D., K. Ericson, et al. (1999). "Pathogenesis and mechanics of spinal cord cysts - A new hypothesis based on magnetic resonance studies of cerebrospinal fluid dynamics." Int J Neuroradiol **5**(2): 61-78.

Greitz, D., A. Franck, et al. (1993). "On the pulsatile nature of intracranial and spinal CSF-circulation demonstrated by MR imaging." Acta Radiol **34**(4): 321-328.

Greitz, D., J. Hannerz, et al. (1994). "MR imaging of cerebrospinal fluid dynamics in health and disease. On the vascular pathogenesis of communicating hydrocephalus and benign intracranial hypertension." Acta Radiol **35**(3): 204-211.

Gupta, S., M. Soellinger, et al. (2009). "Three-dimensional computational modeling of subject-specific cerebrospinal fluid flow in the subarachnoid space." J. Biomech. Eng **131**(2): 1-11.

Hakim, S., J. G. Venegas, et al. (1976). "The physics of the cranial cavity, hydrocephalus and normal pressure hydrocephalus: mechanical interpretation and mathematical model." Surg Neurol **5**(3): 187-210.

Hansen, G. A., R. W. Douglass, et al. (2005). Mesh enhancement: selected elliptic methods, foundations and applications. London,, Imperial College Press.

Heil, M. (1998). "Stokes flow in an elastic tube - A large-displacement fluid-structure interaction problem." International Journal for Numerical Methods in Fluids **28**(2): 243-265.

Heil, M. (2004). "An efficient solver for the fully coupled solution of large-displacement fluid-structure interaction problems." Computer Methods in Applied Mechanics and Engineering **193**(1-2): 1-23.

Heil, M., A. L. Hazel, et al. (2008). "Solvers for large-displacement fluid-structure interaction problems: segregated versus monolithic approaches." Computational Mechanics **43**(1): 91-101.

Henry-Feugeas, M. C., I. Idy-Peretti, et al. (2000). "Origin of subarachnoid cerebrospinal fluid pulsations: a phase-contrast MR analysis." Magn Reson Imaging **18**(4): 387-395.

Huang, T. Y., H. W. Chung, et al. (2004). "Supratentorial cerebrospinal fluid production rate in healthy adults: quantification with two-dimensional cine phase-contrast MR imaging with high temporal and spatial resolution." Radiology **233**(2): 603-608.

Hughes, T. J. R., W. K. Liu, et al. (1981). "Lagrangian-Eulerian Finite-Element Formulation for Incompressible Viscous Flows." Computer Methods in Applied Mechanics and Engineering **29**(3): 329-349.

Hutsler, J. J., W. C. Loftus, et al. (1998). "Individual variation of cortical surface area asymmetries." Cereb. Cortex **8**(1): 11-17.

Jacobson, E. E., D. F. Fletcher, et al. (1996). "Fluid dynamics of the cerebral aqueduct." Pediatr Neurosurg **24**(5): 229-236.

Jacobson, E. E., D. F. Fletcher, et al. (1999). "Computer modelling of the cerebrospinal fluid flow dynamics of aqueduct stenosis." Medical & Biological Engineering & Computing **37**(1): 59-63.

Johanson, C. E., J. A. Duncan, 3rd, et al. (2008). "Multiplicity of cerebrospinal fluid functions: New challenges in health and disease." Cerebrospinal Fluid Research **5**: 10.

Kaczmarek, M., R. P. Subramaniam, et al. (1997). "The hydromechanics of hydrocephalus: steady-state solutions for cylindrical geometry." Bull Math Biol **59**(2): 295-323.

Kalata, W., B. A. Martin, et al. (2009). "MR measurement of cerebrospinal fluid velocity wave speed in the spinal canal." IEEE Trans Biomed Eng **56**(6): 1765-1768.

Kanchi, H. (2006). A three dimensional mesh moving scheme for moving boundary flows and fluid-structure interaction, University of Illinois at Chicago**:** x, 77 leaves.

Karch, R., F. Neumann, et al. (1999). "A three-dimensional model for arterial tree representation, generated by constrained constructive optimization." Comput Biol Med **29**(1): 19-38.

Khurram, R.-U.-A. (2005). A multiscale finite element method for fluid structure interaction problem, University of Illinois at Chicago**:** x, 144 leaves.

Kim, D. S., J. U. Choi, et al. (1999). "Quantitative assessment of cerebrospinal fluid hydrodynamics using a phase-contrast cine MR image in hydrocephalus." Childs Nerv Syst **15**(9): 461-467.

Kim, J., N. A. Thacker, et al. (2007). "Prediction of the jugular venous waveform using a model of CSF dynamics." AJNR Am J Neuroradiol **28**(5): 983-989.

Knezevic, S. (1988). Handbook of regional cerebral blood flow. Hillsdale, N.J., L. Erlbaum Associates.

Kosteljanetz, M. (1985). "Resistance to outflow of cerebrospinal fluid determined by bolus injection technique and constant rate steady state infusion in humans." Neurosurgery **16**(3): 336-340.

Koyanagi, I., Y. Iwasaki, et al. (2005). "Clinical features and pathomechanisms of syringomyelia associated with spinal arachnoiditis." Surg. Neurol. **63**(4): 350-355; discussion 355-356.

Kroin, J. S., A. Ali, et al. (1993). "The distribution of medication along the spinal canal after chronic intrathecal administration." Neurosurgery **33**(2): 226-230; discussion 230.

Kruse, S. A., G. H. Rose, et al. (2008). "Magnetic resonance elastography of the brain." NeuroImage **39**(1): 231-237.

Ku, D. N. (1997). "Blood flow in arteries." Annu. Rev. Fluid. Mech **29**(1): 399-434.

Kurtcuoglu, V., M. Soellinger, et al. (2007). "Computational investigation of subject-specific cerebrospinal fluid flow in the third ventricle and aqueduct of Sylvius." J. Biomech. **40**(6): 1235-1245.

Kuttler, U., M. Gee, et al. (2010). "Coupling strategies for biomedical fluid-structure interaction problems." International Journal for Numerical Methods in Biomedical Engineering **26**(3-4): 305-321.

Lakin, W. D., S. A. Stevens, et al. (2003). "A whole-body mathematical model for intracranial pressure dynamics." J Math Biol **46**(4): 347-383.

LaVan, D. A., T. McGuire, et al. (2003). "Small-scale systems for in vivo drug delivery." Nat Biotechnol **21**(10): 1184-1191.

Le Tallec, P., J. F. Gerbeau, et al. (2005). "Fluid structure interaction problems in large deformation." Comptes Rendus Mecanique **333**(12): 910-922.

Le Tallec, P. and J. Mouro (2001). "Fluid structure interaction with large structural displacements." Computer Methods in Applied Mechanics and Engineering **190**(24-25): 3039-3067.

Levine, D. N. (1999). "The pathogenesis of normal pressure hydrocephalus: a theoretical analysis." Bull Math Biol **61**(5): 875-916.

Levine, D. N. (2008). "Intracranial pressure and ventricular expansion in hydrocephalus: have we been asking the wrong question?" J Neurol Sci **269**(1-2): 1-11.

Lien, F. S. (2000). "A pressure-based unstructured grid method for all-speed flows." International Journal for Numerical Methods in Fluids **33**(3): 355-374.

Linge, S. O., V. Haughton, et al. (2010). "CSF flow dynamics at the craniovertebral junction studied with an idealized model of the subarachnoid space and computational flow analysis." AJNR Am J Neuroradiol **31**(1): 185-192.

Linninger, A. (2011). Biotransport: Internal Laboratory Report. Laboratory for Product and Process Design.

Linninger, A., B. Sweetman, et al. (2009). "Normal and Hydrocephalic Brain Dynamics: The Role of Reduced Cerebrospinal Fluid Reabsorption in Ventricular Enlargement." Annals of Biomedical Engineering **37**(7): 1434-1447.

Linninger, A. A., M. R. Somayaji, et al. (2008). "Prediction of convection-enhanced drug delivery to the human brain." J Theor Biol **250**(1): 125-138.

Linninger, A. A., C. Tsakiris, et al. (2005). "Pulsatile cerebrospinal fluid dynamics in the human brain." IEEE Trans Biomed Eng **52**(4): 557-565.

Linninger, A. A., M. Xenos, et al. (2009). "A mathematical model of blood, cerebrospinal fluid and brain dynamics." J Math Biol **59**(6): 729-759.

Linninger, A. A., M. Xenos, et al. (2007). "Cerebrospinal fluid flow in the normal and hydrocephalic human brain." IEEE Trans Biomed Eng **54**(2): 291-302.

Lohner, R., J. Cebral, et al. (2004). "Large-scale fluid-structure interaction simulations." Computing in Science & Engineering **6**(3): 27-37.

Lorenzo, A. V., L. K. Page, et al. (1970). "Relationship between cerebrospinal fluid formation, absorption and pressure in human hydrocephalus." Brain **93**(4): 679-692.

Loth, F., M. A. Yardimci, et al. (2001). "Hydrodynamic modeling of cerebrospinal fluid motion within the spinal cavity." J Biomech Eng **123**(1): 71-79.

Loudon, C. and A. Tordesillas (1998). "The use of the dimensionless Womersley number to characterize the unsteady nature of internal flow." J. Theor. Biol **191**(1): 63-78.

Luo, X. Y. and T. J. Pedley (1998). "The effects of wall inertia on flow in a two-dimensional collapsible channel." Journal of Fluid Mechanics **363**: 253-280.

Marmarou, A., K. Shulman, et al. (1978). "A nonlinear analysis of the cerebrospinal fluid system and intracranial pressure dynamics." J Neurosurg **48**(3): 332-344.

Martins, A. N., J. K. Wiley, et al. (1972). "Dynamics of the cerebrospinal fluid and the spinal dura mater." Journal of Neurology, Neurosurgery & Psychiatry **35**(4): 468-473.

Materialise Inc (2008). Mimics 12.1 Reference Guide. Belgium, www.materialise.be/mimics/main_ENG.html.

Matthies, H. G., R. Niekamp, et al. (2006). "Algorithms for strong coupling procedures." Computer Methods in Applied Mechanics and Engineering **195**(17-18): 2028-2049.

Meier, U. and P. Bartels (2002). "The importance of the intrathecal infusion test in the diagnosis of normal pressure hydrocephalus." J. Clin. Neurosci **9**(3): 260-267.

Milhorat, T. H., M. W. Chou, et al. (1999). "Chiari I malformation redefined: clinical and radiographic findings for 364 symptomatic patients." Neurosurgery **44**(5): 1005-1017.

Momjian, S., B. K. Owler, et al. (2004). "Pattern of white matter regional cerebral blood flow and autoregulation in normal pressure hydrocephalus." Brain **127**(Pt 5): 965-972.

Morand, H. J. P. and R. Ohayon (1995). Fluid structure interaction : applied numerical methods. Chichester; New York; Paris, Wiley; Masson.

Nagashima, T., T. Shirakuni, et al. (1990). "A two-dimensional, finite element analysis of vasogenic brain edema." Neurol Med Chir (Tokyo) **30**(1): 1-9.

Nield, D. A. and A. Bejan (2006). Convection in porous media. New York, Springer.

Nieuwenhuys, R., J. Voogd, et al. (1988). The human central nervous system : a synopsis and atlas. Berlin ; New York, Springer-Verlag.

Nitikitpaiboon, C. and K. J. Bathe (1993). "An Arbitrary Lagrangian-Eulerian Velocity Potential Formulation for Fluid-Structure Interaction." Computers & Structures **47**(4-5): 871-891.

Nolte, J. and J. W. Sundsten (2002). The human brain: an introduction to its functional anatomy. St. Louis, Mosby.

Nomura, T. and T. J. R. Hughes (1992). "An Arbitrary Lagrangian-Eulerian Finite-Element Method for Interaction of Fluid and a Rigid Body." Computer Methods in Applied Mechanics and Engineering **95**(1): 115-138.

Owler, B. K., S. Momjian, et al. (2004). "Normal pressure hydrocephalus and cerebral blood flow: a PET study of baseline values." J Cereb Blood Flow Metab **24**(1): 17-23.

Owler, B. K., A. Pena, et al. (2004). "Changes in cerebral blood flow during cerebrospinal fluid pressure manipulation in patients with normal pressure hydrocephalus: a methodological study." J Cereb Blood Flow Metab **24**(5): 579-587.

Pardridge, W. M. (2011). "Drug transport in brain via the cerebrospinal fluid." Fluids Barriers CNS **8**(1): 7.

Patankar, S. V. (1980). Numerical heat transfer and fluid flow. New York, McGraw-Hill.

Pedley, T. J. (1980). The fluid mechanics of large blood vessels. Cambridge ; New York, Cambridge University Press.

Pelc, N. J., M. A. Bernstein, et al. (1991). "Encoding strategies for three-direction phase-contrast MR imaging of flow." J Magn Reson Imaging **1**(4): 405-413.

Pellicer, A., F. Gaya, et al. (2002). "Noninvasive continuous monitoring of the effects of head position on brain hemodynamics in ventilated infants." Pediatrics **109**(3): 434-440.

Pena, A., M. D. Bolton, et al. (1999). "Effects of brain ventricular shape on periventricular biomechanics: a finite-element analysis." Neurosurgery **45**(1): 107-116; discussion 116-108.

Pena, A., N. G. Harris, et al. (2002). "Communicating hydrocephalus: the biomechanics of progressive ventricular enlargement revisited." Acta Neurochir Suppl **81**: 59-63.

Penn, R. D. and J. W. Bacus (1984). "The brain as a sponge: a computed tomographic look at Hakim's hypothesis." Neurosurgery **14**(6): 670-675.

Penn, R. D., M. C. Lee, et al. (2005). "Pressure gradients in the brain in an experimental model of hydrocephalus." J Neurosurg **102**(6): 1069-1075.

Peters, A. and E. G. Jones (1984). Cerebral cortex. New York, Plenum Press.

Peters, G. P. and D. W. Smith (2002). "Solute transport through a deforming porous medium." International Journal for Numerical and Analytical Methods in Geomechanics **26**(7): 683-717.

Pettorossi, V. E., C. Di Rocco, et al. (1978). "Communicating hydrocephalus induced by mechanically increased amplitude of the intraventricular cerebrospinal fluid pulse pressure: rationale and method." Exp Neurol **59**(1): 30-39.

Piechnik, S. K., M. Czosnyka, et al. (2001). "A model of the cerebral and cerebrospinal fluid circulations to examine asymmetry in cerebrovascular reactivity." J Cereb Blood Flow Metab **21**(2): 182-192.

Raksin, P. B., N. Alperin, et al. (2003). "Noninvasive intracranial compliance and pressure based on dynamic magnetic resonance imaging of blood flow and cerebrospinal fluid flow: review of principles, implementation, and other noninvasive approaches." Neurosurg Focus **14**(4): e4.

Roszak, R., P. Posadzy, et al. (2009). "Fluid-structure interaction for large scale complex geometry and non-linear properties of structure." Archives of Mechanics **61**(1): 3-27.

Rugonyi, S. and K. J. Bathe (2001). "On finite element analysis of fluid flows fully coupled with structural interactions." Cmes-Computer Modeling in Engineering & Sciences **2**(2): 195-212.

Sack, I., B. Beierbach, et al. (2008). "Non-invasive measurement of brain viscoelasticity using magnetic resonance elastography." NMR Biomed **21**(3): 265-271.

Salamon, G. and J. M. Corbaz (1971). Atlas de la vascularisation arterielle du cerveau chez l'homme = atlas of the arteries of the human brain. Paris, Sandoz.

Saltzman, W. M. and W. L. Olbricht (2002). "Building drug delivery into tissue engineering." Nat Rev Drug Discov **1**(3): 177-186.

Schreiner, W. and P. F. Buxbaum (1993). "Computer-optimization of vascular trees." IEEE Trans Biomed Eng **40**(5): 482-491.

Schreiner, W., R. Karch, et al. (2006). "Optimized arterial trees supplying hollow organs." Med Eng Phys **28**(5): 416-429.

Segal, M. B. (2001). "Transport of nutrients across the choroid plexus." Microsc Res Tech **52**(1): 38-48.

Sherwood, L. (1995). Fundamentals of Physiology: A Human Perspective. St. Paul/Minneapolis, West Pub. Co.

Silbernagl, S. and A. Despopoulos (2009). Color Atlas of Physiology. New York, Thieme.

Silverberg, G. D., G. Heit, et al. (2001). "The cerebrospinal fluid production rate is reduced in dementia of the Alzheimer's type." Neurology **57**(10): 1763-1766.

Smillie, A., I. Sobey, et al. (2005). "A hydroelastic model of hydrocephalus." Journal of Fluid Mechanics **539**(-1): 417-443.

Sorek, S., J. Bear, et al. (1988). "A non-steady compartmental flow model of the cerebrovascular system." J Biomech **21**(9): 695-704.

Sorek, S., J. Bear, et al. (1989). "Resistances and compliances of a compartmental model of the cerebrovascular system." Ann Biomed Eng **17**(1): 1-12.

Sorek, S., M. Feinsod, et al. (1988). "Can NPH be caused by cerebral small vessel disease? A new look based on a mathematical model." Med Biol Eng Comput **26**(3): 310-313.

Souli, M. and D. J. Benson (2010). Arbitrary Lagrangian-Eulerian and fluid-structure interaction: numerical simulation. London; Hoboken, NJ, ISTE; Wiley.

Souli, M. and J. P. Zolesio (2001). "Arbitrary Lagrangian-Eulerian and free surface methods in fluid mechanics." Computer Methods in Applied Mechanics and Engineering **191**(3-5): 451-466.

Starling, E. H. (1896). "On the Absorption of Fluids from the Connective Tissue Spaces." Journal of Physiology **19**(4): 312-326.

Stephensen, H., M. Tisell, et al. (2002). "There is no transmantle pressure gradient in communicating or noncommunicating hydrocephalus." Neurosurgery **50**(4): 763-771.

Sternel, D. C., M. Schafer, et al. (2008). "Efficiency and accuracy of fluid-structure interaction simulations using an implicit partitioned approach." Computational Mechanics **43**(1): 103-113.

Stevens, S. A. (2000). "Mean pressures and flows in the human intracranial system as determined by mathematical simulations of a steady-state infusion test." Neurol Res **22**(8): 809-814.

Sussman, T. and K. J. Bathe (1987). "A Finite-Element Formulation for Nonlinear Incompressible Elastic and Inelastic Analysis." Computers & Structures **26**(1-2): 357-409.

Sweetman, B. and A. A. Linninger (2011). "Cerebrospinal fluid flow dynamics in the central nervous system." Ann Biomed Eng **39**(1): 484-496.

Sweetman, B., A. A. Linninger, et al. (2010). "Constrained Constructive Optimization for Vascular Generation." UIC-LPPD-060910.

Sweetman, B., M. Xenos, et al. (2011). "Three-dimensional computational prediction of cerebrospinal fluid flow in the human brain." Comput Biol Med.

Tan, Z. J., T. Tang, et al. (2006). "A simple moving mesh method for one- and two-dimensional phase-field equations." Journal of Computational and Applied Mathematics **190**(1-2): 252-269.

Taylor, Z. and K. Miller (2004). "Reassessment of brain elasticity for analysis of biomechanisms of hydrocephalus." J Biomech **37**(8): 1263-1269.

Thron, A. K., C. Rossberg, et al. (1988). Vascular anatomy of the spinal cord : neuroradiological investigations and clinical syndromes. Wien ; New York, Springer-Verlag.

Tramo, M. J., W. C. Loftus, et al. (1995). "Surface-Area of Human Cerebral-Cortex and Its Gross Morphological Subdivisions - in-Vivo Measurements in Monozygotic Twins Suggest Differential Hemisphere Effects of Genetic-Factors." J. Cognitive. Neurosci **7**(2): 292-302.

Troupp, H. (1975). "Intracranial pressure in hydrocephalus after subarachnoid haemorrhage." Zentralbl Neurochir **36**(1): 11-17.

Ulug, A. M., T. N. Truong, et al. (2003). "Diffusion imaging in obstructive hydrocephalus." AJNR Am J Neuroradiol **24**(6): 1171-1176.

Upton, M. L. and R. O. Weller (1985). "The morphology of cerebrospinal fluid drainage pathways in human arachnoid granulations." J Neurosurg **63**(6): 867-875.

Ursino, M. and C. A. Lodi (1997). "A simple mathematical model of the interaction between intracranial pressure and cerebral hemodynamics." Journal of Applied Physiology **82**(4): 1256-1269.

Valencia, A., H. Morales, et al. (2008). "Blood flow dynamics in patient-specific cerebral aneurysm models: the relationship between wall shear stress and aneurysm area index." Med. Eng. Phys **30**(3): 329-340.

Versteeg, H. K. and W. Malalasekera (1995). An introduction to computational fluid dynamics : the finite volume method. Harlow, Essex, England Longman Scientific & Technical ;, New York : Wiley.

Versteeg, H. K. and W. Malalasekera (2007). An introduction to computational fluid dynamics : the finite volume method. Harlow, England ; New York, Pearson Education Ltd.

Vierendeels, J., L. Lanoye, et al. (2007). "Implicit coupling of partitioned fluid-structure interaction problems with reduced order models." Computers & Structures **85**(11-14): 970-976.

Wagshul, M. E., J. J. Chen, et al. (2006). "Amplitude and phase of cerebrospinal fluid pulsations: experimental studies and review of the literature." J Neurosurg **104**(5): 810-819.

Wang, H. W. and T. Belytschko (2009). "Fluid-structure interaction by the discontinuous-Galerkin method for large deformations." International Journal for Numerical Methods in Engineering **77**(1): 30-49.

White, D. N., K. C. Wilson, et al. (1979). "The limitation of pulsatile flow through the aqueduct of Sylvius as a cause of hydrocephalus." J Neurol Sci **42**(1): 11-51.

Wilcox, R. K., L. E. Bilston, et al. (2003). "Mathematical model for the viscoelastic properties of dura mater." J Orthop Sci **8**(3): 432-434.

Wilkie, K. P., C. S. Drapaca, et al. (2010). "A theoretical study of the effect of intraventricular pulsations on the pathogenesis of hydrocephalus." Applied Mathematics and Computation **215**(9): 3181-3191.

Womersley, J. R. (1955). "Method for the calculation of velocity, rate of flow and viscous drag in arteries when the pressure gradient is known." J. Physiol **127**(3): 553-563.

Xia, G. H. and C. L. Lin (2008). "An unstructured finite volume approach for structural dynamics in response to fluid motions." Computers & Structures **86**(7-8): 684-701.

Yaksh, T. L. (1999). Spinal drug delivery. Amsterdam ; New York, Elsevier.

Yallapragada, N. and N. Alperin (2004). "Characterization of spinal canal hydrodynamics and compliance using bond graph technique and CSF flow measurements by MRI." Proc Int Soc Magn Resonan Med. **11**: 2658.

Yu, I. W. (1986). "Solution of Large Unsymmetric Eigensystems for Fluid Structure Interaction Problems." Nuclear Science and Engineering **92**(1): 157-161.

Zagzoule, M. and J. P. Marc-Vergnes (1986). "A global mathematical model of the cerebral circulation in man." J Biomech **19**(12): 1015-1022.

Zhang, L., K. Kulkarni, et al. (2007). "Discovery of transport and reaction properties in distributed systems." AIChE Journal **53**(2): 381-396.

Zhang, X. and J. F. Greenleaf (2006). "Noninvasive generation and measurement of propagating waves in arterial walls." J Acoust Soc Am **119**(2): 1238-1243.

Zhao, Y. and A. Forhad (2003). "A general method for simulation of fluid flows with moving and compliant boundaries on unstructured grids." Computer Methods in Applied Mechanics and Engineering **192**(39-40): 4439-4466.

Zhu, D. C., M. Xenos, et al. (2006). "Dynamics of lateral ventricle and cerebrospinal fluid in normal and hydrocephalic brains." J Magn Reson Imaging **24**(4): 756-770.

Zimmerman, R., C. Fleming, et al. (1986). "Periventricular hyperintensity as seen by magnetic resonance: prevalence and significance." Am. J. Roentgenol. **146**(3): 443-450.

Appendix A: Quick Reference/Summary of the SIMPLE Algorithm

Steady-State Navier-Stokes Equations

Overview. Instead of simultaneously solving the momentum and continuity equations to obtain the velocity and pressure fields, we decouple the equations so that the pressure and velocity fields are solved independently. How can this be accomplished? The first step is to assume a pressure field, p^{k-1}, as well as an *x* and *y* velocity field, u^{k-1} and v^{k-1}. Using these "known" fields, we solve for the u^* component of the $\vec{u}^*$ velocity field with the help of the *x* momentum equation and solve for the v^* component of the $\vec{u}^*$ velocity field with the help of the *y* momentum equation.

The next step involves computing a pressure correction, p'. The equation for p' is derived by implementing a Darcy-like flow assumption on the velocity correction. This gives rise to a pure diffusion equation for the pressure correction, which serves to drive the system toward conserving mass. This iterative procedure is repeated successively until the entire flow field satisfies continuity. As an additional check for solution convergence, the calculated velocities may only change slightly from a previous iteration to a current one. The commercial CFD tool Fluent, for example, requires that the velocity field change less than 0.1% from one iteration to the next before reporting a converged solution.

<u>Solution steps for steady-state Navier-Stokes equations</u>

Step 1: Assume pressure, and u-v velocity field;

Possible choices for the initial guesses include velocities equal to the inlet velocities and for pressures one can start with the outlet pressures.

$$\text{Possible choices for initial guesses: } u^{k-1} = u_{in;}\, v^{k-1} = v_{in};\, p^{k-1} = p_{out} \qquad (1\text{-}124)$$

Step 2. Compute current best velocities $\begin{pmatrix} u^* & v^* \end{pmatrix}^T$

Using initial guesses $u^{k-1}, v^{k-1}, p^{k-1}$ we solve separately two linear algebraic system as in Equations (1-125) and (1-126). Equation (1-125) can be interpreted as a convection with known velocity and diffusion problem with the pressure occurring as a source equation, its linear algebra solution (Ax=b) gives u^*. (Steps 2a). Next, solve Equation (1-126) to get v^*. (Steps 2b).

$$x\text{-momentum: } 0 = -\int_{cv} \nabla_x p^{k-1}\, dV - \rho \int_{cv} \vec{u}^{k-1} \cdot \left(\nabla u^*\right) dV + \mu \int_{cv} \nabla \cdot \left(\nabla u^*\right) dV \qquad (1\text{-}125)$$

$$y\text{-momentum: } 0 = -\int_{cv} \nabla_y p^{k-1}\, dV - \rho \int_{cv} \vec{u}^{k-1} \cdot \left(\nabla v^*\right) dV + \mu \int_{cv} \nabla \cdot \left(\nabla v^*\right) dV \qquad (1\text{-}126)$$

If $\begin{pmatrix} u^* & v^* \end{pmatrix}^T$ is equal to $\begin{pmatrix} u^{k-1} & v^{k-1} \end{pmatrix}^T$ we would have already found the solution. Since the initial guesses $\begin{pmatrix} u^{k-1} & v^{k-1} \end{pmatrix}^T$ may be far off from the actual solution, even our calculated vector $\begin{pmatrix} u^* & v^* \end{pmatrix}^T$ is usually not a solution in the first step.

Step 3. Compute Pressure correction, p'

We solve for the pressure correction, p', as a linear algebraic system. To derive the pressure correction equation, we first introduce velocity corrections $\vec{u}' = \begin{pmatrix} u' & v' \end{pmatrix}^T$. These velocity corrections are not new variables, but merely labels used in the derivations. At a control volume face (boundary), velocity corrections are proportional to the pressure gradient corrections across that same face as in Equation (1-127).

$$\vec{u}' = -\frac{\kappa}{\mu}\nabla p' \tag{1-127}$$

Equation (1-127) is similar in form to Darcy's Law. μ and κ account for the diffusion and convective contributions to the velocity correction, respectively. Whereas μ is always set to the actual value of the fluid viscosity, κ is an adjustable constant needed for improving convergence speed. For example, setting κ to 0.01 accelerates convergence speed by about 20 times (compared to when κ is set to 1). In generalized coordinates, (1-127) can be written as in Equation (1-128).

$$\begin{pmatrix} u' \\ v' \end{pmatrix} = -\frac{1}{\mu}\begin{pmatrix} \dfrac{\partial p'}{\partial x} \\ \dfrac{\partial p'}{\partial y} \end{pmatrix} \text{ with } \begin{aligned} \frac{\partial p'}{\partial x} &= \frac{\partial p'}{\partial \xi}\frac{\partial \xi}{\partial x} + \frac{\partial p'}{\partial \eta}\frac{\partial \eta}{\partial x} = \xi_x \frac{\partial p'}{\partial \xi} + \eta_x \frac{\partial p'}{\partial \eta} \\ \frac{\partial p'}{\partial y} &= \frac{\partial p'}{\partial \xi}\frac{\partial \xi}{\partial y} + \frac{\partial p'}{\partial \eta}\frac{\partial \eta}{\partial y} = \xi_y \frac{\partial p'}{\partial \xi} + \eta_y \frac{\partial p'}{\partial \eta} \end{aligned} \tag{1-128}$$

In order to find the desired equation for p', we need the continuity equation. Specifically we let

$$\begin{gathered} \nabla \cdot \vec{u} = 0 \\ \text{or} \\ \int_{cv} \nabla \cdot \vec{u}\, dV = 0 \end{gathered} \tag{1-129}$$

The velocity vector is composed of the current best solution of known velocities, $\begin{pmatrix} u^* & v^* \end{pmatrix}$, plus a required correction, $\begin{pmatrix} u' & v' \end{pmatrix}$, that yet is not yet known as in Equation (1-130).

$$\begin{pmatrix} u \\ v \end{pmatrix} = \begin{pmatrix} u^* \\ v^* \end{pmatrix} + \begin{pmatrix} u' \\ v' \end{pmatrix} \tag{1-130}$$

The yet unknown velocity corrections $\begin{pmatrix} u' & v' \end{pmatrix}$ can be expressed completely in terms of the unknown pressure correction gradients, p', as in eq. (1-131).

$$\begin{aligned} u' &= -\frac{1}{\mu\left|J^{-1}\right|}\left[y_\eta\left(p'_0 - p'_1\right) - y_\xi\left(p'_N - p'_S\right)\right] \\ v' &= -\frac{1}{\mu\left|J^{-1}\right|}\left[-x_\eta\left(p'_0 - p'_1\right) + x_\xi\left(p'_N - p'_S\right)\right] \end{aligned} \tag{1-131}$$

$$u' = -\frac{1}{\mu\left|J^{-1}\right|}\left[y_\eta\left(p'_0 - p'_1\right) - y_\xi\left(p'_N - p'_S\right)\right]$$
$$v' = -\frac{1}{\mu\left|J^{-1}\right|}\left[-x_\eta\left(p'_0 - p'_1\right) + x_\xi\left(p'_N - p'_S\right)\right] \qquad (1\text{-}132)$$

With known velocities, $\left(u^* \quad v^*\right)$, and the unknown $\left(u' \quad v'\right)$, inserted into the continuity equation, (1-129), yield the desired equation for the pressure correction p'. Equation (1-133) is a simple diffusion equation with a source term composed of $\left(u^* \quad v^*\right)$ contributions.

$$\underbrace{\sum_{f=1}^{\#\text{ of faces}} \frac{1}{\mu}\left[\frac{\left(p'_0 - p'_1\right)}{q_3}\left|J^{-1}\right|\right]^f}_{\text{Deviation from Continuity}} = \sum_{f=1}^{\#\text{ of faces}} \underbrace{y_\eta u^* - x_\eta v^*\Big|^f}_{\text{Continuity}} \qquad (1\text{-}133)$$

Solution of (1-133), gives the desired p'. If the p' are close to zero the problem is converged (Convergence Criterion). The final values are $p = p^{k-1} + p'$, and $\left(u \quad v\right)$.

More implementation details follow.

To derive eq (1-133), eqs. (1-134) and (1-135) are needed.

$$u = u^* - \frac{1}{\mu\left|J^{-1}\right|}\left[y_\eta\left(p'_0 - p'_1\right) - y_\xi\left(p'_N - p'_S\right)\right] \qquad (1\text{-}134)$$

$$v = v^* - \frac{1}{\mu\left|J^{-1}\right|}\left[-x_\eta\left(p'_0 - p'_1\right) + x_\xi\left(p'_N - p'_S\right)\right] \qquad (1\text{-}135)$$

Step 4. Pressure and velocity updates.

If convergence has not been reached, we first update the pressure field, $p = p^{k-1} + p'$ (step 4a). p^{k-1} is the pressure value at the previous iteration—the value used in (1-125) and (1-126). In practice, the improved pressure value will be calculated via under-relaxation:

$$p^{new} = p^{k-1} + \alpha_p p', \quad \text{where} \quad 0 < \alpha_p < 1 \qquad (1\text{-}136)$$

This new pressure is the update for the next iteration. Hence, in the second iteration, the previous pressure guess will be updated by setting it equal to $p^{k-1} := p^{new}$; this updated p^{k-1} will be used as the new pressure guess in eqs. (1-125) and (1-126).

Step 4b and 4c. The velocities $\left(u^{new} \quad v^{new}\right)$ are also updated with under-relaxation ($0 < \alpha_u < 1$ and $0 < \alpha_v < 1$);

$$u^{new} = \alpha_u u + (1 - \alpha_u)u^{k-1} \qquad (1\text{-}137)$$
$$v^{new} = \alpha_v v + (1 - \alpha_v)v^{k-1} \qquad (1\text{-}138)$$

The velocity components that will be used in a renewed iteration through steps 1- 4. Program termination is always when the convergence criterion in step 3 is reached or when the velocities no longer change significantly.

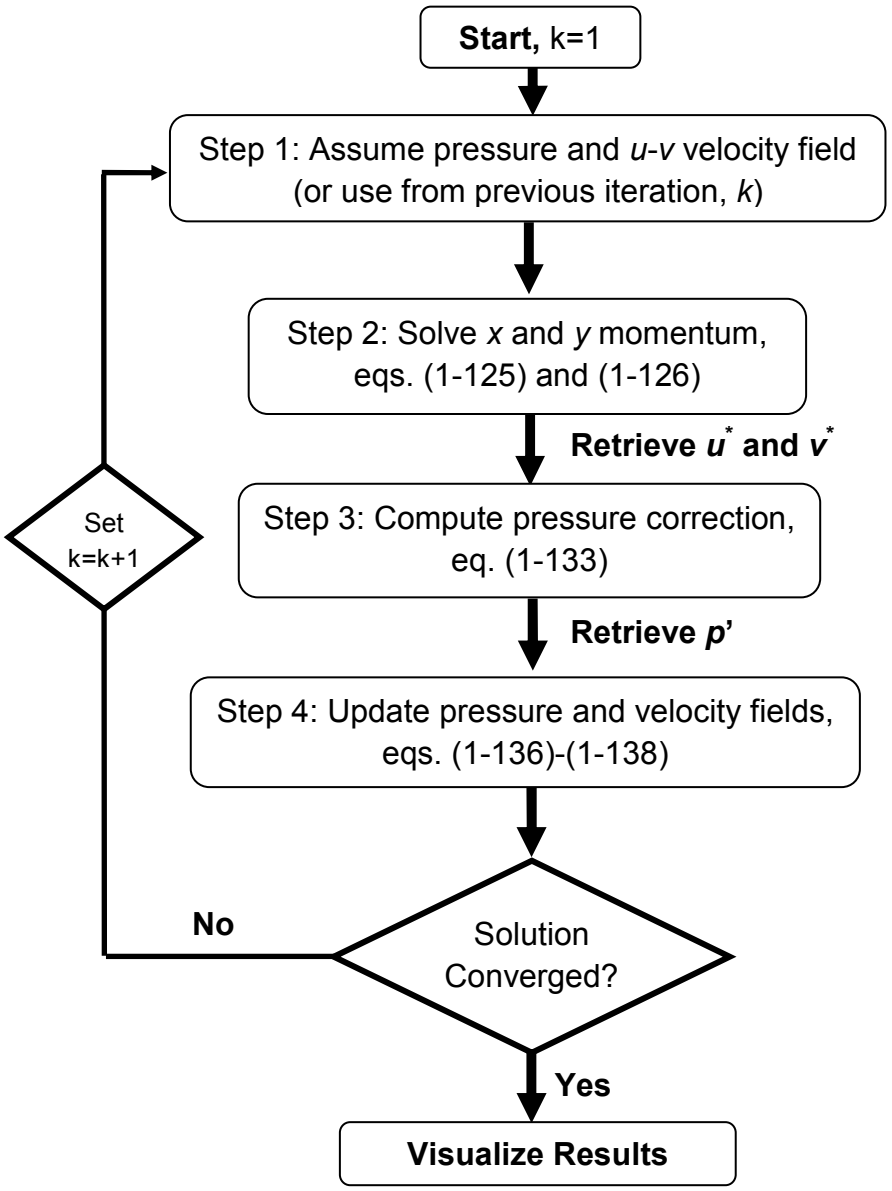

Figure 69. Flow diagram of the SIMPLE method. The numbered steps and equations are described in the text; *k* is the iteration number.

Unsteady (Dynamic) Navier-Stokes Equations

Overview. In the previous section, we had assumed steady-state conditions for the fluid flow field. However, if the flow is subject to dynamic boundary conditions, the flow must be described using the dynamic *x* and *y*-momentum equations (1-139) and (1-140). Each term in (1-139) and (1-140) is integrated in space and time to arrive at the discretized form of the unsteady momentum equations. The continuity equation is not modified in the dynamic situation. Consequently, the pressure correction equation in steady-state and dynamic situations is the same.

$$\rho \int_t^{t+\Delta t} \int_{cv} \frac{\partial u}{\partial t} dV dt = -\int_t^{t+\Delta t} \int_{cv} \nabla_x p \, dV dt - \rho \int_t^{t+\Delta t} \int_{cv} \vec{u} \cdot \nabla u \, dV dt + \mu \int_t^{t+\Delta t} \int_{cv} \nabla \cdot (\nabla u) dV dt \qquad (1\text{-}139)$$

$$\rho \int_t^{t+\Delta t} \int_{cv} \frac{\partial v}{\partial t} dV dt = -\int_t^{t+\Delta t} \int_{cv} \nabla_y p \, dV dt - \rho \int_t^{t+\Delta t} \int_{cv} \vec{u} \cdot \nabla v \, dV dt + \mu \int_t^{t+\Delta t} \int_{cv} \nabla \cdot (\nabla v) dV dt \qquad (1\text{-}140)$$

Discretization of dynamic Navier-Stokes equations

We now describe the discretization of each term in the *x*-momentum equation. Discretization of the *y*-momentum terms are completely analogous and will not be presented.

Local Acceleration Term. The discretizated form of the local acceleration term in the unsteady *x*-momentum equation is derived as follows. Because the fluid grid is fixed in space, u (the x component of the velocity vector) is a function of time and V (the volume/area of a control volume) is not a function of time. With these assumptions, we rewrite the double integral in eq. (1-139) as,

$$\rho \int_t^{t+\Delta t} \int_{cv} \frac{\partial u}{\partial t} dV dt = \rho \int_t^{t+\Delta t} \frac{\partial u}{\partial t} dt \int_{cv} dV ,$$

which ultimately leads to

$$\rho V \int_t^{t+\Delta t} \frac{\partial u}{\partial t} dt = \rho V \int_t^{t+\Delta t} \frac{\partial u}{\partial t} dt \Rightarrow \rho V \left[u^{t+\Delta t} - u^t \right] \qquad (1\text{-}141)$$

Pressure Gradient Term. Spatial integration over the control volume leads to:

$$-\int_{cv} \nabla_x p \, dV = \sum_{f=1}^{\#\text{ of faces}} p \cdot y_\eta \Big|^f$$

Thus, we have for time integration:

$$\int_t^{t+\Delta t} \left(\sum_{f=1}^{\#\text{ of faces}} p \cdot y_\eta \Big|^f \right) dt \qquad (1\text{-}142)$$

Let us recall that the SIMPLE method stands for semi-implicit method for pressure-linked equations. Since the method is semi-implicit, some terms can be treated implicitly while others treated explicitly. We have chosen to treat the pressure term as explicit and the velocity term as implicit. Consequently, in the first iteration of a given time step, we use the converged value of p from the previous time step. Thus, we can remove p from the time integral and rewrite eq. (1-142) as:

$$\sum_{f=1}^{\#\text{ of faces}} p \cdot y_\eta \Big|^f \int_t^{t+\Delta t} dt ,$$

which leads to:

$$\sum_{f=1}^{\#\text{ of faces}} p \cdot y_\eta \Big|^f \Delta t$$

Convective Acceleration Term. The convective term associated with the *x*-momentum is given in eq. (1-143).

$$-\rho\left(\vec{u}^{k-1}\right)\cdot\left(\nabla u^{*}\right) \tag{1-143}$$

$\vec{u}^{k-1}$ is the fluid velocity calculated at a control volume face. By integrating over a control volume, cv we have:

$$-\rho\int_{\text{cv}}\vec{u}^{k-1}\cdot\left(\nabla u^{*}\right)dV$$

We eventually arrive at:

$$\rho\sum_{f=1}^{\#\text{ of faces}}\left(u^{k-1}y_{\eta}-v^{k-1}x_{\eta}\right)u^{*}\Big|^{f}$$

Thus, we have for the time integration:

$$\rho\int_{t}^{t+\Delta t}\left(\sum_{f=1}^{\#\text{ of faces}}\left(u^{k-1}y_{\eta}-v^{k-1}x_{\eta}\right)u^{*}\Big|^{f}\right)dt$$

The velocity from the previous iteration can be removed from the time integral leading to:

$$\rho\sum_{f=1}^{\#\text{ of faces}}\left[\left(u^{k-1}y_{\eta}-v^{k-1}x_{\eta}\right)\int_{t}^{t+\Delta t}u^{*}dt\right]\Bigg|^{f}$$

We need an assumption for how the unknown, u^{*} varies with time from t to $t+\Delta t$. One may propose (Patankar 1980):

$$\int_{t}^{t+\Delta t}u^{*}dt=\left[f\,u^{*,new}+\left(1-f\right)u^{*,old}\right]\Delta t$$

where f is a weighting factor between 0 and 1. Setting f equal to one leads to an implicit time integration; setting f equal to zero, leads to explicit time integration. Since implicit time integration is unconditionally stable, we set f to 1. In this chapter u^{*} has always been assumed to be at the new time level. Thus we write the discretized convective term as

$$\rho\sum_{f=1}^{\#\text{ of faces}}\left[\left(u^{k-1}y_{\eta}-v^{k-1}x_{\eta}\right)u^{*}\right]\Big|^{f}\Delta t$$

Diffusion Term. The discretized diffusion term requires no special treatment other than appending it with Δt as was done in the pressure gradient term and the convective term. Spatial integration over the control volume leads to:

$$-\mu\sum_{f=1}^{\#\text{ of faces}}\left[\frac{u_{0}^{*}-u_{1}^{*}}{q_{3}}\left|J^{-1}\right|\right]\Bigg|^{f}$$

Thus, for time integration we have:

$$-\mu\int_{t}^{t+\Delta t}\left(\sum_{f=1}^{\#\text{ of faces}}\left[\frac{u_{0}^{*}-u_{1}^{*}}{q_{3}}\left|J^{-1}\right|\right]\Bigg|^{f}\right)dt=-\mu\sum_{f=1}^{\#\text{ of faces}}\left[\frac{u_{0}^{*}-u_{1}^{*}}{q_{3}}\left|J^{-1}\right|\right]\Bigg|^{f}\Delta t$$

Final discretized form of dynamic Navier-Stokes equations

Since Δt is common to the pressure gradient, convective, and diffusion terms, both sides of the momentum equation are divided by Δt, and the discretized x and y-momentum equations are written:

x-momentum

$$\rho V\frac{(u^{t+\Delta t}-u^{t})}{\Delta t}=\sum_{f=1}^{\#\text{ of faces}}p\cdot y_{\eta}\Big|^{f}+\rho\sum_{f=1}^{\#\text{ of faces}}\left[\left(u^{k-1}y_{\eta}-v^{k-1}x_{\eta}\right)u^{*}\right]\Big|^{f}-\mu\sum_{f=1}^{\#\text{ of faces}}\left[\frac{u_0^{*}-u_1^{*}}{q_3}\left|J^{-1}\right|\right]\Big|^{f}$$

y-momentum

$$\rho V\frac{(v^{t+\Delta t}-v^{t})}{\Delta t}=-\sum_{f=1}^{\#\text{ of faces}}p\cdot x_{\eta}\Big|^{f}+\rho\sum_{f=1}^{\#\text{ of faces}}\left(u^{k-1}y_{\eta}-v^{k-1}x_{\eta}\right)v^{*}\Big|^{f}-\mu\sum_{f=1}^{\#\text{ of faces}}\left[\frac{v_0^{*}-v_1^{*}}{q_3}\left|J^{-1}\right|\right]\Big|^{f}$$

Ultimately, a linear algebra problem will be solved to compute u^* and v^*. The transition from discrete equations to a linear set of equations is clearer when we bring the unknown variables to the left side and the constants to the right side. In the equations below, u^* and v^* have been rewritten as $u^{t+\Delta t}$ and $v^{t+\Delta t}$. According to the derivation, it seems u^t and v^t should be the values of the velocity components from the previous time step. However, the dynamic Navier-Stokes program is more stable when u^t and v^t are the values of the velocity components from the previous iteration within a given time step. Therefore u^t and v^t will be rewritten as u^{k-1} and v^{k-1}. The pressure term, p^{k-1} is the value of the pressure from the previous iteration within a given time step.

x-momentum

$$\rho V\frac{u_0^{t+\Delta t}}{\Delta t}-\rho\sum_{f=1}^{\#\text{ of faces}}\left[\left(u^{k-1}y_{\eta}-v^{k-1}x_{\eta}\right)u^{t+\Delta t}\right]\Big|^{f}+\mu\sum_{f=1}^{\#\text{ of faces}}\left[\frac{u_0^{t+\Delta t}-u_1^{t+\Delta t}}{q_3}\left|J^{-1}\right|\right]\Big|^{f}=\sum_{f=1}^{\#\text{ of faces}}p^{i-1}\cdot y_{\eta}\Big|^{f}+\rho V\frac{u_0^{k-1}}{\Delta t}\qquad(1\text{-}144)$$

y-momentum

$$\rho V\frac{v_0^{t+\Delta t}}{\Delta t}-\rho\sum_{f=1}^{\#\text{ of faces}}\left[\left(u^{k-1}y_{\eta}-v^{k-1}x_{\eta}\right)v^{t+\Delta t}\right]\Big|^{f}+\mu\sum_{f=1}^{\#\text{ of faces}}\left[\frac{v_0^{t+\Delta t}-v_1^{t+\Delta t}}{q_3}\left|J^{-1}\right|\right]\Big|^{f}=-\sum_{f=1}^{\#\text{ of faces}}p^{i-1}\cdot x_{\eta}\Big|^{f}+\rho V\frac{v_0^{k-1}}{\Delta t}\qquad(1\text{-}145)$$

Solution strategy for dynamic Navier-Stokes equations

The solution steps for the dynamic Navier-Stokes equations follow the same process flow as in Figure 69 except in step 2, eqs. (1-125) and (1-126) are replaced with eqs. (1-144) and (1-145).

Navier-Stokes in Arbitrary Lagrangian-Eulerian Frame

Overview. An Eulerian reference frame is a reference frame in which the quantity of interest (fluid motion for example) is observed by a fixed observer. The classical Navier-Stokes equations are formulated in an Eulerian frame.

When the observer moves with the quantity of interest, the reference frame is referred to as Lagrangian. The classical Newton law and the force balance for a deformable solid (Navier Equations) are written in a Lagrangian form. That is why they do not have the convective term of the substantial derivative in the acceleration term. The mathematical treatment at the moving boundary is said to be Lagrangian because the observer (an imaginary observer sitting on the fluid grid boundary) moves at the same rate as the fluid.

When a fluid domain is stationary, the steady-state or dynamic fluid flow equations introduced earlier in this appendix are applicable. When the domain occupied by the fluid is changing shape as it occurs in moving boundaries, the fluid grid shape and location needs to be

updated to track the motion of the boundaries. A moving mesh is used to express the change in shape, and the conservation balances are written in terms of the moving mesh (ALE Method).

The method is called arbitrary, because there are many ways for the grid to follow the deformed shape. We use a diffusion-type problem to propagate the boundary displacement into the interior of the "moving" mesh. The diffusion problem choice ensures an even distribution of the mesh points away from the moving boundaries and does not require explicit information about the location of the moving wall. Therefore, the diffusion moving mesh update is ideal for moving boundary problems of biological shapes such as the brain implemented with unstructured grids. At a moving boundary, the fluid grid and the fluid move at the same rate (kinematic boundary condition). Internal grid points move according to diffusion such that none of the control volumes in the fluid grid collapse.

Fluid flow inside a moving domain is governed by the Arbitrary Lagrangian-Eulerian (ALE) mathematical framework. First, the motion is the mesh is computed by solving with the diffusion problem; it gives unique displacements of all cell centers, and by averaging, the motion of each cell point. Alternatively, we could just prescribe the motion of the mesh by hand or with an explicit function. Accordingly, the ALE method is termed arbitrary, because it can work with any user defined mesh motion scheme. In flow problems, the fluid grid moves at a different speed than the fluid itself. In solid deformation problems, the grid moves exactly at the speed of the deformation.

In each balance envelope, the fluxes over the face include also an expression accounting for the "motion" of the face. The object of the ALE is to find the states of cell center (e.g. the "Eulerian" velocities) in each step, despite the moving faces enclosing the current cell. Thus the governing flow equations are modified to account for the difference between the convective flux of the fluid with respect to the convective flux of the fluid grid.

Two key points regarding problems involving moving boundaries must be emphasized:

- The local time derivatives in the momentum and continuity equations must be accounted for
- A zero (no-slip) velocity along the moving wall is not appropriate

The first point is due to the fact that the volume (or area in 2D) of the control volumes is changing; the local time derivative accounts for this change. We must account for this volume change to properly balance the change in mass and momentum of a given control volume. The second point is due to the fact that there can be no material separation along the solid-fluid interface. This condition is often referred to as a kinematic boundary condition for the solid-fluid interface. Mathematically it is written,

$$\vec{u}_f = \dot{\vec{d}}$$

where $\vec{u}_f$ is the fluid velocity at the wall and $\dot{\vec{d}}$ is the wall velocity.

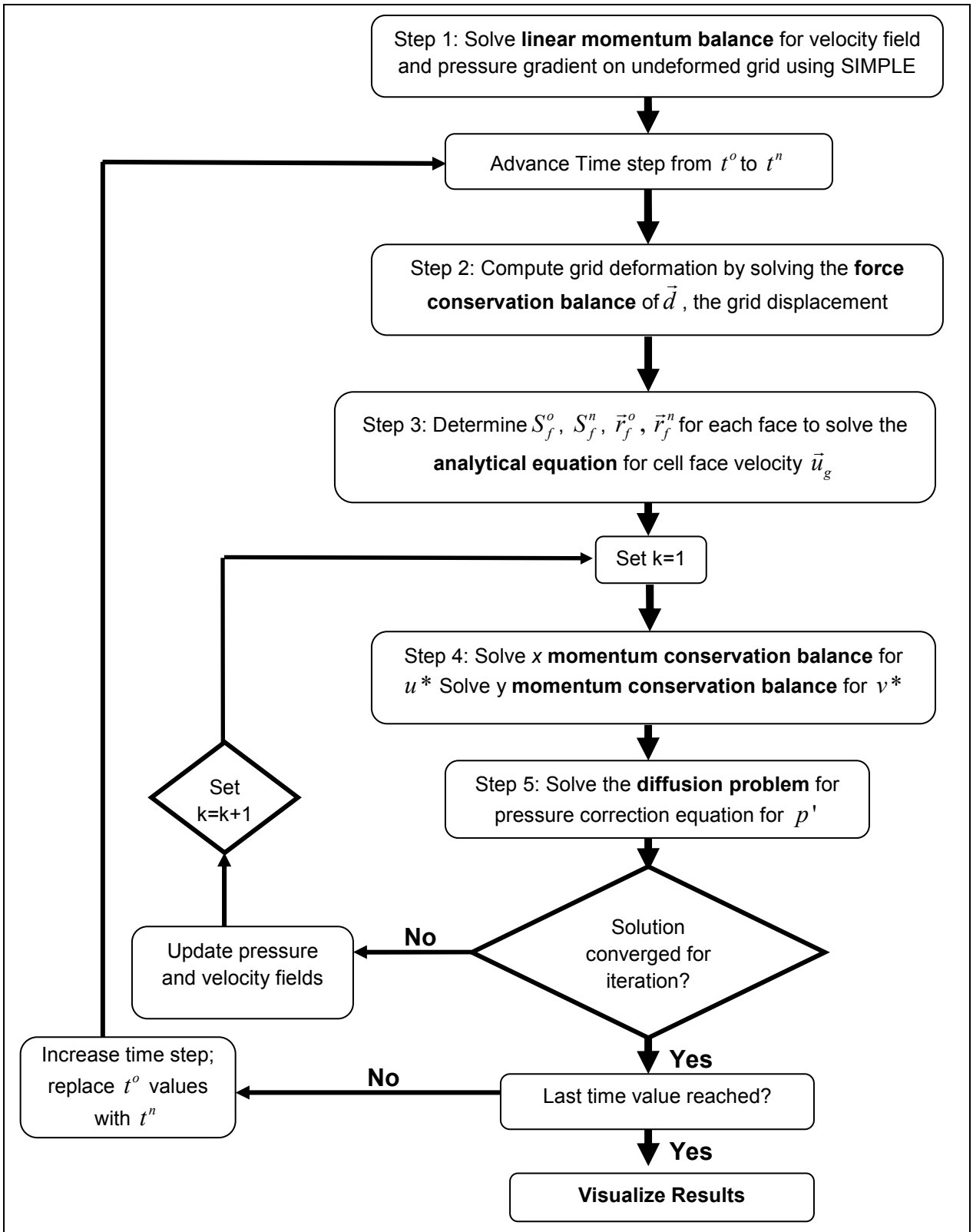

Figure 70. Flow diagram of the SIMPLE method integrated with an ALE approach. The numbered steps and equations are described in the text; *k* is the iteration number.

Appendix B: The SIMPLE Algorithm Derived in Cartesian Coordinates

Discretization of the Fluid Equations in Cartesian Coordinates

Here we present only the steady-state discretization. Consequently, each term of the momentum equation is integrated over a control volume only; the time integration is not considered. Let us refer back to eq. (1-35). We will use $\hat{\vec{n}} = (n_x, n_y) / \sqrt{n_x^2 + n_y^2}$ as the unit outward normal vector to a control volume face.

Pressure Gradient Term

$$-\int_{\text{cv}} \nabla_x p \, dV \quad \overbrace{\Rightarrow}^{\text{Apply Gauss Theorem}} \quad -\oint_{face} p \, \hat{\vec{n}} \, dA$$

Because the integral $\oint_{face} dA$ is the length of the control volume face, that is, $\oint_{face} dA = \sqrt{n_x^2 + n_y^2}$, we have:

$$-\sum_{f=1}^{\#\text{ of faces}} p \begin{pmatrix} n_x \\ n_y \end{pmatrix}$$

For the *x*-momentum, the pressure gradient term is written as:

$$-\sum_{f=1}^{\#\text{ of faces}} p \, n_x \Big|^f$$

For the *y*-momentum, the pressure gradient term is written:

$$-\sum_{f=1}^{\#\text{ of faces}} p \, n_y \Big|^f$$

We actually calculate pressures at the center of a control volume. Thus, the pressure on a face is calculated by averaging the pressures in two adjacent cell centers.

Convective Term

This term causes the Navier-Stokes equations to be nonlinear. To circumvent this problem, we will provide an initial guess ($\vec{u}$, given) for the fluid velocity, such that the momentum equation takes the following form:

$$0 = -\int_{\text{cv}} \nabla_x p \, dV - \rho \int_{\text{cv}} \underbrace{\vec{u}}_{\text{given}} \cdot \overbrace{\nabla u}^{\text{solution variable}} \, dV + \mu \int_{\text{cv}} \nabla \cdot \overbrace{\nabla u}^{\text{solution variable}} \, dV$$

This arrangement is the basis of the SIMPLE algorithm in which $\vec{u}$ is provided via a guess or an earlier iteration. The velocity field resulting from the *x* and *y* momentum equations are then used to correct the pressure field; this will be discussed later. Since $\vec{u} = (u, v)$ is known from a previous iteration, we can take it out of the integral. We will append the superscript *i*-1 to the velocity vector $\vec{u}$ (denoting its value is known from a previous iteration) and append an asterisk to the solution variable, *u*.

$$-\rho \int_{\text{cv}} \vec{u} \cdot \nabla u \, dV = -\rho \left(u^{i-1} \quad v^{i-1} \right) \int_{\text{cv}} \nabla u^* \, dV$$

We now apply Gauss theorem:

$$-\rho\begin{pmatrix} u^{i-1} & v^{i-1}\end{pmatrix}\int_{\text{cv}} \nabla u^* dV = -\rho\begin{pmatrix} u^{i-1} & v^{i-1}\end{pmatrix}\oint_{\text{face}} u^*\,\hat{\vec{n}}\,dA$$

Assuming u^* is constant along the face, dA, and noting that $\hat{\vec{n}} = \left(n_x, n_y\right) / \oint_{face} dA$, we have:

$$-\rho\begin{pmatrix} u^{i-1} & v^{i-1}\end{pmatrix}\int_{\text{face}} u^*\,\hat{\vec{n}}\,dA = -\rho\sum_{f=1}^{\#\text{ of faces}}\begin{pmatrix} u^{i-1} & v^{i-1}\end{pmatrix}\begin{pmatrix} n_x \\ n_y\end{pmatrix}u^*\Big|^f$$

For the *x*-momentum, the convective term is written:

$$-\rho\sum_{f=1}^{\#\text{ of faces}}\left(u^{i-1}n_x + v^{i-1}n_y\right)u^*\Big|^f$$

For the *y*-momentum, the convective term is written:

$$-\rho\sum_{f=1}^{\#\text{ of faces}}\left(u^{i-1}n_x + v^{i-1}n_y\right)v^*\Big|^f$$

The discretization invokes u^* and v^* at the face. u^* at a face is calculated by taking the average of u^* in two adjacent cell centers. The same is done for v^*.

Diffusion Term

$$\mu\int_{\text{cv}}\nabla\cdot\left(\nabla u^*\right)dV \overset{\text{Apply Gauss Theorem}}{=} \mu\oint_{\text{face}}\nabla u^*\cdot\hat{\vec{n}}\,dA$$

Note that $\nabla u^* = \begin{pmatrix}\dfrac{\partial u^*}{\partial x} & \dfrac{\partial u^*}{\partial y}\end{pmatrix}$

Thus, we have,

$$\mu\int_{\text{face}}\begin{pmatrix}\dfrac{\partial u^*}{\partial x} & \dfrac{\partial u^*}{\partial y}\end{pmatrix}\cdot\begin{pmatrix} n_x \\ n_y\end{pmatrix}/\sqrt{n_x^2+n_y^2}\,dA$$

$$\Rightarrow \mu\sum_{f=1}^{\#\text{ of faces}}\left(n_x\frac{\partial u^*}{\partial x} + n_y\frac{\partial u^*}{\partial y}\right)$$

$$\Rightarrow \mu\sum_{f=1}^{\#\text{ of faces}}\left(n_x\frac{u_{\text{center}}-u_{\text{neighbor}}}{x_{\text{center}}-x_{\text{neighbor}}} + n_y\frac{u_{\text{center}}-u_{\text{neighbor}}}{y_{\text{center}}-y_{\text{neighbor}}}\right)$$

From now on, I will abbreviate center as C and neighbor as N. Simplifying the above, we have for the *x*-momentum:

$$\mu\sum_{f=1}^{\#\text{ of faces}}\left(\frac{n_x}{x_{\text{C}}-x_{\text{N}}} + \frac{n_y}{y_{\text{C}}-y_{\text{N}}}\right)(u_{\text{C}}-u_{\text{N}})\Big|^f$$

For the *y*-momentum, the diffusion term is:

$$\mu \sum_{f=1}^{\#\text{ of faces}} \left(\frac{n_x}{x_\text{C} - x_\text{N}} + \frac{n_y}{y_\text{C} - y_\text{N}} \right) (v_\text{C} - v_\text{N}) \Bigg|^f$$

To summarize, eq. (1-37) in its discretized form can be written:

x-momentum $$0 = -\sum_{f=1}^{\#\text{ of faces}} p \cdot n_x \Big|^f - \rho \sum_{f=1}^{\#\text{ of faces}} \left(u^{i-1} n_x + v^{i-1} n_y \right) u^* \Big|^f + \mu \sum_{f=1}^{\#\text{ of faces}} \left(\frac{n_x}{x_\text{C} - x_\text{N}} + \frac{n_y}{y_\text{C} - y_\text{N}} \right) (u_\text{C} - u_\text{N}) \Bigg|^f$$

y-momentum $$0 = -\sum_{f=1}^{\#\text{ of faces}} p \cdot n_y \Big|^f - \rho \sum_{f=1}^{\#\text{ of faces}} \left(u^{i-1} n_x + v^{i-1} n_y \right) v^* \Big|^f + \mu \sum_{f=1}^{\#\text{ of faces}} \left(\frac{n_x}{x_\text{C} - x_\text{N}} + \frac{n_y}{y_\text{C} - y_\text{N}} \right) (v_\text{C} - v_\text{N}) \Bigg|^f$$

The Pressure and Velocity Correction Schemes in Cartesian Coordinates

Implementation

As previously described, the first step in the SIMPLE algorithm is to solve the following momentum equations (assuming steady-state for simplicity):

$$x\text{-momentum: } 0 = -\int_{\text{cv}} \nabla_x p^{i-1} \, dV - \rho \int_{\text{cv}} \vec{u}^{\,i-1} \cdot \left(\nabla u^* \right) dV + \mu \int_{\text{cv}} \nabla \cdot \left(\nabla u^* \right) dV \tag{1-146}$$

$$y\text{-momentum: } 0 = -\int_{\text{cv}} \nabla_y p^{i-1} \, dV - \rho \int_{\text{cv}} \vec{u}^{\,i-1} \cdot \left(\nabla v^* \right) dV + \mu \int_{\text{cv}} \nabla \cdot \left(\nabla v^* \right) dV \tag{1-147}$$

The following form for the velocity correction is proposed:

$$\vec{u}\,' = -\frac{\kappa}{\mu} \nabla p' \tag{1-148}$$

Let us rewrite (1-148) as:

$$\begin{pmatrix} u' \\ v' \end{pmatrix} = -\frac{\kappa}{\mu} \begin{pmatrix} \dfrac{\partial p'}{\partial x} \\ \dfrac{\partial p'}{\partial y} \end{pmatrix}$$

Thus we have two equations for the velocity correction:

$$u' = -\frac{\kappa}{\mu} \left[\frac{p'_\text{C} - p'_\text{N}}{x_\text{C} - x_\text{N}} \right] \tag{1-149}$$

$$v' = -\frac{\kappa}{\mu} \left[\frac{p'_\text{C} - p'_\text{N}}{y_\text{C} - y_\text{N}} \right] \tag{1-150}$$

The velocity correction, $\vec{u}\,'$ is the difference between the correct velocity, $\vec{u}$ and the solution variable, $\begin{pmatrix} u^* & v^* \end{pmatrix}$:

$$\begin{pmatrix} u' \\ v' \end{pmatrix} = \begin{pmatrix} u \\ v \end{pmatrix} - \begin{pmatrix} u^* \\ v^* \end{pmatrix}$$

After rearranging the above expression, eq. (1-151) emerges:

$$\begin{pmatrix} u \\ v \end{pmatrix} = \begin{pmatrix} u^* \\ v^* \end{pmatrix} + \begin{pmatrix} u' \\ v' \end{pmatrix} \tag{1-151}$$

This leads to two equations that represent the correct velocity components, u and v. After substituting eqs. (1-149) and (1-150) into eq. (1-151) we have:

$$u = u^* - \frac{\kappa}{\mu}\left[\frac{p'_{\mathrm{C}} - p'_{\mathrm{N}}}{x_{\mathrm{C}} - x_{\mathrm{N}}}\right] \tag{1-152}$$

$$v = v^* - \frac{\kappa}{\mu}\left[\frac{p'_{\mathrm{C}} - p'_{\mathrm{N}}}{y_{\mathrm{C}} - y_{\mathrm{N}}}\right] \tag{1-153}$$

Note about above. Equations (1-152) and (1-153) require u and v to be calculated at the face. To obtain u at the cell center, compute the average of all face contributions for a given control volume.

If u and v above were the correct velocity, we should expect these velocity components to satisfy continuity for an incompressible fluid:

$$\int_{\mathrm{cv}} \nabla \cdot \vec{u}\, dV = 0 \Rightarrow \oint_{\mathrm{face}} \vec{u} \cdot \vec{n}\, dA = 0$$

With the relation, $\oint_{face} dA = \sqrt{n_x^2 + n_y^2}$, the above can be cast into

$$0 = \sum_{f=1}^{\#\text{of faces}} \begin{pmatrix} u & v \end{pmatrix} \cdot \begin{pmatrix} n_x \\ n_y \end{pmatrix} \Bigg|^f$$

Therefore, the total mass balance is:

$$q = \sum_{f=1}^{\#\text{of faces}} \left(u n_x + v n_y\right) \Big|^f \tag{1-154}$$

For an undeformable fluid grid with an underlying incompressible fluid, q in eq. (1-154) will be zero. For a given face, we can substitute eq. (1-152) and (1-153) into (1-154) and rewrite continuity as:

$$n_x\left[u^* - \frac{\kappa}{\mu}\left(\frac{p'_{\mathrm{C}} - p'_{\mathrm{N}}}{x_{\mathrm{C}} - x_{\mathrm{N}}}\right)\right] + n_y\left[v^* - \frac{\kappa}{\mu}\left(\frac{p'_{\mathrm{C}} - p'_{\mathrm{N}}}{y_{\mathrm{C}} - y_{\mathrm{N}}}\right)\right]$$

This simplifies to:

$$n_x u^* + n_y v^* - \frac{\kappa}{\mu}\left(p'_{\mathrm{C}} - p'_{\mathrm{N}}\right)\left[\frac{n_x}{x_{\mathrm{C}} - x_{\mathrm{N}}} + \frac{n_y}{y_{\mathrm{C}} - y_{\mathrm{N}}}\right]$$

The complete equation which takes into account the contributions from all faces of a control volume is:

$$\sum_{f=1}^{\#\text{ of faces}} \left\{ n_x u^* + n_y v^* - \frac{\kappa}{\mu}\left(p'_{\mathrm{C}} - p'_{\mathrm{N}}\right)\left[\frac{n_x}{x_{\mathrm{C}} - x_{\mathrm{N}}} + \frac{n_y}{y_{\mathrm{C}} - y_{\mathrm{N}}}\right] \right\}\Bigg|^f = 0$$

This leads to the pressure correction equation for p':

$$\sum_{f=1}^{\#\text{ of faces}} \left\{ \frac{\kappa}{\mu}\left(p'_{\mathrm{C}} - p'_{\mathrm{N}}\right)\left[\frac{n_x}{x_{\mathrm{C}} - x_{\mathrm{N}}} + \frac{n_y}{y_{\mathrm{C}} - y_{\mathrm{N}}}\right] \right\}\Bigg|^f = \sum_{f=1}^{\#\text{ of faces}} \left(n_x u^* + n_y v^*\right)\Big|^f \qquad \text{(1-155)}$$

Note about eq. (1-155): First, it should be emphasized that p' is the pressure correction, not the actual pressure. Second, the right-hand-side of eq. (1-155) is continuity (see eq.(1-154)). The left-hand-side seems to describe the deviation from satisfying continuity. If solving the system of equations for the pressure correction, p' leads to p' being zero everywhere, then u^* and v^* satisfy continuity—the left-hand-side will be zero and hence $n_x u^* + n_y v^* = 0$. Thus, at convergence the current velocity field, u^* and v^* satisfies continuity and p' is zero (or sufficiently close to zero) everywhere.

If convergence has not been reached, we apply the relation, $p = p^{i-1} + p'$ to improve the quality of the pressure field. p^{i-1} is the pressure value at the previous iteration. In reality, the improved pressure value will be calculated via under-relaxation:

$$p^{new} = p^{i-1} + \alpha_p p', \quad \text{where} \quad 0 < \alpha_p < 1$$

For the next iteration, p^{i-1} will be set equal to p^{new} and the updated p^{i-1} will be used as the new pressure guess in the momentum equations. The velocities are also updated with under-relaxation. The components that will be used in the momentum equations in the next iteration are:

$$u^{new} = \alpha_u u + \left(1 - \alpha_u\right) u^{i-1}$$
$$v^{new} = \alpha_v v + \left(1 - \alpha_v\right) v^{i-1}$$

From eq. (1-152)

Example Problem for SIMPLE Algorithm Using Cartesian Coordinates

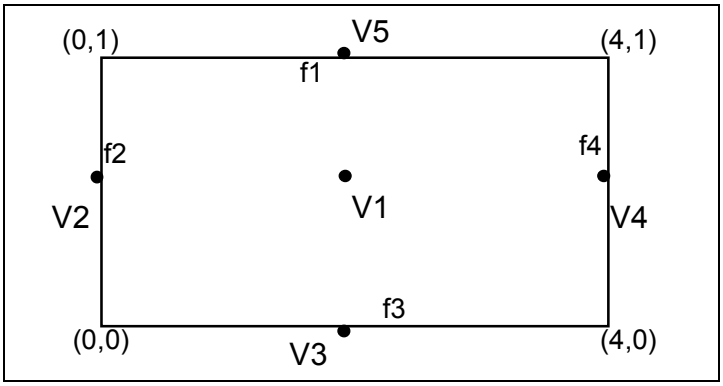

For this problem, set the left boundary to pressure 1 Pa; the right boundary to 0 Pa. Faces 1 and 3 (f1 and f3) are no-slip boundary conditions. Viscosity is 1; density is 1000.

Step 1: Find outward normals for all faces:

Face 1

$(n_x, n_y) = (0, 4)$

Face 2

$(n_x, n_y) = (-1, 0)$

Face 3

$(n_x, n_y) = (0, -4)$

Face 4

$(n_x, n_y) = (1, 0)$

Step 2: Calculate contributions from pressure gradient, convective, and diffusion terms using p^{i-1}, u^{i-1}, and v^{i-1}.

x-momentum

Pressure Gradient Term

Since all pressures are set to zero initially, we only need to calculate the pressure at face 2 (f2). Since f2 is a boundary, one could use the boundary value. But to keep a general scheme, we will average the pressures between v1 and v2:

$$p_{f2} = \frac{p_{V1} + p_{V2}}{2} = \frac{0+1}{2} = 0.5$$

Thus we have for the total face flux for the pressure term:

$$-\sum_{f=1}^{\#\text{ of faces}} p \cdot n_x \Big|^f = -0.5(-1) = 0.5$$

Convective Term

$$-\rho \sum_{f=1}^{\#\text{ of faces}} \left(u^{i-1}n_x + v^{i-1}n_y\right)u^*\Big|^f$$

Since u^{i-1} and v^{i-1} are initially zero, there is no contribution from the convective term on the first iteration.

Diffusion Term

$$\mu \sum_{f=1}^{\#\text{ of faces}} \left(\frac{n_x}{x_C - x_N} + \frac{n_y}{y_C - y_N}\right)(u_C - u_N)\Big|^f \text{ ; recall } \mu = 1$$

Face 1

$$\left(0 + \frac{4}{0.5-1}\right)(u_{V1} - u_{V5}) = -8u_{V1} + 8u_{V5}$$

Face 2

$$\left(\frac{-1}{2-0} + 0\right)(u_{V1} - u_{V2}) = -0.5u_{V1} + 0.5u_{V2}$$

Face 3

$$\left(0 + \frac{-4}{0.5-0}\right)(u_{V1} - u_{V3}) = -8u_{V1} + 8u_{V3}$$

Face 4

$$\left(\frac{1}{2-4} + 0\right)(u_{V1} - u_{V4}) = -0.5u_{V1} + 0.5u_{V4}$$

Step 3: Add up all contributions to establish first equation.

$$0 = 0.5 - 8u_{V1} + 8u_{V5} - 0.5u_{V1} + 0.5u_{V2} - 8u_{V1} + 8u_{V3} - 0.5u_{V1} + 0.5u_{V4}$$
$$\Rightarrow 0 = 0.5 - 17u_{V1} + 0.5u_{V2} + 8u_{V3} + 0.5u_{V4} + 8u_{V5}$$

Step 4: Bring unknowns to left and knowns to right.

$$-17u_{V1} + 0.5u_{V2} + 8u_{V3} + 0.5u_{V4} + 8u_{V5} = -0.5$$

We have 5 control volumes but only 1 equation. The other four equations come from the boundary conditions. We assume that the velocity at the inlet is the same as the velocity in v1. We also assume the velocity at the outlet is the same as the velocity in v1. Thus we have two additional equations:

$$u_{V2} = u_{V1} \Rightarrow u_{V1} - u_{V2} = 0$$
$$u_{V1} = u_{V4} \Rightarrow u_{V1} - u_{V4} = 0$$

We assume “no-slip” at f1 and f3. Thus we have two more equations:

$u_{V3} = 0$

$u_{V5} = 0$

Step 5: Use the five equations and five unknowns to write an Ax=b problem.

$$\begin{bmatrix} -17 & 0.5 & 8 & 0.5 & 8 \\ 1 & -1 & 0 & 0 & 0 \\ 1 & 0 & 0 & -1 & 0 \\ 0 & 0 & 1 & 0 & 0 \\ 0 & 0 & 0 & 0 & 1 \end{bmatrix} \begin{pmatrix} u_{V1} \\ u_{V2} \\ u_{V3} \\ u_{V4} \\ u_{V5} \end{pmatrix} = \begin{pmatrix} -0.5 \\ 0 \\ 0 \\ 0 \\ 0 \end{pmatrix}$$

Using a calculator with matrix functions or Matlab or any other matrix solver, the answer is:

$u_{V1} = 0.03125;\ u_{V2} = 0.03125;\ \ u_{V3} = 0;\ \ u_{V4} = 0.03125;\ u_{V5} = 0$

Step 6: Solve the pressure correction equation to update the pressure and velocity fields.

$$\sum_{f=1}^{\#\text{ of faces}} \left\{ \frac{p'_{\mathrm{C}} - p'_{\mathrm{N}}}{\mu} \left[\frac{n_x}{x_{\mathrm{C}} - x_{\mathrm{N}}} + \frac{n_y}{y_{\mathrm{C}} - y_{\mathrm{N}}} \right] \right\} \Bigg|^f = \sum_{f=1}^{\#\text{ of faces}} \left(n_x u^* + n_y v^* \right) \Big|^f$$

Face 1

$$\frac{p'_{\mathrm{V1}} - p'_{\mathrm{V5}}}{\mu} \left[\frac{n_x}{x_{\mathrm{C}} - x_{\mathrm{N}}} + \frac{n_y}{y_{\mathrm{C}} - y_{\mathrm{N}}} \right] = \left(p'_{\mathrm{V1}} - p'_{\mathrm{V5}} \right) \left[0 + \frac{4}{0.5 - 1} \right] = -8p'_{\mathrm{V1}} + 8p'_{\mathrm{V5}}$$

$0 + 4v^* = 4\dfrac{(v^*_{V1} + v^*_{V5})}{2} = 0$; though we didn't calculate the v* explicitly, if you did, you would find that they should all be zero.

Face 2

$$\left(p'_{\mathrm{V1}} - p'_{\mathrm{V2}} \right) \left[\frac{-1}{2 - 0} + 0 \right] = -0.5p'_{\mathrm{V1}} + 0.5p'_{\mathrm{V2}}$$

$$-1\frac{(u^*_{V1} + u^*_{V2})}{2} = -0.5\left(0.03125 + 0.03125\right) = -0.03125$$

Face 3

$$\left(p'_{\mathrm{V1}} - p'_{\mathrm{V3}} \right) \left[0 + \frac{-4}{0.5 - 0} \right] = -8p'_{\mathrm{V1}} + 8p'_{\mathrm{V3}}$$

$$0 - 4v^* = -4\frac{(v^*_{V1} + v^*_{V3})}{2} = 0$$

Face 4

$$\left(p'_{\mathrm{V1}} - p'_{\mathrm{V4}} \right) \left[\frac{1}{2 - 4} + 0 \right] = -0.5p'_{\mathrm{V1}} + 0.5p'_{\mathrm{V4}}$$

$$1u^* + 0 = 1\frac{(u^*_{V1} + u^*_{V4})}{2} = 0.5(0.03125 + 0.03125) = 0.03125$$

Now we need to add up all contributions (sum the face fluxes):

$$-8p'_{V1} + 8p'_{V5} - 0.5p'_{V1} + 0.5p'_{V2} - 8p'_{V1} + 8p'_{V3} - 0.5p'_{V1} + 0.5p'_{V4} = -0.03125 + 0.03125$$
$$\Rightarrow -17p'_{V1} + 0.5p'_{V2} + 8p'_{V3} + 0.5p'_{V4} + 8p'_{V5} = 0$$

We need four additional equations coming from the boundary conditions. We have from the boundary conditions that p_{f1} is 1 and p_{f4} is 0. So the pressure correction at v2 and v4 is zero:

$$p'_{V2} = 0$$
$$p'_{V4} = 0$$

We also make an assumption about the pressure profile at f1 and f3. We assume that the pressure at these faces is the same as the pressure in the adjacent cell. These means the pressure correction for v5 is the same as the pressure correction for v1 and that the pressure correction for v3 is the same as the pressure correction for v1:

$$p'_{V1} = p'_{V3} \Rightarrow p'_{V1} - p'_{V3} = 0$$
$$p'_{V1} = p'_{V5} \Rightarrow p'_{V1} - p'_{V5} = 0$$

Now we can set up our system of equations for the pressure correction:

$$-8p'_{V1} + 8p'_{V5} - 0.5p'_{V1} + 0.5p'_{V2} - 8p'_{V1} + 8p'_{V3} - 0.5p'_{V1} + 0.5p'_{V4} = -0.03125 + 0.03125$$
$$\Rightarrow -17p'_{V1} + 0.5p'_{V2} + 8p'_{V3} + 0.5p'_{V4} + 8p'_{V5} = 0$$

$$\begin{bmatrix} -17 & 0.5 & 8 & 0.5 & 8 \\ 0 & 1 & 0 & 0 & 0 \\ 0 & 0 & 0 & 1 & 0 \\ 1 & 0 & -1 & 0 & 0 \\ 1 & 0 & 0 & 0 & -1 \end{bmatrix} \begin{pmatrix} p'_{V1} \\ p'_{V2} \\ p'_{V3} \\ p'_{V4} \\ p'_{V5} \end{pmatrix} = \begin{pmatrix} 0 \\ 0 \\ 0 \\ 0 \\ 0 \end{pmatrix}$$

For this system, the pressure corrections are all zero. One consequence of doing the analysis for a one cell grid is that continuity is deceptively satisfied. One should keep in mind that this was a very coarse grid and in reality the solution has really not converged.

Probably from some educated guess, you believe the pressure correction should really be 0.5 for V1. Let's continue the SIMPLE algorithm assuming this is the case. So we will assume the pressure correction equation resulted in

$$p'_{V1} = 0.5; \quad p'_{V2} = 0; \quad p'_{V3} = 0.5; \quad p'_{V4} = 0; \quad p'_{V5} = 0.5$$

Step 7: Calculate "correct" velocity

We need to solve for the correct velocity. I first solve for the velocity correction in the internal control volumes by averaging the contributions from the faces.

$$u_{V1} = \text{Average of } \left\{ u^* - \frac{1}{\mu}\left[\frac{p'_{\mathrm{C}} - p'_{\mathrm{N}}}{x_{\mathrm{C}} - x_{\mathrm{N}}} \right] \right\}$$

Face 1

$$\frac{u^*_{V1} + u^*_{V5}}{2} - \left[\frac{p'_{\mathrm{V1}} - p'_{\mathrm{V5}}}{x_{\mathrm{V1}} - x_{\mathrm{V5}}} \right] = \frac{0.03125 + 0}{2} - \left[\frac{0}{x_{\mathrm{V1}} - x_{\mathrm{V5}}} \right] = 0.015625$$

Face 2

$$\frac{u^*_{V1} + u^*_{V2}}{2} - \left[\frac{p'_{\mathrm{V1}} - p'_{\mathrm{V2}}}{x_{\mathrm{V1}} - x_{\mathrm{V2}}} \right] = \frac{0.03125 + 0.03125}{2} - \left[\frac{0.5 - 0}{2 - 0} \right] = -0.21875$$

Face 3

$$\frac{u^*_{V1} + u^*_{V3}}{2} - \left[\frac{p'_{\mathrm{V1}} - p'_{\mathrm{V3}}}{x_{\mathrm{V1}} - x_{\mathrm{V3}}} \right] = \frac{0.03125 + 0}{2} - \left[\frac{0}{x_{\mathrm{V1}} - x_{\mathrm{V3}}} \right] = 0.015625$$

Face 4

$$\frac{u^*_{V1} + u^*_{V4}}{2} - \left[\frac{p'_{\mathrm{V1}} - p'_{\mathrm{V4}}}{x_{\mathrm{V1}} - x_{\mathrm{V4}}} \right] = \frac{0.03125 + 0.03125}{2} - \left[\frac{0.5 - 0}{2 - 4} \right] = 0.28125$$

So the correct velocity is:

$$\left(0.015625 - 0.21875 + 0.015625 + 0.28125\right)/4 = 0.0234375$$

Basically, what happened here is that I used the velocity vectors and pressure corrections from the faces that surround V1 and averaged their contributions (you see I divided by 4 above) to the velocity correction. This is illustrated in Figure 71; the "correct" velocities at the face are averaged to obtain a "correct" velocity for the control volume.

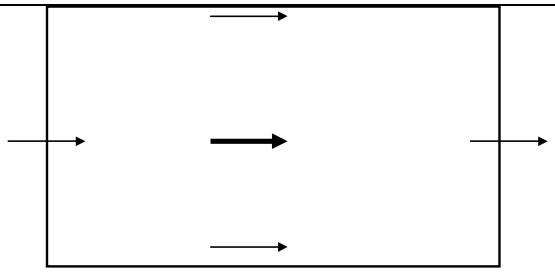

Figure 71. The velocity values at the face (thin arrows) are averaged to obtain a "correct" velocity for the cell center (thick arrow).

The velocity corrections in the other 4 volumes (boundary volumes) are determined from the boundary conditions. Since the velocity at the inlet and outlet is the same as V1 the velocity for V2 and V4 will also be 0.0234375. Since there is no-slip on V3 and V5 their velocities remain zero.

Step 8: Update the pressure field
Using the pressure correction values we need to update the pressure field. The initial pressures were:

$$p_{V1} = 0; p_{V2} = 1; p_{V3} = 0; p_{V4} = 0; p_{V5} = 0$$

The pressure corrections (that we invented) were:

$$p'_{V1} = 0.5; \quad p'_{V2} = 0; \quad p'_{V3} = 0.5; \quad p'_{V4} = 0; \quad p'_{V5} = 0.5$$

Using an under-relaxation parameter for pressure of $\alpha_p = 0.3$ (0.3 is what Fluent uses as a default for the pressure under-relaxation) the updated pressure field is:

$$p_{V1} = 0 + (0.3)(0.5) = 0.15$$
$$p_{V2} = 1 + (0.3)(0) \quad = 1$$
$$p_{V3} = 0 + (0.3)(0.5) = 0.15$$
$$p_{V4} = 0 + (0.3)(0) \quad = 0$$
$$p_{V5} = 0 + (0.3)(0.5) = 0.15$$

This updated pressure field will now be used as p^{i-1} in the next SIMPLE iteration. Though not worked-out in this example, one must remember to apply under-relaxation to the "correct" velocities we calculated earlier. The updated velocities (after applying under-relaxation) then become u^{i-1} and v^{i-1} in the next SIMPLE iteration.

Appendix C: Example Problem for SIMPLE Algorithm Using Generalized Coordinates

The SIMPLE algorithm is demonstrated with a specific example. Figure 72a shows the computational domain with control volumes labeled v1 through v21. The faces are labeled f1 through f24. To motivate the case study, Figure 72b shows the flow field for this problem obtained using the commercial CFD tool, Comsol. The Comsol grid consisted of about 2,000 control volumes.

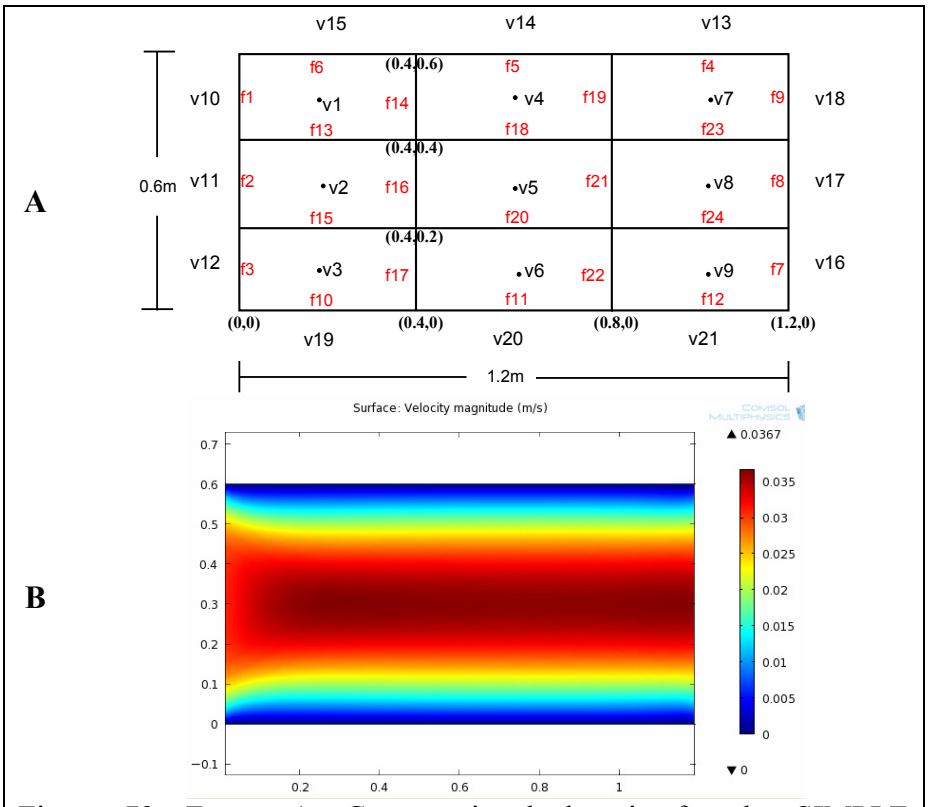

Figure 72. Frame A: Computational domain for the SIMPLE algorithm example. There are nine interior volumes and 12 boundary volumes. Frame B: Flow solution in Comsol. Right: Mesh density used in the Comsol solution.

Important Note: To calculate the pressure at a given face, the pressures in the control volumes adjacent to the face are averaged. For example, to calculate the pressure at face 14, the following calculation is performed:

$$p_{f14} = \frac{p_{v1} + p_{v4}}{2}$$

This simple average procedure is also used for the boundary volumes. For example, if computing the pressure at f1, the following calculation is performed:

$$p_{f1} = \frac{p_{v10} + p_{v1}}{2}$$

In the actual computer program, this average might not be sufficient. More importantly, in the computer implementation, the center of v10 is actually coincident with the center of f1. Thus, one could take the value specified at v10 as the face value instead of calculating an average value based on v10 and v1.

To solve the problem, we adhere to the following steps.

Step 1: Specify boundary conditions

Fluid wall: v19, v20, v21, v15, v14, and v13 should have (u,v) equal to zero for all times.

Pressure inlet: v10, v11, v12 should have 1Pa of pressure

Pressure outlet: v18, v17, v16 should have 0Pa of pressure

Velocity outlet: v18, v17, v16 should be related to v7, v8, v9 by $\frac{\partial u}{\partial x} = \frac{\partial v}{\partial x} = 0$; this specifies that the fluid flow should establish a parabolic profile. It means that the following relationships hold:

- Fluid velocity in v18 equals velocity in v7
- Fluid velocity in v17 equals velocity in v8
- Fluid velocity in v16 equals velocity in v9

Velocity inlet: same argument above applies to inlet boundary as well so that we have:

- Fluid velocity in v10 equals velocity in v1
- Fluid velocity in v11 equals velocity in v2
- Fluid velocity in v12 equals velocity in v3

Step 2: Specify material properties

Density, $\rho = 1000 kg/m^3$; viscosity, $\mu = 1\ \text{Pa}\cdot\text{s}$; Note viscosity here is 1000 times greater than water.

Step 3: Initialize the pressure and velocity fields

All pressures and velocities will be set to zero except for the values we specify for the boundary conditions. Boundary cells, v10, v11, v12 are given a Dirichlet value of 1Pa. The pressure at the outlet boundary cells, v18, v17, v16 is zero.

Step 4: Compute the momentum face fluxes for all control volumes

Volume 1

Pressure gradient term

$$-\left[p_{\text{face}} \cdot y_\eta \Big|^{1} + p_{\text{face}} \cdot y_\eta \Big|^{6} + p_{\text{face}} \cdot y_\eta \Big|^{14} + p_{\text{face}} \cdot y_\eta \Big|^{13} \right]$$

$$p_{\text{face1}} = \frac{1}{2}\left(p_{\text{v1}} + p_{\text{v10}}\right) = 0.5(0+1) = 0.5\ ;\ p_{\text{face6}} = \frac{1}{2}\left(p_{\text{v1}} + p_{\text{v15}}\right) = 0\ ;$$

$$p_{\text{face14}} = \frac{1}{2}\left(p_{\text{v1}} + p_{\text{v4}}\right) = 0\ ;\ p_{\text{face13}} = \frac{1}{2}\left(p_{\text{v1}} + p_{\text{v2}}\right) = 0$$

$$y_{\eta\text{face1}} = 0.2;\ y_{\eta\text{face6}} = 0;\ y_{\eta\text{face14}} = -0.2;\ y_{\eta\text{face13}} = 0$$

$$\Rightarrow -\left[p_{\text{face}} \cdot y_\eta \Big|^{1} + p_{\text{face}} \cdot y_\eta \Big|^{6} + p_{\text{face}} \cdot y_\eta \Big|^{14} + p_{\text{face}} \cdot y_\eta \Big|^{13} \right] = -\left[0.5(0.2) + 0 + 0 + 0\right] = -0.1$$

Convection term (Recall $\rho = 1000 kg/m^3$)

$$-1000\left[0\cdot\overbrace{\left(\frac{u^*_{v1}+u^*_{v10}}{2}\right)}^{\text{face1}}+0\cdot\overbrace{\left(\frac{u^*_{v1}+u^*_{v15}}{2}\right)}^{\text{face6}}+0\cdot\overbrace{\left(\frac{u^*_{v1}+u^*_{v4}}{2}\right)}^{\text{face14}}+0\cdot\overbrace{\left(\frac{u^*_{v1}+u^*_{v2}}{2}\right)}^{\text{face13}}\right]$$

There are zeros multiplying the unknowns in the convective term because we initialize the fluid vectors as zero.

Diffusion term (Recall $\mu = 1\ \text{Pa}\cdot\text{s}$)

$$1\left\{\begin{array}{l}\dfrac{u^*_{v1}-u^*_{v10}}{(0.2)^2+(0)^2}\left[(0.2)(0.2)-(0)(0)\right]+\dfrac{u^*_{v1}-u^*_{v15}}{(0)^2+(-0.1)^2}\left[(0)(0)-(0.4)(-0.1)\right]\\ +\dfrac{u^*_{v1}-u^*_{v4}}{(-0.4)^2+(0)^2}\left[(-0.4)(-0.2)-(0)(0)\right]+\dfrac{u^*_{v1}-u^*_{v2}}{(0)^2+(0.2)^2}\left[(0)(0)-(-0.4)(0.2)\right]\end{array}\right\}$$

The above reduces to the equation for Volume (cell) 1:

$$7.5u^*_{v1}-2u^*_{v2}\ldots-0.5u^*_{v4}\ldots-u^*_{v10}\ldots-4u^*_{v15}-\overbrace{0.1}^{\text{from }\nabla p}=0$$

Volume 2

Pressure gradient term

$$p_{\text{face2}}=\frac{1}{2}\left(p_{v2}+p_{v11}\right)=0.5(0+1)=0.5;\ p_{\text{face16}}=\frac{1}{2}\left(p_{v2}+p_{v5}\right)=0;$$

$$p_{\text{face13}}=\frac{1}{2}\left(p_{v2}+p_{v1}\right)=0;\ p_{\text{face15}}=\frac{1}{2}\left(p_{v2}+p_{v3}\right)=0$$

$$y_{\eta\text{face2}}=0.2;\ y_{\eta\text{face16}}=-0.2;\ y_{\eta\text{face13}}=0;\ y_{\eta\text{face15}}=0$$

$$\Rightarrow -\left[0.5(0.2)+0+0+0\right]=-0.1$$

Convection term

$$-1000\left[0\cdot\overbrace{\left(\frac{u^*_{v2}+u^*_{v11}}{2}\right)}^{\text{face2}}+0\cdot\overbrace{\left(\frac{u^*_{v2}+u^*_{v1}}{2}\right)}^{\text{face13}}+0\cdot\overbrace{\left(\frac{u^*_{v2}+u^*_{v5}}{2}\right)}^{\text{face16}}+0\cdot\overbrace{\left(\frac{u^*_{v2}+u^*_{v3}}{2}\right)}^{\text{face15}}\right]$$

Diffusion term

$$1\left\{\begin{array}{l}\dfrac{u^*_{v2}-u^*_{v11}}{(0.2)^2+(0)^2}\left[(0.2)(0.2)-(0)(0)\right]+\dfrac{u^*_{v2}-u^*_{v1}}{(0)^2+(-0.2)^2}\left[(0)(0)-(0.4)(-0.2)\right]\\ +\dfrac{u^*_{v2}-u^*_{v5}}{(-0.4)^2+(0)^2}\left[(-0.4)(-0.2)-(0)(0)\right]+\dfrac{u^*_{v2}-u^*_{v3}}{(0)^2+(0.2)^2}\left[(0)(0)-(-0.4)(0.2)\right]\end{array}\right\}$$

Above reduces to an equation for Volume (cell) 2:

$$-2u^*_{v1} + 5.5u^*_{v2} - 2u^*_{v3} \ldots - 0.5u^*_{v5} \ldots - u^*_{v11} - \overbrace{0.1}^{\text{from } \nabla p} = 0$$

Volume 3

Pressure gradient term

$$p_{face3} = \frac{1}{2}\left(p_{v3} + p_{v12}\right) = 0.5\left(0+1\right) = 0.5;\ \ p_{face17} = p_{face10} = p_{face15} = 0$$

$$y_{\eta face3} = 0.2;\ \ y_{\eta face17} = -0.2;\ \ y_{\eta face10} = 0;\ \ y_{\eta face15} = 0$$

$$\Rightarrow -\left[0.5(0.2) + 0 + 0 + 0\right] = -0.1$$

Convection term

$$-1000\left[0 \cdot \left(\frac{u^*_{v3} + u^*_{v12}}{2}\right) + 0 \cdot \left(\frac{u^*_{v3} + u^*_{v2}}{2}\right) + 0 \cdot \left(\frac{u^*_{v3} + u^*_{v6}}{2}\right) + 0 \cdot \left(\frac{u^*_{v3} + u^*_{v19}}{2}\right)\right]$$

Diffusion term

$$1\left\{\begin{array}{l} \dfrac{u^*_{v3} - u^*_{v12}}{(0.2)^2 + (0)^2}\left[(0.2)(0.2) - (0)(0)\right] + \dfrac{u^*_{v3} - u^*_{v2}}{(0)^2 + (-0.2)^2}\left[(0)(0) - (0.4)(-0.2)\right] \\ + \dfrac{u^*_{v3} - u^*_{v6}}{(-0.4)^2 + (0)^2}\left[(-0.4)(-0.2) - (0)(0)\right] + \dfrac{u^*_{v3} - u^*_{v19}}{(0)^2 + (0.1)^2}\left[(0)(0) - (-0.4)(0.1)\right] \end{array}\right\}$$

Above reduces to an equation for Volume (cell) 3:

$$\ldots - 2u^*_{v2} + 7.5u^*_{v3} \ldots - 0.5u^*_{v6} \ldots - u^*_{v12} \ldots - 4u^*_{v19} - \overbrace{0.1}^{\text{from } \nabla p} = 0$$

For Volumes 4-9, the only contribution is from the diffusion term (on this first iteration):

Volume 4

$$1\left\{\begin{array}{l} \dfrac{u^*_{v4} - u^*_{v1}}{(0.4)^2 + (0)^2}\left[(0.4)(0.2) - (0)(0)\right] + \dfrac{u^*_{v4} - u^*_{v14}}{(0)^2 + (-0.1)^2}\left[(0)(0) - (0.4)(-0.1)\right] \\ + \dfrac{u^*_{v4} - u^*_{v7}}{(-0.4)^2 + (0)^2}\left[(-0.4)(-0.2) - (0)(0)\right] + \dfrac{u^*_{v4} - u^*_{v5}}{(0)^2 + (0.2)^2}\left[(0)(0) - (-0.4)(0.2)\right] \end{array}\right\}$$

Equation for Volume 4

$$-0.5u^*_{v1} \ldots + 7u^*_{v4} - 2u^*_{v5} \ldots - 0.5u^*_{v7} \ldots - 4u^*_{v14} = 0$$

Volume 5

$$1\left\{\begin{array}{l} \dfrac{u^*_{v5} - u^*_{v2}}{(0.4)^2 + (0)^2}\left[(0.4)(0.2) - (0)(0)\right] + \dfrac{u^*_{v5} - u^*_{v4}}{(0)^2 + (-0.2)^2}\left[(0)(0) - (0.4)(-0.2)\right] \\ + \dfrac{u^*_{v5} - u^*_{v8}}{(-0.4)^2 + (0)^2}\left[(-0.4)(-0.2) - (0)(0)\right] + \dfrac{u^*_{v5} - u^*_{v6}}{(0)^2 + (0.2)^2}\left[(0)(0) - (-0.4)(0.2)\right] \end{array}\right\}$$

Equation for Volume 5:

$$\ldots - 0.5u_{v2}^{*} \ldots - 2u_{v4}^{*} + 5u_{v5}^{*} - 2u_{v6}^{*} \ldots - 0.5u_{v8}^{*} = 0$$

Volume 6

$$1\left\{\begin{array}{l}\dfrac{u_{v6}^{*}-u_{v3}^{*}}{(0.4)^{2}+(0)^{2}}\left[(0.4)(0.2)-(0)(0)\right]+\dfrac{u_{v6}^{*}-u_{v5}^{*}}{(0)^{2}+(-0.2)^{2}}\left[(0)(0)-(0.4)(-0.2)\right] \\ +\dfrac{u_{v6}^{*}-u_{v9}^{*}}{(-0.4)^{2}+(0)^{2}}\left[(-0.4)(-0.2)-(0)(0)\right]+\dfrac{u_{v6}^{*}-u_{v20}^{*}}{(0)^{2}+(0.1)^{2}}\left[(0)(0)-(-0.4)(0.1)\right]\end{array}\right\}$$

Equation for Volume 6:

$$\ldots - 0.5u_{v3}^{*} \ldots - 2u_{v5}^{*} + 7u_{v6}^{*} \ldots - 0.5u_{v9}^{*} \ldots - 4u_{v20}^{*} = 0$$

Volume 7

$$1\left\{\begin{array}{l}\dfrac{u_{v7}^{*}-u_{v4}^{*}}{(0.4)^{2}+(0)^{2}}\left[(0.4)(0.2)-(0)(0)\right]+\dfrac{u_{v7}^{*}-u_{v13}^{*}}{(0)^{2}+(-0.1)^{2}}\left[(0)(0)-(0.4)(-0.1)\right] \\ +\dfrac{u_{v7}^{*}-u_{v18}^{*}}{(-0.2)^{2}+(0)^{2}}\left[(-0.2)(-0.2)-(0)(0)\right]+\dfrac{u_{v7}^{*}-u_{v8}^{*}}{(0)^{2}+(0.2)^{2}}\left[(0)(0)-(-0.4)(0.2)\right]\end{array}\right\}$$

Equation for Volume 7:

$$\ldots - 0.5u_{v4}^{*} \ldots + 7.5u_{v7}^{*} - 2u_{v8}^{*} \ldots - 4u_{v13}^{*} \ldots - u_{v18}^{*} = 0$$

Volume 8

$$1\left\{\begin{array}{l}\dfrac{u_{v8}^{*}-u_{v5}^{*}}{(0.4)^{2}+(0)^{2}}\left[(0.4)(0.2)-(0)(0)\right]+\dfrac{u_{v8}^{*}-u_{v7}^{*}}{(0)^{2}+(-0.2)^{2}}\left[(0)(0)-(0.4)(-0.2)\right] \\ +\dfrac{u_{v8}^{*}-u_{v17}^{*}}{(-0.2)^{2}+(0)^{2}}\left[(-0.2)(-0.2)-(0)(0)\right]+\dfrac{u_{v8}^{*}-u_{v9}^{*}}{(0)^{2}+(0.2)^{2}}\left[(0)(0)-(-0.4)(0.2)\right]\end{array}\right\}$$

Equation for Volume 8:

$$\ldots - 0.5u_{v5}^{*} \ldots - 2u_{v7}^{*} + 5.5u_{v8}^{*} - 2u_{v9}^{*} \ldots - u_{v17}^{*} = 0$$

Volume 9

$$1\left\{\begin{array}{l}\dfrac{u_{v9}^{*}-u_{v6}^{*}}{(0.4)^{2}+(0)^{2}}\left[(0.4)(0.2)-(0)(0)\right]+\dfrac{u_{v9}^{*}-u_{v8}^{*}}{(0)^{2}+(-0.2)^{2}}\left[(0)(0)-(0.4)(-0.2)\right] \\ +\dfrac{u_{v9}^{*}-u_{v16}^{*}}{(-0.2)^{2}+(0)^{2}}\left[(-0.2)(-0.2)-(0)(0)\right]+\dfrac{u_{v9}^{*}-u_{v21}^{*}}{(0)^{2}+(0.1)^{2}}\left[(0)(0)-(-0.4)(0.1)\right]\end{array}\right\}$$

Equation for Volume 9:

$$\ldots - 0.5u_{v6}^{*} \ldots - 2u_{v8}^{*} + 7.5u_{v9}^{*} \ldots - u_{v16}^{*} \ldots - 4u_{v21}^{*} = 0$$

Boundary Equations (Volumes 10-21)

Assumption on flow profile at inlet

V10: $u_{v10}^{*} - u_{v1}^{*} = 0$

V11: $u^*_{v11} - u^*_{v2} = 0$
V12: $u^*_{v12} - u^*_{v3} = 0$

Fluid wall boundary
V13, 14, 15, 19, 20, 21: $u^* = 0$

Assumption on flow profile at outlet
V18: $u^*_{v7} - u^*_{v18} = 0$
V17: $u^*_{v8} - u^*_{v17} = 0$
V16: $u^*_{v9} - u^*_{v16} = 0$

y-momentum
The *y*-momentum equations for this first iteration will match the *x*-momentum equations with the exception of equations coming from vols 1, 2, and 3. In these three volumes, the contribution from the pressure gradient is zero because x_η for faces 1, 2, and 3 is zero.

This means we have two systems of equations:
x-momentum:
$7.5u^*_{v1} - 2u^*_{v2} \ldots - 0.5u^*_{v4} \ldots - u^*_{v10} \ldots - 4u^*_{v15} - 0.1 = 0$
$-2u^*_{v1} + 5.5u^*_{v2} - 2u^*_{v3} \ldots - 0.5u^*_{v5} \ldots - u^*_{v11} - 0.1 = 0$
$\ldots - 2u^*_{v2} + 7.5u^*_{v3} \ldots - 0.5u^*_{v6} \ldots - u^*_{v12} \ldots - 4u^*_{v19} - 0.1 = 0$
$-0.5u^*_{v1} \ldots + 7u^*_{v4} - 2u^*_{v5} \ldots - 0.5u^*_{v7} \ldots - 4u^*_{v14} = 0$
$\ldots - 0.5u^*_{v2} \ldots - 2u^*_{v4} + 5u^*_{v5} - 2u^*_{v6} \ldots - 0.5u^*_{v8} = 0$
$\ldots - 0.5u^*_{v3} \ldots - 2u^*_{v5} + 7u^*_{v6} \ldots - 0.5u^*_{v9} \ldots - 4u^*_{v20} = 0$
$\ldots - 0.5u^*_{v4} \ldots + 7.5u^*_{v7} - 2u^*_{v8} \ldots - 4u^*_{v13} \ldots - u^*_{v18} = 0$
$\ldots - 0.5u^*_{v5} \ldots - 2u^*_{v7} + 5.5u^*_{v8} - 2u^*_{v9} \ldots - u^*_{v17} = 0$
$\ldots - 0.5u^*_{v6} \ldots - 2u^*_{v8} + 7.5u^*_{v9} \ldots - u^*_{v16} \ldots - 4u^*_{v21} = 0$
$-u^*_{v1} \ldots + u^*_{v10} = 0$
$-u^*_{v2} \ldots + u^*_{v11} = 0$
$-u^*_{v3} \ldots + u^*_{v12} = 0$
$u^*_{v13} = 0$
$u^*_{v14} = 0$
$u^*_{v15} = 0$
$u^*_{v19} = 0$
$u^*_{v20} = 0$
$u^*_{v21} = 0$
$u^*_{v7} \ldots - u^*_{v18} = 0$

$$u^*_{v8}\ldots - u^*_{v17} = 0$$
$$u^*_{v9}\ldots - u^*_{v16} = 0$$

y-momentum:

$$7.5v^*_{v1} - 2v^*_{v2}\ldots - 0.5v^*_{v4}\ldots - v^*_{v10}\ldots - 4v^*_{v15} = 0$$
$$-2v^*_{v1} + 5.5v^*_{v2} - 2v^*_{v3}\ldots - 0.5v^*_{v5}\ldots - v^*_{v11} = 0$$
$$\ldots - 2v^*_{v2} + 7.5v^*_{v3}\ldots - 0.5v^*_{v6}\ldots - v^*_{v12}\ldots - 4v^*_{v19} = 0$$
$$-0.5v^*_{v1}\ldots + 7v^*_{v4} - 2v^*_{v5}\ldots - 0.5v^*_{v7}\ldots - 4v^*_{v14} = 0$$
$$\ldots - 0.5v^*_{v2}\ldots - 2v^*_{v4} + 5v^*_{v5} - 2v^*_{v6}\ldots - 0.5v^*_{v8} = 0$$
$$\ldots - 0.5v^*_{v3}\ldots - 2v^*_{v5} + 7v^*_{v6}\ldots - 0.5v^*_{v9}\ldots - 4v^*_{v20} = 0$$
$$\ldots - 0.5v^*_{v4}\ldots + 7.5v^*_{v7} - 2v^*_{v8}\ldots - 4v^*_{v13}\ldots - v^*_{v18} = 0$$
$$\ldots - 0.5v^*_{v5}\ldots - 2v^*_{v7} + 5.5v^*_{v8} - 2v^*_{v9}\ldots - v^*_{v17} = 0$$
$$\ldots - 0.5v^*_{v6}\ldots - 2v^*_{v8} + 7.5v^*_{v9}\ldots - v^*_{v16}\ldots - 4v^*_{v21} = 0$$
$$-v^*_{v1}\ldots + v^*_{v10} = 0$$
$$-v^*_{v2}\ldots + v^*_{v11} = 0$$
$$-v^*_{v3}\ldots + v^*_{v12} = 0$$
$$v^*_{v13} = 0$$
$$v^*_{v14} = 0$$
$$v^*_{v15} = 0$$
$$v^*_{v19} = 0$$
$$v^*_{v20} = 0$$
$$v^*_{v21} = 0$$
$$v^*_{v7}\ldots - v^*_{v18} = 0$$
$$v^*_{v8}\ldots - v^*_{v17} = 0$$
$$v^*_{v9}\ldots - v^*_{v16} = 0$$

It is more convenient to write them in matrix form as:
x-momentum:

$$\begin{bmatrix}
7.5 & -2 & 0 & -0.5 & 0 & 0 & 0 & 0 & 0 & -1 & 0 & 0 & 0 & 0 & -4 & 0 & 0 & 0 & 0 & 0 & 0 \\
-2 & 5.5 & -2 & 0 & -0.5 & 0 & 0 & 0 & 0 & 0 & -1 & 0 & 0 & 0 & 0 & 0 & 0 & 0 & 0 & 0 & 0 \\
0 & -2 & 7.5 & 0 & 0 & -0.5 & 0 & 0 & 0 & 0 & 0 & -1 & 0 & 0 & 0 & 0 & 0 & 0 & -4 & 0 & 0 \\
-0.5 & 0 & 0 & 7 & -2 & 0 & -0.5 & 0 & 0 & 0 & 0 & 0 & 0 & -4 & 0 & 0 & 0 & 0 & 0 & 0 & 0 \\
0 & -0.5 & 0 & -2 & 5 & -2 & 0 & -0.5 & 0 & 0 & 0 & 0 & 0 & 0 & 0 & 0 & 0 & 0 & 0 & 0 & 0 \\
0 & 0 & -0.5 & 0 & -2 & 7 & 0 & 0 & -0.5 & 0 & 0 & 0 & 0 & 0 & 0 & 0 & 0 & 0 & 0 & -4 & 0 \\
0 & 0 & 0 & -0.5 & 0 & 0 & 7.5 & -2 & 0 & 0 & 0 & 0 & -4 & 0 & 0 & 0 & 0 & -1 & 0 & 0 & 0 \\
0 & 0 & 0 & 0 & -0.5 & 0 & -2 & 5.5 & -2 & 0 & 0 & 0 & 0 & 0 & 0 & 0 & -1 & 0 & 0 & 0 & 0 \\
0 & 0 & 0 & 0 & 0 & -0.5 & 0 & -2 & 7.5 & 0 & 0 & 0 & 0 & 0 & 0 & -1 & 0 & 0 & 0 & 0 & -4 \\
-1 & 0 & 0 & 0 & 0 & 0 & 0 & 0 & 0 & 1 & 0 & 0 & 0 & 0 & 0 & 0 & 0 & 0 & 0 & 0 & 0 \\
0 & -1 & 0 & 0 & 0 & 0 & 0 & 0 & 0 & 0 & 1 & 0 & 0 & 0 & 0 & 0 & 0 & 0 & 0 & 0 & 0 \\
0 & 0 & -1 & 0 & 0 & 0 & 0 & 0 & 0 & 0 & 0 & 1 & 0 & 0 & 0 & 0 & 0 & 0 & 0 & 0 & 0 \\
0 & 0 & 0 & 0 & 0 & 0 & 0 & 0 & 0 & 0 & 0 & 0 & 1 & 0 & 0 & 0 & 0 & 0 & 0 & 0 & 0 \\
0 & 0 & 0 & 0 & 0 & 0 & 0 & 0 & 0 & 0 & 0 & 0 & 0 & 1 & 0 & 0 & 0 & 0 & 0 & 0 & 0 \\
0 & 0 & 0 & 0 & 0 & 0 & 0 & 0 & 0 & 0 & 0 & 0 & 0 & 0 & 1 & 0 & 0 & 0 & 0 & 0 & 0 \\
0 & 0 & 0 & 0 & 0 & 0 & 0 & 0 & 0 & 0 & 0 & 0 & 0 & 0 & 0 & 0 & 0 & 0 & 1 & 0 & 0 \\
0 & 0 & 0 & 0 & 0 & 0 & 0 & 0 & 0 & 0 & 0 & 0 & 0 & 0 & 0 & 0 & 0 & 0 & 0 & 1 & 0 \\
0 & 0 & 0 & 0 & 0 & 0 & 0 & 0 & 0 & 0 & 0 & 0 & 0 & 0 & 0 & 0 & 0 & 0 & 0 & 0 & 1 \\
0 & 0 & 0 & 0 & 0 & 0 & 1 & 0 & 0 & 0 & 0 & 0 & 0 & 0 & 0 & 0 & 0 & -1 & 0 & 0 & 0 \\
0 & 0 & 0 & 0 & 0 & 0 & 0 & 1 & 0 & 0 & 0 & 0 & 0 & 0 & 0 & 0 & -1 & 0 & 0 & 0 & 0 \\
0 & 0 & 0 & 0 & 0 & 0 & 0 & 0 & 1 & 0 & 0 & 0 & 0 & 0 & 0 & -1 & 0 & 0 & 0 & 0 & 0
\end{bmatrix}
\begin{pmatrix}
u^*_{v1} \\ u^*_{v2} \\ u^*_{v3} \\ u^*_{v4} \\ u^*_{v5} \\ u^*_{v6} \\ u^*_{v7} \\ u^*_{v8} \\ u^*_{v9} \\ u^*_{v10} \\ u^*_{v11} \\ u^*_{v12} \\ u^*_{v13} \\ u^*_{v14} \\ u^*_{v15} \\ u^*_{v16} \\ u^*_{v17} \\ u^*_{v18} \\ u^*_{v19} \\ u^*_{v20} \\ u^*_{v21}
\end{pmatrix} =
\begin{pmatrix}
0.1 \\ 0.1 \\ 0.1 \\ 0 \\ 0 \\ 0 \\ 0 \\ 0 \\ 0 \\ 0 \\ 0 \\ 0 \\ 0 \\ 0 \\ 0 \\ 0 \\ 0 \\ 0 \\ 0 \\ 0 \\ 0
\end{pmatrix}$$

Solving for the unknown u^*'s yields the Matlab solution, u^*_{v1} through u^*_{v21}:
0.0316; 0.0513; 0.0316; 0.0050; 0.0093; 0.0050; 0.0010; 0.0019; 0.0010; 0.0316; 0.0513; 0.0316; 0; 0; 0; 0.0010; 0.0019; 0.0010; 0; 0; 0
For this being only the first iteration, this value is not so far off from the Comsol solution. Since the target vector for the *y*-momentum is all zeros, the solution for all v^*'s is zero. This is not surprising based on the grid and the pressure boundary conditions.

The u^* and v^* values are now inserted into the pressure correction equation to solve for the pressure correction, p'. It is not possible to present all the equations for the pressure correction in this example. Only the expressions for volume 1 are presented below. Keep in mind that the pressure correction equation assumes velocities are provided at the face. Therefore, one must interpolate adjacent cell velocities to obtain the velocity on the face. The pressure correction equation is now modified, represented in eq. (1-156). The bar indicates the averaged velocity at the cell face.

$$y_\eta \overline{u}^* - x_\eta \overline{v}^* - \frac{1}{\mu}\left[\frac{\left(p'_0 - p'_1\right)}{q_3}\left|J^{-1}\right|\right], \quad \text{where} \quad \begin{aligned} q_3 &= x_\xi^2 + y_\xi^2 \\ \left|J^{-1}\right| &= x_\xi y_\eta - x_\eta y_\xi \end{aligned} \qquad (1\text{-}156)$$

Step 5: Solve the pressure correction equation

Volume 1

Face 1

$$0.2\left(\frac{u^*_{v1} + u^*_{v10}}{2}\right) - 0\cdot\left(\frac{v^*_{v1} + v^*_{v10}}{2}\right) - \frac{1}{1}\left\{\frac{\left(p'_{v1} - p'_{v10}\right)}{(0.2)^2 + (0)^2}\left[(0.2)(0.2) - (0)(0)\right]\right\}$$

$$\Rightarrow 0.2\left(\frac{0.0316+0.0316}{2}\right)-0\cdot\left(\frac{0+0}{2}\right)-\frac{1}{1}\left\{\frac{\left(p'_{v1}-p'_{v10}\right)}{(0.2)^2+(0)^2}\left[(0.2)(0.2)-(0)(0)\right]\right\}$$

Face 6

$$0\cdot\left(\frac{u^*_{v1}+u^*_{v15}}{2}\right)-0.4\left(\frac{v^*_{v1}+v^*_{v15}}{2}\right)-\frac{1}{1}\left\{\frac{\left(p'_{v1}-p'_{v15}\right)}{(0)^2+(-0.1)^2}\left[(0)(0)-(0.4)(-0.1)\right]\right\}$$

$$0\cdot\left(\frac{0.0316+0}{2}\right)-0.4\left(\frac{0+0}{2}\right)-\frac{1}{1}\left\{\frac{\left(p'_{v1}-p'_{v15}\right)}{(0)^2+(-0.1)^2}\left[(0)(0)-(0.4)(-0.1)\right]\right\}$$

Face 14

$$-0.2\left(\frac{0.0316+0.0050}{2}\right)-0\left(\frac{0+0}{2}\right)-\frac{1}{1}\left\{\frac{\left(p'_{v1}-p'_{v4}\right)}{(-0.4)^2+(0)^2}\left[(-0.4)(-0.2)-(0)(0)\right]\right\}$$

Face 13

$$0\cdot\left(\frac{0.0316+0.0513}{2}\right)-(-0.4)\left(\frac{0+0}{2}\right)-\frac{1}{1}\left\{\frac{\left(p'_{v1}-p'_{v2}\right)}{(0)^2+(0.2)^2}\left[(0)(0)-(-0.4)(0.2)\right]\right\}$$

Adding up these four expressions gives the total face flux for the continuity equation for Volume 1. If the total flux is nonzero, the solution has not converged. (Total flux for Volume 1 above is $0.2(0.0316+0.0316)/2-0.2(0.0316+0.0050)/2=\boxed{0.00266}$, so more iterations are necessary). Doing the face fluxes for all volumes yields a system of equations for p'. Once we solve for p', we update the pressure field via:

$$p^{new}=p^{i-1}+\alpha_p p', \quad \text{where} \quad 0<\alpha_p<1$$

If convergence is not reached, p^{i-1} is set equal to p^{new} and the updated p^{i-1} value is inserted into eqs. (1-40) and (1-41) for the next iteration. Also inserted into eqs. (1-40) and (1-41) is the updated velocity, u^{new} which is computed in two steps, described next:

Step 1: Solve for (u,v) using eqs. (1-45) and (1-46):

$$u=u^*-\frac{1}{\mu\left|J^{-1}\right|}\left[y_\eta\left(p'_0-p'_1\right)-y_\xi\left(p'_N-p'_S\right)\right];\quad v=v^*-\frac{1}{\mu\left|J^{-1}\right|}\left[-x_\eta\left(p'_0-p'_1\right)+x_\xi\left(p'_N-p'_S\right)\right],$$

where *u** must be averaged between adjacent cells. Also see notes stated below eqs. (1-45) and (1-46) in section 7.4.4.

Step 2: Apply under-relaxation to obtain:

$$u^{new}=\alpha_u u+(1-\alpha_u)u^{i-1};\quad v^{new}=\alpha_v v+(1-\alpha_v)v^{i-1};$$

Finally, set $u^{i-1}=u^{new}$ and $v^{i-1}=v^{new}$ and then plug u^{i-1} and v^{i-1} into eqs. (1-40) and (1-41) along with p^{i-1}.

Appendix D: Example Problems for Space Conservation Law
Case I

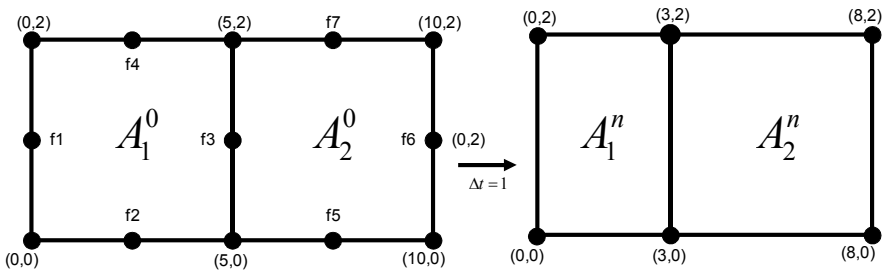

Figure 73. Faces 3 and 6 move left and compress the computational grid.

Control Volume Area before deformation, $t = 0$.

$A_1^0 = A_2^0 = 5(2) = 10$

Control Volume Area after deformation, $t = 1$.

$A_1^n = 3(2) = 6 \qquad A_2^n = 5(2) = 10$

Below, we compute the grid velocity at each face. The methodology and explanation of notation will not be repeated here. Reader is directed instead to section 7.5.4.

face 1

$$\eta^o = (0-0, 2-0) = (0,2) \Rightarrow \vec{S}_{f_1}^o = (2,0)$$

$$u_{g,f_1} = \frac{S_{x,f_1}^o + S_{x,f_1}^n}{2(S_{x,f_1}^n)} \frac{\delta x_{f1}}{\Delta t}; \quad v_{g,f_1} = \frac{S_{y,f_1}^o + S_{y,f_1}^n}{2(S_{y,f_1}^n)} \frac{\delta y_{f1}}{\Delta t}$$

There is no movement on f_1, so $S_{f_1}^n = (2,0)$.

There is no change in the center of f_1, so $\delta x_{f1} = \delta y_{f1} = 0$, therefore $u_{g,f_1} = 0$; $v_{g,f_1} = 0$

face 2

$$\eta^o = (5-0, 0-0) = (5,0) \Rightarrow \vec{S}_{f_2}^o = (0,-5)$$

$$\eta^n = (3-0, 0-0) = (3,0) \Rightarrow \vec{S}_{f_2}^n = (0,-3)$$

$$\delta\vec{r}_{f_2} = r_{f_2}^n - r_{f_2}^o = (1.5-2.5, 0-0) = (-1,0) = (\delta_{x_{f_2}}, \delta_{y_{f_2}})$$

$$u_{g,f_2} = \frac{0+0}{2(0)}\left(\frac{-1}{1}\right) = 0 \; ; \; v_{g,f_2} = \frac{-5+-3}{2(-3)}\left(\frac{0}{1}\right) = 0$$

Both u and v are zero. The face velocity is based on how the face moves in the direction of the normal vector. The face did not move in the direction of the normal vector so there is no velocity for this face.

face 3

$$\eta^o = (5-5, 2-0) = (0,2) \Rightarrow \vec{S}_{f_3}^o = (2,0)$$

$$\eta^n = (3-3, 2-0) = (0,2) \Rightarrow \vec{S}^n_{f_3} = (2,0)$$
$$\delta\vec{r}_{f_3} = r^n_{f_3} - r^o_{f_3} = (3-5, 1-1) = (-2,0) = (\delta_{x_{f_3}}, \delta_{y_{f_3}})$$
$$u_{g,f_3} = \frac{2+2}{2(2)}\left(\frac{-2}{1}\right) = -2 \;;\; v_{g,f_3} = \frac{0+0}{2(0)}\left(\frac{0}{1}\right) = 0$$

We see that the velocity of f_3 = (-2,0). Based on all results so far, we can conclude that f_4, f_5 and f_7 will have zero velocity.

face 6

$$\eta^o = (10-10, 2-0) = (0,2) \Rightarrow \vec{S}^o_{f_6} = (2,0)$$
$$\eta^n = (8-8, 2-0) = (0,2) \Rightarrow \vec{S}^n_{f_6} = (2,0)$$
$$\delta\vec{r}_{f_6} = r^n_{f_6} - r^o_{f_6} = (8-10, 1-1) = (-2,0) = (\delta_{x_{f_6}}, \delta_{y_{f_6}})$$
$$u_{g,f_6} = \frac{2+2}{2(2)}\left(\frac{-2}{1}\right) = -2 \;;\; v_{g,f_6} = \frac{0+0}{2(0)}\left(\frac{0}{1}\right) = 0$$

Therefore, the velocity of f_6 = (-2,0)

Check:

for cell A_1: $\vec{v} = (-2,0)$; $\vec{n} = (2,0)$

$$\vec{v}\cdot\vec{n} = \begin{pmatrix}-2 & 0\end{pmatrix}\begin{pmatrix}2\\0\end{pmatrix} = -4$$

for cell A_2 : $\sum_{f=1}^{4}\vec{v}\cdot\vec{n} = \begin{pmatrix}-2 & 0\end{pmatrix}\begin{pmatrix}-2\\0\end{pmatrix} + \begin{pmatrix}-2 & 0\end{pmatrix}\begin{pmatrix}2\\0\end{pmatrix} = 4-4 = 0$

This result says that A_1 shrunk by four units and that the size of A_2 did not change. This is consistent with the drawings and the calculations at the outset of this problem.

Case II

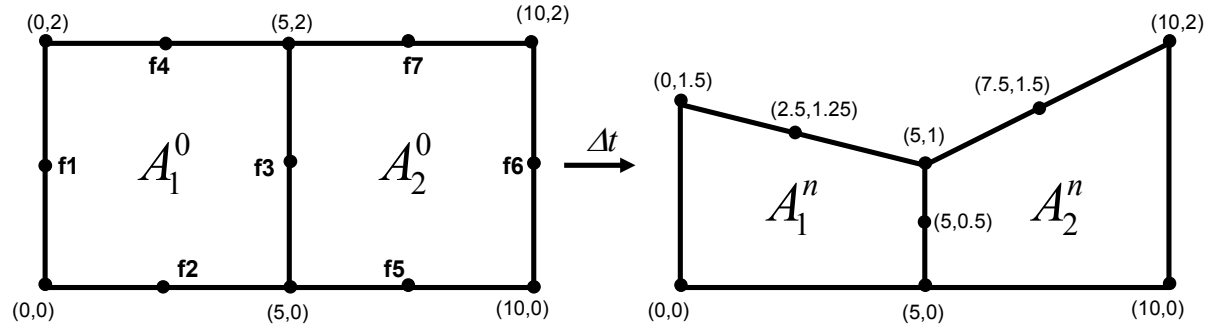

Figure 74. Faces 4 and 7 are compressed downward to deform the grid. In the process, f1 and f3 shrink. F6, f2, and f5 remain the same size.

Control Volume Area before deformation, $t = 0$.

$A_1^0 = A_2^0 = 5(2) = 10$

Control Volume Area after deformation, $t = 1$.

$A_1^n = \frac{1}{2}(\overline{f}_1 + \overline{f}_3)\overline{f}_2 = 6.25$ $\qquad$ $A_2^n = \frac{1}{2}(\overline{f}_3 + \overline{f}_6)\overline{f}_5 = 7.5$

The above has been computed using the area formula for a trapezoid

face 1

$$\eta^o = (0-0, 2-0) = (0,2) \Rightarrow \overline{S}_{f_1}^o = (2,0)$$

$$\eta^n = (0-0, 1.5-0) = (0,1.5) \Rightarrow \overline{S}_{f_1}^n = (1.5,0)$$

$$\delta\vec{r}_{f_1} = r_{f_1}^n - r_{f_1}^o = (0-0, 0.75-1) = (0,-0.25) = (\delta_{x_{f_1}}, \delta_{y_{f_1}})$$

$$u_{g,f_1} = \frac{2+1.5}{2(1.5)}\left(\frac{0}{1}\right) = 0 \;;\; v_{g,f_1} = \frac{0+0}{2(0)}\left(\frac{-0.25}{1}\right) = 0$$

$$\therefore \vec{u}_{f_1} = (0,0)$$

face 2 $\vec{u}_{f_2} = (0,0)$ by inspection $\delta\vec{r}_{f_2} = (0,0)$

face 3

$$\eta^o = (5-5, 2-0) = (0,2) \Rightarrow \overline{S}_{f_3}^o = (2,0)$$

$$\eta^n = (5-5, 1-0) = (0,1) \Rightarrow \overline{S}_{f_3}^n = (1,0)$$

$$\delta\vec{r}_{f_3} = r_{f_3}^n - r_{f_3}^o = (5-5, 0.5-1) = (0,-0.5) = (\delta_{x_{f_3}}, \delta_{y_{f_3}})$$

$$u_{g,f_3} = \frac{2+1}{2(1)}\left(\frac{0}{1}\right) = 0 \;;\; v_{g,f_3} = \frac{0+0}{2(0)}\left(\frac{-0.5}{1}\right) = 0$$

$$\therefore \vec{u}_{f_3} = (0,0)$$

face 4

$$\eta^o = (5-0, 2-2) = (5,0) \Rightarrow \vec{S}^o_{f_4} = (0,-5)$$
$$\eta^n = (5-0, 1-1.5) = (5,-0.5) \Rightarrow \vec{S}^n_{f_4} = (-0.5,-5)$$
$$\delta\vec{r}_{f_4} = r^n_{f_4} - r^o_{f_4} = (2.5-2.5, 1.25-2) = (0,-0.75) = (\delta_{x_{f_4}}, \delta_{y_{f_4}})$$
$$u_{g,f_4} = \frac{0+-0.5}{2(-0.5)}\left(\frac{0}{1}\right) = 0 \;;\; v_{g,f_4} = \frac{-5+-5}{2(-5)}\left(\frac{-0.75}{1}\right) = -0.75$$
$$\therefore \vec{u}_{f_4} = \left(0,-0.75\right)$$

Velocity is zero at f_5 and f_6 by inspection

face 7

$$\eta^o = (10-5, 2-2) = (5,0) \Rightarrow \vec{S}^o_{f_7} = (0,-5)$$
$$\eta^n = (10-5, 2-1) = (5,1) \Rightarrow \vec{S}^n_{f_7} = (1,-5)$$
$$\delta\vec{r}_{f_7} = r^n_{f_7} - r^o_{f_7} = (7.5-7.5, 1.5-2) = (0,-0.5) = (\delta_{x_{f_7}}, \delta_{y_{f_7}})$$
$$u_{g,f_7} = \frac{0+1}{2(1)}\left(\frac{0}{1}\right) = 0 \;;\; v_{g,f_7} = \frac{-5+-5}{2(-5)}\left(\frac{-0.5}{1}\right) = -0.5$$
$$\therefore \vec{u}_{f_7} = \left(0,-0.5\right)$$

Check:

For A_1 : $\vec{u}\cdot\vec{n} = \begin{pmatrix}0 & -0.75\end{pmatrix}\begin{pmatrix}0.5\\5\end{pmatrix} = -3.75$

For A_2 : $\vec{u}\cdot\vec{n} = \begin{pmatrix}0 & -0.5\end{pmatrix}\begin{pmatrix}-1\\5\end{pmatrix} = -2.5$

The normal vectors at $t = 1$ were used for this check.

Case III

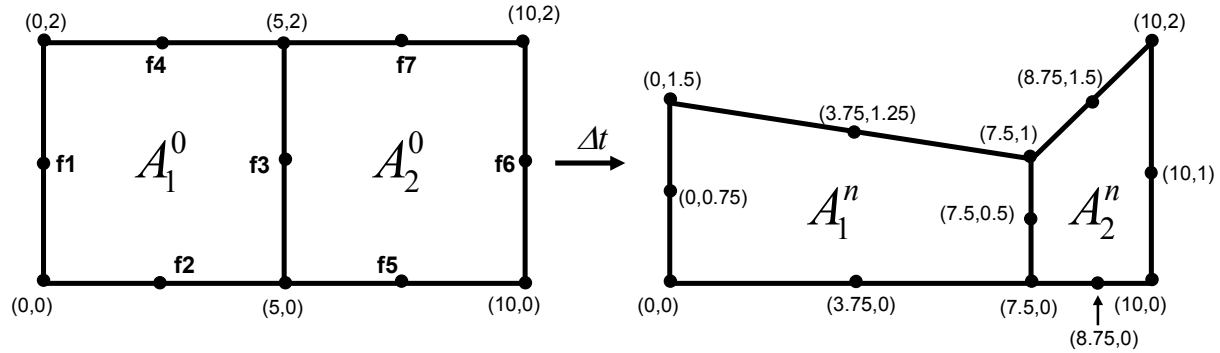

Figure 75. Faces 4 and 7 are compressed downward to deform the grid. In the process, f1, f3, and f5 shrink. F2 elongates. F6 remains the same size.

Control Volume Area before deformation, $t = 0$.

$A_1^0 = A_2^0 = 5(2) = 10$

Control Volume Area after deformation, $t = 1$.

$$A_1^n = \frac{1}{2}(\overline{f}_1 + \overline{f}_3)\overline{f}_2 = \frac{1}{2}(1.5+1)7.5 = 9.375 \qquad A_2^n = \frac{1}{2}(\overline{f}_3 + \overline{f}_6)\overline{f}_5 = \frac{1}{2}(1+2)2.5 = 3.75$$

face 1

$$\eta^o = (0-0, 2-0) = (0,2) \Rightarrow \vec{S}_{f_1}^o = (2,0)$$
$$\eta^n = (0-0, 1.5-0) = (0,1.5) \Rightarrow \vec{S}_{f_1}^n = (1.5,0)$$
$$\delta\vec{r}_{f_1} = r_{f_1}^n - r_{f_1}^o = (0-0, 0.75-1) = (0,-0.25) = (\delta_{x_{f_1}}, \delta_{y_{f_1}})$$
$$u_{g,f_1} = \frac{2+1.5}{2(1.5)}\left(\frac{0}{1}\right) = 0 \;;\; v_{g,f_1} = \frac{0+0}{2(0)}\left(\frac{-0.25}{1}\right) = 0$$
$$\therefore \vec{u}_{f_1} = (0,0)$$

face 2

$$\eta^o = (5-0, 0-0) = (5,0) \Rightarrow \vec{S}_{f_2}^o = (0,-5)$$
$$\eta^n = (7.5-0, 0-0) = (7.5,0) \Rightarrow \vec{S}_{f_2}^n = (0,-7.5)$$
$$\delta\vec{r}_{f_2} = r_{f_2}^n - r_{f_2}^o = (3.75-2.5, 0-0) = (1.25,0) = (\delta_{x_{f_2}}, \delta_{y_{f_2}})$$
$$u_{g,f_2} = \frac{0+0}{2(0)}\left(\frac{1.25}{1}\right) = 0 \;;\; v_{g,f_2} = \frac{-5+-7.5}{2(-7.5)}\left(\frac{0}{1}\right) = 0$$
$$\therefore \vec{u}_{f_2} = (0,0)$$

face 3

$$\eta^o = (5-5, 2-0) = (0,2) \Rightarrow \vec{S}^o_{f_3} = (2,0)$$
$$\eta^n = (7.5-7.5, 1-0) = (0,1) \Rightarrow \vec{S}^n_{f_3} = (1,0)$$
$$\delta\vec{r}_{f_3} = r^n_{f_3} - r^o_{f_3} = (7.5-5, 0.5-1) = (2.5,-0.5) = (\delta_{x_{f_3}}, \delta_{y_{f_3}})$$
$$u_{g,f_3} = \frac{2+1}{2(1)}\left(\frac{2.5}{1}\right) = 3.75 \;;\; v_{g,f_3} = \frac{0+0}{2(0)}\left(\frac{-0.5}{1}\right) = 0$$
$$\therefore \vec{u}_{f_3} = (3.75, 0)$$

face 4

$$\eta^o = (5-0, 2-2) = (5,0) \Rightarrow \vec{S}^o_{f_4} = (0,-5)$$
$$\eta^n = (7.5-0, 1-1.5) = (7.5,-0.5) \Rightarrow \vec{S}^n_{f_4} = (-0.5,-7.5)$$
$$\delta\vec{r}_{f_4} = r^n_{f_4} - r^o_{f_4} = (3.75-2.5, 1.25-2) = (1.25,-0.75) = (\delta_{x_{f_4}}, \delta_{y_{f_4}})$$
$$u_{g,f_4} = \frac{0+-0.5}{2(-0.5)}\left(\frac{1.25}{1}\right) = 0.625 \;;\; v_{g,f_4} = \frac{-5+-7.5}{2(-7.5)}\left(\frac{-0.75}{1}\right) = -0.625$$
$$\therefore \vec{u}_{f_4} = (0.625, -0.625)$$

Velocity is zero at f_5 and f_6 by inspection

face 7

$$\eta^o = (10-5, 2-2) = (5,0) \Rightarrow \vec{S}^o_{f_7} = (0,-5)$$
$$\eta^n = (10-7.5, 2-1) = (2.5,1) \Rightarrow \vec{S}^n_{f_7} = (1,-2.5)$$
$$\delta\vec{r}_{f_7} = r^n_{f_7} - r^o_{f_7} = (8.75-7.5, 1.5-2) = (1.25,-0.5) = (\delta_{x_{f_7}}, \delta_{y_{f_7}})$$
$$u_{g,f_7} = \frac{0+1}{2(1)}\left(\frac{1.25}{1}\right) = 0.625 \;;\; v_{g,f_7} = \frac{-5+-2.5}{2(-2.5)}\left(\frac{-0.5}{1}\right) = -0.75$$
$$\therefore \vec{u}_{f_7} = (0.625, -0.75)$$

Check:

$$\text{For } \Delta A_1 = \sum_{f=1}^{4} \vec{v}_f \cdot \vec{n}_f = \begin{pmatrix} 3.75 & 0 \end{pmatrix}\begin{pmatrix} 1 \\ 0 \end{pmatrix} + \begin{pmatrix} 0.625 & -0.625 \end{pmatrix}\begin{pmatrix} 0.5 \\ 7.5 \end{pmatrix} = -0.625$$
$$\text{For } \Delta A_2 = \sum_{f=3}^{5,6,7} \vec{v}_f \cdot \vec{n}_f = \begin{pmatrix} 3.75 & 0 \end{pmatrix}\begin{pmatrix} -1 \\ 0 \end{pmatrix} + \begin{pmatrix} 0.625 & -0.75 \end{pmatrix}\begin{pmatrix} -1 \\ 2.5 \end{pmatrix} = -6.25$$

These values correspond to the change in area of A_1 and A_2 and are consistent with what was calculated at the outset.

Appendix E: Example Problem for ALE

The following example problem contains one control volume. Because only one control volume is used, the final results of fluid velocity and pressure will not be accurate. However, the example is instructive for understanding the ALE methodology. To simplify the computations, the case is steady state. To begin, consider a grid with dimensions as specified in Figure 76. The pressures at the inlet and outlet are specified as shown. The evolution and solution to the problem involves two specific stages, each with several main tasks as follows:

Stage 1: Velocity Calculation for Initial Grid, Shown in Figure 76
Provide an initial value for the velocity and pressure in volume 1
Solve the *x* and *y* momentum
Solve the pressure correction
Accept updated pressure and velocity field

Stage 2: Velocity Calculation for Deformed Grid, Shown in Figure 76
Deform the grid as shown in Figure 77
Solve the *x* and *y* momentum
Solve the pressure correction
Accept updated pressure and velocity field

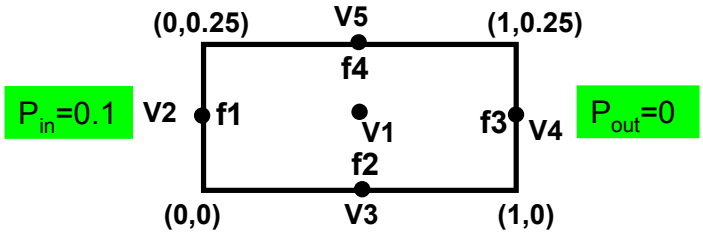

Figure 76. Control volume used for example problem for ALE calculations

Solution

Stage 1: Calculate Velocity and Pressure on Initial Grid

Step 1: Initialize pressure and velocity fields

$$p = [0, 0.1, 0, 0, 0]; \; u = [0, 0, 0, 0, 0]; \; v = [0, 0, 0, 0, 0]$$

Note: The array index corresponds to the volume number—element 1 of the array corresponds to volume 1, et cetera.

Step 2: Set up a metrics table

It is easiest to set up a table of face metrics to which we can refer.

Volume	Face	x_ξ	y_ξ	x_η	y_η	q_3	$\lvert J^{-1} \rvert$
1	f1	0.5	0	0	0.25	0.3125	0.125
	f2	0	0.125	-1	0	0.015625	0.125
	f3	-0.5	0	0	-0.25	0.3125	0.125
	f4	0	-0.125	1	0	0.015625	0.125

Step 3: Compute face fluxes for pressure gradient term
The only pressure contribution comes from face 1. Instead of calculating an average for the face, we will take the actual value of the pressure at face 1, which is 0.1.

$$p_{face1} = p_{v2} = 0.1$$

$$p_{face1} \cdot y_\eta = 0.1 \cdot 0.25 = 0.025$$

Step 4: Compute face fluxes for diffusion term

$$\mu\left[\frac{u_{v1}-u_{v2}}{q_3}|J| + \frac{u_{v1}-u_{v3}}{q_3}|J| + \frac{u_{v1}-u_{v4}}{q_3}|J| + \frac{u_{v1}-u_{v5}}{q_3}|J|\right]$$

$$= 1\left[\frac{u_{v1}-u_{v2}}{0.3125}0.125 + \frac{u_{v1}-u_{v3}}{0.015625}0.125 + \frac{u_{v1}-u_{v4}}{0.3125}0.125 + \frac{u_{v1}-u_{v5}}{0.015625}0.125\right]$$

Step 5: Compute face fluxes for convective term
There will be no contribution from the convective term on this iteration since all velocities are initially set to zero.

Step 6: Set up linear algebra system
Equation 1: $16.8u_{v1} - 0.4u_{v2} - 8u_{v3} - 0.4u_{v4} - 8u_{v5} = 0.025$

Equation 2: $u^*_{v2} - u^*_{v1} = 0$

Equation 3: $u^*_{v3} = 0$

Equation 4: $u^*_{v4} - u^*_{v1} = 0$

Equation 5: $u^*_{v5} = 0$

Step 7: Solve system

$$\begin{bmatrix} 16.8 & -0.4 & -8 & -0.4 & -8 \\ -1 & 1 & 0 & 0 & 0 \\ 0 & 0 & 1 & 0 & 0 \\ -1 & 0 & 0 & 1 & 0 \\ 0 & 0 & 0 & 0 & 1 \end{bmatrix} \begin{pmatrix} u_{v1} \\ u_{v2} \\ u_{v3} \\ u_{v4} \\ u_{v5} \end{pmatrix} = \begin{pmatrix} 0.025 \\ 0 \\ 0 \\ 0 \\ 0 \end{pmatrix}$$

$$\Rightarrow (u_{v1}, u_{v2}, u_{v3}, u_{v4}, u_{v5}) = (0.0015625, 0.0015625, 0, 0.0015625, 0)$$

Since x_η for face 1 is zero, there is no contribution to the *v*-velocity from the pressure. Therefore, the *v* velocity is zero everywhere on the first iteration.

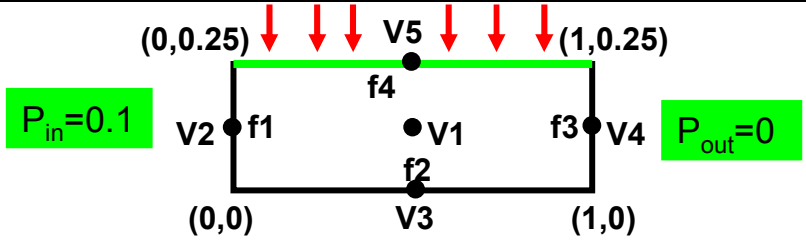

Figure 77. The grid is deformed by forcing face 4 to move downward. The ALE method is used to recalculate the flow field.

Stage 2: Advance one time step; Δt = 1

Step 1: Take converged pressure and velocity fields as initial guess for new time step

$$p=[0,0.1,0,0,0];\quad u=[0.0015625,0.0015625,0,0.0015625,0];\quad v=[0,0,0,0,0]$$

Step 2: Calculate $\vec{u}_g$

Based on prior case studies, only f4 will have a velocity; it is calculated as follows:

Face 4

$$\eta^0=(1-0,0.25-0.25)=(1,0)\Rightarrow \vec{S}^0_{f4}=(0,-1)$$

$$\eta^n=(1-0,0.2-0.2)=(1,0)\Rightarrow \vec{S}^n_{f4}=(0,-1)$$

$$\delta\vec{r}_{f4}=(0.5-0.5,0.2-0.25)=(0,-0.05)$$

$$u_{g,f4}=\frac{0+0}{2(0)}\left(\frac{0}{1}\right)=0;\ v_{g,f4}=\frac{-1+-1}{2(-1)}\left(\frac{-0.05}{1}\right)=-0.05$$

$$\Rightarrow \vec{u}_{g,f4}=(0,-0.05)$$

Step 3: Calculate face fluxes for the pressure gradient, convective, and diffusion terms

Pressure Gradient Term

$$-\left[\left.p_{\text{face}}\cdot y_\eta\right|^1+\left.p_{\text{face}}\cdot y_\eta\right|^2+\left.p_{\text{face}}\cdot y_\eta\right|^3+\left.p_{\text{face}}\cdot y_\eta\right|^4\right]$$

$$p_{\text{f1}}=0.1;\ p_{\text{f2}}=0;\ p_{\text{f3}}=0;\ p_{\text{f4}}=0$$

$$\left.y_\eta\right|^{f1}=-0.2$$

$$\Rightarrow -[0.1\cdot(-0.2)]=0.2$$

Convective Term

$$-\rho\sum_f^{\#\text{ of faces}}\left[\left(u^{i-1}-u_g\right)\cdot y_\eta-\left(v^{i-1}-v_g\right)x_\eta\right]u^*\Big|^f$$

$$-\rho\left\{\begin{array}{l}\left[(0.0015625-0)(0.2)-(0-0)(0)\right]u^*_{\text{v2}}+\left[(0-0)(0)-(0-0)(-1)\right]u^*_{\text{v3}}+\\ \ldots+\left[(0.0015625-0)(-0.2)-(0-0)(0)\right]u^*_{\text{v4}}+\left[(0-0)(0)-(0-(-0.05)(-1)\right]u^*_{\text{v5}}\end{array}\right\}$$

Diffusion Term

$$\mu\left\{\frac{u^*_{v1}-u^*_{v2}}{(0.5)^2}[0.5(0.2)]+\frac{u^*_{v1}-u^*_{v3}}{0+(0.1)^2}[-(-1)(0.1)]+\frac{u^*_{v1}-u^*_{v4}}{(-0.5)^2}[-0.5(-0.2)]+\frac{u^*_{v1}-u^*_{v5}}{0^2+(-0.1)^2}[-(1)(-0.1)]\right\}$$

$$\Rightarrow 0.4\left(u^*_{v1}-u^*_{v2}\right)+10\left(u^*_{v1}-u^*_{v3}\right)+0.4\left(u^*_{v1}-u^*_{v4}\right)+10\left(u^*_{v1}-u^*_{v5}\right)$$

$$20.8u^*_{v1}-0.4u^*_{v2}-10u^*_{v3}-0.4u^*_{v4}-10u^*_{v5}$$

Step 3: Add contributions from ∇p, $\vec{u}\cdot\nabla\vec{u}$, and $\nabla^2\vec{u}$

$$20.8u^*_{v1}-0.0875u^*_{v2}-10u^*_{v3}-0.7125u^*_{v4}-60u^*_{v5}+0.02=0$$

Step 4: Decide on boundary conditions and establish mathematical relationships

Assume velocity at volume 2 equals velocity at volume 1

$u^*_{v2}=u^*_{v1}\Rightarrow u^*_{v2}-u^*_{v1}=0$

Assume velocity at volume 4 equals velocity at volume 1

$u^*_{v4}=u^*_{v1}\Rightarrow u^*_{v4}-u^*_{v1}=0$

Set velocity at volumes 3 and 5 equal to zero (no-slip boundary condition)

$u^*_{v3}=0;\ \ u^*_{v5}=0$

Step 5: Write all equations and place in matrix form

Equation 1: $20.8u^*_{v1}-0.0875u^*_{v2}-10u^*_{v3}-0.7125u^*_{v4}-60u^*_{v5}+0.02=0$

Equation 2: $u^*_{v2}-u^*_{v1}=0$

Equation 3: $u^*_{v3}=0$

Equation 4: $u^*_{v4}-u^*_{v1}=0$

Equation 5: $u^*_{v5}=0$

$$\begin{bmatrix}20.8 & -0.0875 & -10 & -0.7125 & -60\\ -1 & 1 & 0 & 0 & 0\\ 0 & 0 & 1 & 0 & 0\\ -1 & 0 & 0 & 1 & 0\\ 0 & 0 & 0 & 0 & 1\end{bmatrix}\begin{pmatrix}u^*_{v1}\\ u^*_{v2}\\ u^*_{v3}\\ u^*_{v4}\\ u^*_{v5}\end{pmatrix}=\begin{pmatrix}-0.02\\ 0\\ 0\\ 0\\ 0\end{pmatrix}$$

Step 6: Solve system in Matlab

Solution of above system is:

$u=[0.001,0.001,0,0.001,0];\quad v=[0,0,0,0,0]$

Step 7: Solve Pressure Correction Equation

$$\frac{V^n-V^0}{\Delta t}+\sum_{f=1}^{\#\text{ of faces}}\left\{y_\eta\left(u^*_f-u_g\right)-x_\eta\left(v^*_f-v_g\right)-\frac{1}{\mu}\left[\frac{p'_0-p'_1}{q_3}\left|J^{-1}\right|\right]\right\}\Bigg|^f=0$$

Appendix F: Validation of the ALE Program — Comparisons with Fluent

This validation study considers an 18 by 18 grid. The *x*-velocity (0.003m/s) is specified at the inlet and the pressure (0.001 Pa) is specified at the outlet. My results are given in the left column; results from Fluent in the right column. The first set of pressure, *x*-velocity, and *y*-velocity results are obtained on an undeformed grid. The second set of pressure, *x*-velocity, and *y*-velocity results are obtained after three grid deformation steps. For all results, the "in-house" code and the Fluent results differ by only a small amount.

Pressure

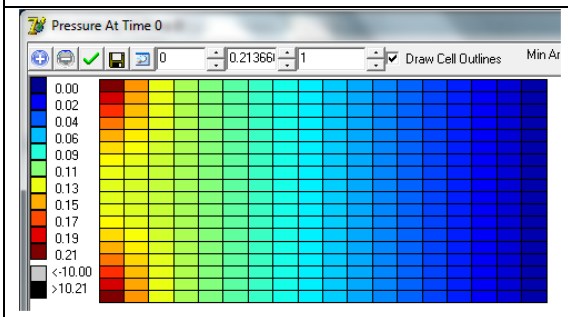

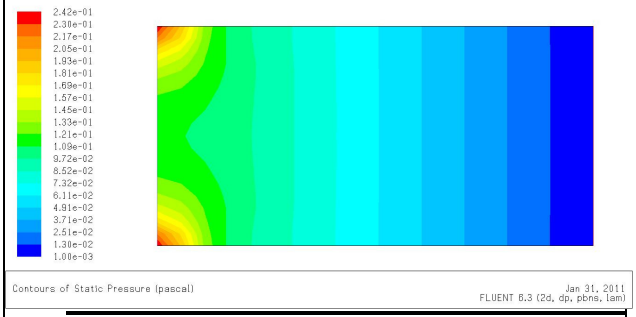

***x*-velocity**

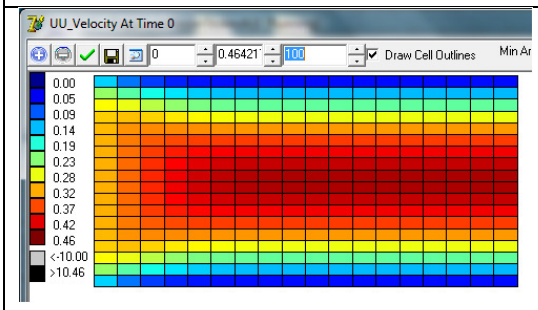

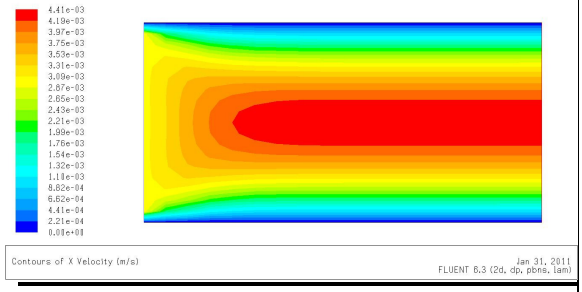

***y*-velocity**

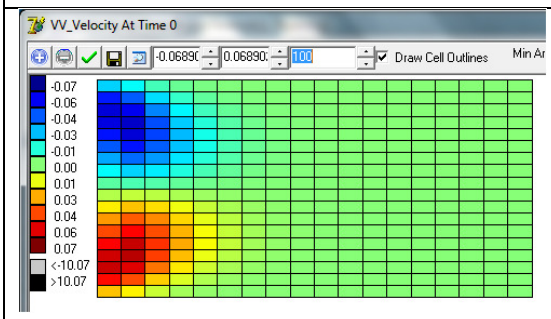

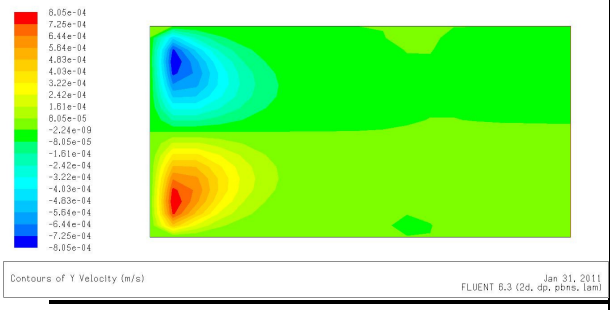

Pressure

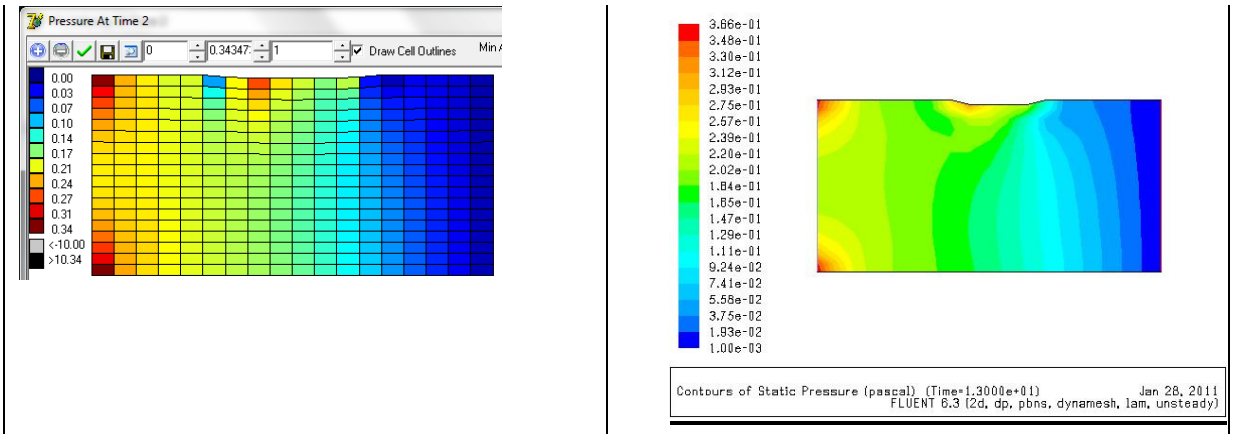

***x*-velocity**

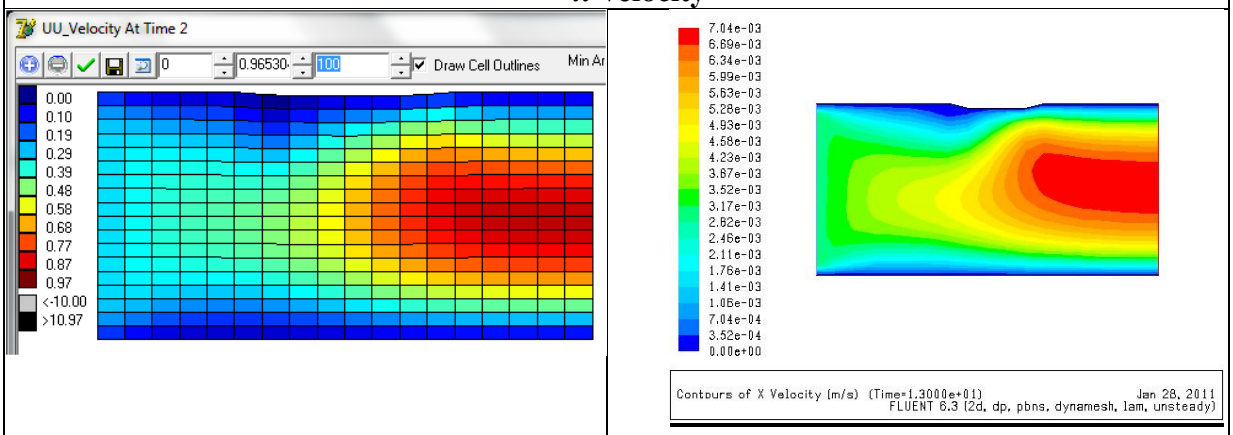

***y*-velocity**

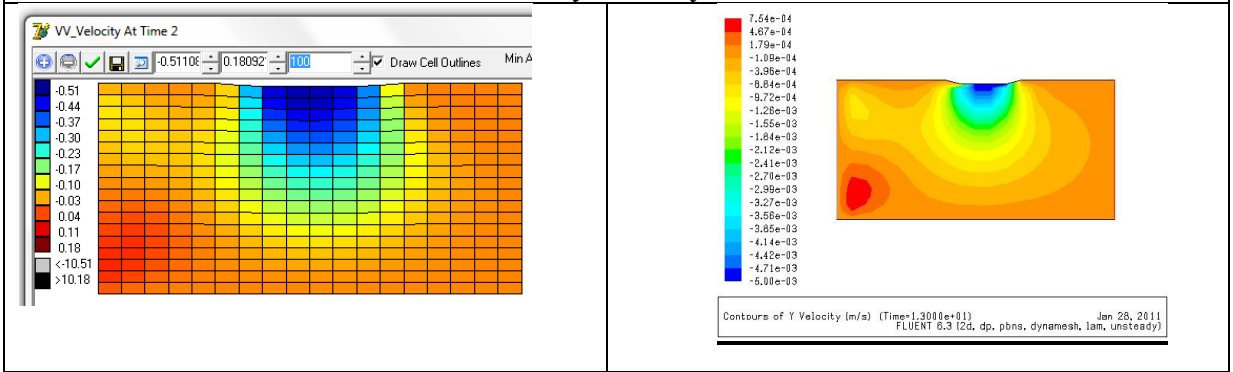

Figure 78. Validation of ALE computer program. The "in-house" computer program results are given in the left column. Fluent results are given in the right column.

Appendix G: Strain and Stress—Instructions for Implementation

The FSI program contains procedures for calculating the strain and stress of the brain tissue. The strain and stress measures documented in (Linninger 2011) was implemented:

Strain

$$\varepsilon = \begin{bmatrix} \varepsilon_x & \varepsilon_{xy} \\ \varepsilon_{xy} & \varepsilon_y \end{bmatrix} = \begin{bmatrix} \dfrac{\partial \alpha}{\partial x} & \dfrac{\partial \alpha}{\partial y} + \dfrac{\partial \beta}{\partial x} \\ \dfrac{\partial \alpha}{\partial y} + \dfrac{\partial \beta}{\partial x} & \dfrac{\partial \beta}{\partial y} \end{bmatrix}$$

Stress

$$\sigma = \begin{bmatrix} \sigma_x & \sigma_{xy} \\ \sigma_{xy} & \sigma_y \end{bmatrix}$$

The stress components are computed using a linear elastic constitutive model:

$$\sigma_x = \lambda\left(\varepsilon_x + \varepsilon_y\right) + 2G\varepsilon_x = \lambda\left(\frac{\partial \alpha}{\partial x} + \frac{\partial \beta}{\partial y}\right) + 2G\frac{\partial \alpha}{\partial x} \tag{1-157}$$

$$\sigma_y = \lambda\left(\varepsilon_x + \varepsilon_y\right) + 2G\varepsilon_y = \lambda\left(\frac{\partial \alpha}{\partial x} + \frac{\partial \beta}{\partial y}\right) + 2G\frac{\partial \beta}{\partial y} \tag{1-158}$$

$$\sigma_{xy} = G\varepsilon_{xy} = G\left(\frac{\partial \alpha}{\partial y} + \frac{\partial \beta}{\partial x}\right) \tag{1-159}$$

Contributions to the strain components are:

$$\frac{\partial \alpha}{\partial x} = \frac{\partial \alpha}{\partial \xi}\frac{\partial \xi}{\partial x} + \frac{\partial \alpha}{\partial \eta}\frac{\partial \eta}{\partial x} = \xi_x \frac{\partial \alpha}{\partial \xi} + \eta_x \frac{\partial \alpha}{\partial \eta} = \frac{y_\eta}{\left|J^{-1}\right|}\left(\alpha_{cell} - \alpha_{neighbor}\right) - \frac{y_\xi}{\left|J^{-1}\right|}\left(\alpha_{North} - \alpha_{South}\right) \tag{1-160}$$

$$\frac{\partial \alpha}{\partial y} = \frac{\partial \alpha}{\partial \xi}\frac{\partial \xi}{\partial y} + \frac{\partial \alpha}{\partial \eta}\frac{\partial \eta}{\partial y} = \xi_y \frac{\partial \alpha}{\partial \xi} + \eta_y \frac{\partial \alpha}{\partial \eta} = -\frac{x_\eta}{\left|J^{-1}\right|}\left(\alpha_{cell} - \alpha_{neighbor}\right) + \frac{x_\xi}{\left|J^{-1}\right|}\left(\alpha_{North} - \alpha_{South}\right) \tag{1-161}$$

$$\frac{\partial \beta}{\partial x} = \frac{\partial \beta}{\partial \xi}\frac{\partial \xi}{\partial x} + \frac{\partial \beta}{\partial \eta}\frac{\partial \eta}{\partial x} = \xi_x \frac{\partial \beta}{\partial \xi} + \eta_x \frac{\partial \beta}{\partial \eta} = \frac{y_\eta}{\left|J^{-1}\right|}\left(\beta_{cell} - \beta_{neighbor}\right) - \frac{y_\xi}{\left|J^{-1}\right|}\left(\beta_{North} - \beta_{South}\right) \tag{1-162}$$

$$\frac{\partial \beta}{\partial y} = \frac{\partial \beta}{\partial \xi}\frac{\partial \xi}{\partial y} + \frac{\partial \beta}{\partial \eta}\frac{\partial \eta}{\partial y} = \xi_y \frac{\partial \beta}{\partial \xi} + \eta_y \frac{\partial \beta}{\partial \eta} = -\frac{x_\eta}{\left|J^{-1}\right|}\left(\beta_{cell} - \beta_{neighbor}\right) + \frac{x_\xi}{\left|J^{-1}\right|}\left(\beta_{North} - \beta_{South}\right) \tag{1-163}$$

We take $\frac{x_\xi}{\left|J^{-1}\right|}, \frac{x_\eta}{\left|J^{-1}\right|}, \frac{y_\xi}{\left|J^{-1}\right|}$, and $\frac{y_\eta}{\left|J^{-1}\right|}$ to be in the deformed (current) configuration—after the grid has been updated with computed displacements.

Because we are using a collocated approach (all states are solved in the cell center). Thus, $\frac{\partial \alpha}{\partial x}$, $\frac{\partial \alpha}{\partial y}$, $\frac{\partial \beta}{\partial x}$, and $\frac{\partial \beta}{\partial y}$ in eqs. (1-160)-(1-163) are computed at the cell center. Equations (1-160)-(1-163) seem to indicate that for a given control volume, neighboring cells will contribute to the strain measure for a given control volume. Thus, I compute the strain components for a given control volume by averaging the contributions from all neighboring control volumes:

$$\frac{\partial \alpha}{\partial x} = \frac{1}{\#\text{ of faces}} \sum_{1}^{\#\text{ of faces}} \left[\frac{y_\eta}{\left|J^{-1}\right|}\left(\alpha_{cell} - \alpha_{neighbor}\right) - \frac{y_\xi}{\left|J^{-1}\right|}\left(\alpha_{North} - \alpha_{South}\right) \right] \tag{1-164}$$

$$\frac{\partial \alpha}{\partial y} = \frac{1}{\#\text{ of faces}} \sum_{1}^{\#\text{ of faces}} \left[-\frac{x_\eta}{\left|J^{-1}\right|}\left(\alpha_{cell} - \alpha_{neighbor}\right) + \frac{x_\xi}{\left|J^{-1}\right|}\left(\alpha_{North} - \alpha_{South}\right) \right] \tag{1-165}$$

$$\frac{\partial \beta}{\partial x} = \frac{1}{\#\text{ of faces}} \sum_{1}^{\#\text{ of faces}} \left[\frac{y_\eta}{\left|J^{-1}\right|}\left(\beta_{cell} - \beta_{neighbor}\right) - \frac{y_\xi}{\left|J^{-1}\right|}\left(\beta_{North} - \beta_{South}\right) \right] \tag{1-166}$$

$$\frac{\partial \beta}{\partial y} = \frac{1}{\#\text{ of faces}} \sum_{1}^{\#\text{ of faces}} \left[-\frac{x_\eta}{\left|J^{-1}\right|}\left(\beta_{cell} - \beta_{neighbor}\right) + \frac{x_\xi}{\left|J^{-1}\right|}\left(\beta_{North} - \beta_{South}\right) \right] \tag{1-167}$$

The stress components in eqs. (1-157)-(1-159) are then computed using the components of the strain tensor: ε_x, ε_y, ε_{xy}.

Appendix H: Proof of the Approximated Diffusion Flux Term

Eq. (1-168) gives the total diffusion flux, q_{total} for a given control volume.

$$q_{total} = -\mu \sum_{f=1}^{\#\text{ of faces}} \left[\frac{q_1}{\left|J^{-1}\right|}\left(u_0^* - u_1^*\right) - \frac{q_2}{\left|J^{-1}\right|}\left(u_N^* - u_S^*\right) \right]^f \tag{1-168}$$

If $\vec{e}_\xi$ and $\vec{e}_\eta$ are nearly perpendicular, we can set q_2 equal to zero. Thus, for a single face, (1-168) can be written as

$$q_{face} = -\mu \frac{q_1}{\left|J^{-1}\right|}\left(u_0^* - u_1^*\right) \tag{1-169}$$

We will derive an alternate form of the above which does not contain the $\left|J^{-1}\right|$. First note that

$$\vec{e}_\xi \times \vec{e}_\eta = \begin{vmatrix} i & j & k \\ x_\xi & y_\xi & 0 \\ x_\eta & y_\eta & 0 \end{vmatrix} = 0\hat{i} - 0\hat{j} + \left(x_\xi y_\eta - x_\eta y_\xi\right)\hat{k}$$

The magnitude of the above vector is given by:

$$\left|\vec{e}_\xi \times \vec{e}_\eta\right| = \left|\vec{e}_\xi\right|\left|\vec{e}_\eta\right| \sin\theta$$

Since we assume θ is 90°, we have,

$$\left|\vec{e}_\xi \times \vec{e}_\eta\right| = \left|\vec{e}_\xi\right|\left|\vec{e}_\eta\right| = A_{\text{parallelogram}}$$

The above relation equals the area of the parallelogram, $A_{\text{parallelogram}}$, defined by $\vec{e}_\xi$ and $\vec{e}_\eta$. Since the *i* and *j* components are zero, the area of the parallelogram is

$$\left(x_\xi y_\eta - x_\eta y_\xi\right).$$

Recall that $\left|J^{-1}\right|$ also equals $\left(x_\xi y_\eta - x_\eta y_\xi\right)$. Thus, we have that $\left|J^{-1}\right| = \left|\vec{e}_\xi\right|\left|\vec{e}_\eta\right|$. Therefore, we can write eq. (1-169) as

$$q_D^f = -\mu \frac{q_1}{\left|\vec{e}_\xi\right|\left|\vec{e}_\eta\right|}\left(u_0^* - u_1^*\right) \tag{1-170}$$

Recall that q_1 is defined as

$$q_1 = x_\eta^2 + y_\eta^2 = \left|\vec{e}_\eta\right|\left|\vec{e}_\eta\right|$$

Thus, we can rewrite eq. (1-170) as

$$q_D^f = -\mu \frac{\left|\vec{e}_\eta\right|\left|\vec{e}_\eta\right|}{\left|\vec{e}_\xi\right|\left|\vec{e}_\eta\right|}\left(u_0^* - u_1^*\right) \Rightarrow -\mu \frac{\left|\vec{e}_\eta\right|}{\left|\vec{e}_\xi\right|}\left(u_0^* - u_1^*\right) \tag{1-171}$$

An alternative form is derived similarly:

$$q_D = -\mu \frac{q_1}{\left|J^{-1}\right|}\left(u_0^* - u_1^*\right) = -\mu \frac{\left|\vec{e}_\eta\right|\left|\vec{e}_\eta\right|}{\left|\vec{e}_\xi\right|\left|\vec{e}_\eta\right|} \cdot \frac{\left|\vec{e}_\xi\right|}{\left|\vec{e}_\xi\right|}\left(u_0^* - u_1^*\right)$$

$$\Rightarrow -\mu \frac{\left|\vec{e}_\eta\right|\left|\vec{e}_\eta\right|}{\left|\vec{e}_\xi\right|\left|\vec{e}_\eta\right|} \cdot \frac{\left|\vec{e}_\xi\right|}{\left|\vec{e}_\xi\right|}\left(u_0^* - u_1^*\right) \Rightarrow -\mu \frac{\left|\vec{e}_\xi\right|\left|\vec{e}_\eta\right|}{\left|\vec{e}_\xi\right|\left|\vec{e}_\xi\right|} \cdot \left(u_0^* - u_1^*\right)$$

Which ultimately leads to

$$\Rightarrow -\mu \frac{\left|J^{-1}\right|}{q_3} \cdot \left(u_0^* - u_1^*\right) \tag{1-172}$$

Eq. (1-172) is implemented in my fluid-structure interaction program.

Appendix I: Generating a Random Point in a Quadrilateral

Our implementation of constrained constructive optimization (CCO) requires that we generate random sample points within the perfusion domain and connect them to existing segments. In our implementation of the ***confined*** CCO algorithm, the domain is not analytical (circle, square), but is constructed of quadrilaterals. Therefore, we must generate sample points within quadrilaterals, and we propose the following method. Consider the quadrilateral in Figure 79; it is divided into lower and upper triangles; the lower triangle is shaded in the figure.

The shaded triangle is bounded by two functions which both involve *x* and *y*, namely, *y = x*, and *y = (1/5)x*. The third boundary is *x = 5*. It would not be a simple matter trying to generate a random point in such a domain. When we morph (transform) the shaded triangle into the (ξ,η) domain, the boundary is much simpler. The domain is bounded by the lines $\eta = 1-\xi$, $\eta = 0$, and $\xi = 0$. Because the domain boundaries are simpler functions than in the original domain, generating a random point in the transformed triangle will be much easier than in the original domain. For a point (ξ,η) to lie in the transformed domain, ξ can take on values $\xi \in [0,1]$, while η can take on values, $\eta \in [0,1-\xi]$. The transformation from the (x,y) domain to the (ξ,η) domain ensures one-to-one point correspondence. Thus, a random point generated in the transformed domain has a corresponding point in the (x,y) domain.

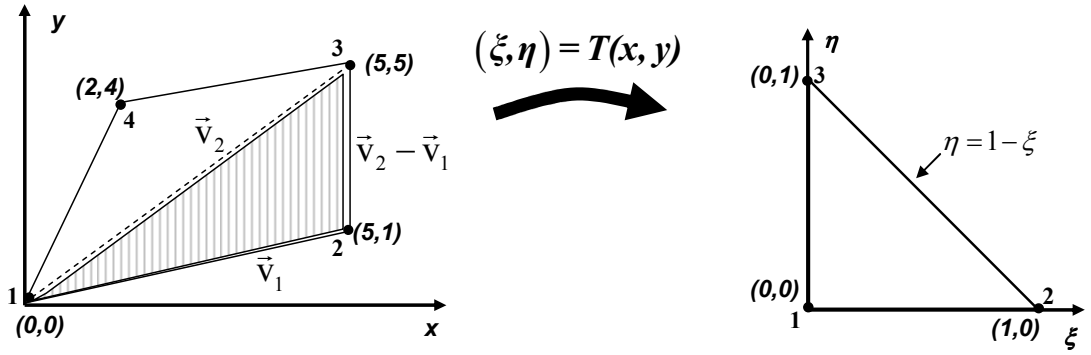

Figure 79. The triangle in the (x,y) domain is morphed (transformed) into the (ξ,η) domain according to the transformation, $T(x,y)$. The vector $\vec{v}_1$ is morphed into the vector ξ=(1,0); the vector $\vec{v}_2$ is morphed into the vector η=(0,1); the vector $\vec{v}_2 - \vec{v}_1$ is morphed into the hypotenuse $\eta = 1-\xi$. The transformed triangle has legs of length one, and is bounded by $\xi = 0$, $\eta = 0$, and $\eta = 1-\xi$.

How to Transform the Domain

The challenge lies in determining how to relate a point in the (x,y) domain to a point in the (ξ,η) system, and vice-versa. First, note that the vertices in the shaded triangle (Figure 79) correspond to the vertices of the triangle in the (ξ,η) domain. We choose one vertex in the (x,y) domain to be the "origin" and the remaining two vertices will be used to construct two

vectors. For this example, we choose the origin vertex to be point 1. The first vector, $\vec{v}_1$ will be directed from point 1 to point 2; the other vector, $\vec{v}_2$ will be directed from point 1 to point 3:

$$\vec{v}_1 = pt2 - pt1 = (5,1) - (0,0) = (5,1)\,;\ \vec{v}_2 = pt3 - pt1 = (5,5) - (0,0) = (5,5)$$

The vectors $\vec{v}_1$ and $\vec{v}_2$ provide a mapping from one coordinate system to another in the following way:

$$\begin{pmatrix} x \\ y \end{pmatrix} = \overset{\vec{v}_1\ \vec{v}_2}{\begin{bmatrix} 5 & 5 \\ 1 & 5 \end{bmatrix}} \begin{pmatrix} \xi \\ \eta \end{pmatrix}, \quad \text{where } A = \begin{bmatrix} 5 & 5 \\ 1 & 5 \end{bmatrix} \text{ and } A^{-1} = \frac{1}{20}\begin{bmatrix} 5 & -5 \\ -1 & 5 \end{bmatrix}$$

The coordinates $(0,0)$, $(5,1)$, and $(5,5)$ in the (x,y) domain define the bounds of the (ξ,η) domain as shown below:

$$\begin{pmatrix} \xi \\ \eta \end{pmatrix} = A^{-1}\begin{pmatrix} x \\ y \end{pmatrix} = \frac{1}{20}\begin{bmatrix} 5 & -5 \\ -1 & 5 \end{bmatrix}\begin{pmatrix} x \\ y \end{pmatrix}$$

For $(x,y) = (0,0)$:

$$\begin{pmatrix} \xi \\ \eta \end{pmatrix} = \frac{1}{20}\begin{bmatrix} 5 & -5 \\ -1 & 5 \end{bmatrix}\begin{pmatrix} 0 \\ 0 \end{pmatrix} = \begin{pmatrix} 0 \\ 0 \end{pmatrix}$$

For $(x,y) = (5,1)$:

$$\begin{pmatrix} \xi \\ \eta \end{pmatrix} = \frac{1}{20}\begin{bmatrix} 5 & -5 \\ -1 & 5 \end{bmatrix}\begin{pmatrix} 5 \\ 1 \end{pmatrix} = \begin{pmatrix} 1 \\ 0 \end{pmatrix}$$

For $(x,y) = (5,5)$:

$$\begin{pmatrix} \xi \\ \eta \end{pmatrix} = \frac{1}{20}\begin{bmatrix} 5 & -5 \\ -1 & 5 \end{bmatrix}\begin{pmatrix} 5 \\ 5 \end{pmatrix} = \begin{pmatrix} 0 \\ 1 \end{pmatrix}$$

This demonstrates that the (x,y) points transform to (ξ,η) points in the following way:

(x,y)		(ξ,η)
$(0,0)$	$\Rightarrow$	$(0,0)$
$(5,1)$		$(1,0)$
$(5,5)$		$(0,1)$

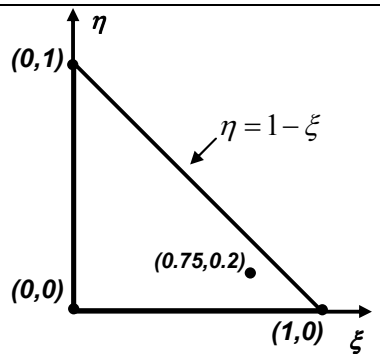

Figure 80. A point, (0.75, 0.2) is generated at random in the (ξ,η) domain. The coordinates lie in the domain bounded by $\xi=\eta=0$ and $\eta=1-\xi$.

The procedure above established how to transform any point from the (x,y) domain to the (ξ,η) domain. We are now ready to select a random point in the (ξ,η) domain and relate it back to a point in the (x,y) domain. The first step is to generate a ξ value between 0 and 1. For this example, ξ is 0.75. Because the domain is bounded by $\eta=0$ and $\eta=1-\xi$, η can assume any value between 0 and $1-\xi$. For this example, η is 0.2. The random point in the (ξ,η) is shown in Figure 80. The points in the (x,y) domain corresponding to $\xi=0.75, \eta=0.2$ are:

$$\begin{pmatrix} x \\ y \end{pmatrix} = \begin{bmatrix} 5 & 5 \\ 1 & 5 \end{bmatrix} \begin{pmatrix} 0.75 \\ 0.2 \end{pmatrix} = \begin{pmatrix} 5*0.75+5*0.2 \\ 1*0.75+5*0.2 \end{pmatrix} = \begin{pmatrix} 4.75 \\ 1.75 \end{pmatrix}$$

As Figure 81 shows, this point safely lies in the (x,y) domain as we desired.

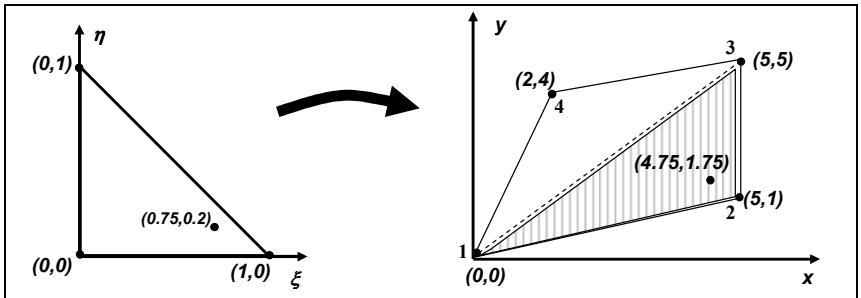

Figure 81. The random point, (0.75,0.2) in the (ξ,η) domain has a corresponding point, (4.75,1.75) in the (x,y) domain.

Additional Example

The quadrilateral in the previous example was a special case in which one of the vertices were at (0,0). A quadrilateral in which none of its vertices are (0,0) is shown in Figure 82. Generating the sample point in this domain corresponds to the general case. As before, we choose at random

whether to generate the random point in the lower or upper triangle. As before, we will assume the lower triangle has been chosen at random.

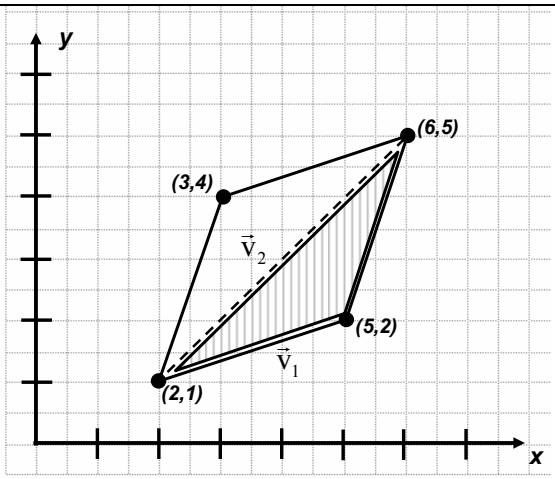

Figure 82. Quadrilateral in which none of the vertices are (0,0). Generating the sample point in this domain corresponds to the general case.

Vectors $\vec{v}_1$ and $\vec{v}_2$ are constructed:

$$\vec{v}_1 = (5,2) - (2,1) = (3,1);\ \vec{v}_2 = (6,5) - (2,1) = (4,4)$$

This leads to the system:

$$\begin{pmatrix} x \\ y \end{pmatrix} = \overset{v_1\ v_2}{\begin{bmatrix} 3 & 4 \\ 1 & 4 \end{bmatrix}} \begin{pmatrix} \xi \\ \eta \end{pmatrix} \text{ where } A = \begin{bmatrix} 3 & 4 \\ 1 & 4 \end{bmatrix} \text{ and } A^{-1} = \frac{1}{8}\begin{bmatrix} 4 & -4 \\ -1 & 3 \end{bmatrix}$$

The vertices of the (ξ, η) domain correspond to the vertices of the (x, y) domain:

$$\begin{pmatrix} \xi \\ \eta \end{pmatrix} = A^{-1}\begin{pmatrix} x \\ y \end{pmatrix} = \frac{1}{8}\begin{bmatrix} 4 & -4 \\ -1 & 3 \end{bmatrix}\begin{pmatrix} x \\ y \end{pmatrix}$$

For $(x, y) = (2,1)$:

$$\begin{pmatrix} \xi \\ \eta \end{pmatrix} = \frac{1}{8}\begin{bmatrix} 4 & -4 \\ -1 & 3 \end{bmatrix}\begin{pmatrix} 2 \\ 1 \end{pmatrix} = \begin{pmatrix} 0.5 \\ 0.125 \end{pmatrix}$$

For $(x, y) = (5,2)$:

$$\begin{pmatrix} \xi \\ \eta \end{pmatrix} = \frac{1}{8}\begin{bmatrix} 4 & -4 \\ -1 & 3 \end{bmatrix}\begin{pmatrix} 5 \\ 2 \end{pmatrix} = \begin{pmatrix} 1.5 \\ 0.125 \end{pmatrix}$$

For $(x, y) = (6, 5)$:

$$\begin{pmatrix} \xi \\ \eta \end{pmatrix} = \frac{1}{8}\begin{bmatrix} 4 & -4 \\ -1 & 3 \end{bmatrix}\begin{pmatrix} 6 \\ 5 \end{pmatrix} = \begin{pmatrix} 0.5 \\ 1.125 \end{pmatrix}$$

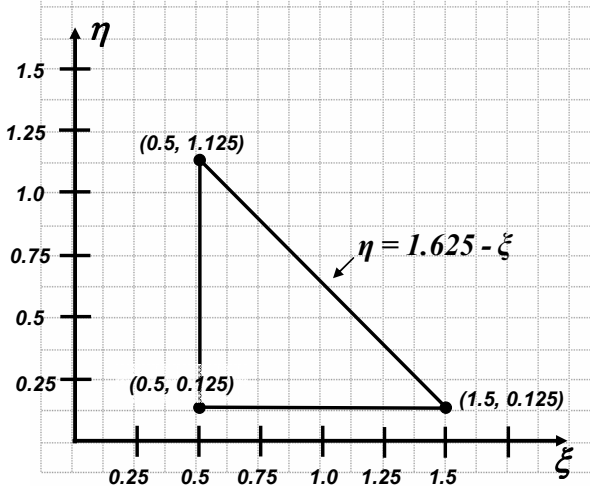

Figure 83. Lower triangle of Figure 82 transformed into the (ξ, η) domain. As noted before, the legs of the triangle have length of one.

Notice that the triangle in the (ξ, η) domain has legs with length one, but that the origin is not at (0,0). This is because the origin of the (x, y) domain was not (0,0), but (2,1). We could choose random points adhering to $\xi \in [0.5, 1.5]$ and $\eta \in [0.125, 1.625 - \xi]$. However, our approach will be to keep the ξ domain as $\xi \in [0,1]$ and η as $\eta \in [0, 1 - \xi]$. We will then shift the coordinates of the random point, offsetting ξ and η by the origin, (0.5, 0.125). Let us assume random ξ and η have been generated as: $\xi = 0.25$, $\eta = 0.5$. Thus the actual random point generated in the transformed triangle is:
$\xi = 0.5 + 0.25 = 0.75$; $\eta = 0.5 + 0.125 = 0.625$. The corresponding random point in the (x, y) domain is:

$$\begin{pmatrix} x \\ y \end{pmatrix} = \begin{bmatrix} 3 & 4 \\ 1 & 4 \end{bmatrix}\begin{pmatrix} 0.75 \\ 0.625 \end{pmatrix} = \begin{pmatrix} 4.75 \\ 3.25 \end{pmatrix}$$

An alternative procedure would be to calculate the point in the (x, y) domain corresponding to $(\xi, \eta) = (0.25, 0.5)$ and perform the shift in the (x, y) domain. For example:

$$\begin{pmatrix} x \\ y \end{pmatrix} = \begin{bmatrix} 3 & 4 \\ 1 & 4 \end{bmatrix}\begin{pmatrix} 0.25 \\ 0.5 \end{pmatrix} = \begin{pmatrix} 2.75 \\ 2.25 \end{pmatrix}$$

We then offset this point by the origin we chose for the (x, y) domain—(2,1). It follows that the random point (x_{random}, y_{random}) is:

$$\begin{pmatrix} x_{random} \\ y_{random} \end{pmatrix} = \begin{pmatrix} 2 \\ 1 \end{pmatrix} + \begin{bmatrix} 3 & 4 \\ 1 & 4 \end{bmatrix} \begin{pmatrix} 0.25 \\ 0.5 \end{pmatrix} = \begin{pmatrix} 2 \\ 1 \end{pmatrix} + \begin{pmatrix} 2.75 \\ 2.25 \end{pmatrix} = \begin{pmatrix} 4.75 \\ 3.25 \end{pmatrix}$$

This offsetting of the (*x,y*) point is the actual implementation in the CCO confined vasculature code. As shown in Figure 84, point (4.75, 3.25) lies safely in the (x, y) domain.

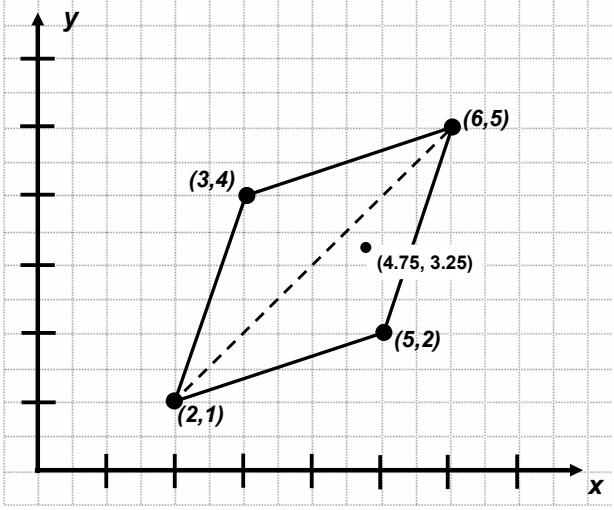

Figure 84. Random point (4.75, 3.25) in the (x, y) domain corresponds to point (0.75, 0.625) in the (ξ, η) domain.

Appendix J: Steps for Preparing Vessel-Brain-CSF Interaction Simulation
Required Steps:

1. Create 2D geometry points for brain and CSF using Image J
    a. Load an image of the brain into Image J and click points making up the boundary of CSF and brain tissue
    b. Export these points in .xls format
    c. Open .xls file and reflect the y-coordinates across the x-axis because otherwise Gambit will read the points upside down.
    d. Scale the points such that the length and width are in SI units and are comparable with real brain dimensions.
2. Import the points into Gambit. In Gambit you will mesh the fluid and solid domains and apply boundary conditions. There is a very strict protocol you should follow. You should know that the fluid and solid faces at the FSI boundary must have a means of communicating with one another. If the node points or boundary face numbers along the interface are the same, it is a straightforward matter to apply the displacements from the solid to the fluid domain. I have ensured that the node points and the boundary face numbers along the FSI boundary are the same by using the following procedure:
    a. Create faces for the fluid and solid domains.
    b. Mesh the edges of the interface (where solid and fluid domains are in contact with one another) first.
    c. Mesh all other edges that are not on the interface.
    d. Mesh faces one at a time. Do not mesh them at the same time. Since you have meshed all the edges already, you should specify Interval count equal to 1.
    e. In my implementation, I used two individual meshes. To do this, I deleted one of the meshes and exported the other. When you delete one of the meshes make sure you do not choose the option "Remove unused lower mesh". If you select that option, you will delete the nodes of the meshed edges. The idea here is to maintain the nodes of the meshed edges so that the node numbers on the interface will be the same.
    f. After you have exported one of the meshes, click the Undo arrow. This will bring back the mesh you just deleted. Since you now want to export the other mesh, delete the mesh you exported previously. After you have deleted that mesh (again being careful not to select "Remove unused lower mesh"), export the second mesh.
3. Create a vessel base tree structure (BTS) using the Network Viewer project in Delphi
    a. Load an image of vasculature, either a histological image or an accurate artistic rendering
    b. Select points that follow the trajectory of the vessels.
    c. Join points always from proximal to distal
    d. All this is documented in a conversation with Nick Vaičaitis. The recordings are included in my DVD package.
4. Using the Vasculature Generation application, load the brain mesh created in Gambit and the BTS that was created in Network Viewer
5. Click the Rough Scale button and position/anchor the vasculature to the brain mesh
6. Add a vessel growth stage

7. After generation, compare the root radius of the original BTS file and the newly generated vasculature file. Determine the scaling factor by dividing the first point (x-coordinate needed only) of the new file by the first point of the BTS file.
8. In the Vasculature Generation tree viewer, find the Gambit Reader source pascal file. Find the readpointcoordinate procedure. Change the scale from 1 to 1/value determined in step 7.
9. Load the brain mesh and the newly formed vasculature file. As the vasculature file gets loaded, it gets scaled down to its proper physiological size.
10. Enter a value in the Edit 1 box for the root radius. Click the Qterm variable button and save the file. All downstream radii are updated when you perform this procedure.
11. To verify the scaled-down vasculature fits in the brain mesh, change the scale in Gambit Reader source back to 1.
12. To link the vasculature with the brain mesh, run the Search Algorithm in the FSI code.

VITA

I. PROFESSIONAL EXPERIENCE

A. Education

Graduate Student Research Assistant, University of Illinois at Chicago, 2007-date.
Bioengineering, M.S., University of Illinois at Chicago, 2007.
Biochemistry, B.S., University of Illinois at Chicago, Honors College, 2001.

B. Awards and Honors

1. Chancellor's Supplemental Graduate Fellowship, 2011. University of Illinois at Chicago, Chicago, IL.
2. Chancellor's Supplemental Graduate Fellowship, 2010. University of Illinois at Chicago, Chicago, IL.
3. ADINA News, October 2010. Highlighting published work from Cerebrospinal Fluid Flow Dynamics in the Central Nervous System, *Annals of Biomedical Engineering*, 2010. http://www.adina.com/newsgH77.shtml accessed November 5, 2010.
4. ADINA News, February 2010. Highlighting published work from Normal and hydrocephalic brain dynamics—the role of reduced cerebrospinal fluid reabsorption in ventricular enlargement, *Annals of Biomedical Engineering*, 2009. http://www.adina.com/newsgH64.shtml, accessed April 9, 2010.
5. 1st Place, Student Research Forum Competition. "A Poroelastic-Fluid Interaction Model to Quantify Human Brain Intracranial Dynamics," Poster 146, April 2009, University of Illinois at Chicago, Chicago, IL.
6. Graduate Student Council Travel Award, 2008. University of Illinois at Chicago, Chicago, IL.

C. Industrial Experience

1. Math and Chemistry Instructor, American School of Correspondence, Lansing, IL, 1999-2003.
2. Scientist, Silliker Laboratories, South Holland, IL, 2001-2002.
3. Science Teacher, Eastern Christian Middle School, Wyckoff, NJ, 2003-2004.
4. Math Teacher, Block Junior High, East Chicago, IN, 2003-2005.

II. PUBLICATIONS

A. Papers in Refereed Journals

1. **B. Sweetman** and A. Linninger. Cerebrospinal fluid flow dynamics in the central nervous system. *Annals of Biomedical Engineering*. 39(1):484-496. 2011.
2. **B. Sweetman**, M. Xenos, L. Zitella, and A. Linninger. Three-dimensional computational prediction of cerebrospinal fluid flow in the human brain. *Computers in Biology and Medicine*. **41**(2):67-75. 2011.
3. R. Penn, S. Basati, **B. Sweetman**, X. Guo, A. Linninger. Ventricular wall movements and CSF flow in hydrocephalus. *Journal of Neurosurgery,* Published online, February, 2011, DOI: 10.3171/2010.12.JNS10926.

4. A. Linninger, **B. Sweetman**, and R. Penn. Normal and hydrocephalic brain dynamics—the role of reduced cerebrospinal fluid reabsorption in ventricular enlargement. *Annals of Biomedical Engineering*. **37**(7):1434-1447. 2009.
5. A. Linninger, M. Xenos, **B. Sweetman**, S. Ponkshe, X. Guo, and R. Penn. A mathematical model of blood, cerebrospinal fluid and brain dynamics. *Journal of Mathematical Biology*. DOI 10.1007/s00285-009-0250-2, 2009.
6. G. Liao, M. Kreitzer, **B. Sweetman**, and J. Leonard. The Postsynaptic Density Protein PSD-95 Differentially Regulates Insulin- and Src-Mediated Current Modulation of Mouse NMD A Receptors Expressed in Xenopus Oocytes. *Journal of Neurochemistry*. **75**(1):282-287. 2000.

B. Refereed Proceedings Articles

1. B. Sweetman, S. Basati, M. Iyer, and A. Linninger, "Mathematical modeling—knowledge acquisition about brain physics". Foundations of Computer-Aided Process Design, Beaver Run Resort, Breckenridge, Colorado, June 7 - 12, 2009, Poster #65.
2. B. Sweetman, S. Basati, M. Iyer, and A. Linninger, "Modeling and design of distributed systems; methods and algorithms". 10th International Symposium on Process Systems Engineering, Salvador-Bahia-Brazil, August 16–20, 2009, Paper, 227-1.

C. Abstract, Posters and Presentations at Technical Conferences and Meetings

1. B. Sweetman, N. Vaičaitis, O. Ivanchenko, and A.A. Linninger. "A fluid-structure interaction model for cerebral vasculature, brain tissue, and cerebrospinal fluid". Optimization and Control, Biomedical engineering. 21st European Symposium on Computer-Aided Process Engineering; Porto Carras, Chalkidiki, Greece. May 29-June 1, 2011.
2. B. Sweetman, A. Linninger, and R. Penn. "Measurements and Computational Modeling of Cerebrospinal Fluid Flow in Humans". Systems Biology, Bioinformatics and Computational Biology. Oral Presentation. BMES 2010 Annual Fall Meeting, October 6–9, 2010; Austin Convention Center, Austin, TX.
3. B. Sweetman, R. Penn, and A. Linninger. "Three-dimensional Cerebrospinal Fluid Flow Model of the Central Nervous System". Extended Abstract Submitted for Student Award. BMES 2010 Annual Fall Meeting, October 6–9, 2010; Austin Convention Center, Austin, TX.
4. A.A. Linninger and B. Sweetman. "Brain Research with ANSYS FLUENT." Presentation at the 2010 ANSYS Regional Conferences, Hyatt Lodge, Oak Brook, IL, June 7, 2010.
5. B. Sweetman and A. Linninger. "Experimental measurements and computational prediction of cerebrospinal fluid flow in the human brain." Poster 185. UIC Student Research Forum, April 20, 2010, University of Illinois at Chicago, Chicago, IL.
6. B. Sweetman, O. Ivanchenko, N. Sindhwani, and A. Linninger. "Stress Analysis in Porous Media Due to Convection Enhanced Delivery". Poster 134. UIC Student Research Forum, April 2009, University of Illinois at Chicago, Chicago, IL.
7. B. Sweetman, A. Linninger, and R. Penn. "A Poroelastic-Fluid Interaction Model to Quantify Human Brain Intracranial Dynamics". Poster 146. UIC Student Research Forum, April 2009, University of Illinois at Chicago, Chicago, IL.
8. B. Sweetman, S. Basati, M. Iyer, and A. Linninger. "Mathematical modeling—knowledge acquisition about brain physics". Foundations of Computer-Aided Process Design, Beaver Run Resort, Breckenridge, Colorado, June 7 - 12, 2009, Poster #65.

9. B. Sweetman, S. Basati, M. Iyer, and A. Linninger. “Modeling and design of distributed systems; methods and algorithms”. 10th International Symposium on Process Systems Engineering, Salvador-Bahia-Brazil, August 16–20, 2009, Paper, 227-1.
10. O. Ivanchenko, B. Sweetman, N. Sindhwani, and A. Linninger. “Stress Analysis in Porous Media Due to Convection Enhanced Delivery”. 10th US National Congress on Computational Mechanics, Columbus, Ohio, Session 2.3.1, July 16-19, 2009.
11. B. Sweetman, S. Basati, M. Harihara Iyer, and A. Linninger. “A Poroelastic-Fluid Interaction Model to Quantify Human Brain Intracranial Dynamics”. Student Poster Session; Poster 9, Midwest Biomedical Engineering Conference, April 4, Illinois Institute of Technology, Chicago, IL, 2008.
12. M. Harihara Iyer, S. Basati, B. Sweetman, and A. Linninger. “Convection Enhancement of Drug Delivery to the Brain”. Student Poster Session; Poster 15, Midwest Biomedical Engineering Conference, April 4, Illinois Institute of Technology, Chicago, IL, 2008.
13. S. Basati, M. Harihara Iyer, B. Sweetman, and A. Linninger. “An Impedance Sensor to Monitor Cerebral Ventricular Volume”. Student Poster Session; Poster 11, Midwest Biomedical Engineering Conference, April 4, Illinois Institute of Technology, Chicago, IL, 2008.
14. B. Sweetman, A. Politis, and A. Linninger. “Finite Element Brain Model and Cerebral Vasculature for the Prediction of Pathological CSF Flow”. Computational Biology, Poster Session 6, P6.63. BMES 2008 Annual Fall Meeting, October 2-4, Renaissance Grand Hotel, St. Louis, MO, 2008.
15. A. Linninger, S. Basati, and B. Sweetman. “An Impedance Sensor to Monitor Cerebral Ventricular Volume”. Nano to Micro, Poster Session 5, P5.88. BMES 2008 Annual Fall Meeting, October 2-4, Renaissance Grand Hotel, St. Louis, MO, 2008.
16. A. Linninger, M. Harihara Iyer, M. Somayaji, S. Basati, B. Sweetman, and A. Politis. “Computational Approach for Predicting Transport of Macromolecules in the Brain Interstitium”, Computational Biotransport and Drug Delivery, Session 410. BMES 2008 Annual Fall Meeting, October 2-4, Renaissance Grand Hotel, St. Louis, MO, 2008.
17. R. Penn, B Sweetman and A. Linninger. “Blood cerebral spinal fluid and brain dynamics in communicating hydrocephalus”. Hydrocephalus Congress 2008, Paper O.010, Hannover, Germany, September 17-20, 2008.
18. N. Shamsi, B. Sweetman, and A. Linninger. “Modeling Cerebral Blood Flow”. 19th Annual Argonne Symposium for Undergraduates in Science, Engineering and Mathematics. November 7-8, 2008. Argonne National Laboratory, APS Conference Center, Argonne IL.
19. M. Xenos, S. Ponkshe, B. Sweetman, and A. Linninger. “Intracranial Dynamics and Transport Phenomena of Neurotransmitters in Normal and Hydrocephalic Humans”. AIChE Annual Meeting, November 4-9, Salt Lake City, UT, 2007.
20. B. Sweetman, K. Tawse, M. Xenos, and A. Linninger. “Poroelastic-Fluid Interaction and the Prediction of Pathological Intracranial Dynamics in the Human Brain”. AIChE Annual Meeting, November 4-9, Salt Lake City, UT, 2007.
21. M. Xenos, M.R. Somayaji, B. Sweetman, and A. Linninger. “A Computational Approach to Soft-Tissue Fluid-Structure Interaction”. Paper 226i, AIChE Annual Meeting, November 12 - 17, San Francisco, CA, 2006.

D. Other Publications

1. A. Linninger, B. Sweetman and R. Penn. “Image Reconstruction and Computational Analysis for Quantifying Brain Physics”, Mimics Innovation Award, 2009.
2. S. Thomas, S. Naik, B. Sweetman, A. Linninger. “Computer Generation of Three Dimensional Human Cerebral Vasculature Models”, *Journal of Young Investigators*, 2009. **19**(17):1-8.

E. Technical Reports

1. B. Sweetman and S. Basati. "Summary of Hydrocephalus Literature". LPPD, 2007.
2. B. Sweetman and A. Linninger. "Finite Strain Theory". LPPD, 2008.
3. A. Politis, M. Xenos, B. Sweetman, and A. Linninger. "File Formats for Unstructured Computational Meshes: Gambit Meshfile (*msh) in 2- and 3-D". LPPD, 2008.
4. B. Sweetman, L. Zitella and A. Linninger. "Hyperbolic (Wave) and Parabolic (Diffusion) Partial Differential Equations and their Applications to Vasculature Dynamics". LPPD, 2008.
5. B. Sweetman and A. Linninger. "Force is a Flux". LPPD, 2009.
6. B. Sweetman, A. Linninger, and N. Vaičaitis. "Constrained Constructive Optimization for Vascular Generation". LPPD, 2010.

III. TEACHING EXPERIENCE

A. Classroom Instruction

1. Math and Chemistry Instructor, American School of Correspondence, Lansing, IL, 1999-2003.
2. Science Teacher, Eastern Christian Middle School, Wyckoff, NJ, 2003-2004.
3. Math Teacher, Block Junior High, East Chicago, IN, 2003-2005.

B. Mentoring of Undergraduate Students

1. Kirstin Tawse, “Cerebrospinal Fluid-Tissue Interactions in the Human Brain”, 2006.
2. Nabiha Shamsi, “Cerebral Vasculature Reconstruction & Modeling”, 2008.
3. Laura Zitella, “Three Dimensional Fluid-Structure Interaction Model of the Human Brain”, 2008-date.
4. Smit Naik, “Algorithms for Microvasculature Reconstruction”, 2009.
5. Shinita Thomas, “Microvasculature Reconstruction & Modeling”, 2009.
6. Dexter Teng, “Generated Models of the Microvasculature Using Constrained Constructive Optimization”, 2010.
7. Nicholas Vaičaitis, “Computational Modeling of Cerebral Vasculature”, 2010.